University of Sheffield

Microscale imaging of novel porous media used in polymer electrolyte fuel cells

by:

Mustafa ERCELIK

A Thesis submitted in accordance with the requirements for the degree of Doctor of Philosophy

The University of Sheffield

Faculty of Engineering,

Department of Mechanical Engineering

Energy 2050

December, 2024

The candidate confirms that the work submitted is his own and that appropriate credit has been given where reference has been made to the works of others.

This copy has been supplied on the understanding that it is a copyright material and that no quotation from the thesis may be published without proper acknowledgement.

The right of Mustafa Ercelik to be identified as Author of this work has been asserted by his in accordance with the Copyright, Designs and Patents Act 1988.

ABSTRACT

The polymer electrolyte fuel cell (PEFC) is a promising clean power conversion technology that directly converts chemical energy into electrical energy at relatively low operation temperatures. A wet-proofed, porous layer located between the catalyst layer and flow-field plate in the PEFC is termed as the gas diffusion layer (GDL). The commercially available GDLs are mostly made of electrically conductive carbon fibre-based materials. However, such materials are likely to be subject to different types of degradation. Hence, many studies have been conducted to investigate alternative materials for the GDLs.

Metal foams have attracted a good deal of attention to be used as GDL materials and this is due to their appealing features: high mechanical strength, high and controllable porosity, high electrical and thermal conductivity, and high specific surface area. Nickel (Ni) foam is particularly of great interest to PEFC developers, and this is owing to, in addition to the above-mentioned features, its relatively high corrosion resistance. To this end, the main aim of this work is to further explore the viability of the use of nickel foams for PEFC GDLs.

The first phase of this thesis focuses on developing a computationally economical X-ray computed tomography (X-ray CT) framework to precisely estimate the crucial structural and transport properties of nickel foam-based GDL. The findings indicate that the nickel foam-based GDL shows a greater level of uniformity and isotropy in comparison to the traditional carbon-based GDLs, along with enhanced structural

and transport properties, thereby reinforcing its potential as a suitable GDL material for PEFC applications.

The second phase of the thesis is to investigate the effects of compression on the key structural and transport characteristics using a custom-built compression device and X-ray computed tomography-based models. A key discovery from this research is that, in contrast to porosity and ligament thickness, the average pore size considerably decreases with compression. Moreover, the study revealed that the gas permeability, as opposed to effective diffusivity, exhibits a significant degree of anisotropy under compression. This observation is critical for PEFC modelling, as the GDL properties are commonly assumed to be isotropic.

The last phase of the thesis presents a three-dimensional model that was developed to study the impact of the compression imposed by the ribs of the bipolar plates on the fuel cell performance operating with carbon fibre-based or nickel foam-based GDLs. The findings show that the nickel foam-based GDLs display a significantly more uniform oxygen and water distribution than the conventional carbon-based counterpart. Notably, while reduced channel sizes tend to improve cell performance, they also demand increased pumping power because of substantial pressure drop in the flow channels. For the carbon-based PEFCs, the highest net power density observed was 0.473 W/cm^2 with 1 mm channel height and 0.75 mm channel width. Conversely, the nickel foam-based PEFCs reached the highest net power density at 0.945 W/cm^2 with a channel height of 0.25 mm and a width of 1 mm.

ACKNOWLEDGEMENT

First and foremost, I would like to express my deepest gratitude to my supervisors: Dr Kevin J. Hughes, Dr Mohammed S. Ismail, Professor Derek B. Ingham, Professor Mohamed Pourkashanian, and Professor Lin Ma for their endless support and countless scientific discussions.

My gratitude extends to the Republic of Turkey Ministry of National Education for financial supporting my PhD study at the University of Sheffield. Without their support, I could not have started this fantastic scientific journey in the UK.

I extend my thanks to my fuel cell research group friends for their friendship: Jinbei, Fernando, Florence, Fatma, Isaac, Fahad, and Allan. I will miss our Tuesday morning coffees, guys. Thanks also to my Energy2050 research group friends: Wenjun, Lei, Celal and Suleyman. I would also like to thank my friends in Sheffield: Dr Merve Kuman, Dr Aytac Gul and Dr Yunus Celik.

Special thanks to Professor Enrico Dall'Ara and Dr Amnael Orozco from the Skeletal Analysis laboratories for granting me full access to the X-ray computed tomography facility and for their kind help.

Last but not least, I would like to express my sincere appreciation to Cansel Kocakabak for her unwavering support and understanding.

DEDICATION

This thesis is devoted to the lives lost in the devastating Turkey-Syria earthquake and to the loved ones they left behind.

PUBLICATIONS, CONFERENCES AND WORKSHOPS

A-) Journal Papers

The work in ***Chapter-3*** of this thesis has appeared in the publication as follows:

1- **Ercelik, M.**, Ismail, M. S., Ingham, D. B., Hughes, K. J., Ma, L., & Pourkashanian, M. (2023). Efficient X-ray CT-based numerical computations of structural and mass transport properties of nickel foam-based GDLs for PEFCs. Energy, 262, 125531. DOI: https://doi.org/10.1016/j.energy.2022.125531.

The work in ***Chapter-4*** of this thesis has appeared in the publication as follows:

2- **Ercelik, M.**, Ismail, M. S., Hughes, K. J., Ingham, D. B., Ma, L., & Pourkashanian, M. (2024). X-ray CT-based numerical investigation of nickel foam-based GDLs under compression. International Journal of Hydrogen Energy, 50, 1338-1357. DOI: https://doi.org/10.1016/j.ijhydene.2023.07.001.

The work in ***Chapter-5*** of this thesis has appeared in the publication as follows:

3- **Ercelik, M.**, Ismail, M. S., Hughes, K. J., Ingham, D. B., Ma, L., & Pourkashanian, M. (2024). Polymer electrolyte fuel cell operating with nickel foam-based gas diffusion layers: a numerical investigation. International Journal of Hydrogen Energy. (In press). https://doi.org/10.1016/j.ijhydene.2024.05.084.

B-) Poster Presentations

1- **Ercelik, M.**, Ismail, M. S., Ingham, D. B., Hughes, K. J., Ma, L., & Pourkashanian, M. (2021). The Impact of Compression on Nickel Foam Based GDL Properties. 1st UK-Japan Symposium on Advanced Materials for Hydrogen and Fuel Cells.

- The poster presentation was awarded first prize in the symposium.

2- **Ercelik, M.**, Ismail, M. S., Ingham, D. B., Hughes, K. J., Ma, L., & Pourkashanian, M. (2024). Nickel Foam-based Gas Diffusion Layers. 2nd UK-Japan Symposium on Advanced Materials for Hydrogen and Fuel Cells.

CONTENTS

LIST OF FIGURES

LIST OF TABLES

NOMENCLATURE

Abbreviations

ACL	Anode catalyst layer
AFFP	Anode flow-field plate
AFC	Alkaline fuel cell
AFM	Atomic force microscopy
AGDL	Anode gas diffusion layer
AMPL	Anode microporous layer
BTU	British thermal unit
BET	Brunauer–Emmett–Teller
CCL	Cathode catalyst layer
CFD	Computational fluid dynamics
CFFP	Cathode flow-field plate
CFSF	Copper fibre sintered felt
CGDL	Cathode gas diffusion layer
CHP	Combined heat power
CL	Catalyst layer

CMPL	Cathode microporous layer
CT	Computed tomography
DMFC	Direct methanol fuel cell
DSC	Differential scanning calorimetry
EDS	Energy dispersive spectroscopy
EVs	Electric vehicles
FCEVs	Fuel cell electric vehicles
FFP	Flow-field plate
FIB-SEM	Focused ion beam scanning electron microscopy
GDL	Gas diffusion layer
HOR	Hydrogen oxidation reaction
HT-PEFC	High temperature-Polymer electrolyte fuel cell
ICEVs	Internal combustion engine vehicles
Inc.	Incorporation
Ind.	Industry
M	Membrane
MEA	Membrane electrode assembly
MFC	Microbial fuel cell

MIP	Mercury intrusion porosimetry
MOR	Methanol oxidation reaction
MPL	Microporous layer
MPS	Microporous substrate
MRI	Magnetic resonance imaging
MSR	Methanol stream reformer
NASA	The National Aeronautics and Space Administration
NR	Neutron radiography
ORC	Organic Rankine cycle
ORR	Oxygen reduction reaction
PEFC	Polymer electrolyte fuel cell
PEMEC	Proton exchange membrane electrolyser cell
PFSA	Perfluorosulfononic acid
PPI	Pores per inch
PTFE	Polytetrafluoroethylene (Teflon)
RVE	Representative volume element
SEM	Scanning electron microscopy
SOFC	Solid oxide fuel cell

SSA	Specific surface area (m^{-1})
SSSFF	Sintered stainless steel fibre felt
TGA	Thermogravimetric analysis

Symbols

A	Cell active area (cm^2)
C	Concentration (mol/m^3)
ΔC	Concentration difference (mol/m^3)
C_p	Isobaric specific heat capacity (J/(kg·K))
D	Diffusion coefficient (cm^2/s)
D_{O2}	Bulk oxygen diffusivity into nitrogen (cm^2/s)
D_{ij}^{eff}	Effective diffusivity of the species *i* into species *j* (cm^2/s)
E_{cell}	Cell power density (W/cm^2)
E_{pump}	Required pumping power density (W/cm^2)
E_{Net}	Net power density (W/cm^2)
F	Faraday's constant (C/mol)
h	Channel height (mm)
i	Volumetric current densities

i_a^{ref}	Reference current density of anode
i_c^{ref}	Reference current density of cathode
$\boldsymbol{I}$	Identity matrix
J	Molar flux (mol/(m^2·s))
k	Specific heat ratio of air (-)
K	Permeability (m^2)
L	Length (mm)
$\dot{m}_{air}$	Air mass flow rate (kg/s)
M_k	molecular weight of species k (kg·mol^{-1})
ΔP	Pressure difference (Pa)
R	Universal gas constant (J/(mol·K))
S	Source term
T	Temperature (°C)
u	Fluid velocity (m/s)
u_{mag}	Velocity magnitude (m/s)
u_x	Velocity in through-plane direction (m/s)
u_y	Velocity in in-plane direction (m/s)
V	Cell voltage (V)

w	Channel height (mm)
X_{comp}	Compression ratio (-)
X_k	Mass fraction of species k
$X_{H_2}^{ref}$	Hydrogen mass fraction at reference conditions
$X_{O_2}^{ref}$	Oxygen mass fraction at reference conditions

Chemical Symbols

CO_2	Carbon dioxide
e^-	Electron
H^+	Hydrogen ion
H_2	Hydrogen
KOH	Potassium hydroxide
$LaCoO_3$	Lanthanum cobaltite
$LaFeO_3$	Lanthanum ferrite
$LaMnO_3$	Lanthanum manganite
Ni	Nickel
O_2	Oxygen
Pt/C	Carbon-supported platinum

Pt-Ru/C	Carbon-supported platinum – ruthenium
SO_3H^+	Sulfonic acid
Y_2O_3	Yttrium (III) oxide
YSZ	Y_2O_3 stabilized ZrO_3
ZrO_3	Zirconate

Greek Symbols

a_a	Anode specific surface areas
a_c	Cathode specific surface areas
$\alpha_{a,a}$	Anodic charge transport coefficient at anode electrode
$\alpha_{a,c}$	Cathodic charge transport coefficient at anode electrode
$\alpha_{c,a}$	Anodic charge transport coefficient at cathode electrode
$\alpha_{c,c}$	Cathodic charge transport coefficient at cathode electrode
ϕ_s	Electrical potentials of solid phase
ϕ_l	Electrical potentials of membrane phase

ε	Porosity
ρ	Fluid density (kg/m^3)
μ	Dynamic viscosity of fluid (Pa·s)
λ	Thermal conductivity (W/m·K)
τ	Tortuosity (-)
η_{comp}	Efficiency of compressor
$\eta_{act,a}$	Anodic activation overpotential (V)
$\eta_{act,c}$	Cathodic activation overpotential (V)

Subscripts & superscripts

a	Anode
air	Air
ave	Average
c	Cathode
cell	Cell
comp	Compressor
eff	Effective
exp	Experimental

H_2	Hydrogen
i,j	The species i into species j
inlet	Inlet
IP	In-plane
k	Species k
m	Mass
mag	Magnitude
Net	Net
outlet	Outlet
O_2	Oxygen
pump	Pumping
ref	Reference conditions
TP	Through-plane
x	x-direction
y	y-direction

Chapter 1

Introduction to Fuel Cell Technologies

1.1 INTRODUCTION

The polymer electrolyte fuel cell (PEFC) is a promising clean power conversion technology that converts chemical energy to electrical energy at low operation temperatures efficiently without any combustion process. There is a great number of PEFC-employing applications ranging from small electronic devices such as mobile phones to automotive (e.g. buses) and stationary power plants [1–3].

The cathode electrode is the main source of the performance loss of PEFC due to the low utilization of the cathode catalyst and the slow reaction rate [4]. Therefore, the main aim of this project is to image and investigate the conventional and state-of-

the-art cathode electrodes using X-ray computed tomography (X-ray CT). These captured images will be used to obtain insights into how to better design the cathode electrodes through first performing pore-scale simulations and to extract effective morphological and transport parameters.

1.2 CLEAN ENERGY DEMAND

One of the crucial problems the world is facing is to fulfil the energy demand of human beings with sustainable, clean, and suitable ways [2]. In previous decades, the world has undergone rapid climate change [5]. Clearly, the main contribution to this crucial problem is the production of carbon dioxide (CO_2) by fossil fuel combustion. To date, fossil fuels have been widely utilized in order to meet people's enhancing needs. More than 70% of the world's electrical energy is generated by fossil fuels [6]. This fuel combustion process to generate energy has caused the greenhouse effect by produced CO_2. Figure 1.1 interprets the energy consumption in different sectors in quadrillion British Thermal Unit (BTU) from 2010 to 2020 [7]. It is apparently seen that the transportation sector is the most dominant fraction of the global energy utilization. To exemplify, in 2014, the transportation sector comprised of in the order of 55% of the global total energy consumption and 30.9% of the CO_2 emission [7]. Since the outset of the 20th century, both greenhouse gasses and global temperature are inclined to increase exponentially with time [8].

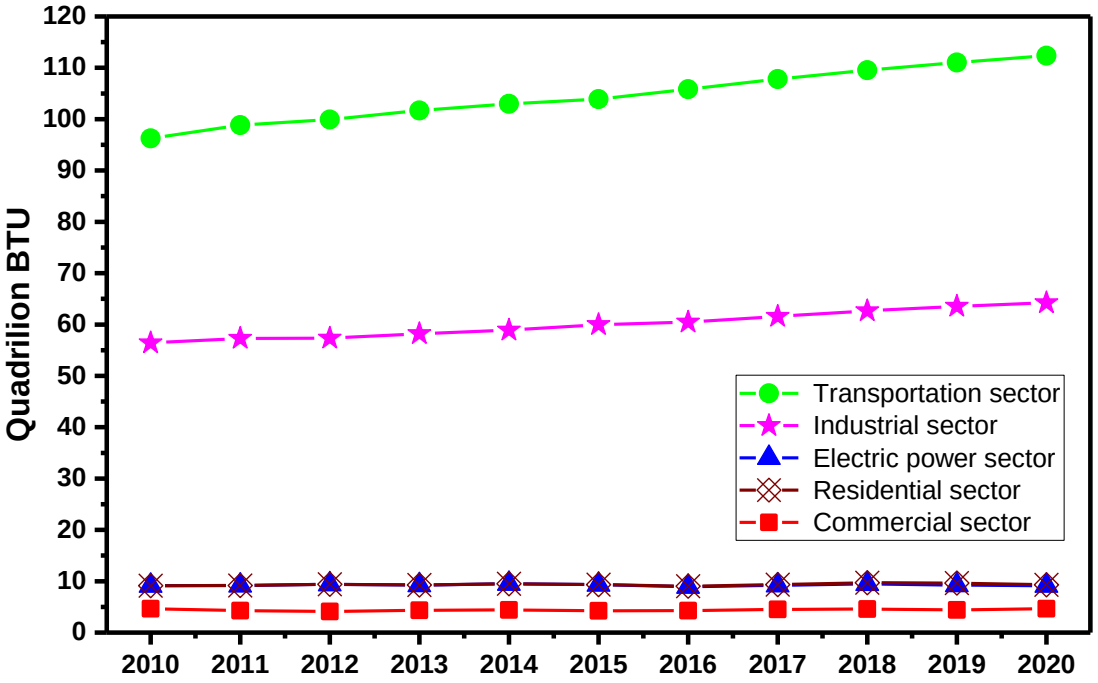

Figure 1. 1 – Energy consumption in different sectors between 2010 and 2020 (adapted from [8]).

Fossil fuels are not only unsustainable and contaminant but also they are inclined to be affected by economic and political issues between countries. To exemplify, the Arab-Israeli conflict in October 1973 ignited the 1973 oil crisis which is also called "the first oil shock" and the price of oil sharply quadrupled from 3 $/barrel to 11.65 $/barrel [9,10]. In subsequent years, governments have understood the importance of alternative energy systems such as solar, wind, ocean-wave, and hydropower so as to take measures [11]. In terms of the transportation sector, this crisis has pushed not only governments but also scientists and entrepreneurs to develop oil-free technologies to apply in vehicles [8]. It is foreseen that the oil demand for using vehicles will have considerably abated by the 2020s, albeit the growing global car

sector (the number of cars will have doubled by 2040) [12]. In addition, the quantity of electric vehicles will have reached 900 million by 2040 due to supplementary policies and infrastructural investments.

All around the world, the electric vehicle technology is thought to be due to their both environment-friendly and low energy cost feature [8]. In terms of operation costs, electric vehicles (EVs) are much more economical than internal combustion engine vehicles (ICEVs). The operation cost of EVs is 2 cents per mile, while that of ICEVs is 12 cents per mile [13]. Moreover, an average ICEV driver wastes approximately 41 hours and 40 minutes per year at gas stations to purchase fuel. In addition, EVs are extremely convenient to be integrated with cutting-edge-technology electricity generation techniques, such as fuel cells, solar panels, as well as regenerative braking systems. During the last decade, there remains numerous researches with regards to fuel cell applications on EVs [14–16]. Fuel cell electric vehicles (FCEVs) utilize electricity, such as conventional EVs but their electricity source is a fuel cell stack rather than batteries [2]. The first time a fuel cell powered electric vehicle, named Electrovan, was launched commercially was in 1966 by General Electric [17]. An alkaline fuel cell system and pressurized hydrogen and oxygen tanks were employed in this vehicle. In the last decade, the polymer electrolyte fuel cell (PEFC) has been widely used in FCEVs due to its inherent advantages [18]. The PEFC-based FCEVs use pure hydrogen and oxygen and therefore only pure water is emitted rather than traditional tailpipe pollutants. Furthermore, this sort of fuel cell exhibits high power density and their operation temperature

ranges are fairly low (60 – 80°C). In 2004, the Japanese industrial giant Honda introduced their PEFC-powered FCEVs, the model FCX Clarity. They had developed this vehicles by 2007. In 2007, the model FCX Clarity which is the first PEFC-powered car was presented in Los Angeles [19]. The other breakthrough moment was the announcement of Toyota's new PEFC-powered FCEVs MIRAI, which means "the future" in Japanese, with an affordable price ($57,500) in December 2014 [20]. Other renowned PEFC-powered FCEVs are Nissan X – Trail FCV 04, Benz F – Cell, Mercedes – Benz F800, Hyundai Tucson Fuel Cell, Hyundai ix35 FCEV, Ford Focus FCV, Volkswagen Golf Hymotion, and Kia Borrego FCEv [7,16]. Even though PEFC-powered FCEV technology is seen to be highly promising, there remains many challenges to be overcome in order to increase PEFC performance. The main problems are the degradation phenomenon of the PEFC components, flooding-sourced performance losses, highly costly materials used in catalyst layer, and life duration.

1.3 FUEL CELL TECHNOLOGY

Previous studies predominantly defined the fuel cell as an electrochemical device which transposes the chemical energy of fuels and oxidants to useful electrical energy without any combustion reaction [1,21,22]. Unlike batteries, fuel cells are able to generate electricity as long as fuel and oxidants are supplied. This is the paramount difference between a fuel cell and a battery.

The basic principles of the fuel cell were discovered by Christian Schonbein in 1838. Due to the observations of Mr Schonbein, the first fuel cell was developed by Sir William Grove in 1839 [1]. In 1932, Thomas Francis Bacon initiated the manufacture

of the first fuel cell stack utilizing hydrogen and oxygen. During World War II, Bacon had developed a fuel cell system to use in the Royal Navy submarines [23]. A 5 kW fuel cell stack was developed and manufactured by him in 1952. In terms of the practical applications of fuel cells, the first time a fuel cell was used in a system was the Gemini program, the U.S. space program, in the early 1960s. In the following years, NASA had used the fuel cell technology in the Apollo program in order to produce electricity for astronauts' life support systems, navigation systems, and communication systems. As mentioned before, General Motors manufactured a fuel cell-powered van named Electrovan in the middle of the 1960s. In the end of 1980s, Perry Energy Systems and Ballard Ind. collaborated to develop a PEFC-powered submarine [1]. In 1993, fuel cell powered buses were demonstrated by Ballard Ind. In the beginning of 2000, most vehicle giants were profoundly inspired by fuel cell technology as aforementioned in Chapter 1.2.

1.3.1 The types of fuel cells

There are numerous numbers of fuel cells used as an energy production system in many applications. Fuel cells can be categorised by the type of electrolyte or the fuel they used. The main type of fuel cells are the alkaline fuel cell (AFC), polymer electrolyte fuel cell (PEFC), solid oxide fuel cell (SOFC), direct methanol fuel cell (DMFC), phosphoric acid fuel cell (PAFC), and molten carbonate fuel cell (MCFC) are the most prevalent fuel cell types. Figure 1.2 illustrates the comparison of these fuel cell types.

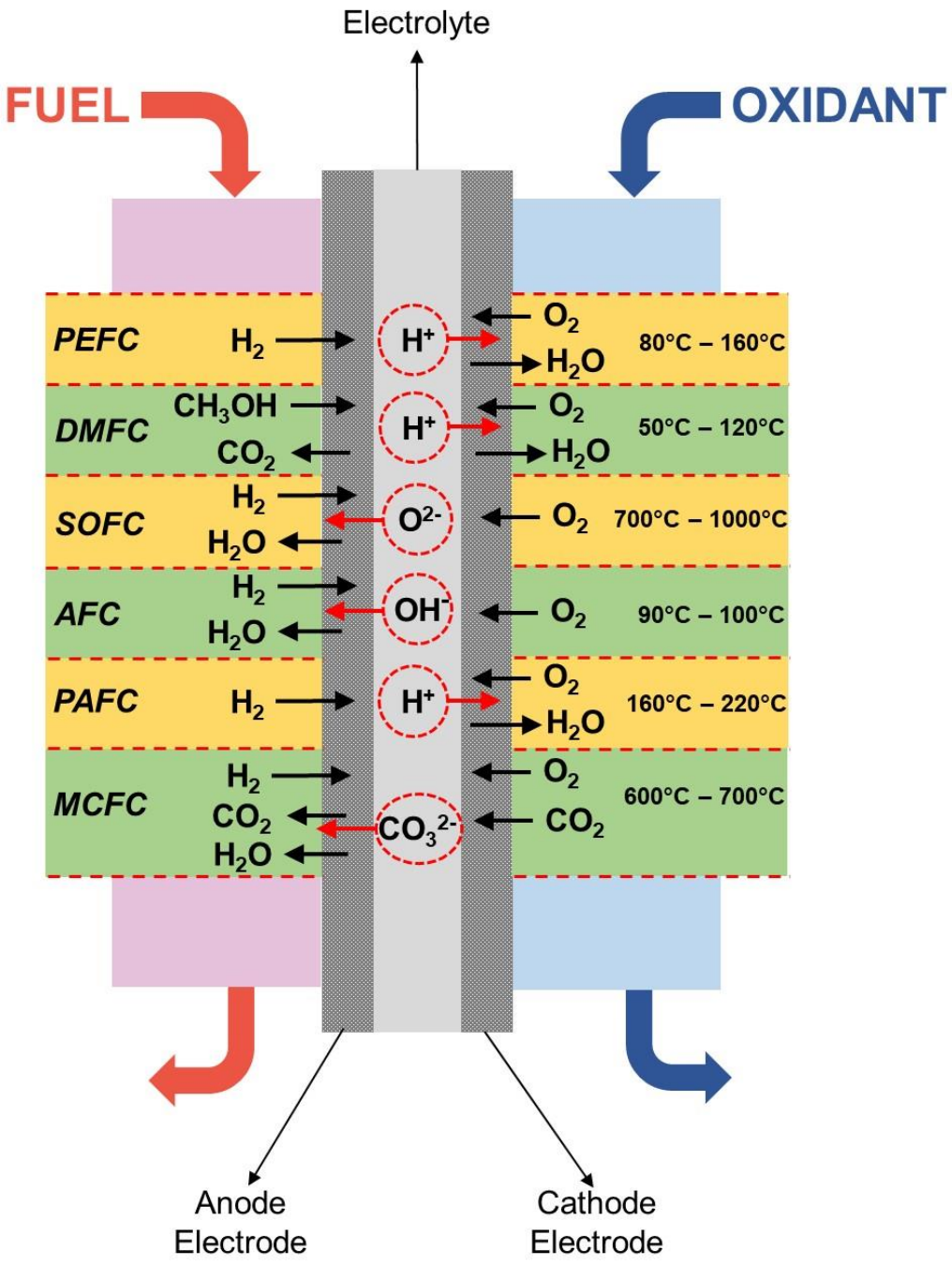

Figure 1. 2 – Different fuel cell types.

1.3.1.1 Alkaline fuel cell (AFC)

The alkaline fuel cell (AFC) utilizes potassium hydroxide (KOH) solution as an electrolyte in their applications [24,25]. The high concentration KOH solution (85 wt

%) is employed at high operation temperatures (~220°C), whereas the diluted KOH solution (35-50 wt %) is used at lower operation temperatures (<120°C). Equation (1.1) and Equation (1.2) exhibit the electrochemical reactions occurring at both the anode and cathode electrodes, respectively. Equation (1.3) shows the overall reaction. The most important advantages of this sort of fuel cell are the lower cost of materials and high efficiency (~60 %). The earliest AFC concepts were used in space missions in the 1950s by both the U.S. and the Soviet Union [25,26].

$$\text{Anode:} \quad 2H_2 + 4OH^- \rightarrow 4H_2O + 4e^- \qquad \textbf{(1.1)}$$

$$\text{Cathode:} \quad O_2 + 2H_2O + 4e^- \rightarrow 4OH^- \qquad \textbf{(1.2)}$$

$$\text{Overall:} \quad 2H_2 + O_2 \rightarrow 2H_2O \qquad \textbf{(1.3)}$$

1.3.1.2 Solid oxide fuel cell (SOFC)

The solid oxide fuel cell (SOFC) is a sort of elevated temperature fuel cell which is operated between a range of temperatures 500°C – 1000°C [27]. That is because the higher electrolyte temperatures are demanded to secure proper ionic conductivity of O^{2-} in the solid phase ceramic electrolyte [25]. A solid, non-porous metal oxide Y_2O_3 stabilized ZrO_3 (YSZ) or Gadolium doped Ceria (GDC) is typically employed as an electrolyte in SOFC [1,28]. Also, nickel/yttria stabilized zirconia (Ni/YSZ) and perovskite-type oxides ($LaMnO_3$, $LaCoO_3$, $LaFeO_3$, etc.) are mostly used as the SOFC anode and cathode materials [24,29]. In terms of the bipolar plates, they are made by cermet, doped ceramic, or metallic materials in order to supply high-temperature

endurance. The main advantages of these sort of fuel cell systems are (i) produced by non-precious materials, (ii) fuel type flexibility (for instance, methane, methanol, ethanol, and biomass sourced gasses such as carbon monoxide), and (iii) highly applicable to integrated other type's electricity generation systems to enhance the overall electrical efficiency and produce useful products such as steam and hot water. In the literature, there is much research being conducted regarding the combined SOFC and other traditional energy and electricity generation methods, especially combined heat power (CHP) and Organic Rankine Cycle (ORC) [30–33]. The anode and cathode as well as the overall electrochemical reactions are given as follows:

Anode: $H_2 + O^{2-} \rightarrow H_2O + 2e^-$ **(1.4a)**

$CO + O^{2-} \rightarrow CO_2 + 2e^-$ **(1.4b)**

Cathode: $O_2 + 4e^- \rightarrow 2O^{2-}$ **(1.5)**

Overall: $H_2 + O_2 + CO \rightarrow H_2O + CO_2$ **(1.6)**

1.3.1.3 Polymer electrolyte fuel cell (PEFC)

The polymer electrolyte fuel cell (PEFC) is an electrochemical device that generates electricity through the energy of hydrogen and oxygen without any burning reaction. The architecture of a standard PEFC is composed of anode and catalyst layers, wherein the electrochemical reactions occur, gas diffusion layers, a proton conductive electrolyte (especially Nafion®-based membrane), and flow-field plates. During the half cell reaction at the anode side, which is also named the hydrogen

oxidation reaction (HOR), hydrogen ions (H^+) and electrons (e^-) synchronously occurred. These hydrogen ions migrate through the electrolyte from the anode to cathode. Besides, the electrons move in the same direction via an external circuit; therefore, desirable electricity is generated. In the cathode side, oxygen reduction reaction (ORR) takes place and water and heat are produced. The HOR, ORR, and the overall reaction are given as follows, respectively:

$$\text{Anode:} \quad H_2 \rightarrow 2H^+ + 2e^- \qquad \textbf{(1.7)}$$

$$\text{Cathode:} \quad \frac{1}{2}O_2 + 2H^+ + 2e^- \rightarrow H_2O + heat \qquad \textbf{(1.8)}$$

$$\text{Overall:} \quad \frac{1}{2}O_2 + H_2 \rightarrow H_2O + heat \qquad \textbf{(1.9)}$$

In comparison to internal combustion engines, PEFC are becoming more prominent in the transportation and aerospace sectors due to its many advantages [25]. The main merits of the PEFC are (i) low working temperature range (50-80 °C), (ii) high power density, (iii) environmentally friendly side products (pure water), and (iv) quiet and vibration-free operation [34]. Due to these advantages, this kind of fuel cells has become highly popular for the transportation sector as aforementioned in Chapter 1.3. However, there remain numerous challenges for the PEFC technology, such as degradation of PEFC components, albeit its advantages and potential. The prominent problems observed in PEFC are the flooding-sourced performance losses (especially in the cathode gas diffusion layer), highly costly materials used in the catalyst layer, and the life duration.

1.3.1.4 Direct methanol fuel cell (DMFC)

The direct methanol fuel cell can be defined as a subcategory of the PEFC that utilize a methanol solution as the fuel. Likewise the PEFC, DMFC employs carbon-supported platinum catalyst (Pt/C), a proton conductive electrolyte (mostly a Nafion®-based membrane), gas diffusion layers, and flow-field plates. However, carbon-supported platinum – ruthenium catalyst (Pt - Ru/C) is used as an anode catalyst in DMFC due to the decrease in the detrimental effect of the intermediates from the surface [35]. The operation temperature range of DMFCs is from 60°C to 80°C; however, there are some articles in regards to the high temperature DMFCs which employ temperature-resistive composite membranes rather than commercial Nafion®-based membranes [36]. The foremost merits of DMFC are (i) lower emission values, (ii) high energy density of methanol (3800 kcal / L), (iii) easy storage capacity, and (iv) ability to operate without a reformer [37,38]. The application areas of DMFCs are portable devices, such as laptops and backup power systems and some vehicles such as boats and caravans [24]. The electrochemical reactions occur at the anode and cathode sides, which are named methanol oxidation reaction (MOR) and oxygen reduction reaction (ORR), are given by, respectively;

$$\text{Anode:} \quad CH_3OH + H_2O \rightarrow CO_2 + 6H^+ + 6e^- \qquad \textbf{(1.10)}$$

$$\text{Cathode:} \quad \frac{1}{2}O_2 + 6H^+ + 6e^- \rightarrow 3H_2O \qquad \textbf{(1.11)}$$

The overall electrochemical reaction is given by;

$$\text{Overall:} \quad CH_3OH + \frac{1}{2}O_2 \rightarrow CO_2 + 2H_2O \qquad \textbf{(1.12)}$$

1.3.1.5 Phosphoric acid fuel cell (PAFC)

The phosphoric acid fuel cell (PAFC) uses highly concentrated (>95%) phosphoric acid solution (H_3PO_4) containing a porous silicon carbide (SiC) ceramic matrix as an electrolyte. This type of fuel cell operates around 160-220°C temperature range. Pure hydrogen or hydrogen-rich gases are fed as fuel at the anode side, whereas air is fed at the cathode side as an oxidant. Equation (1.13) and (1.14) show the electrochemical reactions that happened at both the anode and cathode electrodes, respectively. Equation (1.15) exhibits the overall reaction. Compared to the PEFC, this type of fuel cell employs a liquid-based acidic electrolyte and operates at a higher operation temperature. In addition, the efficiency of PAFC is lower than the other type of fuel cells (35%-50%). PAFC stacks (~200kW/stack) are commercially available to generate electricity for stationary applications [1].

$$\text{Anode:} \quad H_2 \rightarrow 2H^+ + 2e^- \qquad \textbf{(1.13)}$$

$$\text{Cathode:} \quad \frac{1}{2}O_2 + 2H^+ + 2e^- \rightarrow H_2O + heat \qquad \textbf{(1.14)}$$

$$\text{Overall:} \quad \frac{1}{2}O_2 + H_2 \rightarrow H_2O + heat \qquad \textbf{(1.15)}$$

1.3.1.6 Molten carbonate fuel cell (MCFC)

Molten carbonate fuel cell (MCFC) employs combined alkali (Na, K, Li) carbonates as an electrolyte in a porous ceramic matrix. The operating temperature range is 600°C – 700°C for MCFCs. Therefore, this type of fuel cell does not require to be fed pure hydrogen at the anode side. Coal-derived gasses or natural gas can be fed as fuel at the anode side. Air is used at the cathode side as an oxidant. One advantage of MCFC is that it does not have to use expensive metals as catalysts due to high operating temperatures. The electrochemical reactions that occurred at both anode and cathode sides are represented in Equation (1.16) and (1.17), respectively. Equation (1.18) shows the overall reaction. The MCFC can be used for large-scale stationary heat and power applications.

$$\text{Anode:} \quad H_2 + CO_3^{3-} \rightarrow H_2O + CO_2 + 2e^- \quad \textbf{(1.16)}$$

$$\text{Cathode:} \quad \frac{1}{2}O_2 + CO_2 + 2e^- \rightarrow CO_3^{2-} \quad \textbf{(1.17)}$$

$$\text{Overall:} \quad \frac{1}{2}O_2 + H_2 \rightarrow H_2O + heat \quad \textbf{(1.18)}$$

1.4 MAIN FUEL CELL COMPONENTS

A standard PEFC is made up of anode and cathode flow-field plates, and a membrane electrode assembly (MEA). In terms of the MEA, it consists of a proton-conductive membrane, anode and cathode catalyst layers, and anode and cathode gas diffusion layers (microporous layers and substrate). Figure 1.3 exhibits these main components

of the standard PEFC and in the subsequent chapters provide detailed insights in regards to these prominent components (from Chapter 1.4.1 to Chapter 1.4.4).

During the PEFC operation, humidified hydrogen (H_2) gas was fed through the anode flow-field plate which possesses parallel channels to the gas diffusion layer surface. The supplied H_2 diffuses through the void spaces of the anode gas diffusion layer substrate into the anode microporous layer. Due to the porous structure of the anode microporous layer, H_2 reaches the anode catalyst layer and HOR occurs (Equation (1.7)); there hydrogen ions (H^+) and electrons arise after this reaction. These electrons flow through an external circuit to the cathode side. At the same time, hydrogen ions (H^+) pass from the anode catalyst layer to the cathode catalyst layer due to the proton conductive Nafion ionomers in the anode catalyst layer and the membrane. In the cathode side, oxygen gas (O_2) or air is supplied through the cathode flow – field plates. In the ideal conditions, this oxygen gas should be smoothly transferred from the cathode flow – field plate to the cathode catalyst layer due to the superior porous structures of both the cathode gas diffusion layer and the cathode microporous layer. In the cathode catalyst layer, Equation (1.8) applies; hence, liquid water and heat are produced during this reaction. Excessive water is forced to leave from the cathode reaction region due to the capillary pressure which predominantly depends on the porous structure of the cathode gas diffusion layer [39].

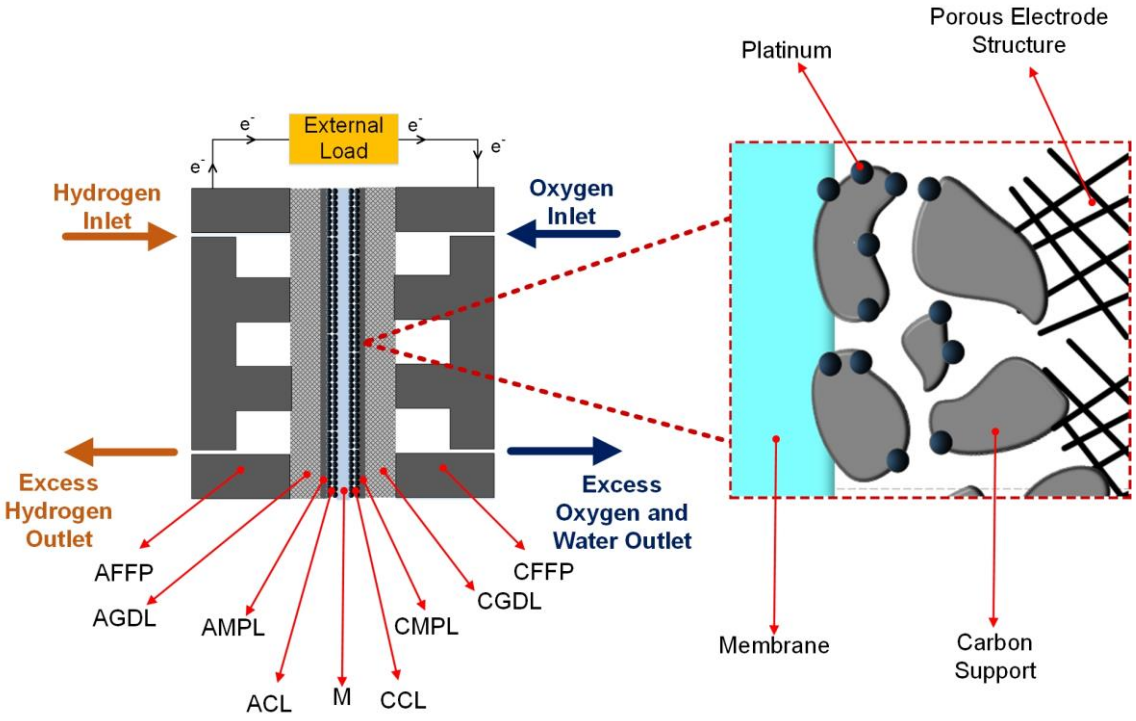

Figure 1. 3 – The main components of PEFC. AFFP: anode flow – field plate, AGDL: anode gas diffusion layer, AMPL: anode microporous layer, ACL: anode catalyst layer, M: membrane, CCL: cathode catalyst layer, CMPL: cathode microporous layer, CGDL: cathode gas diffusion layer, CFFP: cathode flow – field plate.

1.4.1 Membrane

A membrane used in the PEFC can be defined as a selective permeable barrier that allows hydrogen ions to pass to the other side whereas it physically separates both the electrochemical sides of the fuel cell. One of the most extensively used PEFC membrane is commercially available Nafion® membranes which are perfluorosulfononic acid (PFSA) type membranes [40]. Nafion® membrane's chemical structure is demonstrated in Figure 1.4. It is apparent that the Teflon (PTFE) backbone of the membrane exhibits a hydrophobic characteristic, while sulfonic acid (SO_3H^+) at the end of the side chain shows high hydrophilic. The membrane hydration is crucial

in order for the ions transportation from the anode side to the cathode side. This hydration is generally secured by the humidification process of the inlet gasses and the production of liquid water during the ORR at the cathode side. Nonetheless, excessive liquid water is likely to render flooding which hinders the transport of reactant gasses to the reaction regions. Moreover, too small amount of water will reduce the durability of the membrane and this situation causes the electrodes to stand to the membrane surface inadequately [41]. Inevitably, it is clear that the water management is essential to enhance the performance of the PEFC. This phenomenon is profoundly investigated in Chapter 1.4.3. In the literature, the required properties of a membrane can be; (i) high proton conductivity, (ii) electrical isolation, (iii) to prevent oxygen pass from cathode to anode, (iv) to prevent hydrogen crossover from anode to cathode, and (v) to provide mechanical and chemical stability under the working conditions [24].

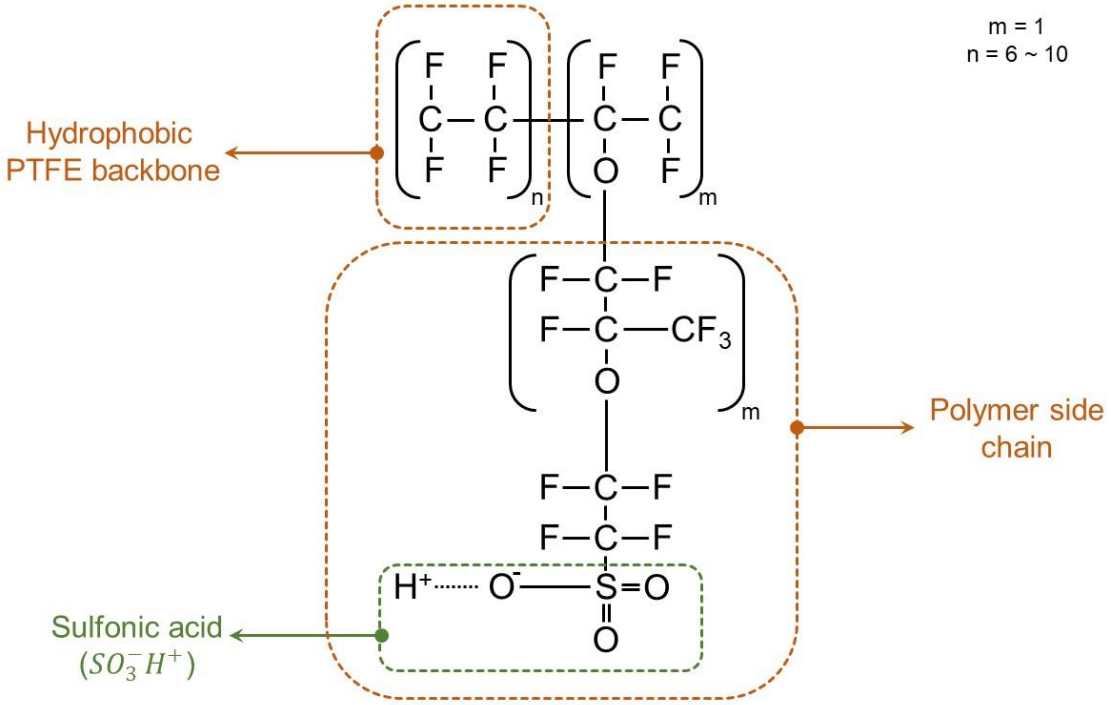

Figure 1. 4 – The chemical structure of the Nafion® membrane.

1.4.2 Anode and cathode catalyst layers

The anode and cathode catalyst layers can broadly be defined as the electrochemical structures where the HOR and ORR occur, respectively [22]. Traditional anode and cathode catalyst layers are compositions of larger carbon particles supported by noble metals (mostly platinum), ionomer particles (Nafion particles), and void spaces [21]. Therefore, the consummate catalyst layers are able to be defined as; (i) to include high catalytic activity, (ii) to secure large surface area, (iii) to own continues pathways for effective proton transport, (iv) to include uninterrupted void space networks for effective reactant and product transportation, (v) to supply continuous paths for effective electron conduction, and (vi) to secure excellent stability.

The PEFC catalyst platinum nanoparticles (~2 – 3 nm) are not employed by themselves because of their tremendously expensive nature, hence they are combined with intrinsically high-surface-area carbon powder such as Vulcan XC – 72 (~30 -40 nm) [21,42]. By means of this catalyst modification, it is possible to use less amount of precious catalyst material to create a larger effective catalyst surface. To exemplify, at the outset of the PEFC technology, highly large amount of platinum was utilized to manufacture the catalyst layer (up to 28 mg cm^{-2}), yet this loading value was decreased to 0.3 – 0.4 mg cm^{-2} [1]. The most renowned carbon support materials are Vulcan XC72R (Cabot Corp.), Black Pears BP 2000, and Ketjen Black International (Shanghai Tengmin Industry Co., Ltd.).

1.4.3 Anode and cathode gas diffusion layers

A wet-proofed, porous layer between the catalyst layer and flow-field plate is named as the gas diffusion layer (GDL) [1]. Commercially available GDLs are mostly made of electrically conductive carbon-based materials due to the superior characteristic of carbon. The largest GDL manufacturing giants all around the world are Ballard Ind., Sigracet Group, Toray Inc., Freudenberg Group, E TEK, and CeTech [43].

Carbon fibres are employed to manufacture both carbon papers and carbon cloth which have intrinsically non-woven and woven architecture, respectively. In addition, carbon paper GDLs possess two sort of fibre structures; straight fibres and spaghetti fibres [43]. The carbon paper is bound by webbing (carbonized thermoset resin); on the other hand, no binder is required in the carbon cloth due to its woven structure [44]. The fibre structures of these carbon papers and carbon cloth are exhibited in

Figure 1.5. The pore size distribution, electrical conductivity, and the fuel cell performance is directly related to the arrangement of these fibres.

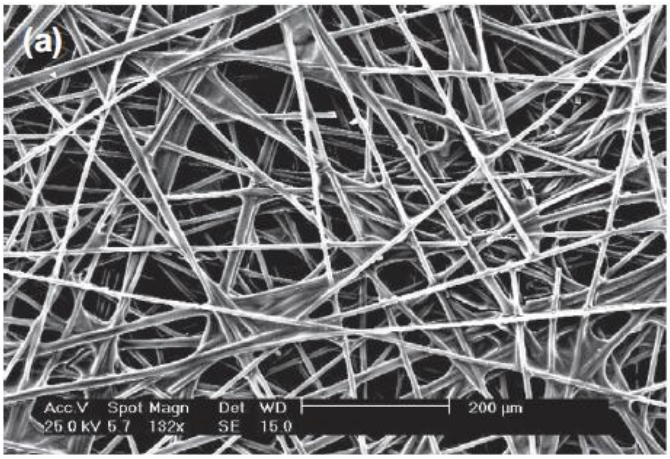

(a)

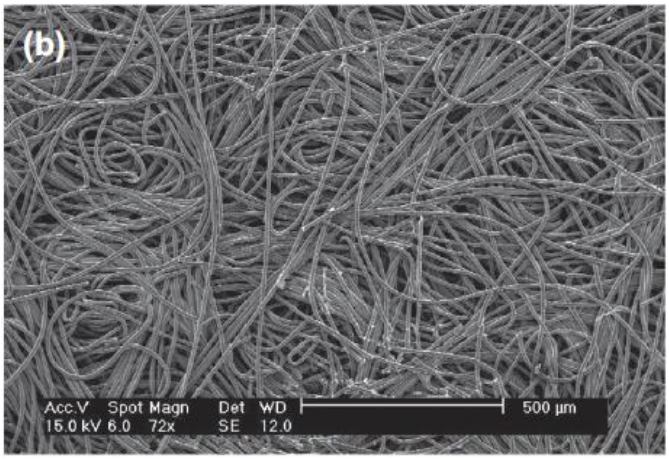

(b)

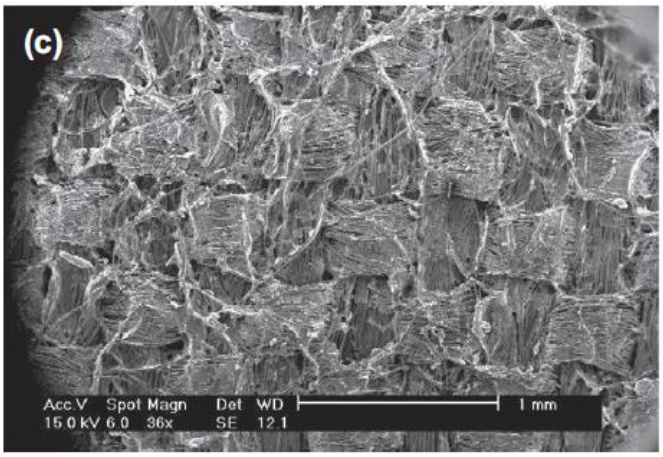

(c)

Figure 1. 5 – The structure of (a) carbon paper possessing straight fibres, (b) carbon paper possessing spaghetti fibres, and (c) carbon cloth [43].

The GDLs have a crucial role in the fuel cell working by controlling the mass, heat and electron transport [1,45]. The essential roles of the GDL in a PEFC operation condition can be listed as (i) to regulate the reactants and by-products between the catalyst layer and the flow-field plate, (ii) to impart proper pathways for electron conduction from the CL to the flow-field plate, (iii) to handle a proper water management balance between the membrane hydration and water removal, and (iv) to reinforce the CL as a mechanically rigid backbone [43,46]. In addition to these roles, some requirements listed below should be fulfilled by an optimal GDL; (i) possess adequate porosity, (ii) secure a balance between hydrophobicity and hydrophilicity, (iii) provide high through- and in-plane electrical and thermal conductivity, (iv) remain a crack-free morphology and long-term operation availability, (v) mechanical and chemical stability during operation conditions, and (vi) lower cost [1,21].

In some applications, an additional layer, which is named as the microporous layer (MPL), is coated on the fibre structure of the GDL to enhance the mass, heat, and electricity transport [45]. The MPL is a simple composite structure made of carbon or graphite powder and a polymeric binder. An ideal MPL should perform the following functions; (i) to improve the reactant and oxidant distribution on the CLs, (ii) to reduce the liquid water saturation from the CL to the flow-field plate, (iii) to reduce the interfacial electrical resistance of the CL and GDL, (iv) to improve the mechanical compatibility between the GDL and CL, (v) to secure a mechanical backing for fragile CL, and (vi) to increase the catalytic utilization by suppressing the precious metal catalyst particles into the GDL [46]. The average pore size in the MPL is of the order of 1 – 10 µm, whereas this value is approximately 10 – 100 µm for GDL and about 0.001 – 5 µm for CL.

Water transport management is one of the crucial issues in the GDL in order to prevent flooding. It is inevitable that the electron, hydrogen ion, and mass transport are strongly affected by excess water [47]. This situation can be defined as “the flooding” which is one of the reasons for the low performance on the ORR. On the one hand, an adequate amount of hydration is a must for proton conductive membranes since the PFSA type membranes are only able to possess proton conductivity when they are perfectly hydrated [48]. On the other hand, excess liquid water is likely to clog the porous pathways in the GDL and hence this situation can attribute to hinder the oxygen transport from flow-field plates to CL. Therefore, water management aspects are becoming more vital for fuel cell studies.

During the cell operation, water is produced into the membrane / CCL interface as a side product of ORR [39,49]. A portion of water is forced to move to the anode side owing to the hydraulic pressure occurring at the membrane/CCL interface. This transport is known as “back diffusion”. In addition, a small amount of water is carried from the anode side to the cathode side due to the hydrogen ion transport. This phenomenon is named as the electro-osmotic drag. All these water movements in a PEFC are depicted in Figure 1.6.

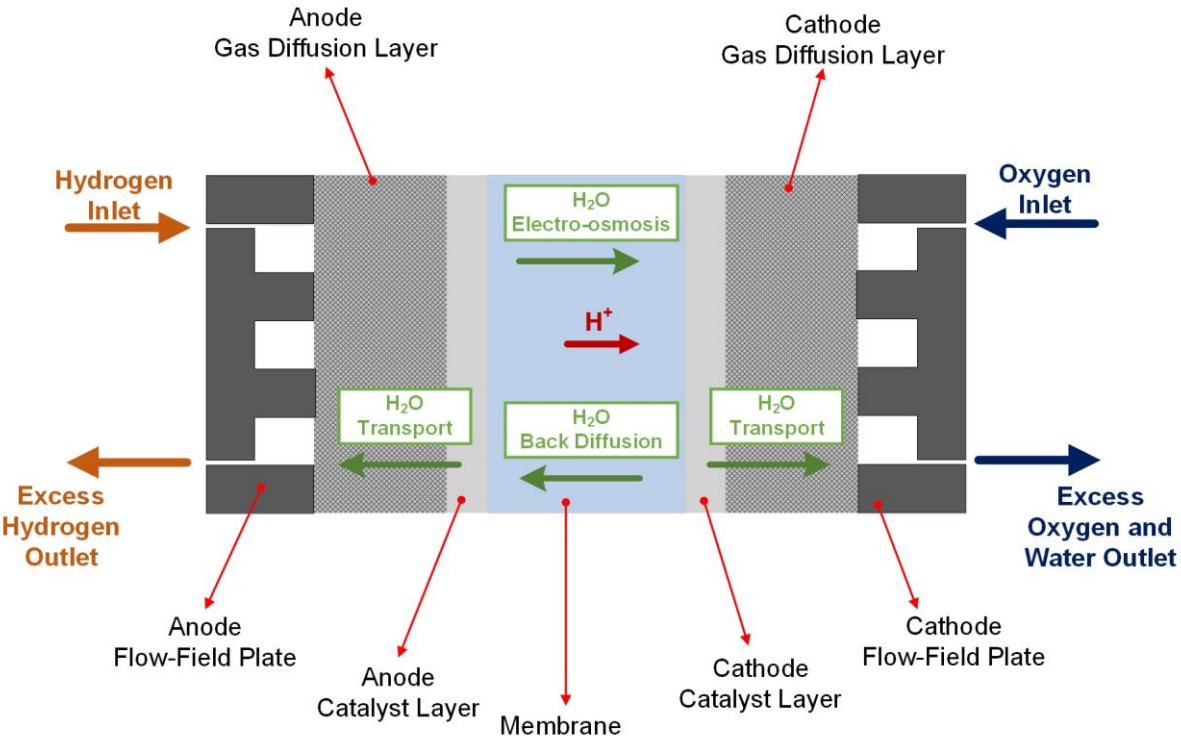

Figure 1.6 – Water movement into a PEFC (adapted from [49]).

1.4.4 Flow-Field Plates

The anode and cathode flow-field plates are employed as reactant and oxygen distributors and water collectors in the PEFC. According to Li and Sabir [50], flow-field plates consist of more than 60% of the total weight and 30% of the total cost in a fuel

cell stack. To date, many researchers have focused on not only the effect of the FFP design to achieve a more efficient reactant and oxidant distribution but also the rib and channel geometries to optimize the FFP [25,51]. In the literature, there are many sorts of flow field designs that have been evaluated; such as parallel, serpentine, parallel serpentine, interdigitated, mesh, and spiral. In addition to the traditional designs, bio-inspired flow-field designs are likely to draw more attention due to their superior capacity of a uniform velocity distribution [52].

The flow-field plates are one of the most prominent components of PEFC stacks which have to fulfil some crucial functions during the operation [1,50]. These functions are as follows; (i) electrically linking adjacent cells, (ii) separating the gases in adjacent cells, (iii) providing a structural support for the cell, and (iv) conducting heat from the cell to the cooling channels. In addition, the flow-fields should be electron conductive, highly corrosion resistant, cheap, and easy to manufacture.

In terms of flow-field materials, graphite is the most used material due to its superior chemical stability in the fuel cell environment [1]. On the other hand, graphite possesses a porous nature which makes it tend to be destructive in a PEFC environment. Moreover, graphite is inherently inclined to be brittle because of its fragile character. Furthermore, the graphite manufacturing process is genuinely more costly than that of metal-based materials. Due to these reasons, metal-based flow-field plates have been developed by numerous research groups. Although these kind of metal materials (such as aluminium, steel, titanium, and nickel) are prone to corrode into the PEFC operation environment, metallic FFPs exhibit excellent thermal

and electrical conductivity, low gas permeability, low-cost, easy manufacturing, and have a thinner structure compared to the graphite FFPs [53].

1.5 ELECTROCHEMISTRY OF FUEL CELL

An operating PEFC possesses a cathode electrode with a higher potential than the anode electrode. This electrical potential difference between the cathode and anode electrodes is named the actual cell potential. The best possible cell potential for a PEFC under standard conditions and utilising pure hydrogen and oxygen gas is 1.229V, also known as the reversible cell voltage. However, due to continuous electrochemical reactions and related irreversibility's, a fuel cell always faces energy losses that result in electric potential losses during actual operation, thereby the cell potential is likely to decline to approximately 1 V. These electrical potential losses are denoted as "overpotentials" and cause a notable decline in the fuel cell potential [54].

As for the PEFC performance testing, a polarisation curve is widely used to gain a better insight into the overall cell performance. Polarisation curves fundamentally show the relation between the current density and its cell voltage. It should be noted that the fuel cell voltage losses can be categorised into three regions; activation polarisation, ohmic polarisation, and concentration polarisation (displayed in Figure 1.7). These regions are categorised according to the dominant influencing transport phenomena in the current density range. However, it should be noted that all transport phenomena are likely to be present in very wide current density ranges [39]. The output cell voltage (E_{cell}) may be given as Equation 1.19:

$$E_{cell} = E_{OCV} - \eta_{act} - \eta_{ohm} - \eta_{con} \qquad \textbf{(1.19)}$$

where E_{OCV} designates the open circuit voltage, η_{act} is the activation polarisation losses, η_{ohm} is the ohmic losses, and η_{con} is the concentration polarisation losses.

The activation polarisation losses, dominant at low current densities, cause energy losses due to sluggish electrochemical reactions on the catalyst surfaces. Even though these losses occur at both the anode and cathode, the oxygen reduction reaction (ORR) is much slower than the hydrogen oxidation reaction (HOR); therefore, the oxygen reduction reaction (ORR) requires much higher overpotentials. Notably, in the activation polarisation region, the cell voltage is high; however, the current density is quite low. Thereby, the power density output is low and practically this region is unlikely to be used for PEFC operation. Activation polarisation is naturally non-linear and could be represented by the Butler-Volmert model as Equation 1.20:

$$i = i_0 \left[exp\left(\frac{\alpha_{anode}\, n\, F}{RT}\eta_{act}\right) - exp\left(\frac{\alpha_{cathode}\, n\, F}{RT}\eta_{act}\right) \right] \qquad \textbf{(1.20)}$$

where i is the current density (A/m^2), i_0 is the exchange current density (A/m^2), α_{anode} and $\alpha_{cathode}$ respectively denote anodic and cathodic charge transfer coefficient, n is the number of electrons are transferred, F is the Faraday's constant (96485 C/mol), R is the universal gas constant (8.314 J mol^{-1}K^{-1}), T is the temperature, and η_{act} is the activation polarisation losses (V).

The second region is the ohmic polarisation which is associated with the moderate current densities. In the ohmic polarisation region, the losses occur owing to the resistance of the ions flow through the electrolyte and the electrons flow through the electrically conductive fuel cell components. These ohmic losses could be expressed

by the Ohmic law as given in Equation (1.21). This polarisation region inherently possesses a linear characteristics (as can be seen in Figure 1.7).

$$\eta_{ohm} = i \cdot \sum R_{\Omega} \qquad \textbf{(1.21)}$$

where η_{ohm} denotes the ohmic losses, i is the current density (A/m^2), and R_{Ω} is the total internal resistance (including ionic, electronic, and contact resistance) ($\Omega \cdot m^2$).

The third region is the concentration polarisation region which is restricted by the reactant and side-product transports from/to the reaction sites. These losses are mainly led by gas diffusion, excess water flooding (into CL, GDL, and FFP channel). It should be noted that the concentration polarisation losses are dominant at the high current densities (shown in Figure 1.7).

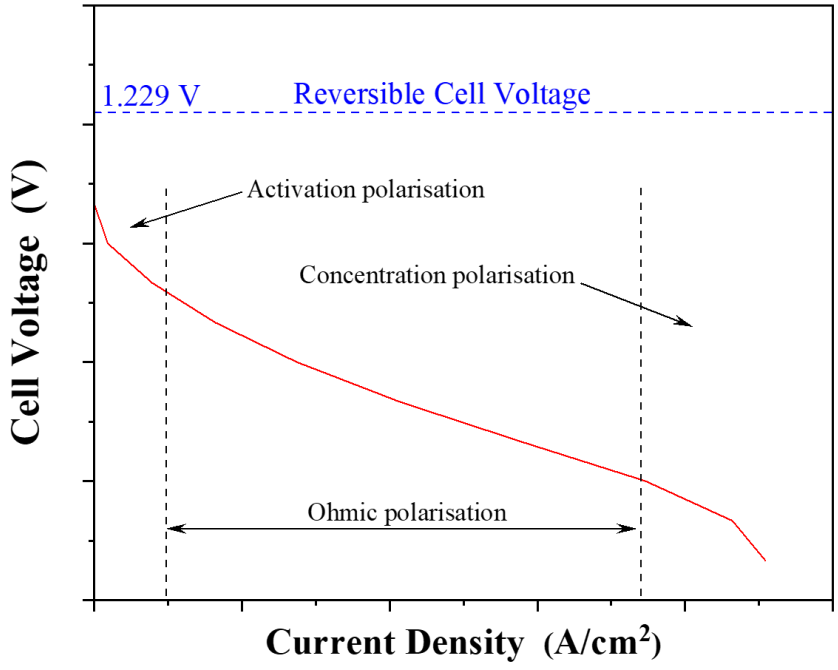

Figure 1.7 – A typical polarisation curve of the PEFC.

1.6 GAPS IN KNOWLEDGE AND RESEARCH OBJECTIVES

The cathode gas diffusion layer (GDL) possesses a critical function in the PEFC by controlling the mass, heat, and electron transport. However, the majority of commercial GDLs are made from anisotropic fragile carbon fibres. As for transportation applications, these sorts of fragile and brittle structures are unlikely to be ideal materials because of the probable vibrations and shocks during the operation of the vehicles. Besides, these materials tend to deform under a compression force because of their macro-scale pores and fragile nature. Apparently, the extensive clamping force directly affects the transport characteristics of the porous GDL materials. Therefore, the superior metal based-materials, especially nickel foam, used for PEFCs are critically reviewed and investigated in this thesis. In particular, nickel foam material has a great potential to be utilized in PEFCs as a cathode GDL due to its outstanding interior characteristics such as lower density, higher surface area, superior gas permeability, and higher electrical and thermal conductivity.

Although nickel foam has been employed in different energy-related applications, there have been no reported studies in the literature that have thoroughly investigated the transport properties of the nickel foam numerically and its potential to be used as PEFC GDLs. In addition, there have been only a few studies in regards to the X-ray computed tomography (X-ray CT) investigation of the nickel foam-based flow fields; however, the X-ray CT detailed inspection of the nickel foam-based GDLs has not been fully studied yet. Moreover, the structural and transport characteristics

of the nickel foam-based GDLs under the PEFC compression conditions have not been detailed examined in detail by X-ray CT. In terms of the computationally-economic X-ray CT based model, there have been no elaborated studies about the effects of the nickel foam-based GDLs on the structural and transport characteristics under the operational compression conditions. To this end, nickel foam will be computationally investigated using X-ray CT to assess its suitability to act as a GDL in PEFCs through estimating it's morphological and transport characteristics which will be compared and contrasted with conventional GDLs. In addition, the effects of the fuel cell compression on the morphological and transport characteristics of nickel foam-based GDL will be examined by X-ray CT. In the last phase of the thesis, the developed nickel foam-based GDLs will be numerically investigated under the realistic rib and channel compression to provide much better insight into the overall cell performance.

1.7 RESEARCH OUTLINE

This thesis is divided into six chapters. The first chapter is a brief introduction into the global energy demand and the fundamentals of fuel cell technology. The first chapter also presents the main fuel cell types, components, and the fundamental electrochemistry of fuel cell investigations. At the end of the chapter, the aims of the thesis and the outline are given briefly.

The second chapter is a comprehensive literature review of the porous metal materials-based GDLs and FFPs used for PEFCs. In the first part of the chapter, there is a brief introduction to the range of porous metal materials used in engineering applications. Afterwards, different types of porous metal materials used in PEFCs are

reviewed. The last part of the chapter introduces the X-ray computed tomography (X-ray CT) imaging technology and provides fundamental information about this non-destructive and non-invasive imaging method. Next, the captured image processing and the construction of the 3D microscale porous structure are briefly described. Finally, at the end of the chapter, the X-ray CT imaging of the PEFC GDLs is reviewed in detail.

The third chapter is the first technical chapter. First, the structural properties (porosity, tortuosity, pore size, ligament thickness and specific surface area) and transport properties (gas permeability and effective diffusivity) are investigated by nickel foam based-GDLs using X-ray CT based computationally-economic COMSOL Multiphysics numerical models.

The fourth chapter is the second technical chapter that the developed computationally-economic X-ray CT-based numerical model was employed to evaluate the effects of the nickel foam-based GDLs on the structural and transport characteristics under the fuel cell operation compression conditions.

The fifth chapter is the third technical chapter that nickel foam-based GDL used PEFC are comprehensively investigated under the realistic rib and channel compression. A 3-D numerical model was developed using the COMSOL Multiphysics 6.0. The results are compared with the commercial carbon-based GDL used PEFCs.

The sixth chapter is the conclusion and future works. The key findings of Chapters 3, 4, and 5 are highlighted, and recommendations for future works are shared in this chapter.

1.8 REFERENCES

[1] Barbir F. PEM Fuel Cells - Theory and Practice. 2nd ed. 2012.

[2] Wilberforce T, Alaswad A, Palumbo A, Dassisti M, Olabi AG. Advances in stationary and portable fuel cell applications. Int J Hydrogen Energy 2016;41:16509–22. https://doi.org/10.1016/j.ijhydene.2016.02.057.

[3] St-Pierre J, Jia N. Successful Demonstration of Ballard PEMFCS for Space Shuttle Applications. J New Mater Electrochem Syst 2002;5:263–71.

[4] Litster S, Epting WK, Wargo EA, Kalidindi SR, Kumbur EC. Morphological analyses of polymer electrolyte fuel cell electrodes with nano-scale computed tomography imaging. Fuel Cells 2013;13:935–45. https://doi.org/10.1002/fuce.201300008.

[5] Padilha JC, da Trindade LG, de Souza RF, Miguel M. An evaluation of the potential of the use of wasted hydroelectric capacity to produce hydrogen to be used in fuel cells in order to decrease CO2 emissions in Brazil. Int J Hydrogen Energy 2009;34:7898–902. https://doi.org/10.1016/j.ijhydene.2009.07.074.

[6] Hasanuzzaman M, Zubir US, Ilham NI, Seng Che H. Global electricity demand, generation, grid system, and renewable energy polices: a review. Wiley Interdiscip Rev Energy Environ 2017;6:1–18. https://doi.org/10.1002/wene.222.

[7] Das HS, Tan CW, Yatim AHM. Fuel cell hybrid electric vehicles: A review on power conditioning units and topologies. Renew Sustain Energy Rev

2017;76:268–91. https://doi.org/10.1016/j.rser.2017.03.056.

[8] Galich A, Marz L. Alternative energy technologies as a cultural endeavor: A case study of hydrogen and fuel cell development in Germany. Energy Sustain Soc 2012;2:1–10. https://doi.org/10.1186/2192-0567-2-2.

[9] Garavini G. Completing decolonization: The 1973 “oil shock” and the struggle for economic rights. Int Hist Rev 2011;33:473–87. https://doi.org/10.1080/07075332.2011.595593.

[10] Ilie L. Economic considerations regarding the first oil shock , 1973 - 1974 2007:1973–4.

[11] da Trindade LG, Pereira EC. SPEEK/Zeolite/Ionic-Liquid Anhydrous Polymer Membranes for Fuel-Cell Applications. Eur J Inorg Chem 2017;2017:2369–76. https://doi.org/10.1002/ejic.201601559.

[12] International Energy Agency. World energy outlook 2010: executive summary. 2017.

[13] Tie SF, Tan CW. A review of energy sources and energy management system in electric vehicles. Renew Sustain Energy Rev 2013;20:82–102. https://doi.org/10.1016/j.rser.2012.11.077.

[14] Tang Y, Yuan W, Pan M, Wan Z. Experimental investigation on the dynamic performance of a hybrid PEM fuel cell/battery system for lightweight electric vehicle application. Appl Energy 2011;88:68–76. https://doi.org/10.1016/j.apenergy.2010.07.033.

[15] Xu L, Ouyang M, Li J, Yang F, Lu L, Hua J. Application of Pontryagin's Minimal Principle to the energy management strategy of plugin fuel cell electric vehicles. Int J Hydrogen Energy 2013;38:10104–15. https://doi.org/10.1016/j.ijhydene.2013.05.125.

[16] Wang FC, Fang WH. The development of a PEMFC hybrid power electric vehicle with automatic sodium borohydride hydrogen generation. Int J Hydrogen Energy 2017;42:10376–89. https://doi.org/10.1016/j.ijhydene.2017.03.040.

[17] Marks C, Rishavy EA, Wyczalek FA. Electrovan - A fuel cell powered vehicle. SAE Tech Pap 1967;76:992–1002. https://doi.org/10.4271/670176.

[18] Uzunoglu M, Alam MS. Dynamic modeling, design and simulation of a PEM fuel cell/ultra-capacitor hybrid system for vehicular applications. Energy Convers Manag 2007;48:1544–53. https://doi.org/10.1016/j.enconman.2006.11.014.

[19] Alaswad A, Baroutaji A, Achour H, Carton J, Al Makky A, Olabi AG. Developments in fuel cell technologies in the transport sector. Int J Hydrogen Energy 2016;41:16499–508. https://doi.org/10.1016/j.ijhydene.2016.03.164.

[20] Yoshida T, Kojima K. Toyota MIRAI fuel cell vehicle and progress toward a future hydrogen society. Electrochem Soc Interface 2015;24:45–9. https://doi.org/10.1149/2.F03152if.

[21] O'Hayre R., Cha S., Colella W. PF. Fuel Cell Fundamentals. New Jersey: John Wiley & Sons., Inc.; 2016.

[22] Zamel N. The catalyst layer and its dimensionality - A look into its ingredients and how to characterize their effects. J Power Sources 2016;309:141–59. https://doi.org/10.1016/j.jpowsour.2016.01.091.

[23] Andújar JM, Segura F. Fuel cells: History and updating. A walk along two centuries. Renew Sustain Energy Rev 2009;13:2309–22. https://doi.org/10.1016/j.rser.2009.03.015.

[24] Colpan CO, Nalbant Y, Ercelik M. Fundamentals of Fuel Cell Technologies. Compr Energy Syst 2018;4–5:1107–30. https://doi.org/10.1016/B978-0-12-809597-3.00446-6.

[25] Mench MM. Fuel Cell Engines. 2008. https://doi.org/10.1002/9780470209769.

[26] Bidault F, Brett DJL, Middleton PH, Abson N, Brandon NP. A new application for nickel foam in alkaline fuel cells. Int J Hydrogen Energy 2009;34:6799–808. https://doi.org/10.1016/j.ijhydene.2009.06.035.

[27] Mansor NB. Development of Catalysts and Catalyst Supports for Polymer Electrolyte Fuel Cells. University College London, 2014.

[28] Abdalla AM, Hossain S, Azad AT, Petra PMI, Begum F, Eriksson SG, et al. Nanomaterials for solid oxide fuel cells: A review. Renew Sustain Energy Rev 2018;82:353–68. https://doi.org/10.1016/j.rser.2017.09.046.

[29] Maguire E, Gharbage B, Marques FMB, Labrincha JA. Cathode materials for intermediate temperature SOFCs. Solid State Ionics 2000;127:329–35. https://doi.org/10.1016/S0167-2738(99)00286-6.

[30] Ebrahimi M, Moradpoor I. Combined solid oxide fuel cell, micro-gas turbine and organic Rankine cycle for power generation (SOFC-MGT-ORC). Energy Convers Manag 2016;116:120–33. https://doi.org/10.1016/j.enconman.2016.02.080.

[31] Fontell E, Kivisaari T, Christiansen N, Hansen JB, Pålsson J. Conceptual study of a 250 kW planar SOFC system for CHP application. J Power Sources 2004;131:49–56. https://doi.org/10.1016/j.jpowsour.2004.01.025.

[32] Staffell I. Zero carbon infinite COP heat from fuel cell CHP. Appl Energy 2015;147:373–85. https://doi.org/10.1016/j.apenergy.2015.02.089.

[33] Weber C, Maréchal F, Favrat D, Kraines S. Optimization of an SOFC-based decentralized polygeneration system for providing energy services in an office-building in Tōkyō. Appl Therm Eng 2006;26:1409–19. https://doi.org/10.1016/j.applthermaleng.2005.05.031.

[34] Timurkutluk B, Chowdhury MZ. Numerical Investigation of Convergent and Divergent Parallel Flow Fields for PEMFCs. Fuel Cells 2018;18:441–8. https://doi.org/10.1002/fuce.201800029.

[35] Das S, Dutta K, Kundu PP. Nickel nanocatalysts supported on sulfonated polyaniline: Potential toward methanol oxidation and as anode materials for DMFCs. J Mater Chem A 2015;3:11349–57. https://doi.org/10.1039/c5ta01837d.

[36] Ozden A, Ercelik M, Devrim Y, Colpan CO, Hamdullahpur F. Evaluation of sulfonated polysulfone/zirconium hydrogen phosphate composite membranes for direct methanol fuel cells. Electrochim Acta 2017;256:196–210. https://doi.org/10.1016/j.electacta.2017.10.002.

[37] Basri S, Kamarudin SK, Daud WRW, Yaakub Z. Nanocatalyst for direct methanol fuel cell (DMFC). Int J Hydrogen Energy 2010;35:7957–70. https://doi.org/10.1016/j.ijhydene.2010.05.111.

[38] Patel PP, Datta MK, Jampani PH, Hong D, Poston JA, Manivannan A, et al. High performance and durable nanostructured TiN supported Pt50-Ru50 anode catalyst for direct methanol fuel cell (DMFC). J Power Sources 2015;293:437–46. https://doi.org/10.1016/j.jpowsour.2015.05.051.

[39] Zamel N, Li X. Effective transport properties for polymer electrolyte membrane fuel cells - With a focus on the gas diffusion layer. Prog Energy Combust Sci 2013;39:111–46. https://doi.org/10.1016/j.pecs.2012.07.002.

[40] Devi N, Ray S, Shukla A, Bhat SD, Pesala B. Tracking the hydration dynamics of Nafion fuel cell membranes using terahertz spectroscopy 2019:64. https://doi.org/10.1117/12.2511029.

[41] Tan WC, Saw LH, Thiam HS, Xuan J, Cai Z, Yew MC. Overview of porous media/metal foam application in fuel cells and solar power systems. Renew Sustain Energy Rev 2018;96:181–97. https://doi.org/10.1016/j.rser.2018.07.032.

[42] Epting WK, Gelb J, Litster S. Resolving the three-dimensional microstructure of polymer electrolyte fuel cell electrodes using nanometer-scale X-ray computed tomography. Adv Funct Mater 2012;22:555–60. https://doi.org/10.1002/adfm.201101525.

[43] El-kharouf A, Pollet BG. Gas Diffusion Media and Their Degradation. Elsevier Inc.; 2012. https://doi.org/10.1016/B978-0-12-386936-4.10004-1.

[44] Mathias MF, Roth J, Fleming J, Lehnert W. Diffusion media materials and characterisation. Handb Fuel Cells 2010. https://doi.org/10.1002/9780470974001.f303046.

[45] Ozden A, Shahgaldi S, Li X, Hamdullahpur F. A review of gas diffusion layers for proton exchange membrane fuel cells—With a focus on characteristics, characterization techniques, materials and designs. Prog Energy Combust Sci 2019;74:50–102. https://doi.org/10.1016/j.pecs.2019.05.002.

[46] Ozden A, Alaefour IE, Shahgaldi S, Li X, Colpan CO, Hamdullahpur F. Gas Diffusion Layers for PEM Fuel Cells: Ex- and In-Situ Characterization. Elsevier; 2018. https://doi.org/10.1016/B978-0-12-813734-5.00040-8.

[47] Weber AZ, Borup RL, Darling RM, Das PK, Dursch TJ, Gu W, et al. A critical review of modeling transport phenomena in polymer-electrolyte fuel cells. J Electrochem Soc 2014;161:F1254–99. https://doi.org/10.1149/2.0751412jes.

[48] Jiao K, Li X. Water transport in polymer electrolyte membrane fuel cells. Prog Energy Combust Sci 2011;37:221–91. https://doi.org/10.1016/j.pecs.2010.06.002.

[49] Li H, Tang Y, Wang Z, Shi Z, Wu S, Song D, et al. A review of water flooding issues in the proton exchange membrane fuel cell. J Power Sources 2008;178:103–17. https://doi.org/10.1016/j.jpowsour.2007.12.068.

[50] Li X, Sabir I. Review of bipolar plates in PEM fuel cells: Flow-field designs. Int J Hydrogen Energy 2005;30:359–71. https://doi.org/10.1016/j.ijhydene.2004.09.019.

[51] Yoon YG, Lee WY, Park GG, Yang TH, Kim CS. Effects of channel and rib widths of flow field plates on the performance of a PEMFC. Int J Hydrogen Energy 2005;30:1363–6. https://doi.org/10.1016/j.ijhydene.2005.04.008.

[52] Saripella BP, Koylu UO, Leu MC. Experimental and computational evaluation of performance and water management characteristics of a bio-inspired proton exchange membrane fuel cell. J Fuel Cell Sci Technol 2015;12:1–9. https://doi.org/10.1115/1.4032041.

[53] Hamilton PJ, Pollet BG. Polymer electrolyte membrane fuel cell (PEMFC) flow field plate: Design, materials and characterisation. Fuel Cells 2010;10:489–509. https://doi.org/10.1002/fuce.201000033.

[54] Ozden A. Development and Characterization of Graphene - based Microporous Layers for Proton Exchange Membrane Fuel Cells. 2018.

Chapter 2

Literature Review

2.1 POROUS METAL – BASED GDLS AND FLOW-FIELDS

2.1.1 Introduction

Porous metal materials are becoming more prevalent materials to employ in various engineering fields because they possess alluring superior properties, such as high porous architecture, controllable permeability, high superior electrical and thermal conductivity, and high specific surface area. Clearly, the combination of these characteristics cannot be observed with dense metals and ceramics [1]. Even though porous metal materials were initially used in engineering applications at the outset of the 20^{th} century, sintered powder and meshes were used commercially in

engineering applications. For example, sintered powder has been employed to manufacture batteries, filters as well as self-lubricated bearing systems since the 1920's.

Porous metal materials are attracting immense worldwide attention for developing new theories, models, technologies and application areas. For instance, metal-based porous materials have hitherto been used for some engineering applications such as filtration and separation, heat exchangers, flow distributors, heat pipes, catalyst supports. Intrinsically, porous metal materials can be divided into two main subcategories: closed-cell porous materials and open-cell porous materials. The former shows good mechanical strength and load-carrying capacity but it cannot access their internal pores. In terms of the latter type of porous materials, the load-bearing is likely not to be the primary aim. Yet, this kind of material is mainly used for fluid flows, heat and thermal management applications. In the PEFC and DMFC studies, this type of material is mostly used as a flow-field/flow distributor, gas diffusion layer as well as a catalyst support [2]. To date, numerous research studies have been conducted to comprehensively investigate the possible implementation of these materials in PEFC and DMFC. Usually, carbon is the most chosen material used for PEFC and DMFC components such as flow-field plates, gas diffusion layers as well as catalyst supports. With respect to the flow-field plates, they comprise 60% of the total weight and 30% of the total cost of a PEFC stack [3]. The traditional graphite flow field plates are fabricated by grooving either one or both sides of the graphite plates using cutting methods. However, the drawbacks of this type of graphite flow

field plates are that they are brittle, thus problematic to manufacture, and have high material and manufacturing costs. In addition, the conventional flow-field designs (serpentine, parallel, interdigitated, etc.) mostly utilize the classical channel/land configurations which usually results in channel flooding and non-uniform reactant gas distribution, thereby both the fuel cell performance and lifetime can be adversely affected [4,5]. On the other hand, porous metal materials (particularly, aluminium-, nickel-, stainless steel- as well as copper- based) could be an excellent remedy to overcome all these difficulties due to their very thin and light nature and of an easy processed structure. As a result of these difficulties, considerable efforts have been made to develop alternative materials to use in gas diffusion layers and flow field plates. According to some researchers, using metal foams is supposed to be a solution in order to avoid these problems [6]. In the recent years, there has been an upward trend in the porous metal materials used as the PEFC and DMFC components and this change is undergoing, what is frequently called “metal revolution” in the PEFC society [7].

Metal porous materials, for instance, sintered stainless steel fibre felts; aluminium fibre felts; titanium, copper, and nickel meshes; aluminium, stainless steel, titanium, nickel, and nickel-chromium alloy foams; and copper foils have been hitherto a promising material to be used in PEFCs to remove the handicaps of the traditional carbon-based MPSs. In terms of the conventional carbon-based MPSs, they normally constitute of anisotropic fragile carbon fibres and a high proportion of their volume is comprised of macro-scale pores. In terms of the transportation applications, such

kind of brittle and extra-fine carbon fibres in MPSs can be seen to be ‘’doubtful” because of the potential vibrations and shocks during the operation of the fuel cell [8]. Moreover, such materials are inevitably prone to deformation under a compressive force because of their macro-scale pores and fragile nature [9]. Not only the flow-field plates but also the GDLs and other fuel cell components have to be able to withstand the clamping force on the fuel cell under realistic working conditions. The excessive clamping deformations increases the random pore characteristics, such as the uncontrolled alternation in the pore characteristics, and a significant reduction in the porosity. As a result of these deformations, the capillary pressure tends to increase and the water is driven through the MPS. Thus, this undesired incident facilitates the “water flooding” phenomenon.

Metal-based materials have been researched and developed as potential substrates due to their superior intrinsic properties such as mechanical strength, plasticity, high electrical and thermal conductivity, controllable pore size, permeability, high specific surface area, etc. Although metal based materials possess the above mentioned merits, they are still under the development stage for the use in new technology and industry. In the literature, there remains much scope to profoundly unravel the mechanisms of the porous materials used in PEFC and DMFC performance. In 1990, Hryniewicz et al. [10] conducted a precursory study on the fuel cell area and investigated the nickel porous sinter as the electrodes for hydrocarbon fuel cells at a moderate temperature. They pointed out that the sinters provided high real surface

area and sufficient porosity. In addition, different sizes of nickel particles were used and the smallest particle size was preferred since it produced the greatest porosity.

Metal-foam materials and metal fibre sintered felts are extensively employed as catalyst supports in microreactors owing to their superior pore structure and excellent mechanical performance. Although nickel foam, aluminium foam, FeCrAl foam, and Cu-Zn foam have been used in microreactors in order to generate hydrogen. However, the metal fibre sintered felt is a state-of-the-art type material which has reticulated the 3D architecture, and completely connected the pore size and high porosity. Due to these inherent characteristics of the metal fibre sintered felt, the catalyst is able to be supported on the surface of the metal fibre sintered felt, and the adherence strength of the catalyst is likely to be enhanced. Thus, stainless steel fibre sintered felts (316) have hitherto been employed as the catalyst support in microreactors to decompose ammonia [11].

2.1.2 Copper fibre felt-based GDLs and flow-field plates

The copper fibre sintered felt can be defined as a state-of-the-art material that possesses a 3D net-like structure and fully connected pores high porosity. This felt is intrinsically a good electrical and thermal conductivity but such a felt has a lower corrosion resistance and it is inherently prone to corrode in PEFC operational conditions. Thereby, this material has been seldom used as a GDL and the flow-field plate in fuel cell applications [12]. To overcome this issue, alloying treatments or surface coating methods are used to improve the corrosion resistance of copper-based fuel cell components for PEFC applications [13,14]. Graphene has been

recently started to be employed as a corrosion-resistant coating for stainless steel, copper as well as nickel-coated flow-fields used in PEFCs [14–17]. For example, the graphene treatment on the copper is likely to enhance the metal corrosion resistance 1.5 times higher than bare copper [18]. Ren et al. [14] pointed out that the charge transfer resistance of the graphene coated copper is on the order of 3 times higher than that of the bare copper. Therefore, the graphene coatings are expected to improve the corrosion resistance of copper-based bipolar plates. In addition, the graphene coated copper flow-field using PEFC clearly outperformed that of the bare copper flow-field [15]. The reason why the bare copper flow-field showed lower performance after 5 h working is because of the surface oxidation. Figure 2.1 shows photographs of the copper fibre felt-based flow-field and the assembled PEFC.

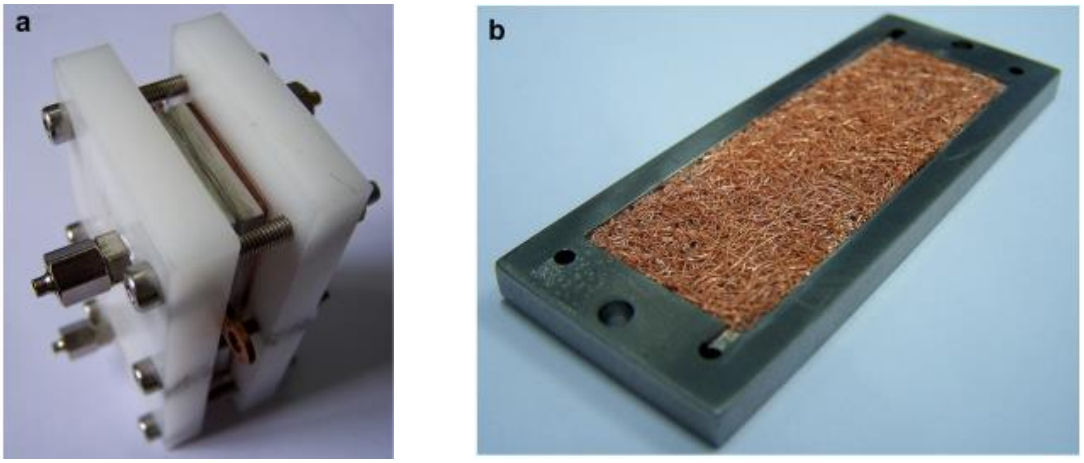

Figure 2. 1 – Photographs of (a) the assembled copper fibre felt-based PEFC and (b) the copper fibre felt-based flow-field plate (adapted from [12]).

Tang et al. [19] manufactured the highly porous copper fibre sintered felt (CFSF) using the sintering method and compared this material as a catalyst support to that of sintered stainless steel fibre felt (SSSFF) for the hydrogen production process. Recently, Li et al. [20] manufactured and investigated the porous copper fibre sintered felt as an alternative flow field plate to use for PEFC. They reported that the copper fibre sintered felt provides more uniform pressure and velocity distribution compared to the serpentine FFPs. Notably, the best performance was obtained from 70% porosity copper fibre sintered felt-based FFP on 70°C cell temperature. Likewise, in a very recent study by Lian et al. [21], copper fibre sintered felt was employed as a FFP for PEFC. The sintering process of the copper fibres created tortuous pathways through the fibres; resulting in increased water transport capability. The experimental findings revealed a notable increase in pressure drop as the porosity decreased. For example, the pressure drop was measured at 0.51 kPa for 80% porosity, whereas it rose to 2.08 kPa for 60% porosity. It should be noted that the fuel and oxidant supplies become more difficult and required pumping power is likely to increase considerably. Moreover, the optimum porosity was determined as 70% and the peak power density was ~19% higher than serpentine FFP.

2.1.3 Copper foil-based GDLs and flow-field plates

Copper materials have hitherto attracted substantial attention for exploiting as a GDL material due to its affordable cost, superior thermal and electrical conductivity, exceptional resistance to electromigration, and high durability [22]. In addition, etching techniques have been used to convert copper foils in porous materials with

a collection of micron-scale holes in order for them to be utilised in fuel cells as a GDL. With the aim of achieving the required patterns of holes, a proper mask design is needed to regulate several factors, such as the chemical etchant type, etching duration, etching rate, and operation temperature. For example, Zhang et al. [22] experimentally evaluated the impact of the mask shape, mask width and etching time for super thin copper (110) foil. The etching rates that are requires to acquire micro-scale features are approximately 1-2 µm/min, and this is primarily dominated by the mask width owing to the mass transport resistance. In another attempt to investigate the copper foil for the PEFCs, by Zhang et al. [23], a metallic porous gas diffusion layer, with enhanced electrical and thermal conductivities, comprising of a 12.5 µm thick copper foil (Cu110), was developed and evaluated under PEFC operational conditions. At the lower flow rates, the fuel cell using the copper foil-based GDL renders an enhanced water management ability. In addition, the fuel cell performance is not affected by the lower flow rates, in contrast to the commercial Toray TGP-H-060 carbon paper which is likely to decline up to 30%. SEM images of the copper foil based GDL is shown in Figure 2.2.

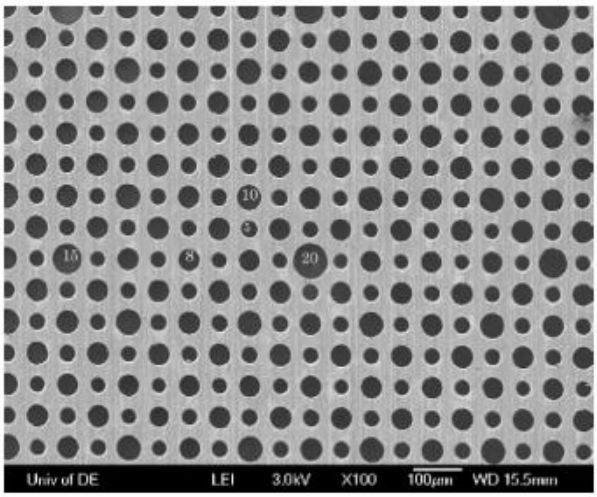

Figure 2.2 – SEM image of the copper foil-based GDL [23].

2.1.4 Stainless steel fibre felt-based GDLs and flow-field plates

Li et al. [24] utilized the stainless steel (316L) fibre felt material at both the cathode backing layer and cathode current collector for micro DMFC applications. In the scope of this work, the novel structure could significantly hinder the methanol crossover; therefore, the performance was likely to be enhanced at higher methanol concentrations. Moreover, the water management at room temperatures inclined to be improved due to the stainless steel cathode electrode. Likewise, Yi et al. [8] experimentally investigated the sintered stainless steel (316L) fibre felt as gas diffusion layers in PEFC. The sintered stainless steel fibre felt is layered with an amorphous carbon (a-C) film in order to improve the corrosion resistance and decrease the contact resistance. The outcome clearly showed that the sintered stainless steel fibre felt GDL is an auspicious solution to enhance the fluid permeability of the GDL under compression owing to its intrinsically higher

compressive modules and ductility. Similarly, Lu et al. [25] experimentally evaluated the feasibility of stainless steel fibre felt FFPs for PEFC. The results showed that gold-coated stainless steel fibre felt FFP produced 125 mW/cm^2 at 2500 mA/cm^2. According to their findings, the coating may increase the corrosion resistance of stainless steel fibres.

Tang et al. [19] manufactured a highly porous copper fibre sintered felt (CFSF) using the sintering method and compared this material as a catalyst support to the sintered stainless steel fibre felt (SSSFF) for the hydrogen production process. The Cu/Zn/Al/Zr catalyst was coated on the CFSF surface by the impregnation technique and the catalyst-coated CFSF was employed in the methanol steam reformer (MSR) in order to produce hydrogen. As a result of this study, the CFSF material indicated augmented stability of the catalyst layer, an increase in the contact time as well as an increase in the colliding opportunities of the CFSF surface and methanol-water mixture. Furthermore, the CFSF revealed that the methanol conversion, the reformate gas flow rate, and H_2 generation rate for MSR using CFSF are superior to the SSSFF.

2.1.5 Perforated stainless steel sheet-based GDLs and flow-field plates

The potential use of a perforated stainless steel sheet as a MPL was experimentally evaluated by Leeuwer et al. [26]. The paramount goal in this study was to provide insight into alternative MPLs, i.e. graphene foam, perforated graphitic layer, and perforated stainless steel sheet, with improved interface characteristics. In the scope of this scientific study, the commercial MPL exhibited a considerably higher in-plane resistivity compared to the alternative MPLs. The main reasons for the higher in-

plane resistivity were the presence of non-conductive PTFE and the particulate characteristic of carbon. Furthermore, the perforated stainless steel sheet exhibited the lowest in-plane resistivity due to the inherently nonporous architecture which renders an uninterrupted pathway for the in-plane electrical conduction. The overall through-plane resistance also strongly depends on the compression force. In addition, the perforated stainless steel sheet possesses the most uniform and smoothest surface.

Likewise, Blanco et al. [27] analysed how the structural parameters of perforated stainless steel sheets affect the PEFC performance, i.e. the sheet thickness, the channel width, the channel depth, the perforation diameter. They reported that the perforated stainless steel sheet as a GDL reveals poorer performance than the commercial Sigracet® 25BC GDL and this is because of the lack of in-plane diffusion, the perforated stainless steel sheet showed a similar performance at the low current densities regardless of the geometric dimensions mentioned above. As for the in-situ and ex-situ tested perforated stainless steel sheet-based PEFCs, the best performance, and the lowest resistance were observed by the perforated stainless steel sheet with 1 mm perforations and 34.7% open area owing to the best balance between the electrical contact and gas permeability. Also, the potential improvement in the manufacturing capabilities of this sort of perforated material is supposed to facilitate the utilisation of such materials for specific fuel cell applications.

More recently, Tanaka et al. [28] focused on the development of carbon-based MPLs to cover the top surface of the perforated stainless steel sheet to augment the gas

diffusion from the perforated holes to the solid area of the MPSs in order to hinder flooding on the hydrophilic surface of the MPSs' holes. For this aim, they experimentally and numerically evaluated the MPL coated perforated stainless steel sheet as a GDL and the channel/land ratio of the flow-field plate design in PEFCs. According to their findings, the microporous layer was a key component in the hindering the flooding and to promote the gas diffusion in this sort of perforated metal sheet-based GDLs. In addition, the clamping force exhibited an immense implication on the electrical resistance, contact resistance, and gas diffusion around the MPL, therefore, the cell performance has a significant correlation with the clamping force.

2.1.6 Metal mesh-based GDLs and flow-field plates

Tanaka and Shudo [29], developed a 50 µm thick stainless steel fibre with 0.1 µm thick gold plating microcoils to be employed on the cathode side of the PEFCs as both MPS and flow-field plate. The main motivation in the developing of this up-to-date system stemmed from the need for eliminating the flooding in the GDL. The microcoil-based PEFCs yielded a flood-free performance, whilst a grooved flow-field plate with a Toray TGP-H-060 GDL showed there was flooding because of the non-uniform architecture of the commercial carbon paper. In addition, it should be noted that the microcoil-based PEFC exhibited a higher-frequency resistance than that of the grooved flow-field plates with a Toray TGP-H-060 GDL and this was because of the differences in the electron conduction path and the in-plane electron conductivity in the MPL.

The same researchers (Tanaka and Shudo [30]) reported, when using a straight-shaped or meandering-shape corrugated stainless steel meshes as both MPS and flow-field plate placed directly on the MPL, then it is likely to render a reduction in the flooding. In terms of the polarisation curve, the corrugated-mesh-based PEFC exhibited a lower flooding tendency at higher current densities, whereas the fuel cells using such materials were prone to show a considerably high-frequency resistance because of the lower contact area between the corrugated-mesh and MPL.

Tanaka and Shudo [31] evaluated the use of a corrugated stainless steel mesh GDL in PEFCs instead of use of the conventional carbon-based flat GDLs. This study yielded that the corrugated stainless steel mesh GDL attributes more uniformly distributed gasses to lower the flooding even at higher current densities. However, the inner electrical resistance of the corrugated stainless steel mesh GDL used in the fuel cell is much higher than that in the conventional fuel cell since the corrugated mesh GDL and the MPL possess a low contact area with just point contacts. Furthermore, the contact resistance and the conductivities of each of the materials in the corrugated stainless steel mesh GDL using PEFCs were evaluated under several different clamping forces. In addition, an electrical-electrochemical-mechanical model was developed by STAR-CCM+ software to investigate the impact of the electrical resistance on the PEFC performance.

2.1.7 Metal foam-based GDLs and flow-field plates

Metal foams can be defined as new types of porous materials that have gained considerable attention owing to its superb characteristics which are suitable over a

broad spectrum of engineering applications [32,33]. Various names such as, cellular solids, cellular metal, porous metal, cellular metallic material, sintered porous structures, syntactic foam, etc., have been suggested as a suitable name for the metal foams [34]. Such materials possess excellent intrinsic properties, such as the high large surface area (owing to its elaborate architecture), low density, superb gas permeability, excellent electrical and thermal conductivity, and high strength-to-weight ratio. Thereby, metal foams can be considered as an auspicious material used in energy applications, such as fuel cells and batteries. In engineering, the terms "pore" and "cell" are prone to be misunderstood because these terms are used to define the same structure in a different manner. The "pore" term means a small void/space/perforation. Likewise, the "cell" term can be defined as a minute unit/structure/compartment in a larger structure. In the literature, metal foams are divided into two main groups named closed-cellular metal foams and open-cellular metal foams. The closed-cellular metal foams generally consist of continuous walls that separate the cells from each other. On the other hand, open-cellular metal foams are inherently inclined to enable the fluid to flow through one cell to another. Open-cellular metal foams can be defined as auspicious materials to be utilized for the future automotive fuel cell applications since such materials are extremely light, have great porosity (more than 80%), as well as superior electrical and heat conductivity [35]. At this moment, the term metal foam is used for only open-cellular metal foams. Figure 2.3 indicates the open-cellular metal foam, closed-cellular metal foams, as well as the terms "pore" and "cell" in an open-cellular metal-foam.

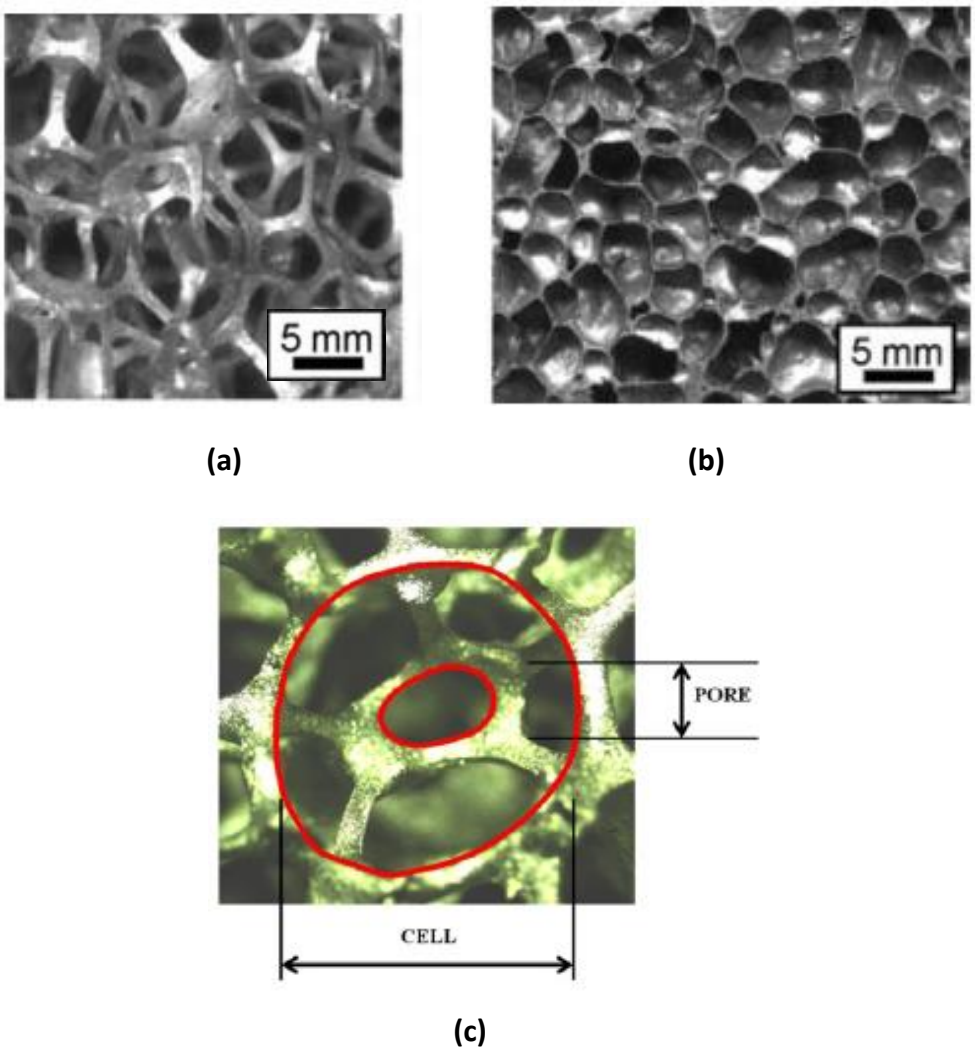

Figure 2.3 – An illustration of (a) the open-cellular metal foam, (b) closed-cellular metal foam, and (c) the terms of "pore" and "cell" in open-cellular metal foam (adapted from [36,37]).

The metal foam applied PEFCs are prone to exhibit reduced mass transport losses and higher performance [35]. In addition, such foams can secure a tortuous gas flow through the structure and a low pressure drop between the inlet and outlet. More recently, the same research group has developed a 3D computational fluid dynamic electrochemical model for metal foam-based flow fields and they have compared it

to a conventional flow-field both experimentally and numerically [38]. The results show that the metal foam-based flow field secures smoother hydrogen and oxygen distributions between the inlet and outlet and outperformed the conventional flow-field. Moreover, according to the model outcomes, the metal foam-based flow-field showed better water and heat management than the conventional flow-field.

Wang [39] proposed an approach to develop a flow-field approach for the metal foam to provide support over the GDL and decrease the contact resistance under the channel. A 3D numerical model was constructed to examine the low humidity operations of the PEFC with both a traditional hollow channel designed flow-field and a metal foam-filled channel designed flow-field. According to the simulations outcomes, the metal foam-filled channel designed flow-field exhibited an enhanced heat and electrical transport capacity and a design flexibility for possible further studies. In addition, the conducted analyses indicated that the in-plane channel dimension and the GDL thermal property have a negligible effect on the local temperature variations and ohmic losses for the metal foam filled channel designed flow-field, however, they are prominent for the traditional hollow channel designed flow-field. Likewise, in 2014, the effectiveness of metal foam-based flow-field plates was examined for PEFC to replace conventional serpentine flow-field plates by the use of both computational fluid dynamics (CFD) models and experimental methods [40]. The conducted analyses and experiments clarified that the optimised metal foam can ensure superior gas flow through the fuel cell, diminish the pressure drop between the inlet and outlet, and increase the PEFC performance compared to the

traditional serpentine flow-field design. In the same year, Choi et al. [41] developed a promising next-generation titanium (Ti) foam-based GDL to utilise as an anode GDL in PEFC. The results indicated that the Ti foam-based GDL used PEFC's current density at 0.7V (~0.46 A/cm^2) is approximately 160% higher than carbon based Toray-060 GDL (0.28 A/cm^2). Moreover, they highlighted that the Ti foam-based GDL possesses superior corrosion resistance and provides a long-term reliability and chemical stability. More recently, the performance of the metal foam-based FFP was numerically compared to the serpentine FFP by Son et al. [42]. According to this study, metal foam–based FFP with two-turn serpentine channel structure showed about 6% higher performance than traditional serpentine FFP. Nevertheless, it should be noted that the longer flow path means the higher pressure drop which requests higher parasitic pumping power.

A 3D steady-state PEFC model using porous metal foam as a flow field material has been developed and compared to the traditional flow field plate which possesses rectangular channels [2]. They emphasized that the permeability has a crucial effect on the performance of the fuel cell. The decreasing permeability of flow field plate indicated better cell performance. As a result, traditional machined channelled flow field plates cannot be decreased below the 10^{-8} m^2 permeability values because of the difficulties in the machining process. For this reason, the metal foam flow field plate is proposed as the flow field plate for PEFCs. This phenomenon may be explained by the increase in the pressure drop which can enhance the mass transfer between the flow field and the electrode-membrane reaction interface through

forced convection. In addition, the numerical results of Hontanon et al. [43] reinforced the outcome. In addition, Ni-Cr metal foam, stainless steel (SS-316) metal foam, conventional multi-parallel machined stainless steel (SS-316), as well as carbon cloth were investigated experimentally as flow fields in PEFC. The performance of Ni-Cr metal foam based flow field is higher than that of other material based flow fields followed by stainless steel (SS-316) metal foam, conventional multi-parallel machined stainless steel (SS-316), and carbon cloth [44]. The main reason why the carbon paper showed the lowest performance is because of the high contact pressure in the cell which induces the pressing of the cloth and the clogging of the void spaces in the carbon cloth. Likewise and more recently, the potential usage of the Ni-Cr foam as FFP was evaluated for PEFCs by Lee et al. [45]. They emphasised the stainless steel-based FFP has some potential drawbacks such as lower electrical conductivity and corrosion resistance. They found that the uncoated Ni-Cr foam-based FFP and self-assembled three-dimensional graphene coated FFP show highly close power density performances; 340 mW/cm^2 and 380 mW/cm^2 (at 0.5V), respectively. However, when the Ni-Cr foam was coated with web-like graphene and gold, the power density performance significantly improved; 480 mW/cm^2 and 500 mW/cm^2 (at 0.5V), respectively. This situation arises from the reduced ohmic and kinetic resistances.

The performance improvement of the PTFE-coated metal foam-based flow field used for PEFC has been inspected by Tsai et al. [46]. Compared with the conventional graphite serpentine flow-field based PEFC, the PTFE-treated metal foam-based PEFC

exhibited a better performance. Likewise, the performance of three different flow-fields (parallel, baffle restricted, and metal foam-based) were studied numerically by Afshari et al. [47]. It is apparent from their studies that when using metal foam as a cathode flow-field then it was likely to enhance the current density and oxygen concentration at the cathode catalyst surface and more effectively spread them. In addition, the temperature distribution was much more uniform compared to the other flow-fields. They also concluded that increasing the metal foam porosity is likely to enhance the current density value and diminish the pressure drop, whilst it does not affect the temperature distribution. A very recent experimental study was conducted by Wilberforce et al. [48] to elaborately investigate the Aluminium foam-based, copper foam-based, and stainless steel foam-based flow field plates compared to serpentine flow field plates. They found that the metal foam based FFPs exhibit superior performance with using less hydrogen and oxygen consumption than the serpentine one. It should be noted that the Aluminium foam-based FFP generates more current compared to other metal foam-based FFPs with lower weight structure.

More recently, Azarafza et al. [49], numerically analysed the conventional parallel, serpentine, and interdigitated cathode flow-field configurations and metal foam-based flow-field on the cathode side of a PEFC. They established a 3D, multiphase, non-isothermal CFD model, which includes the anisotropic nature of GDLs. The outcome exhibited that the highest fuel cell performance is observed with the metal foam-based flow-field plate and this was because it has the lowest water saturation, more uniform current density and temperature distribution as well as the relatively

moderate pressure drop were rendered in this flow-field. Similarly, Bao et al. [50] proposed a 3D volume of fluid dynamics model to examine both single- and two-phase flow dynamics in metal foam-based flow-field and conventional parallel flow-field. The results showed that the gas convection and uniform distribution are improved in a metal foam-based flow-field compared to the conventional parallel channels. In addition, even though water removal is relatively slower in metal foam-based flow fields compared to the parallel design, the connected void structure renders numerous gas pathways and supplies gas with high concentration. Hence, the water flooding in the flow-field reduces owing to the outstanding porous structure of the metal foam and a large number of pores which induce many gas pathways. Likewise, the potential of the metal foam-based flow-field to enhance the water management capacity for PEFCs has been also investigated most recently by Wu et al. [51] via an in-operando neutron radiography technique. They have emphasised that using metal-foam based flow-field improves the reactant distribution uniformity by eradicating the classical "land/channel" geometry. The outcome of this study primarily showed that the metal foam-based flow field has a superior tolerance to dehydration at 1000 mA cm^{-2} than the serpentine flow field. Thus, the maximum power density of the metal foam-based flow field is about twice higher than that of the serpentine design owing to the excellent characteristics of the metal foam. Awin and Dukhan [52] experimentally evaluated the various aluminium foam-based FFPs with various porosity values and compared them to the conventional serpentine FFP. They first reported that all aluminium foam-based FFPs succeeded to remain their operating temperature within the allowable ranges for

safe operating temperature. Secondly, the output power of the aluminium foam-based FFPs surpassed the performance of the conventional serpentine FFP in all cases. The best performance improvement was recorded for the lowest porous case (ε= ~70%) as about 10%. Thirdly, they stated that the aluminium foam-based FFPs consumed less oxygen (4.2%) and hydrogen (4%) than serpentine one whereas they improved the conversion efficiency by 3.9%. Finally, they also emphasised that the new aluminium foam-based FFP designs can help to reduce the weight by approximately 28% compared to graphite-based serpentine FFPs.

The performance of the metal foam based high-temperature polymer electrolyte fuel cell (HT-PEFC) as the flow-field plate was experimentally evaluated by Tseng et al. [53]. The outcomes yielded that metal foam-based flow-fields entails high gas permeability, superb gas convection and diffusion, and enhances the reaction opportunity with the catalysts. In addition, the porous structure of the metal foam was able to decrease the contact resistance between the flow-field plate and the carbon paper. The HT-PEFC with a metal foam showed 20% higher current density (at 0.6 V) than that of the conventional graphite serpentine flow channels. Moreover, the long-term stability (200 and 300 hours) exhibited that there is no substantial increase in the resistance. Moreover, the mass resistance is likely to be insignificant in metal foam-based fuel cells. Jo and Ju [54], showed the consequence of utilising metal foam as a flow-field plate for realistic low humidification automotive PEFC environment, that was numerically evaluated, and the water management capacities of such contemporary flow-fields compared to the serpentine flow-field designs. The

results clarified that the use of metal foam-based flow fields for PEFCs induces higher fuel cell performance than serpentine flow-fields. In addition, the harmful oxygen depletion is eradicated and the membrane hydration is likely to be better due to the weaker convective flow and the absence of the channels and ribs in metal foam based flow-fields. On the other hand, the excess water in the metal foam-based fuel cell was efficiently removed, therefore the flooding occurred due to the weaker convective flow. For this reason, they suggested the use of metal foam-based flow-fields for low humidity PEFC applications.

2.1.7.1 Copper foam-based GDLs and flow-field plates

In the fuel cell literature, copper foam based GDLs and FFPs are attracting more attention owing to the excellent properties of copper. Copper is one of the ideal materials to be used as a GDL or FFP since it is a cheap material, has 3D pores, high porosity, increased electrical conductivity, and likely to exhibit high performance [55]. Parvanian and Panjepour [56] evaluated the utilisation of copper foam for the flow-field in PEFCs. They concluded that the copper foam is a potential to employ as a FFP owing to its significant superior bending strength with decreasing porosity. In addition, the permeability of the copper foams is less than 10^{-8} m^2, which is an ideal value of the permeability, therefore they are promising to employ for PEFCs as FFPs. More recently, Park et al. [55], investigated the feasibility of the various copper foams for PEFC to be used as a FFP. They concluded that the optimized copper foam possessing a large contact area and small ribs are ideal for the mass transfer and ohmic resistance. Moreover, the pressure produced on the inside of the copper foam

increased the reactant's partial pressure, therefore this led to an enhanced performance.

2.1.7.2 Nickel foam-based GDLs and flow-field plates

The nickel foam reveals it to have an exceptional potential to function as a suitable material owing to its large surface area (due to the highly complex geometry), lower density, superior gas permeability and high strength-to-weight ratio [57]. Nickel foams also provide relatively higher electrical conductivity, catalytic activity, and corrosion resistance, thus the Ni foams are employed in numerous energy applications, such as batteries and solar cells as electrodes, SOFCs as current collectors, PEFCs (as GDLs and flow-field plates) etc. Furthermore, nickel foams have perfect characteristics for heat transfer and thermal management systems, such as heat exchangers [32]. In addition, such foams possess excellent mechanical properties and are lightweight. Furthermore, the nickel foams show a much better resistant to corrosion than copper foam and other metal foams [58]. The characteristic of the nickel form has variable important parameters, such as the permeability, the size of pores, pores per inch (PPI), etc.

As mentioned in the Chapter 2.1.7, there are two type of metal foams; the closed cellular metal foams and the open-cellular metal foams. In contrast to the closed cellular metal foams, the open cellular metal foams are able to allow the fluid to flow through one cell to another. As for the closed cellular metal foams, such metal foams were made by continuous walls which separate one cell from the other. The cell geometry is generally spherical shape. The characteristics of the metal foams are able

to be adjusted to meet the design requirements. As of now, the term metal foam is only used to define open-cellular metal foams. In the literature, there are many nickel foam manufacturing methods, namely: (i) freeze casting, (ii) vapour deposition, (iii) 3D printing, (iv) electrolytic deposition, and (v) powder metallurgy.

According to Tan et al. [32], there has been an incremental increasing trend to utilise the metal foams for renewable energy applications. For instance, metal foams have been started to be used in solar energy harvesting systems as a heat transfer media as well as in fuel cells as an electrode, GDL, and flow-field plate. Due to a declining trend of the cost of foams, such materials are becoming more popular in fuel cells. For instance, an US company, Alcoa, presented a new continuous foam casting method and one of their aims was to reduce the foams' manufacturing cost. They estimated that the cost of such materials is reduced to 5 US$/kg when the large-scale mass production will become available [1]. The cost of the nickel foam activated carbon cathode in microbial fuel cells (MFC) is also 1/30 of that of carbon cloth Pt cathode [59]. According to Hussain et al. [58], the cost of nickel foam is lower than that of copper foam, aluminium foam, and graphite/graphene foam. Bidault et al. [60] evaluated the use of nickel foam as a cathode electrode substrate in alkaline fuel cells. Compared to the nickel mesh, nickel foams possesses a lower weight-to-surface ratio as well as it being considerably less expensive than the nickel mesh. In this study, silver deposited onto the nickel foam producing an outstanding electrochemical performance compared with that of the nickel mesh owing to a decline in both the ohmic resistance and ORR charge transfer resistance. More

recently, Toghyani et al. [61] has developed a 3D CFD model to investigate the performance of the nickel foam-based flow-field using a proton exchange membrane electrolyser cell (PEMEC) and compared the cell performance with conventional parallel and serpentine flow-field plates. The numerical results indicated that the simple nickel foam-based flow-field produced the highest performance owing to the uniform current density distribution, the uniform distribution of the hydrogen mass fraction as well as the lower temperature gradients. Moreover, the outcomes are that the pressure drop in the nickel foam-based flow field plate is significantly lower than that in the serpentine flow-field plate. They concluded that the pressure drop of the system inclines to be considerably enhanced by decreasing the permeability; however, the performance is slightly improved.

Tseng et al. [62] experimentally evaluated the possibility of using nickel foam based flow-field plates in PEFCs. To prevent the corrosion, nickel foams were treated with a corrosion resistant material, such as PTFE, and thus they did not only hinder the corrosion but also reinforced hydrophobicity. The porosity of the nickel foam is about 95-98% and they applied compression to it to increase the electrical conductivity, albeit with a slight decrease in porosity. The results show that the non-PTFE coated nickel foam-based PEFC experiences water flooding at a very early stage (at 0.74 V and 139 mA cm^{-2}), therefore the performance severely deteriorates. On the other hand, 40% PTFE-treated nickel foam based PEFCs show a better performance than that of the 60% PTFE-treated. Therefore, they concluded that 40% PTFE treatment is the optimum value for this study. When the PTFE content is below the optimum level,

water occurs and the gas transport decreases. On the other hand, if the PTFE content is higher than the optimum value, the porosity is severely affected because of the obstructed pores. The through-plane and in-plane pores are shown in the Figure 2.4. Moreover, the behaviour of the metal foam under compression is examined and the pore size in the through-plane direction is likely to be larger than that in the in-plane direction due to the uni-directional compression. This means that the gas flow capacity is better in the through-plane direction than the in-plane direction. Moreover, both the electrical conductivity and the cell performance improves due to the compression. Tabe et al. [63] experimentally investigated the nickel foam-based cathode flow-field plate used in the PEFC under high and low humidity conditions and strived to clarify the internal phenomenon in the cell which affect the cell performance. They also compared the cell performance with conventional serpentine and straight flow-field plane designs. Their results exhibited that the nickel foam-based PEFC is more stable rather than the conventional design-based PEFCs at higher current densities; however, at the lower current densities, such flow fields tend to be less stable than conventional designs. In addition, the nickel foam-based flow-fields were observed to produce a higher cell performance than conventional designs due to their hydrophilic porous nature. As a result of this property, the nickel foam-based flow-field is prone to be superior in draining the excess water from the GDL surface. On the other hand, the temperature increases in the nickel foam-based flow-field plate and it is likely to be larger than in the conventional designs because of the low heat removal capacity. Thereby, the nickel foam-based PEFC is inclined to be unstable at relatively low humidities. Baroutaji et al. [64] used a nickel foam-based flow-field

for air breathing PEFCs and compared their results with the serpentine flow-plate results. The results demonstrated that the nickel foam-based PEFC exhibited better cell performance than that of the serpentine based. In addition, the impact of the hydrophobic treatment on the nickel foam-based flow-field plate was examined and it is stated that the PTFE coated nickel foam-based flow-field possessed superior hydrophobicity and corrosion resistance to the uncoated nickel foam-based flow-field plates. More recently, Shin et al. [65], utilised four nickel foams with different cell size (450 μm, 580 μm, 800 μm, and 1200 μm) as the cathode flow-field plate and experimentally improved the cell performance. Also they developed a mixed type nickel foam which was made by 450 μm cell size nickel foam as a front triangular and 800 μm nickel foam as a back triangular. The former was used to increase the contact surface and the latter was utilized to boost the gas diffusion. Finally, they suggested that the mixed type nickel foam may be an ideal flow-field to increase the cell performance. According to their results, the mixed nickel foam-based flow-field design is able to increase the fuel cell maximum power by approximately 60.1% compared to the conventional serpentine flow-field design. Kim et al. [66] experimentally evaluated the potential usage of the nickel foam-based FFP for PEFCs. The results exhibit that the nickel foam-based FFP (for both anode and cathode sides) provides approximately 35% higher power density (1.21 W/cm^2) compared to the conventional parallel type FFP (0.90 W/cm^2). Especially, there is an apparent improvement in the concentration polarisation region when nickel foam is utilised as anode and cathode FFPs. The reasons behind this phenomenon are improvements in gas diffusion, water management and lower electrical resistance when the nickel

foam is chosen as FFP. Likewise, Chen et al. [67] pointed out that the nickel foam-based FFPs has a good potential to handle the water flooding issue in PEFCs. Therefore, they conducted many experimental works to evaluate the up-to-date FFPs performance and durability. According to their findings, the increased compression ratio (~70%) on cathode make ensures the voltage stability during a 3-hour current density test. On the other hand, the similar stability was obtained from ~40% compressed nickel foam on the anode side. Moreover, the optimised nickel foam-based FFPs exhibit approximately 10% higher power density than conventional graphite parallel FFP. The reason for this situation is the air velocity is likely to increase with the nickel foam compression; thereby, the pressure drop through the inlet and outlet is significantly enhanced. Thus, the accumulated water is forced to evacuate the reaction area. Moreover, the compression increases the contact area between nickel foam and membrane electrode assembly (MEA). Similarly, Liu et al. [68] aimed to improve the PEFC performance using nickel foam-based FFPs with various compression ratios. It should be noted that the higher compressed nickel foam-based FFPs show better performance owing to lower electrical resistance, smaller pore diameter and uniform flow distribution. The maximum power density for optimised nickel foam-based FFP was enhanced by 6% (1.76 W/cm^2) with the conventional graphite serpentine FFP (1.66 W/cm^2). In 2021, Wan et al. [69] similarly proposed the use of nickel foam as a promising FFP for PEFCs due to eliminate the channel/rib geometry. This experimental study aimed to evaluate the impact of different arrangements of nickel foam-based and graphite-based FFPs on the anode or cathode sides. The results demonstrated that employing nickel foam on both the

anode and cathode sides resulted in a highly uniform temperature distribution at the membrane, which is vital for ensuring the membrane durability. Furthermore, utilising nickel foam on both sides appeared to be an effective strategy to prevent water flooding within a relative humidity range of between 0% and 80%. However, it is important to note that this configuration had certain drawbacks for 100% relative humidity conditions. The experimental findings indicated that incorporating a nickel foam-based FFP on anode side and a graphite-based FFP on cathode side resulted ~16% higher performance compared to using graphite-based FFPs on both sides PEFC. On the other hand, whilst the nickel foam-based FFPs were utilised on the both sides of PEFC, only a modest improvement of ~9% in performance was observed than the fully graphite-based PEFC configuration. Inevitably, this configuration used nickel foam on both sides encountered the flooding phenomenon, particularly on the cathode side. This flooding led to liquid water accumulation and reverse diffusion into the anode side. Even though the authors did not provide a specific suggestion to address this issue, it is plausible to optimise the interior structure of the nickel foam (by identify the ideal clamping ratio) and increasing the air stoichiometry are likely to handle this problem. In a more recent study by Park et al. [70], they mainly aimed to decrease the component cost of large-scale stationary PEFC applications by using nickel foam-based FFPs. For this goal, the mass transfer characteristics of reactant and oxidant were numerically investigated through the GDL and nickel foam-based FFP and experimentally validated. The findings revealed that using the nickel foam-based FFP led to an enhancement in water removal efficiency by approximately 6.55%. Moreover, the PEFC performance increased by ~9% when nickel foam-based

FFPs used. The authors also emphasised that the cell performance is likely to be enhanced by ~15% in case of using highly porous and permeable GDL. It can be seen that the optimised GDL properties indeed have a significant effect on the cell performance.

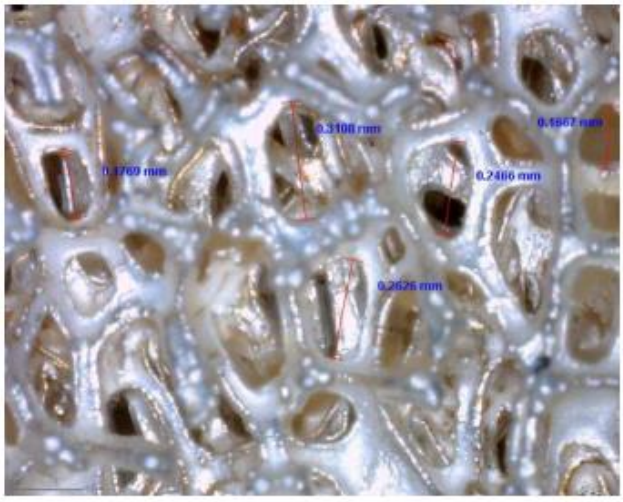

(a)

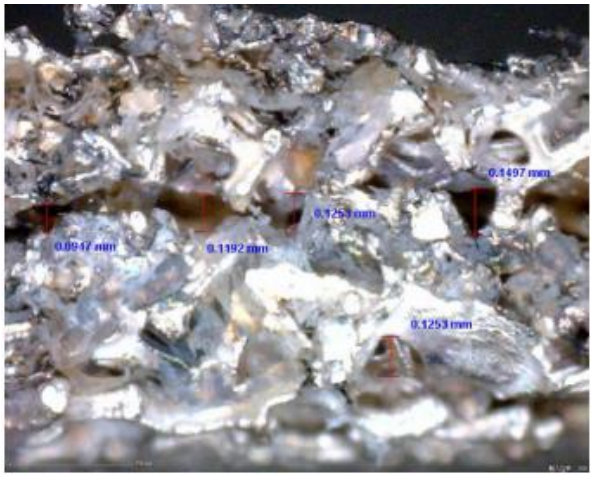

(b)

Figure 2.4 – Photographs of (a) the through-plane and (b) the in-plane pores of nickel foam (adapted from [71]).

More recently, the mechanical behaviour of nickel foam-based flow field plates under a clamping force was investigated via X-ray computed tomography (X-ray CT), electrochemical tests and a finite element analysis [72]. They found that the cell performance improved by 42% when the clamping force was increased from 20% to 70%. This considerable increase in the performance can be explained by a decline in the interfacial contact resistance between the nickel foam and GDL. Moreover, the interfacial contact area between the nickel foam and GDL is about 10 times higher than that of the nickel foam and a stainless steel flow-field plate. In the same year, Fly et al. [73] conducted ex-situ experiments to visualise the movement of the liquid water into the nickel foam-based flow-field plate to consider the effect of the hydrophobicity, pore size, as well as air flow rate. In addition, a two-phase CFD model was developed to investigate the fundamental water transport behaviour in the nickel foam-based flow-field plate. Both the experimental and numerical results showed that the air flow rate does not have a significant impact on the water removal in the nickel foam-based flow-field plate owing to the higher surface tension between the water and foam pore ligaments, and this is in contrast to the conventional flow-fields. In addition, the hydrophobic foam was observed to be prone to transporting the water away from the injection point faster than the hydrophilic foam. They also emphasised that the best way to manage the water distribution in the nickel foam-based PEFC is to control the hydrophobicity and the pore size.

2.1.8 Summary

This section is a short literature review of porous metal-based GDLs and flow-field plates. The reviewed porous metal-based GDLs and flow fields can be listed as follows;

- Copper fibre felt-based GDLs and flow-field plates
- Copper foil-based GDLs and flow-field plates
- Stainless steel fibre felt-based GDLs and flow field plates
- Perforated stainless steel sheet-based GDLs and flow field plates
- Metal mesh-based GDLs and flow field plates
- Metal foam-based GDLs and flow field plates
- Copper foam-based GDLs and flow field plates
- Nickel foam-based GDLs and flow field plates

The abovementioned studies have shown that nickel foam-based PEFC components are likely to enhance the cell performance since they have great potential to improve the mass transfer and water management. Thus, the nickel foam-based GDLs are receiving more attention owing to its superior structure and potential as a cathode GDL. However, it can be clearly seen in the report that the most of the nickel foam-based PEFCs studies have focused on the flow-field plates rather than GDLs. However, very few studies have examined nickel foam-based GDLs for PEFCs. Besides, although the nickel foam-based materials have been experimentally investigated in the literature, there are no any comprehensive studies that have been conducted to investigate the transport characteristics of such sorts of metal-based GDLs.

2.2 X-RAY COMPUTED TOMOGRAPHY (X-RAY CT)

X-ray computed tomography (X-ray CT) has been defined as a non-destructive and non-invasive imaging method that uses X-rays to generate two dimensional (2D) transmission images of a specimen from different orientations [74]. These captured images have been then employed to generate three dimensional (3D) structures via software to give a good insight into the interior architecture of the specimen. X-ray tomography utilizes the capacity of the X-ray radiation to penetrate the objects examined [75]. The first X-ray CT imaging system was invented by Godfrey Hounsfield and Allen Cormack in 1972 and as a result they won the Nobel Prize in 1979 [76,77]. The 'tomography' term is derived from two Greek words, *'tomos'* and *'graphein'*, which mean 'slice' and 'to write or record the image', respectively [74].

Both the X-ray CT technique and the magnetic resonance imaging (MRI) technique have existed in the medical imaging field since the 1970s to provide 2D x-ray images. Despite both techniques being similar to each other, both of them use electromagnetic radiation, the former employs ionizing radiation while the latter uses non-ionizing radiation like radio frequency radiation [74]. Therefore, these two techniques are employed in different application areas. MRI is likely to be convenient to investigate the soft animal tissues, whereas X-ray CT is prone to examine the higher atomic number elements of compound structures. After the invention of X-ray CT systems to be employed in the medicine sector, the potentials of these systems were discovered to be used in geology and engineering areas [78]. Early geology applications of X-ray CT were mostly regarding the soil science, petroleum geology

and sedimentology. Moreover, this imaging technique is able to be used in industry to obtain a much better insight into the interior structures and physical properties (e.g., porosity, tortuosity) and detect some material defects such as cracks, voids, detrimental fatigues, and geometrical defects [75,78,79]. Besides, more recently X-ray CT imaging methods have been employed to investigate the electrodeposition of metallic lithium batteries [80].

2.2.1 Fundamental principles of X-ray computed tomography

A standard X-ray CT system comprises an x-ray source, a rotational stage with a sample holder, and an x-ray detector to measure the x-ray density, as shown in Figure 2.5 [81]. The emitted x-ray from the source crosses throughout the sample and is logged by the detector which is located next to the rotational stage. Afterwards, the rotating stage is turned 0.5° or 1° to repeat this process until the rotating stage is rotated 360°. In the last step, the 2D transmission slices are compiled to create the 3D structure of the sample.

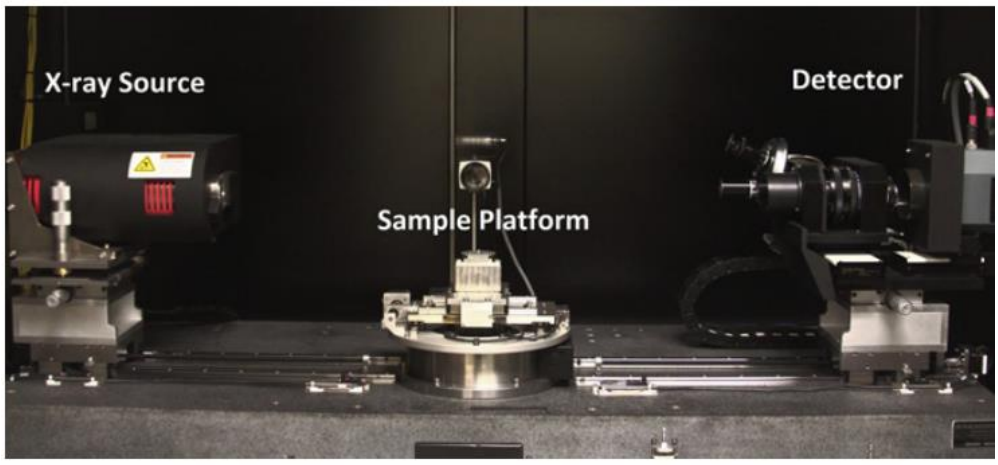

Figure 2.5 – A standard X-ray CT system and its components [81].

Among the imaging methods, the X-ray CT technique has superiorities over the other imaging techniques. The advantages of this system are as follows: (i) available for non-destructive investigation, (ii) being able to quickly and accurately examine the interior structure of the sample, (iii) significantly lower inspection cost, and (iv) the samples are able to be investigated under the realistic working conditions [74,82]. In the fuel cell researches to investigate the interior structure of the GDL, there are 2 types of X-ray computed tomography that are used frequently; (i) microscale X-ray computed tomography (μ-X-ray CT) and nanoscale X-ray computed tomography (nano-X-ray CT). The range of the provided resolution of the μ-X-ray CT is 1-10 μm, whilst the provided resolution of the nano-X-ray CT is under than 100 nm [83].

2.2.1.1 2D image acquisition

Image acquisition can be defined as the digitally encoded representation of the visual characteristic of an inner structure of an object. In the X-ray CT imaging technique, 2D grey shadow slices are captured by the detector for each position of the sample holder as the abovementioned. After that, the obtaining of these greyscale slices are compiled by an image processing software such as MATLAB® image processing Toolbox, Fiji, CT-analyser software, Avizo Lite® [81,84,85].

2.2.1.2 Threshold and image processing

To discriminate the void volumes and solid volumes on the greyscale, the heuristic thresholding method and Otsu's thresholding method has been frequently used. The Otsu's thresholding method is utilized to decide the optimum greyscale level to be employed [86]. Yet, this method is likely not to be always trustworthy and it is prone

to be costly when the number of images is high. On the other hand, the heuristic thresholding method is implemented using a reference 2D scanning electron microscopy (SEM) image. Subsequently, the greyscale image is adjusted according to the average pore diameter and fibre diameter into the reference 2D SEM image [83,85,87]. This thresholding method is relatively faster and more trustworthy than the previous method [87].

2.2.1.3 3D reconstruction process

The captured and thresholded 2D binary images are compiled in order to create the 3D structure. This process is named as 3D reconstruction process. To generate the 3D microporous structure, several software and algorithms are employed such as the SkyScan reconstruction software, Fiji/ImageJ software, marching cubes algorithm, double time cubes algorithm [85]. As a result of the reconstructed 3D model, the structural and transport parameters (i.e. porosity, tortuosity, surface area, pore size distribution, anisotropy, permeability, and effective diffusivity) can be examined.

2.2.2 X-ray computed tomography for PEFC studies

Reducing the cost of the fuel cell electric vehicles (FCEV) is one of the most crucial concerns for the commercialization of this technology [88,89]. The cost of the precious platinum (Pt) consists of an important part of the total PEFC cost. The higher current density operation with lower Pt loading is likely to be a useful method to decrease the costs. Thus, it is possible to reduce not only the total Pt usage in PEFC but also the stack size. However, under the high current density operation conditions, the oxygen, water, and electron transports are inclined to increase that

causes the over potential is affected severely. Clearly, understanding the mass transport phenomenon in porous materials is critical to reduce not only the oxygen and electron losses and also the flooding phenomena which is mentioned detailed in Section 1.4.3. Due to all these aims to understand these phenomena, the inherently elaborate microstructure of the GDL should be examined by microscale X-ray computed tomography.

In the fuel cell and X-ray CT literature, there are numerous scientific studies to give insight into the interior 3D structure of the commercially available woven and non-woven GDL's fluid flow analysis. The porosities and thicknesses of the commercial carbon-based GDLs are in the order of 0.6 – 0.9 and 100 – 400 μm [90]. Moreover, the mean pore radii are about 10 μm. However, such GDLs show high anisotropy between the through-plane and in-plane directions as a result of the carbon fibres arrangements in the planes. Besides, such structural properties of the GDLs are likely to vary in the material plane through the machine and cross-machine directions because of the orientation of the fibres [91].

Fishman et al. [92] examined the heterogeneous in-plane and through-plane porosity distributions of the commercial carbon fibre paper, carbon felt and carbon cloth GDLs used in PEFC by both μ-X-ray CT and nano-X-ray CT. They aimed to contribute to obtaining a better comprehension of the GDL porosity to provide superior input data for multiphase transport modelling. They represented the carbon felt GDL microstructure to have a more uniform core region and a higher difference between the average core porosity and effective bulk porosity than the carbon paper GDL.

Besides, all investigated GDLs possess a linear transitional region which provides high porosity regions to the GDL. In this study, the authors emphasised that the through-plane porosity is likely to be non-uniform because of the GDL manufacturing methods and they recommended that the paper GDL manufacturing methods should be remedied to decrease the peaks and valleys in the GDL core region. In another study, in order to understand the structural properties of commercial GDLs under compression was inspected by the μ-X-ray CT technique [90]. The GDL porosity, tortuosity, and pore-size distribution were evaluated under different compressions via the μ-X-ray CT technique. The GDL porosity and the pore size distribution were able to be calculated from the reconstructed 3D model whereas the tortuosity was determined by a finite-element simulation. The findings presented that the porosity values of all GDLs are likely to decrease with compression. In terms of the tortuosity, the TGP series and SGL series GDLs exhibited the highest tortuosity and heterogeneity rather than the MRC and H2315. In addition, the tortuosity exponent of the MRC and Freudenberg GDLs were the lowest under the compression due to the pores shapes. James et al. [81] investigated the porous transport properties such as the gas diffusion, tortuosity factor, permeability, and electrical conductivity of commercial SGL – 30 – BA GDL under 3 different non-homogeneous compression values (0%, 20%, and 40%) by μ-X-ray CT. The results showed that the electrical conductivity and diffusivity are largest in the in-plane directions due to the carbon fibres alignment direction. Moreover, the through-plane effective diffusivity was likely to decline with the compression whereas the effective electrical conductivity was prone to increase. Under the uncompressed condition, the in-plane effective electrical conductivity

was approximately 3 – 4 times higher than that of the through-plane. Furthermore, under the non-homogeneous compression conditions, the transport properties were different about a factor of about 2 under the channel and land. The outcomes also presented that the effective diffusivities are in the range of 15% and 50% of the predicted the Bruggeman relation. Inoue et al. [88] provided insight into the oxygen transport resistance and electron transport resistance of the MPL and GDL under compression (0 – 4 MPa) by the μ-X-ray CT in dry conditions. In addition, a numerical reconstruction from these captured microporous structures was created to investigate the oxygen transport. Moreover, they compared the oxygen diffusion characteristics with the experimental results to understand the presented structures' physical limits. Their reconstructed 3D structure revealed both gas diffusion properties and electrical conductivity were almost equivalent to the experimental values of the same components.

The quantitative liquid water examination for the Toray – H – 060 GDL was conducted in both the vertical and horizontal cell concepts via in-situ μ-X-ray CT imaging under the realistic conditions [93]. Although the liquid water flowing into the GDL can be reconstructed, the blurred boundaries occurred because of the liquid water droplets in the channel. Therefore, the neutron radiography (NR) technique was also used to collaborate with the μ-X-ray CT imaging to understand the elaborate liquid water – porous structure interaction. Likewise, two anode MPL coated GDLs were investigated with combined X-ray CT (for *ex-situ* characterisation) and NR (for i*n-operando* analysis) to evaluate the liquid water distribution [94]. In this study, for the

first time both the structure and composition of the GDLs (captured by X-ray CT, TGA, SEM, and EDS) are compared against the in-plane water distribution under the operation (obtained NR) in order to understand the relationship between the PEFC structure and performance. In 2018, the microstructure of the commercial carbon felt GDLs (SGL10 BA and SGL 10 BC) and carbon paper GDLs (SGL 25 BA and SGL 25 BC) used in the PEFC was examined by μ-X-ray CT and the liquid water accumulation into the various GDLs' microstructure was observed as a function of the current density via *in-operando* synchrotron x-ray radiography [95]. The results revealed that the core region of the carbon felt GDLs are likely to possess more uniform porosity. On the other hand, the carbon fibres in the GDL have a more tendency to penetrate the MPL under the compression. In terms of the water management, the water accumulation in carbon felt GDLs without MPL was more significant than carbon felt type GDLs without MPL. In addition, both the MPL coated carbon felt and carbon fibre GDLs had similar liquid water content due to the presence of the MPL. In another study, the effects of the cathode inlet gas relative humidity and the current density on the through-plane water accumulation and the mass transport resistance in the cathode GDLs (SGL – 25 – BA , SGL – 25 – BC and SGL – 29 – BC) were *in-situ* and *in-operando* examined by μ-X-ray CT and synchrotron X-ray radiography techniques [96]. The results exhibited the lower cathode relative humidity at the lower current densities (<0.5 A· cm^{-2}), and the liquid water was not monitored. In this range, the cathode inlet relative humidity reinforced the ionomer hydration. Consequently, the lower cathode relative humidity levels in the higher oxygen transport resistances were observed owing to the low ionomer hydration in the catalyst layer. At the

intermediate current densities (1.5 – 2.1 A· cm^{-2}), the liquid water saturation into the GDL was considerably sensitive to the cathode relative humidity, therefore the increased cathode relative humidity levels were observed in the highest oxygen transport resistances. At the higher current densities (>3 A· cm^{-2}), high liquid water saturation values were observed for all inlet relative humidity levels owing to the high generation of liquid water. For this reason, the oxygen transport resistance was less sensitive to the cathode inlet relative humidity. In addition, the outcomes showed that the liquid water was prone to gather in the higher local porosity in the GDL.

In the PEFC literature, the effects of the hot-pressing methods on the microstructure have been also inspected by μ-X-ray CT technique. In 2017, Meyer et al. [97] investigated the effects of the various hot-pressing temperatures (at 100°C, 130°C, and 170°C) on the PEFC microstructure by nano-X-ray CT, thermogravimetric analysis (TGA), atomic force microscopy (AFM), and differential scanning calorimetry (DSC). When the hot-pressing temperature was 170°C, the Nafion membrane was destroyed and penetrated the electrode, therefore the catalyst layer became degraded and the pores in the GDL are filled. They concluded that a 130°C hot-pressing temperature was the optimum value because of the superior interface between the Nafion and catalyst layer. Hack et al. [98] examined the electrochemical and mechanical microstructure of membrane electrode assemblies (MEAs) which were hot-pressed or non-hot-pressed and assessed the MEAs at the beginning-of-test and end-of-test. They utilized the μ-X-ray CT imaging method to provide insight to changes into the electrode's microstructure. The results demonstrated that the solid phase volume

fraction and interfacial contact area decreased from the beginning-of-test to end-of the test with the same degradation rate for both hot-pressed and non-hot pressed MEAs.

Garcia-Salaberri et al. [91] provided insight into the transport processes that occurred in carbon fibre paper to assist to understand the PEFC performance and durability. The representative elementary volume (REV) in carbon fibre papers is examined by μ-X-ray CT images using the lattice Boltzmann method to evaluate the regional characteristics (core and surface region) and the permeability, mass diffusivity as well as the electrical and thermal conductivity in both the through-plane and in-plane directions. The outcomes of the study demonstrated that the high porous surface region decreases the through-plane electrical and thermal conductivity. Kotaka et al. [89] comprehensively examined the inherent structure of the GDL under the various compression conditions (0 – 3 MPa) by nano-X-ray CT and analysed the oxygen and electron transport in the both MPL and GDL in order to show the relation between the inherent structure and transport. They emphasized that the interior GDL structure is the most dominant aspect of the transport resistance. The findings showed that the mass transport in the GDL is highly reliant on the local microstructural variations (e.g. local pore/solid volume ratio and connectivity). Nonetheless, the numerical and experimental results for the electron transport in the MPL were highly different because of the effect of the PTFE volume fraction and the effect of the contact resistance between the carbon particles. Also they concluded that the reducing of the contact resistance between the particles and/or contact

points is critical to the enhancement of the electron transport in the MPL to reach the higher current densities. Likewise, Atkinson et al. [99] showed the morphological changes of the MPL and GDL under various compression levels via μ-X-ray CT. They used carbon paper type (SGL-29-BC) and carbon felt type (Freudenberg H2315 C2) GDLs in this elaborated study. The results showed that the initial structure of the SGL GDL changed suddenly with the clamping force, however the inner structural change of the Freudenberg GDL was more moderate. This situation is likely to detrimentally affect the oxygen diffusivity in SGL GDLs. In terms of the MPL, the increasing clamping force induced a decrease of the surface cracks and depths.

Fly et al. [72] investigated the superior mechanical behaviour of the nickel foam–based flow field PEFC under the various compression values by electrochemical tests, μ-X-ray CT imaging, compression tests, and numerical modelling. The results captured by μ-X-ray CT demonstrated that when the compression on the nickel foam-based flow field increased, the transport losses are likely to be enhanced because of a decrease in the flow field porosity which severely affects the reactant distribution and produced liquid water removal. On the other hand, increasing the compression is supposed to enhance the fuel cell performance due to the reducing contact resistance. Under the 25% compression conditions, the nickel foam ligaments are penetrating more than 50% of the GDL thickness. Besides, the peak power value was enhanced by 42% when the compression was increased from 20% to 70%. Moreover, the intersection between the nickel foam – based flow field and carbon paper – based GDL possess superior contact areas (10 times higher than between the nickel foam

and stainless steel flow field) and a continuous porosity distribution profile. Recently, Park et al. [100] aimed to investigate the flow characteristics of nickel foam for different fluid velocities using a μ-X-ray CT-based numerical model. Their study focused on examining the behaviour of fluid particles at various velocities within the nickel foam. They concluded that at high velocities, fluid particles near the nickel foam ligaments tend to lose their kinetic energy due to friction. Therefore, the velocity decreases, even reaching zero at certain points, and creates vortices. Moreover, they recommended that pressure drop should be minimised to decrease the required pumping power. In 2021, Wu et al. [101] evaluated the different compression levels (6%, 37%, and 69%) for nickel foam-based FFP by using μ-X-ray CT and experimental methods. The findings indicated that increased compression considerably decreased the average pore size, porosity, permeability, and ohmic resistance; whereas it enhanced the tortuosity. They figure out that the best performance, with a power density of 853 mW/cm^2, was observed at the 37% compressed nickel foam. Additionally, the results exhibited that the lowest compression level (6%) resulted in the highest accumulation of liquid water compared to the moderate and maximum compression levels.

In the fuel cell literature, although there are numerous X-ray CT investigations of the carbon-based GDLs and very rare X-ray CT investigation of the nickel foam-based FFP, there have been no comprehensive studies on the nickel foam-based GDLs for PEFCs under the operation conditions by X-ray CT.

2.2.3 Summary

In Section 2.2, the fundamental X-ray CT imaging technique is briefly introduced and a literature review of the X-ray CT imaging for GDLs is reported. In addition, in the literature, there are only a few studies in regards to the X-ray computed tomography (X-ray CT) investigation of the nickel foam-based flow fields; however, the X-ray CT detailed inspection of the nickel foam-based GDLs has not been fully studied in the literature. Therefore, the transport characteristic of the nickel foam-based GDLs under the working conditions have not been detailed examined by X-ray CT. Moreover, while there are very few numerical models regarding the carbon-based GDLs, there have been no comprehensive study about the channel optimisation and the analysis of pumping power demand for nickel foam-based GDL used in PEFC.

2.3 REFERENCES

[1] Lefebvre LP, Banhart J, Dunand DC. Porous metals and metallic foams: Current status and recent developments. Adv Eng Mater 2008;10:775–87. https://doi.org/10.1002/adem.200800241.

[2] Kumar A, Reddy RG. Modeling of polymer electrolyte membrane fuel cell with metal foam in the flow-field of the bipolar/end plates. J Power Sources 2003;114:54–62. https://doi.org/10.1016/S0378-7753(02)00540-2.

[3] Li X, Sabir I. Review of bipolar plates in PEM fuel cells: Flow-field designs. Int J Hydrogen Energy 2005;30:359–71. https://doi.org/10.1016/j.ijhydene.2004.09.019.

[4] Ghanbarian A, Kermani MJ, Scholta J, Abdollahzadeh M. Polymer electrolyte membrane fuel cell flow field design criteria – Application to parallel serpentine flow patterns. Energy Convers Manag 2018;166:281–96. https://doi.org/10.1016/j.enconman.2018.04.018.

[5] Trogadas P, Cho JIS, Neville TP, Marquis J, Wu B, Brett DJL, et al. A lung-inspired approach to scalable and robust fuel cell design. Energy Environ Sci 2018;11:136–43. https://doi.org/10.1039/c7ee02161e.

[6] Murphy OJ, Cisar A, Clarke E. Low-cost light weight high power density PEM fuel cell stack. Electrochim Acta 1998;43:3829–40. https://doi.org/10.1016/S0013-4686(98)00143-1.

[7] Liu Y, Wang H, Li J, Lu Y, Xue Q, Chen J. Microfibrous entrapped Ni/Al2O3 using SS-316 fibers for H2 production from NH3. AIChE J 2007;53:1845–9. https://doi.org/10.1002/aic.11208.

[8] Yi P, Peng L, Lai X, Li M, Ni J. Investigation of sintered stainless steel fiber felt as gas diffusion layer in proton exchange membrane fuel cells. Int J Hydrogen Energy 2012;37:11334–44. https://doi.org/10.1016/j.ijhydene.2012.04.161.

[9] Dhanushkodi SR, Capitanio F, Biggs T, Mérida W. Understanding flexural, mechanical and physico-chemical properties of gas diffusion layers for polymer membrane fuel cell and electrolyzer systems. Int J Hydrogen Energy 2015;40:16846–59. https://doi.org/10.1016/j.ijhydene.2015.07.033.

[10] Hryniewicz T, Skubała W, Chrzczonowicz M. Porous sinters for elevated-temperature natural-gas fuel cells. Powder Technol 1990;61:217–23. https://doi.org/10.1016/0032-5910(90)80087-F.

[11] Liu Y, Wang H, Li J, Lu Y, Xue Q, Chen J. Microfibrous entrapped Ni/Al2O3 using SS-316 fibers for H2 production from NH3. AIChE J 2007;53:1845–9. https://doi.org/10.1002/aic.11208.

[12] Tang Y, Yuan W, Pan M, Wan Z. Feasibility study of porous copper fiber sintered felt: A novel porous flow field in proton exchange membrane fuel cells. Int J Hydrogen Energy 2010;35:9661–77. https://doi.org/10.1016/j.ijhydene.2010.06.101.

[13] Nikam V V., Reddy RG. Copper alloy bipolar plates for polymer electrolyte

membrane fuel cell. Electrochim Acta 2006;51:6338–45. https://doi.org/10.1016/j.electacta.2006.04.019.

[14] Ren YJ, Anisur MR, Qiu W, He JJ, Al-Saadi S, Singh Raman RK. Degradation of graphene coated copper in simulated proton exchange membrane fuel cell environment: Electrochemical impedance spectroscopy study. J Power Sources 2017;362:366–72. https://doi.org/10.1016/j.jpowsour.2017.07.041.

[15] Lee YH, Noh ST, Lee JH, Chun SH, Cha SW, Chang I. Durable graphene-coated bipolar plates for polymer electrolyte fuel cells. Int J Hydrogen Energy 2017;42:27350–3. https://doi.org/10.1016/j.ijhydene.2017.09.053.

[16] Pu NW, Shi GN, Liu YM, Sun X, Chang JK, Sun CL, et al. Graphene grown on stainless steel as a high-performance and ecofriendly anti-corrosion coating for polymer electrolyte membrane fuel cell bipolar plates. J Power Sources 2015;282:248–56. https://doi.org/10.1016/j.jpowsour.2015.02.055.

[17] Stoot AC, Camilli L, Spiegelhauer SA, Yu F, Bøggild P. Multilayer graphene for long-term corrosion protection of stainless steel bipolar plates for polymer electrolyte membrane fuel cell. J Power Sources 2015;293:846–51. https://doi.org/10.1016/j.jpowsour.2015.06.009.

[18] Singh Raman RK, Chakraborty Banerjee P, Lobo DE, Gullapalli H, Sumandasa M, Kumar A, et al. Protecting copper from electrochemical degradation by graphene coating. Carbon N Y 2012;50:4040–5. https://doi.org/10.1016/j.carbon.2012.04.048.

[19] Tang Y, Zhou W, Pan M, Chen H, Liu W, Yu H. Porous copper fiber sintered felts: An innovative catalyst support of methanol steam reformer for hydrogen production. Int J Hydrogen Energy 2008;33:2950–6. https://doi.org/10.1016/j.ijhydene.2008.04.006.

[20] Li S, Zhou W, Liu R, Huang J, Chu X. Fabrication of porous metal fiber sintered sheet as a flow field for proton exchange membrane fuel cell. Curr Appl Phys 2020;20:686–95. https://doi.org/10.1016/j.cap.2020.03.001.

[21] Lian Y, You C, Zhu Z, Zhu X, Li X, Zhou W. Preparation and performance of a self-humidifying fuel cell using a fiber sintered sheet as flow field. J Power Sources 2022;536:231513. https://doi.org/10.1016/j.jpowsour.2022.231513.

[22] Zhang FY, Prasad AK, Advani SG. Investigation of a copper etching technique to fabricate metallic gas diffusion media. J Micromechanics Microengineering 2006;16:3–8. https://doi.org/10.1088/0960-1317/16/11/N02.

[23] Zhang FY, Advani SG, Prasad AK. Performance of a metallic gas diffusion layer for PEM fuel cells. J Power Sources 2008;176:293–8. https://doi.org/10.1016/j.jpowsour.2007.10.055.

[24] Li Y, Zhang X, Nie L, Zhang Y, Liu X. Stainless steel fiber felt as cathode diffusion backing and current collector for a micro direct methanol fuel cell with low methanol crossover. J Power Sources 2014;245:520–8. https://doi.org/10.1016/j.jpowsour.2013.06.122.

[25] Lu G, Ge P, Hou Q, Ren B, Jia X, Liao Q. Experimental Investigation of Proton

Exchange Membrane Fuel Cell with Commercial Stainless Steel Fiber Felt as Flow Field. Int J Electrochem Sci 2022;17:1–17. https://doi.org/10.20964/2022.09.31.

[26] Leeuwner MJ, Wilkinson DP, Gyenge EL. Novel Graphene Foam Microporous Layers for PEM Fuel Cells: Interfacial Characteristics and Comparative Performance. Fuel Cells 2015;15:790–801. https://doi.org/10.1002/fuce.201500031.

[27] Blanco M, Wilkinson DP, Wang H. Perforated metal sheets as gas diffusion layers for proton exchange membrane fuel cells. Electrochem Solid-State Lett 2012;15:20–3. https://doi.org/10.1149/2.017203esl.

[28] Tanaka S, Bradfield WW, Legrand C, Malan AG. Numerical and experimental study of the effects of the electrical resistance and diffusivity under clamping pressure on the performance of a metallic gas-diffusion layer in polymer electrolyte fuel cells. J Power Sources 2016;330:273–84. https://doi.org/10.1016/j.jpowsour.2016.08.121.

[29] Tanaka S, Shudo T. Significant performance improvement in terms of reduced cathode flooding in polymer electrolyte fuel cell using a stainless-steel microcoil gas flow field. J Power Sources 2014;248:524–32. https://doi.org/10.1016/j.jpowsour.2013.09.119.

[30] Tanaka S, Shudo T. Corrugated mesh flow channel and novel microporous layers for reducing flooding and resistance in gas diffusion layer-less polymer electrolyte fuel cells. J Power Sources 2014;268:183–93.

https://doi.org/10.1016/j.jpowsour.2014.04.159.

[31] Tanaka S, Shudo T. Experimental and numerical modeling study of the electrical resistance of gas diffusion layer-less polymer electrolyte membrane fuel cells. J Power Sources 2015;278:382–95. https://doi.org/10.1016/j.jpowsour.2014.12.077.

[32] Tan WC, Saw LH, Thiam HS, Xuan J, Cai Z, Yew MC. Overview of porous media/metal foam application in fuel cells and solar power systems. Renew Sustain Energy Rev 2018;96:181–97. https://doi.org/10.1016/j.rser.2018.07.032.

[33] Hu H, Zhao Y, Li Y. Research progress on flow and heat transfer characteristics of fluids in metal foams. Renew Sustain Energy Rev 2023;171:113010. https://doi.org/10.1016/j.rser.2022.113010.

[34] Sajid Hossain M, Shabani B. Metal foams application to enhance cooling of open cathode polymer electrolyte membrane fuel cells. J Power Sources 2015;295:275–91. https://doi.org/10.1016/j.jpowsour.2015.07.022.

[35] Carton JG, Olabi AG. Representative model and flow characteristics of open pore cellular foam and potential use in proton exchange membrane fuel cells. Int J Hydrogen Energy 2015;40:5726–38. https://doi.org/10.1016/j.ijhydene.2015.02.122.

[36] Bianchi E, Heidig T, Visconti CG, Groppi G, Freund H, Tronconi E. An appraisal of the heat transfer properties of metallic open-cell foams for strongly exo-/endo-

thermic catalytic processes in tubular reactors. Chem Eng J 2012;198–199:512–28. https://doi.org/10.1016/j.cej.2012.05.045.

[37] Han XH, Wang Q, Park YG, T'Joen C, Sommers A, Jacobi A. A review of metal foam and metal matrix composites for heat exchangers and heat sinks. Heat Transf Eng 2012;33:991–1009. https://doi.org/10.1080/01457632.2012.659613.

[38] Carton JG, Olabi AG. Three-dimensional proton exchange membrane fuel cell model: Comparison of double channel and open pore cellular foam flow plates. Energy 2017;136:185–95. https://doi.org/10.1016/j.energy.2016.02.010.

[39] Wang Y. Porous-Media Flow Fields for Polymer Electrolyte Fuel Cells. J Electrochem Soc 2009;156:B1124. https://doi.org/10.1149/1.3183781.

[40] Baroutaji A, Carton J, Stokes J, Olabi A-G. Design and development of proton exchange membrane fuel cell using open pore cellular foam as flow plate material. J Energy Challenges Mech 2014;1:95–102.

[41] Choi H, Kim OH, Kim M, Choe H, Cho YH, Sung YE. Next-generation polymer-electrolyte-membrane fuel cells using titanium foam as gas diffusion layer. ACS Appl Mater Interfaces 2014;6:7665–71. https://doi.org/10.1021/am500962h.

[42] Son J, Um S, Kim YB. Relationship between number of turns of serpentine structure with metal foam flow field and polymer electrolyte membrane fuel cell performance. Renew Energy 2022;188:372–83. https://doi.org/10.1016/j.renene.2022.02.001.

[43] Hontanon E, Escudero MJ, Bautista C, Daza L. Using Computational Fluid Dynamics Techniques 2000.

[44] Kumar A, Reddy RG. Materials and design development for bipolar/end plates in fuel cells. J Power Sources 2004;129:62–7. https://doi.org/10.1016/j.jpowsour.2003.11.011.

[45] Lee GW, Shim GH, Kim JM, Seol C, Kim JH, Kim SM, et al. Two/three-dimensional reduced graphene oxide coating for porous flow distributor in polymer electrolyte membrane fuel cell. Int J Hydrogen Energy 2020;45:12972–81. https://doi.org/10.1016/j.ijhydene.2020.02.092.

[46] Tsai BT, Tseng CJ, Liu ZS, Wang CH, Lee CI, Yang CC, et al. Effects of flow field design on the performance of a PEM fuel cell with metal foam as the flow distributor. Int J Hydrogen Energy 2012;37:13060–6. https://doi.org/10.1016/j.ijhydene.2012.05.008.

[47] Afshari E, Mosharaf-Dehkordi M, Rajabian H. An investigation of the PEM fuel cells performance with partially restricted cathode flow channels and metal foam as a flow distributor. Energy 2017;118:705–15. https://doi.org/10.1016/j.energy.2016.10.101.

[48] Wilberforce T, Ijaodola O, Baroutaji A, Ogungbemi E, Olabi AG. Effect of Bipolar Plate Material on Proton Exchange Membrane Fuel Cell Performance. Energies 2022;15:1–15. https://doi.org/10.3390/en15051886.

[49] Azarafza A, Ismail MS, Rezakazemi M, Pourkashanian M. Comparative study of

conventional and unconventional designs of cathode flow fields in PEM fuel cell. Renew Sustain Energy Rev 2019;116:109420. https://doi.org/10.1016/j.rser.2019.109420.

[50] Bao Z, Niu Z, Jiao K. Numerical simulation for metal foam two-phase flow field of proton exchange membrane fuel cell. Int J Hydrogen Energy 2019;44:6229–44. https://doi.org/10.1016/j.ijhydene.2019.01.086.

[51] Wu Y, Cho JIS, Whiteley M, Rasha L, Neville TP, Ziesche R, et al. Characterization of water management in metal foam flow-field based polymer electrolyte fuel cells using in-operando neutron radiography. Int J Hydrogen Energy 2019. https://doi.org/10.1016/j.ijhydene.2019.11.069.

[52] Awin Y, Dukhan N. Experimental performance assessment of metal-foam flow fields for proton exchange membrane fuel cells. Appl Energy 2019;252:113458. https://doi.org/10.1016/j.apenergy.2019.113458.

[53] Tseng CJ, Heush YJ, Chiang CJ, Lee YH, Lee KR. Application of metal foams to high temperature PEM fuel cells. Int J Hydrogen Energy 2016;41:16196–204. https://doi.org/10.1016/j.ijhydene.2016.06.149.

[54] Jo A, Ju H. Numerical study on applicability of metal foam as flow distributor in polymer electrolyte fuel cells (PEFCs). Int J Hydrogen Energy 2018;43:14012–26. https://doi.org/10.1016/j.ijhydene.2018.01.003.

[55] Park JE, Hwang W, Lim MS, Kim S, Ahn CY, Kim OH, et al. Achieving breakthrough performance caused by optimized metal foam flow field in fuel cells. Int J

Hydrogen Energy 2019;44:22074–84. https://doi.org/10.1016/j.ijhydene.2019.06.073.

[56] Parvanian AM, Panjepour M. Mechanical behavior improvement of open-pore copper foams synthesized through space holder technique. Mater Des 2013;49:834–41. https://doi.org/10.1016/j.matdes.2013.01.077.

[57] Lee S, Tam J, Li W, Yu B, Cho HJ, Samei J, et al. Multi-scale morphological characterization of Ni foams with directional pores. Mater Charact 2019;158. https://doi.org/10.1016/j.matchar.2019.109939.

[58] Hussain A, Tso CY, Chao CYH. Experimental investigation of a passive thermal management system for high-powered lithium ion batteries using nickel foam-paraffin composite. Energy 2016;115:209–18. https://doi.org/10.1016/j.energy.2016.09.008.

[59] Cheng S, Wu J. Air-cathode preparation with activated carbon as catalyst, PTFE as binder and nickel foam as current collector for microbial fuel cells. Bioelectrochemistry 2013;92:22–6. https://doi.org/10.1016/j.bioelechem.2013.03.001.

[60] Bidault F, Brett DJL, Middleton PH, Abson N, Brandon NP. A new application for nickel foam in alkaline fuel cells. Int J Hydrogen Energy 2009;34:6799–808. https://doi.org/10.1016/j.ijhydene.2009.06.035.

[61] Toghyani S, Afshari E, Baniasadi E. Metal foams as flow distributors in comparison with serpentine and parallel flow fields in proton exchange

membrane electrolyzer cells. Electrochim Acta 2018;290:506–19. https://doi.org/10.1016/j.electacta.2018.09.106.

[62] Jo A, Ahn S, Oh K, Kim W, Ju H. Effects of metal foam properties on flow and water distribution in polymer electrolyte fuel cells (PEFCs). Int J Hydrogen Energy 2018;43:14034–46. https://doi.org/10.1016/j.ijhydene.2018.01.134.

[63] Tabe Y, Nasu T, Morioka S, Chikahisa T. Performance characteristics and internal phenomena of polymer electrolyte membrane fuel cell with porous flow field. J Power Sources 2013;238:21–8. https://doi.org/10.1016/j.jpowsour.2013.03.047.

[64] Baroutaji A, Carton JG, Stokes J, Olabi AG. Application of Open Pore Cellular Foam for air breathing PEM fuel cell. Int J Hydrogen Energy 2017;42:25630–8. https://doi.org/10.1016/j.ijhydene.2017.05.114.

[65] Shin DK, Yoo JH, Kang DG, Kim MS. Effect of cell size in metal foam inserted to the air channel of polymer electrolyte membrane fuel cell for high performance. Renew Energy 2018;115:663–75. https://doi.org/10.1016/j.renene.2017.08.085.

[66] Kim M, Kim C, Sohn Y. Application of Metal Foam as a Flow Field for PEM Fuel Cell Stack. Fuel Cells 2018;18:123–8. https://doi.org/10.1002/fuce.201700180.

[67] Chen X, Yang C, Sun Y, Liu Q, Wan Z, Kong X, et al. Water management and structure optimization study of nickel metal foam as flow distributors in proton exchange membrane fuel cell. Appl Energy 2022;309:118448.

https://doi.org/10.1016/j.apenergy.2021.118448.

[68] Liu R, Zhou W, Li S, Li F, Ling W. Performance improvement of proton exchange membrane fuel cells with compressed nickel foam as flow field structure. Int J Hydrogen Energy 2020;45:17833–43. https://doi.org/10.1016/j.ijhydene.2020.04.238.

[69] Wan Z, Sun Y, Yang C, Kong X, Yan H, Chen X, et al. Experimental performance investigation on the arrangement of metal foam as flow distributors in proton exchange membrane fuel cell. Energy Convers Manag 2021;231:113846. https://doi.org/10.1016/j.enconman.2021.113846.

[70] Park D, Ham S, Sohn YJ, Choi YY, Kim M. Mass transfer characteristics according to flow field and gas diffusion layer of a PEMFC metallic bipolar plate for stationary applications. Int J Hydrogen Energy 2023;48:304–17. https://doi.org/10.1016/j.ijhydene.2022.09.261.

[71] Tseng CJ, Tsai BT, Liu ZS, Cheng TC, Chang WC, Lo SK. A PEM fuel cell with metal foam as flow distributor. Energy Convers Manag 2012;62:14–21. https://doi.org/10.1016/j.enconman.2012.03.018.

[72] Fly A, Meyer Q, Whiteley M, Iacoviello F, Neville T, Shearing PR, et al. X-ray tomography and modelling study on the mechanical behaviour and performance of metal foam flow-fields for polymer electrolyte fuel cells. Int J Hydrogen Energy 2019;44:7583–95. https://doi.org/10.1016/j.ijhydene.2019.01.206.

[73] Fly A, Kim K, Gordon J, Butcher D, Chen R. Liquid water transport in porous metal foam flow-field fuel cells: A two-phase numerical modelling and ex-situ experimental study. Energies 2019;12. https://doi.org/10.3390/en12071186.

[74] Sun, W, Brown, S B, Leach RK. An overview of industrial X-ray computed tomography. Eng 32 2012.

[75] Kritikos Samardziova M. Generating of STL models of plastic part and its effect on the final accuracy in computed tomography. Mater Sci Forum 2019;952:295–304. https://doi.org/10.4028/www.scientific.net/MSF.952.295.

[76] Cromwell V, Kortum DJ, Bradley DJ. The Use of a Medical Computer Tomography (CT) System To Observe Multiphase Flow in Porous Media. SPE Annu. Tech. Conf. Exhib., Society of Petroleum Engineers; 1984. https://doi.org/10.2118/13098-MS.

[77] Corcoran HC, Brown SB, Robson S, Speller RD, McCarthy MB. Observations on the performance of X-Ray computed tomography for dimensional metrology. Int Arch Photogramm Remote Sens Spat Inf Sci - ISPRS Arch 2016;41:25–31. https://doi.org/10.5194/isprsarchives-XLI-B5-25-2016.

[78] Mees F, Swennen R, … MVG-GS, 2003 U. Applications of X-ray computed tomography in the geosciences. Geol Soc London 2003:1–6.

[79] Nicoletto G, Anzelotti G, Konečná R. X-ray computed tomography vs. metallography for pore sizing and fatigue of cast Al-alloys. Procedia Eng 2010;2:547–54. https://doi.org/10.1016/j.proeng.2010.03.059.

[80] Eastwood DS, Bayley PM, Chang HJ, Taiwo OO, Vila-Comamala J, Brett DJL, et al. Three-dimensional characterization of electrodeposited lithium microstructures using synchrotron X-ray phase contrast imaging. Chem Commun 2015;51:266–8. https://doi.org/10.1039/c4cc03187c.

[81] James JP, Choi HW, Pharoah JG. X-ray computed tomography reconstruction and analysis of polymer electrolyte membrane fuel cell porous transport layers. Int J Hydrogen Energy 2012;37:18216–30. https://doi.org/10.1016/j.ijhydene.2012.08.077.

[82] De Chiffre L, Carmignato S, Kruth JP, Schmitt R, Weckenmann A. Industrial applications of computed tomography. CIRP Ann - Manuf Technol 2014;63:655–77. https://doi.org/10.1016/j.cirp.2014.05.011.

[83] Ostadi H, Rama P, Liu Y, Chen R, Zhang X, Jiang K. Threshold Fine-Tuning and 3D Characterisation of Porous Media Using X-ray Nanotomography. Curr Nanosci 2010;6:226–31. https://doi.org/10.2174/157341310790945623.

[84] Kulkarni N, Meyer Q, Hack J, Jervis R, Iacoviello F, Ronaszegi K, et al. Examining the effect of the secondary flow-field on polymer electrolyte fuel cells using X-ray computed radiography and computational modelling. Int J Hydrogen Energy 2019;44:1139–50. https://doi.org/10.1016/j.ijhydene.2018.11.038.

[85] Rama P, Liu Y, Chen R, Ostadi H, Jiang K, Gao Y, et al. A numerical study of structural change and anisotropic permeability in compressed carbon cloth polymer electrolyte fuel cell gas diffusion layers. Fuel Cells 2011;11:274–85. https://doi.org/10.1002/fuce.201000037.

[86] Otsu, N. A threshold selection method from gray-level histograms. IEEE Trans Syst Man Cybern 1996;9:62–6.

[87] Ostadi H, Jiang K, Prewett PD. Micro/nano X-ray tomography reconstruction fine-tuning using scanning electron microscope images. Micro Nano Lett 2008;3:106–9. https://doi.org/10.1049/mnl:20080030.

[88] Inoue G, Yokoyama K, Ooyama J, Terao T, Tokunaga T, Kubo N, et al. Theoretical examination of effective oxygen diffusion coefficient and electrical conductivity of polymer electrolyte fuel cell porous components. J Power Sources 2016;327:610–21. https://doi.org/10.1016/j.jpowsour.2016.07.107.

[89] Kotaka T, Tabuchi Y, Mukherjee PP. Microstructural analysis of mass transport phenomena in gas diffusion media for high current density operation in PEM fuel cells. J Power Sources 2015;280:231–9. https://doi.org/10.1016/j.jpowsour.2015.01.111.

[90] Zenyuk I V., Parkinson DY, Connolly LG, Weber AZ. Gas-diffusion-layer structural properties under compression via X-ray tomography. J Power Sources 2016;328:364–76. https://doi.org/10.1016/j.jpowsour.2016.08.020.

[91] García-Salaberri PA, Zenyuk I V., Shum AD, Hwang G, Vera M, Weber AZ, et al. Analysis of representative elementary volume and through-plane regional characteristics of carbon-fiber papers: diffusivity, permeability and electrical/thermal conductivity. Int J Heat Mass Transf 2018;127:687–703. https://doi.org/10.1016/j.ijheatmasstransfer.2018.07.030.

[92] Fishman Z, Hinebaugh J, Bazylak A. Microscale tomography investigations of heterogeneous porosity distributions of PEMFC GDLs. J Electrochem Soc 2010;157:1643–50. https://doi.org/10.1149/1.3481443.

[93] Eller J, Rosén T, Marone F, Stampanoni M, Wokaun A, Bchi FN. Progress in in situ X-ray tomographic microscopy of liquid water in gas diffusion layers of PEFC. J Electrochem Soc 2011;158. https://doi.org/10.1149/1.3596556.

[94] Meyer Q, Ashton S, Boillat P, Cochet M, Engebretsen E, Finegan DP, et al. Effect of gas diffusion layer properties on water distribution across air-cooled, open-cathode polymer electrolyte fuel cells: A combined ex-situ X-ray tomography and in-operando neutron imaging study. Electrochim Acta 2016;211:478–87. https://doi.org/10.1016/j.electacta.2016.06.068.

[95] Banerjee R, Chevalier S, Liu H, Lee J, Yip R, Han K, et al. A Comparison of Felt-Type and Paper-Type Gas Diffusion Layers for Polymer Electrolyte Membrane Fuel Cell Applications Using X-Ray Techniques. J Electrochem Energy Convers Storage 2018;15:1–10. https://doi.org/10.1115/1.4037766.

[96] Muirhead D, Banerjee R, George MG, Ge N, Shrestha P, Liu H, et al. Liquid water saturation and oxygen transport resistance in polymer electrolyte membrane fuel cell gas diffusion layers. Electrochim Acta 2018;274:250–65. https://doi.org/10.1016/j.electacta.2018.04.050.

[97] Meyer Q, Mansor N, Iacoviello F, Cullen PL, Jervis R, Finegan D, et al. Investigation of Hot Pressed Polymer Electrolyte Fuel Cell Assemblies via X-ray Computed Tomography. Electrochim Acta 2017;242:125–36.

https://doi.org/10.1016/j.electacta.2017.05.028.

[98] Hack J, Heenan TMM, Iacoviello F, Mansor N, Meyer Q, Shearing P, et al. A Structure and Durability Comparison of Membrane Electrode Assembly Fabrication Methods: Self-Assembled Versus Hot-Pressed. J Electrochem Soc 2018;165:F3045–52. https://doi.org/10.1149/2.0051806jes.

[99] Atkinson RW, Garsany Y, Gould BD, Swider-Lyons KE, Zenyuk I V. The Role of Compressive Stress on Gas Diffusion Media Morphology and Fuel Cell Performance. ACS Appl Energy Mater 2018;1:191–201. https://doi.org/10.1021/acsaem.7b00077.

[100] Park SH, Seo DH, Jeong JH. Experimental and numerical analysis of thermal flow in open-cell porous metal during Darcy-Forchheimer transition regime. Appl Therm Eng 2020;181:116029. https://doi.org/10.1016/j.applthermaleng.2020.116029.

[101] Wu Y, Lu X, Cho JIS, Rasha L, Whiteley M, Neville TP, et al. Multi-length scale characterization of compression on metal foam flow-field based fuel cells using X-ray computed tomography and neutron radiography. Energy Convers Manag 2021;230:1–10. https://doi.org/10.1016/j.enconman.2020.113785.

Chapter 3

A Novel Computationally Economical Approach for Determining the Structural and Transport Characteristics of the Nickel Foam-based PEFCs

3.1 SUMMARY

Nickel foams are excellent candidate materials for gas diffusion layers (GDLs) for polymer electrolyte fuel cells (PEFCs) and this is due to their superior structural and transport properties. A highly computationally-efficient framework has been developed to not only estimate the key structural and mass transport properties but also to examine the multi-dimensional uniformity and/or the isotropy of these properties. Specifically, multiple two-dimensional X-ray CT images and/or numerical models have been used to computationally determine the porosity, the tortuosity,

the pore size distribution, the ligament thickness, the specific surface area, the gas permeability and the effective diffusivity of a typical nickel foam sample. The results show that, compared to the conventionally used carbon substrate, the nickel foam sample demonstrate a high degree of uniformity and isotropy and that it has superior structural and mass transport properties, thus underpinning its candidacy as a GDL material for PEFCs. All the computationally-estimated properties, which were found to be consistent with the corresponding literature data, have been presented and thoroughly discussed.

3.2 INTRODUCTION

The polymer electrolyte fuel cell (PEFC), which directly converts the chemical energy of hydrogen and oxygen into electrical energy, is a favourable power source for a multitude of portable, stationary and automotive applications [1–6]. A wet-proofing, porous layer located between the catalyst layer and flow-field plate is termed as the gas diffusion layer (GDL) [7,8]. The main functions of the gas diffusion layers are to: (i) supply reactant gases of oxygen and hydrogen to the active areas in the catalyst layer, (ii) mitigate the detrimental impact of excess water and (iii) electrically connect between the catalyst layers and the flow field plates to power the external load [9–11].

Water (mostly in the form of liquid) is produced as a by-product of the oxygen reduction reaction (ORR) taking place at the cathode catalyst layer. Furthermore, the reactant gasses fed to the fuel cell are mostly humidified to ensure the initial

humidification of the membrane electrolyte. Insufficient or excess amount of water are both detrimental for the operation of the fuel cell. Namely, an insufficient amount of water causes the membrane to dry out, and subsequently reduce the membrane ionic conductivity. On the other hand, an excess amount of water, which is likely to occur at high current densities, induces flooding which may partially/completely block the voids within the GDL and hinder the transport of the reactant gases to the catalyst layers, thus resulting in mass transport losses [12–16]. These losses are more detrimental while the PEFC is operated at the saturated conditions. Thus the water management in PEFC (particularly at its cathode) is highly crucial for its sustainable operation.

The commercially available GDLs are customarily made of electrically conductive carbon fibre-based materials and they are often made in the form of carbon papers or carbon cloths [17–19]. However, such materials are likely to be, due to their low mechanical strength, subject to different types of degradation: mechanical degradation due to compression; thermal degradation arising from freeze/thaw cycles; dissolution; and erosion caused by the flow of gases [20–22]. Hence, many studies have been conducted to explore and investigate alternative materials for the GDLs.

Metal foam-based materials have attracted a great deal of attention as promising components in a variety of energy and engineering related applications such as: filtration and separation, heat exchangers, flow distributors, thermal energy storage, heat pipes, electrolysers, catalyst supports, lithium-ion batteries, etc. [23–32] .

Recent studies have reported that nickel foams are promising materials that could be used as PEFC cathode flow field plates (FFPs) and/or GDLs and this is, compared to the conventionally-used materials, due to their higher: volume-to-weight ratio, cost effectiveness, electrical and thermal conductivity, porosity and specific surface area [33–36]. Some recent investigations experimental investigation have explored the potential use of the nickel foam as a cathode FFP and showed that such a FFP demonstrates better fuel cell performance and durability than those of the conventional graphite FFPs [35,37–42]. For instance, Shin et al. [41] experimentally tested a PEFC equipped with various nickel foam-based cathode FFPs and compared it with that running with a conventional graphitic serpentine FFP. They showed that the fuel cells operating with nickel foam cathode FFP are more stable and demonstrates a 50.6% better performance than that of the graphitic serpentine FFP. Likewise, similar findings were reported by Liu et al. [42] who indicated that the catalytic activity and gas diffusion are likely to increase when using cathode nickel foam FFPs.

The PEFC performance is highly influenced by the structural and effective transport characteristics of the GDLs and as such it is important to estimate these characteristics and subsequently understand how various quantities are transported within the GDLs [43]. A variety of methods are used to estimate the structural GDL characteristics and the following are some examples [3]. Mercury intrusion porosimetry (MIP) is widely used to determine the GDL porosity and the pore size distribution; see for example [44–46]. Under vacuum conditions, gradually-increased

pressure is applied to force the non-wetting mercury to penetrate the pores and subsequently determine the pore size distribution and the porosity of the porous media. The superficial two-dimensional images generated by the scanning electron microscopy (SEM) are often used to measure the thickness of the fibres; see for example [47]. However, these superficial images do not necessarily provide accurate measurement of the fibre thickness. The Brunauer–Emmett–Teller (BET) absorption method is normally used to estimate the specific area of the GDL materials, e.g. [48,49]. Most of the characterisation techniques, including the above mentioned ones, provide some "global" properties of the investigated material [50]; however, they do not resolve the heterogeneity of some materials that often lead to significant anisotropic transport properties as is the case for typical GDL materials.

X-ray computed tomography (CT) has been a handy tool to resolve the nano- or micro-scale local structural variation within the investigated PEFC materials, including the GDLs. Compared to other similar techniques, the X-ray CT technique is (i) non-destructive, (ii) quick and accurate, (iii) cost-effective and (iv) enable the examination under the realistic working conditions [51–53]. The micro-structure of the carbon fibre based GDL has been extensively investigated using X-ray CT. For example, Zenyuk et al. [54], Fishman et al. [45,55,56], James et al. [57], Meyer et al. [58,59], Fazeli et al. [60], and Garcia-Salaberri et al. [61] used X-ray CT to determine the structure-related properties such as porosity, tortuosity and pore size distribution. On the other hand, the microstructure of nickel foams as alternative materials for PEFCs was investigated using X-ray CT in several studies [62–65]. For instance, Fly et

al. [63] performed imaging using the μ-X-ray CT and conducted electrochemical and mechanical tests to investigate the potential use of nickel foam as a FFP. The X-ray CT images show that the contact area between the nickel foam and the carbon paper GDL is ten times higher than that between the nickel foam and the stainless-steel FFP. Furthermore, the X-ray CT-based 3D models have also been employed to determine the structural and transport characteristics of the carbon-based and metal foam-based materials [66–68]. However, these 3D models require high computational resources and are very computationally expensive. To reduce the computational time, some researchers [69,70] have investigated the structural properties of some conventional GDL materials using a two-dimensional Lattice-Boltzmann model that was created by employing SEM images. However, the SEM images do not provide information regarding the interior structure of the investigated material.

To the best of the author's knowledge, there have been no in depth studies on the structural and the transport characteristics of the nickel foams as potentially-used GDLs in PEFCs. Therefore, the characteristics of a typical nickel foam have been estimated using a workflow that involves imaging using an X-ray CT facility, image processing and numerical modelling. In this chapter, the non-uniformity of the material has been innovatively resolved through solving multiple computationally-economic two-dimensional models representing some local slices of nickel foam within the imaged structure. The estimated properties using the above workflow (i.e. imaging, image processing and numerical modelling) have been presented and discussed.

3.3 METHODOLOGY

3.3.1 X-ray CT and Image Processing

X-ray CT images were captured using the SKYSCAN 1172 X-ray microscopy platform (Bruker, US). The platform comprises: an X-ray source, a rotational stage with a specimen holder and an X-ray detector to measure the X-ray density (Figure 3.1). A commercially-available nickel foam sheet with 99.5% purity (GoodFellow, Cambridge Ltd., UK) was punched, creating 12.7 mm-diameter samples. The specimen was fixed on the rotational stage in the through-plane direction by a plastic-made apparatus. The emitted X-ray from the source crosses throughout the sample and then the detector that is located next to the rotational stage collects it. The scan was performed every time that the stage was rotated by 0.7° until the full 180° rotation was reached. The exposure time was 0.885 second and 1025 projections (i.e. two-dimensional slices) were collected. The source voltage was 80 kV and the beam current was 124 µA. The image resolution was 7 µm per pixel.

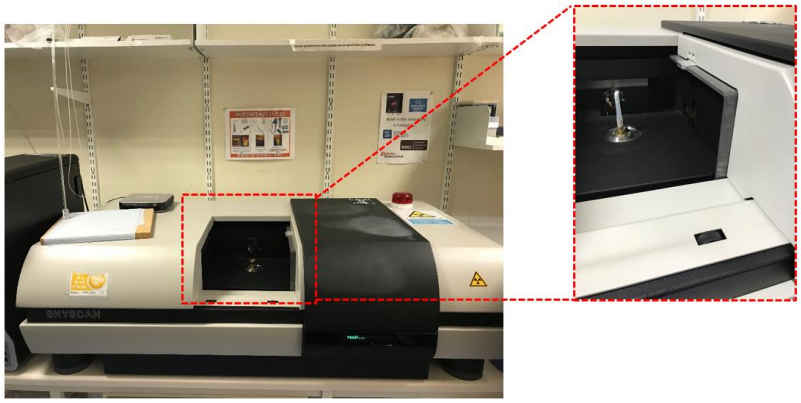

(a)

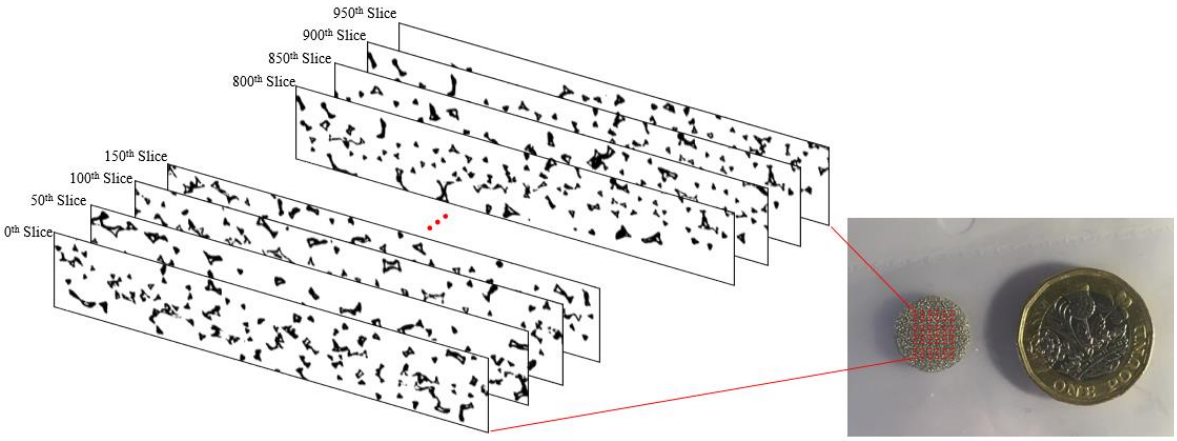

(b)

Figure 3.1 – Photographs of (a) the SKYSCAN X-ray CT platform and (b) the obtained two-dimensional slices.

The captured slices were 2D grey shadows and were processed by the NRecon Reconstruction (SKYSCAN, Belgium) software to reconstruct the cross-section images from the X-ray CT projection images and Bruker CTan Micro-CT software to threshold the slices. The scanning and image processing processes were given step by step in the Appendix-I. To discriminate between the gaseous and solid phases, Otsu's

thresholding method was used. The processed images were imported to COMSOL Multiphysics® 5.5 using MATLAB® and LiveLink™ for MATLAB®.

3.3.2 Numerical modelling

The continuity equation and conservation of momentum equation were, using COMSOL Multiphysics® 5.5, solved for 20 two-dimensional computational domains, representing 20 equally-spaced scanned slices taken within 350 µm distance of the scanned nickel foam sample. The length and height of each slice are 6.65 and 1.05 mm, respectively. The flow within the computational domains was assumed to be steady-state, laminar (Reynolds numbers << 2300) and incompressible (Mach numbers << 0.3) and as such the continuity and momentum equations are expressed as follows:

$$\nabla \cdot (\rho \boldsymbol{u}) = 0 \qquad \textbf{(3.1)}$$

where ∇ is the operator ($\frac{\partial}{\partial x} + \frac{\partial}{\partial y}$), ρ is the fluid density (kg/m^3), and $\boldsymbol{u}$ is the velocity vector.

$$\rho(\boldsymbol{u} \cdot \nabla)\boldsymbol{u} = \nabla \cdot \left[-p\boldsymbol{I} + \mu(\nabla \boldsymbol{u} + (\nabla \boldsymbol{u})^T) - \frac{2}{3}\mu(\nabla \cdot \boldsymbol{u})\boldsymbol{I}\right] \qquad \textbf{(3.2)}$$

where p is the pressure, I is the identity matrix, and μ is the dynamic viscosity (Pa·s). The conservation of chemical species (oxygen gas in our case) is given by:

$$\nabla \cdot (-D_{O2} \nabla C_{O2}) = R \qquad \textbf{(3.3)}$$

where D_{O2} is oxygen diffusion coefficient (cm^2/s), C_{O2} is the oxygen concentration (mol/m^3), and R is the source term which is zero in our case (there is no reaction taking place within the GDL).

The 2D meshing procedure is conducted for each of the 20 slices using the COMSOL Multiphysics® 5.5 software. To ensure mesh-independent solutions, the number of elements has been systemically changed and the property of interest has been computed for all the various meshes and the computation time has been observed for the all the corresponding meshes. For example, Figure 3.2 shows how the computed through- and in-plane gas permeability and the corresponding computation time changes with the number for elements for the 200th CT slice. The figure shows that the computed permeability values become almost insensitive to the number of elements with around 600,000 elements (the corresponding times are reasonably short: 100-200 seconds). The mesh independency test has been performed for all the 20 equally-spaced CT nickel foam slices and the minimum number of elements that achieves the mesh-independent solution was found to be between 400,000 and 650,000. The fluid flow was assumed to be air (mimicking the real-life situation in which air is fed to the cathode side of the fuel cell) and some arbitrary values of air velocity and oxygen concentration were used for the boundary conditions. Namely, the velocity was prescribed at the inlet of the domain (0.1 m/s) and the pressure was set at the outlet of the domain (0 Pa). Note that the bulk oxygen diffusivity coefficient D_{O2} at 20°C and 1 atm is around 0.219 cm^2/s [71]. In addition, it is assumed that the inlet air comprises 21% oxygen and 79% nitrogen. As for the

conservation of the species, the inlet oxygen concentration, $C_{in,O2}$, is 8.73 mol/m^3 and the outlet oxygen concentration is 7.73 mol/m^3. It has been shown in the Appendix–II how the inlet concentration of oxygen has been calculated. The governing equations (3.2) and (3.3) were solved independently for each direction (i.e. through-plane direction (Figure 3.3a) and in-plane direction (Figure 3.3b)) to respectively solve for the distributions of velocity and oxygen concentration within the computational domain and subsequently estimate the gas permeability and effective diffusivity for each principal direction. It is noteworthy that the convective term is not considered in Equation (3.3) as the objective is to estimate the effective diffusivity of the porous media and for this to be achieved, one only needs to solve for the concentration, and not the velocities. It should be noted that symmetry boundary conditions were used for the left and the right sides (through-plane case) and wall boundary conditions were used for top and bottom sides (in-plane case). The solid-phase within the domains (Figure 3.3) are the white areas and the no-slip boundary conditions were used for the walls of these areas. The simulations were performed assuming that the temperature of the inlet is 20°C. The models were numerically solved using a small workstation (Inter® Xenon® CPU E3-1246 v3@ 3.50 GHz, 16 GB installed RAM) and the computational time for each modelled slice was found to be between 140 and 220s. The estimated properties using the above workflow (i.e. imaging, image processing and numerical modelling) have been presented and discussed. Figure 3.4 is a flow chart that schematically shows the methodology and the order of the investigations.

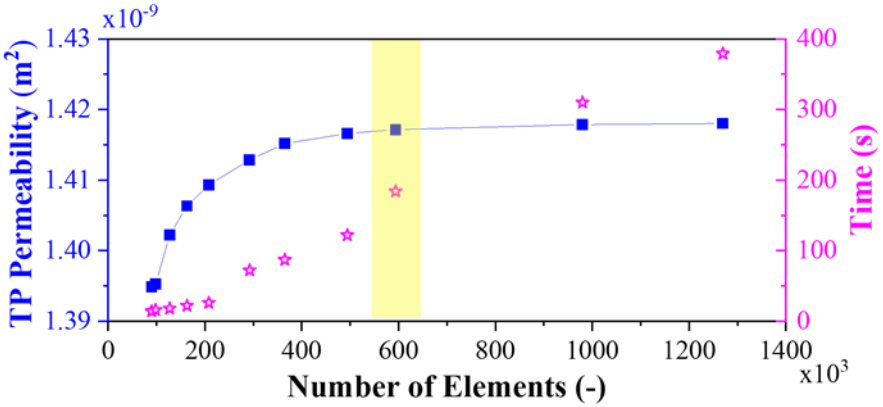

(a)

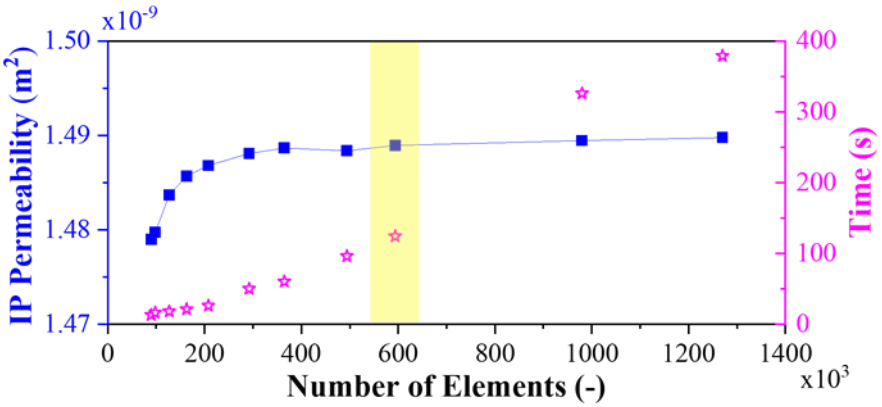

(b)

Figure 3.2 – Change of through-plane (a) and in-plane (b) permeability (and the corresponding computation time) of the 200th slice with number of elements. Yellow strip shows the selected number of elements which is around 600,000.

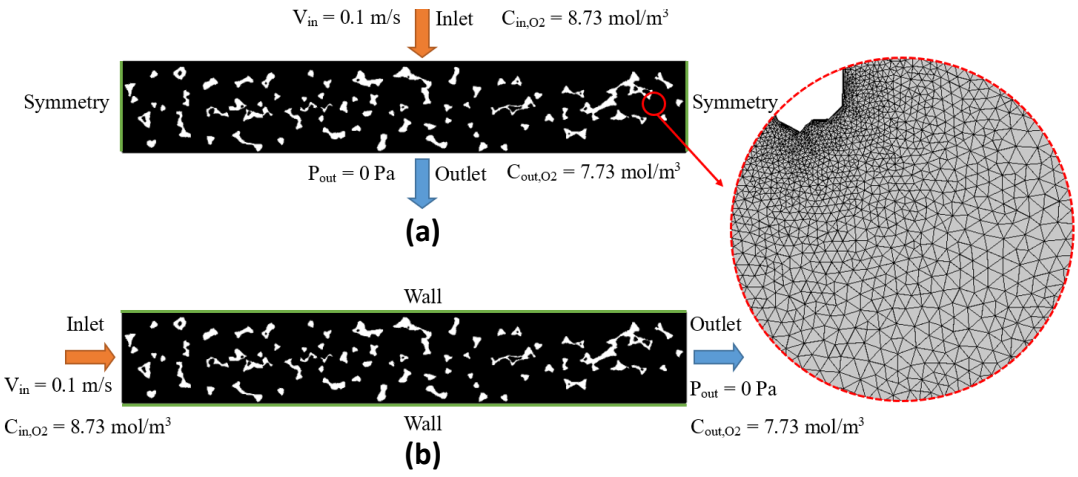

Figure 3.3 – The meshed computational domain for a typical modelled nickel foam slice, labelled with boundary conditions, when solving the conservation of momentum and conservation of species equations in (a) the through-plane and (b) the in-plane directions. Note that the white areas in the domains represent the solid phase (i.e. the ligaments of the nickel foam).

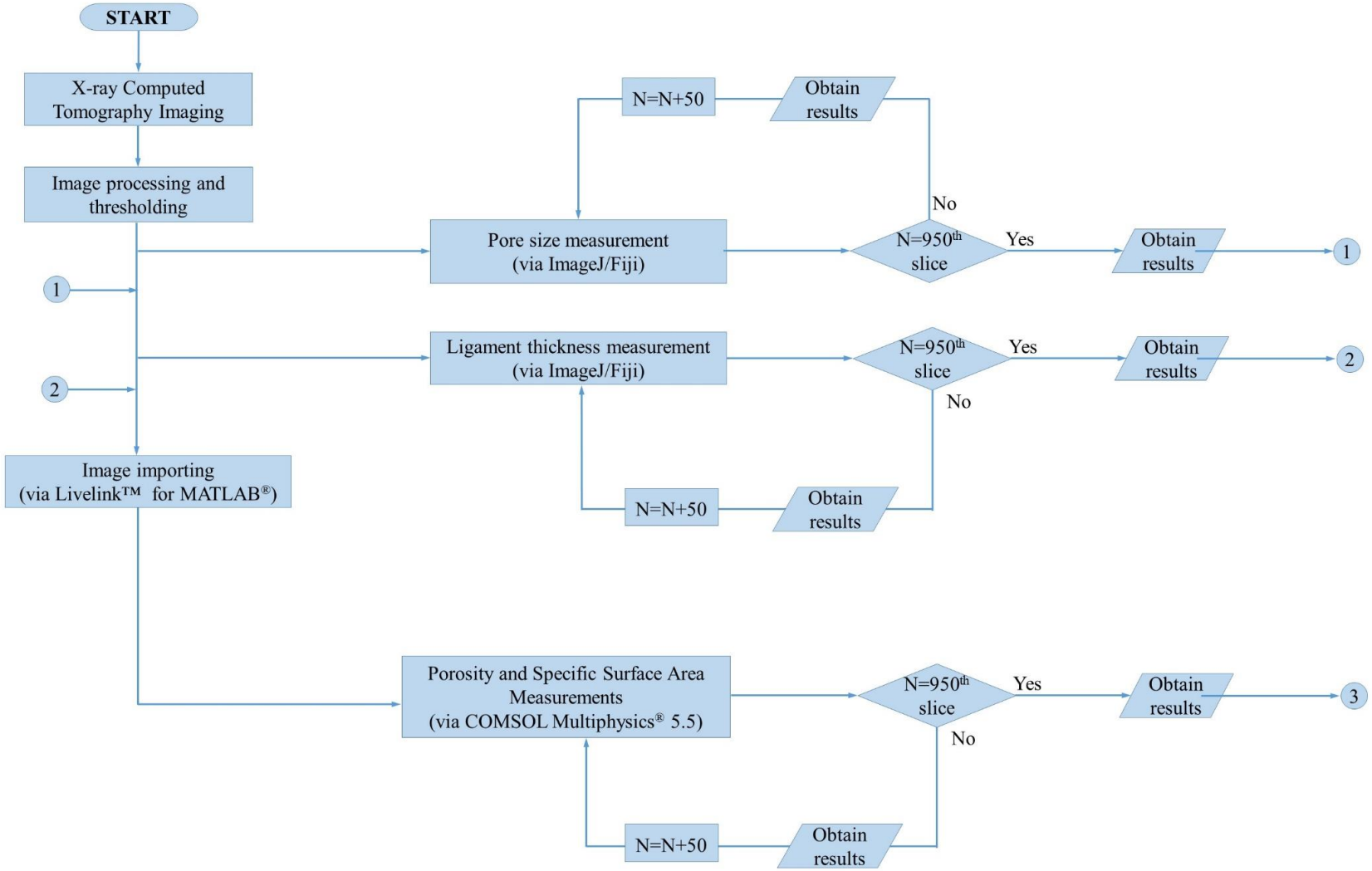

Figure 3.4 – The flow chart of the methodology.

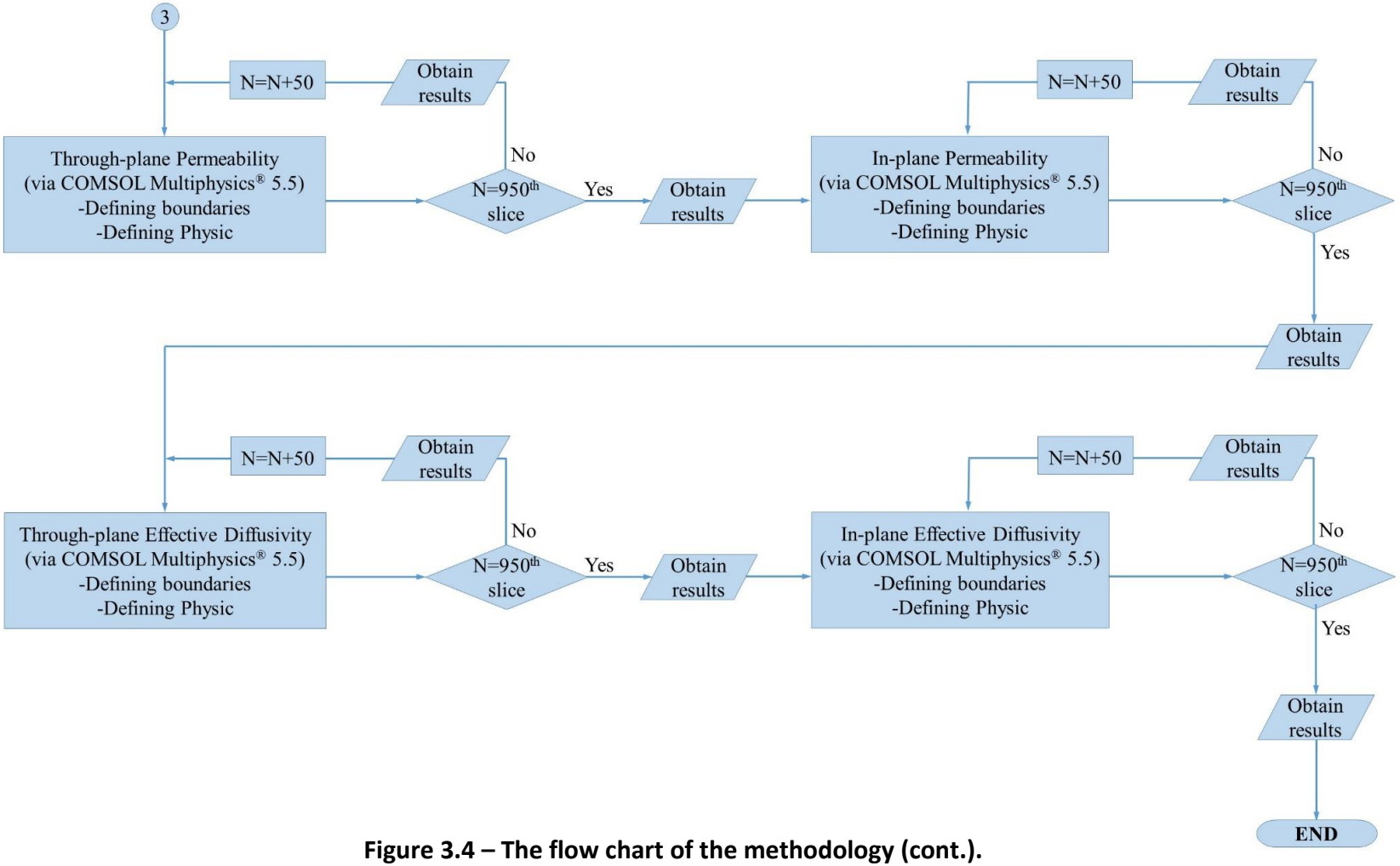

Figure 3.4 – The flow chart of the methodology (cont.).

3.3.3 Structural properties

3.3.3.1 Porosity

The porosity (ε) is the ratio between the void volume and the total volume of the porous medium. All the transport properties of the porous media are a strong function of the porosity. For example, the mass transport properties (e.g. gas permeability and diffusivity) increase with increasing porosity while the electrical and thermal conductivity decrease with increasing porosity [72]. The porosity values are often determined using mercury intrusion porosimetry (MIP) or other standard porosimetry methods. The maximum reported value for the porosity of a commercially available carbon fibre-based GDL is 0.9 while the porosity of nickel foam could be as high as 0.98 [3,73,74], signalling higher transport properties of the latter structure (i.e. the nickel foam). The porosity of the nickel foam sample was estimated for each imaged slice by using the COMSOL Multiphysics® 5.5 to measure the void phases and solid phases. The porosity of the nickel foam sample was estimated for each imaged slice within the Geometry node of the COMSOL Multiphysics® 5.5 by separately measuring the areas for each of the void and the solid phases. Evidently, the porosity for each slice is estimated by dividing the area of the void by the total area (which is the sum of the void and solid phases [75]:

$$\varepsilon = \frac{Void\ phases}{Total\ phases} \qquad \textbf{(3.4)}$$

3.3.3.2 Tortuosity

The tortuosity (τ) is, as implied by its name, a measure of how tortuous is the pathway for the transported fluid; the higher is the tortuosity, the longer is the pathway for the fluid. It also provides insight into the interconnections between the pores of the porous media. The following Equations (3.5) and (3.6) (which were found to be suitable for two-dimensional domains) could be (and have been in this work) used to estimate the tortuosity values [70,76]:

$$\tau_{TP} = \frac{u_{mag}}{u_y} \quad \textbf{(3.5)}$$

$$\tau_{IP} = \frac{u_{mag}}{u_x} \quad \textbf{(3.6)}$$

where u_{mag} is the velocity magnitude averaged over the computational domain and u_y and u_x are, respectively, the velocity components in the through- and in-plane directions, averaged over the computational domain.

3.3.3.3 Pore size distribution

The "pore" term means a small void/space/perforation that connects the cells. The pore size distribution strongly impacts on the transport of reactant gases and liquid water within the GDLs, particularly those at the cathode side, and subsequently impacts the performance of the fuel cell [19,41]. The pore size distribution was estimated for the selected imaged 20 slices using an open-source ImageJ/Fiji software package [77]. All the pores are manually measured and counted through the slices using ImageJ/Fiji software and the pore size distributions have been given in Section 3.4.3. It should be noted that, with SEM images, one could only compute

the pore size distribution on the surface of the scanned structure while the X-ray CT enables one to obtain the multiple local interior pore size distribution of the structure.

3.3.3.4 Ligament thickness distribution

The ligament or the strut is a solid metal rod that forms the cellular structure in the nickel foam. The ligament thickness directly affects the electrical and the thermal conductivity, and the mechanical strength of the nickel foam. As with the pore size distribution, the range of the ligament thickness of the nickel foam and its distribution was determined for the selected imaged 20 slices using an open-source ImageJ/Fiji software [77]. Likewise measuring the pore size, the ligaments have been manually measured and counted through the slices, and the ligament thickness distributions have been presented in Section 3.4.4.

3.3.3.5 Specific surface area

The specific surface area is the surface area of the material per unit of volume [78]. As with the other above mentioned structural properties, the specific surface area of the nickel foam affects the mass, heat and charge transport distributions [79,80]. The nickel foams inherently possess a very high surface area and this is due to their tetradecahedron structure [81]. The Brunauer Emmett Teller (BET) volumetric and gravimetric methods are often used to measure the specific surface area of porous materials, including the metal foams [82,83]. Further, the knowledge of the porosity and the pore size distribution allows for the estimation of the specific surface area as

demonstrated in [84,85]. The total length of the borders and the area of the solid phase were calculated within COMSOL Multiphysics® 5.5 and when these two quantities are divided, the specific surface area is obtained for the investigated slice.

3.3.4 Mass transport properties

3.3.4.1 Gas Permeability

The gas permeability is, as implied by the name, a measure how permeable is the porous medium to gases. The low permeability of the GDL leads to higher gas pressure gradients which leads to higher water saturation in the cathode GDLs and potentially undesirable water flooding phenomena particularly at the cathode side [3,18,86–91]. Furthermore, the high gas permeability increases the convective flow, which translates into an increased amount of the reacting gas supplied to the catalyst layer and ultimately better fuel cell performance [8,12,92–98]. Therefore, it is always desirable for the GDL materials to demonstrate high permeability values. For sufficiently low velocities, the viscous resistance is dominant and the inertial resistance is negligible and this enables one to use the simple linear equation of Darcy's Law (rather than the Forchheimer equation) to estimate the permeability of the porous media, K, as follows [93,94,99]:

$$\frac{\Delta P}{L} = \frac{\mu}{K} u \qquad \textbf{(3.7)}$$

where ΔP is the pressure difference across either the thickness (through-plane) or the length (in-plane) of the GDL material (L) and μ is the dynamic viscosity of the flowing fluid. Following the solution of the conservation of the momentum equation,

as described in Section 3.3.2, the pressure drop was computed for each of the 20 modelled nickel foam slices in both the through- and in-plane directions; this enables one to calculate the respective gas permeability values. It should be noted that u has been set to be the velocity prescribed at inlet of the computational domain (i.e. 0.1 m/s). It should be noted that the gas permeability is an intrinsic property of the material and it is therefore invariant with velocity. Figure 3.5 shows that the pressure gradient changes linearly with the inlet velocity and Figure 3.6 shows that the gas permeability values (in both directions) for arbitrarily selected CT slices are almost insensitive to the inlet velocity. The through-plane gas permeability of the nickel foam was also experimentally estimated using an in-house setup [8,95] to validate the corresponding computed permeability values. The setup consists of top and bottom fixtures, a flow controller (HFC-202, Teledyne Hastings, UK) and a differential pressure sensor (PX653, Omega, UK). The through-plane gas permeability experimental setup is shown in Figure 3.7. Seven circular samples (25.4 mm in diameter) were punched out of a nickel foam sheet and each sample was placed between the fixtures. Nitrogen gas was passed through the sample and the pressure drop was recorded for each flow rate. Finally, using all the knowledge of all the parameters shown in Equation 3.7, the gas permeability of each sample was calculated and then the gas permeability values for all the samples were averaged. It should be noted that the dynamic viscosity of nitrogen is 1.751×10^{-5} Pa.s at 20°C which was the temperature of the room in which the test was conducted [100].

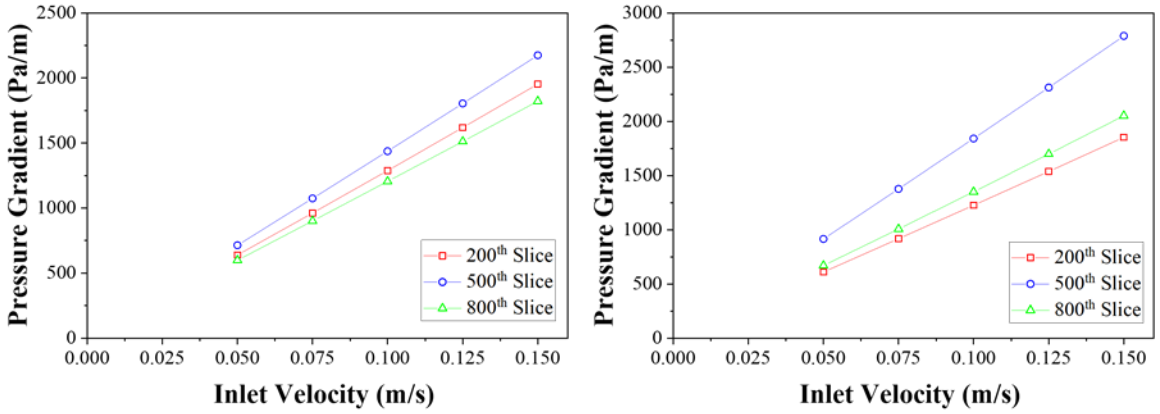

Figure 3.5 – Pressure gradient versus inlet velocity for (a) through-plane and (b) in-plane directions for the 200th, 500th and 800th slices.

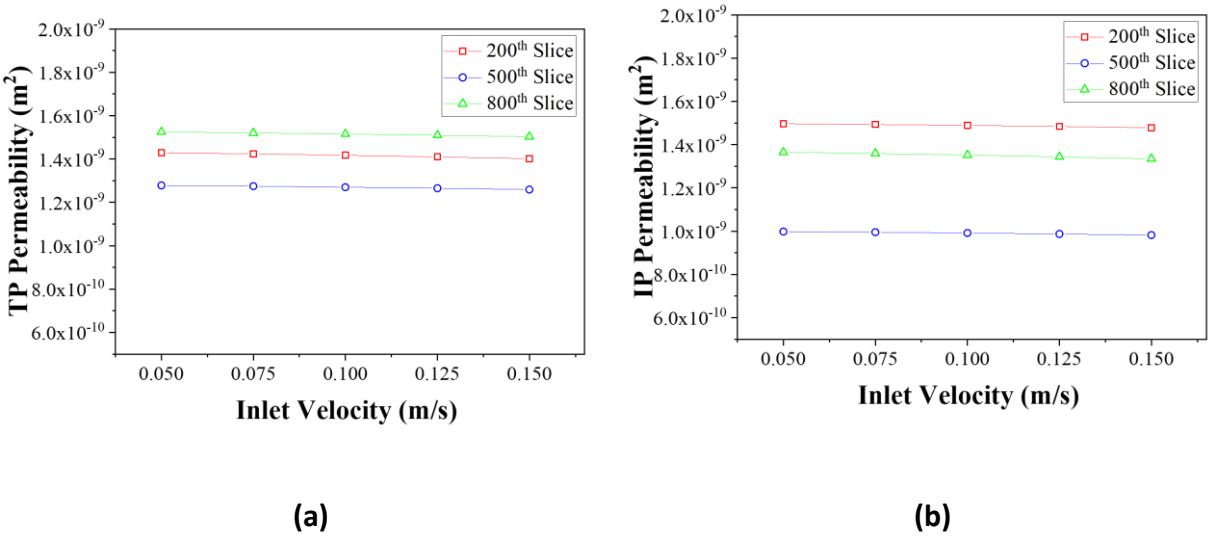

Figure 3.6 – Permeability versus inlet velocity for (a) through-plane and (b) in-plane directions for the 200th, 500th, and 800th slices.

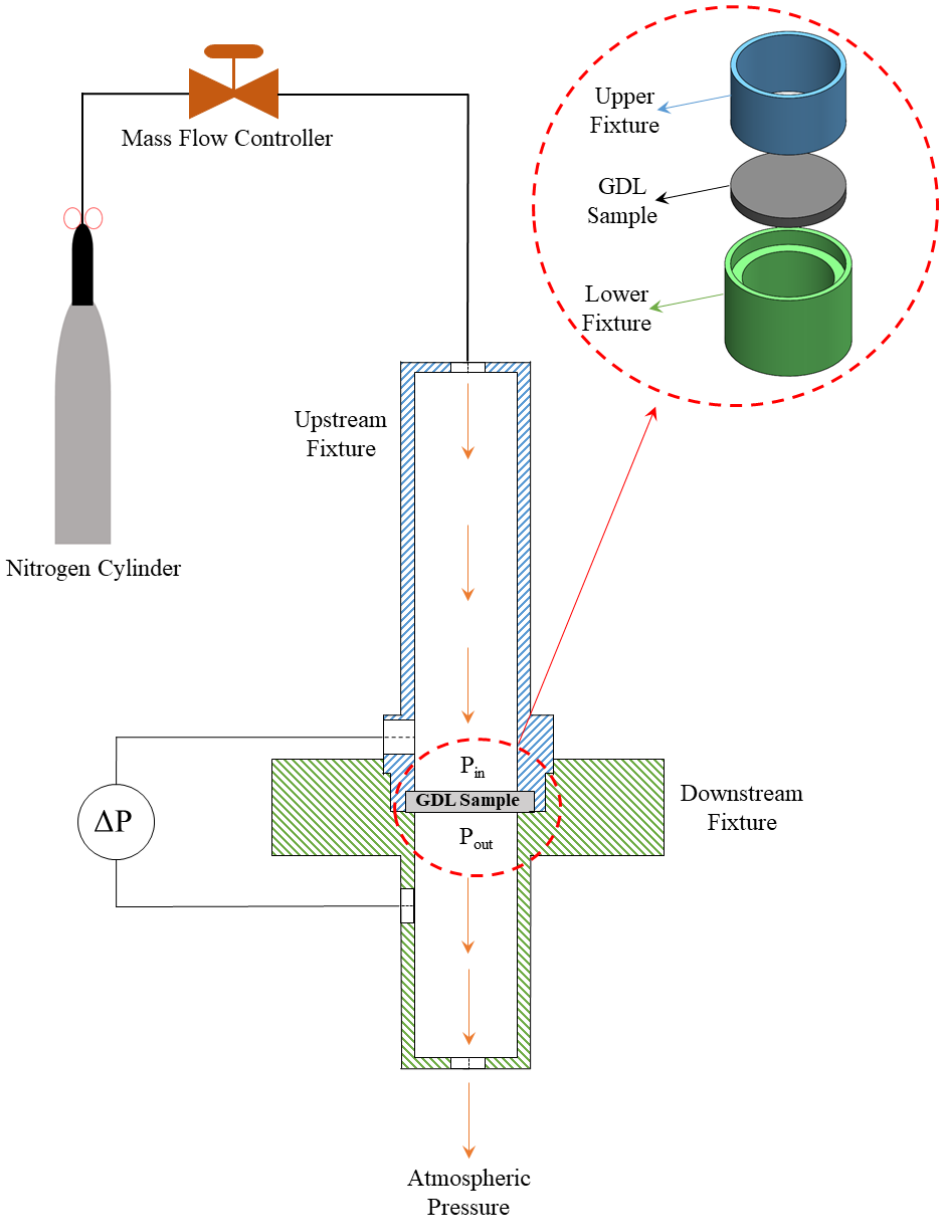

Figure 3.7 – A diagram of the through-plane gas permeability experimental setup (adapted from [101]).

3.3.4.2 Effective Diffusivity

Diffusion is the main mode of transport for the gases in the conventional carbon fibre based GDLs and this is due to their relatively low permeability (> 10-13 m²) [96] and is, at least, expected to play a crucial role in transporting the chemical species within the nickel foam based GDLs. The effective diffusivity is a measure on how diffusive the chemical species into each other within the porous medium. The effective diffusivity of the species i into the species j within the GDL, D_{ij}^{eff}, could be estimated using the following form of Fick's law:

$$J = D_{ij}^{eff} \frac{\Delta C}{L} \qquad \textbf{(3.8)}$$

where J is the molar flux (mol/(m^2·s)), and ΔC is the concentration difference between the inlet and outlet across either the thickness (through-plane) or the length (in-plane) of the GDL material (L). The molar flux was, following the solution of the conservation of the chemical species equation as described in Section 3.3.2, computed for each of the 20 modelled nickel foam slices in both the through- and in-plane directions. With this and with the knowledge of ΔC (1 mol/m³) and L (1.05 mm for the through-plane direction and 6.65 mm for the in-plane direction), the respective effective diffusivities could be calculated. It should be noted that the species i and j were taken to be oxygen and nitrogen in this study, mimicking the real-life situation in PEFCs where air is typically fed into the cathode of the fuel cell. In addition, it is worth mentioning that the concentration difference does not have an impact on the estimated effective through- or in-plane diffusivity of oxygen as the molar flux proportionally changes with the concentration difference, thus

maintaining the proportionality factor (the effective diffusivity of oxygen) constant; see Figure 3.8 and Tables A3.1 and A3.2 in the Appendix-III.

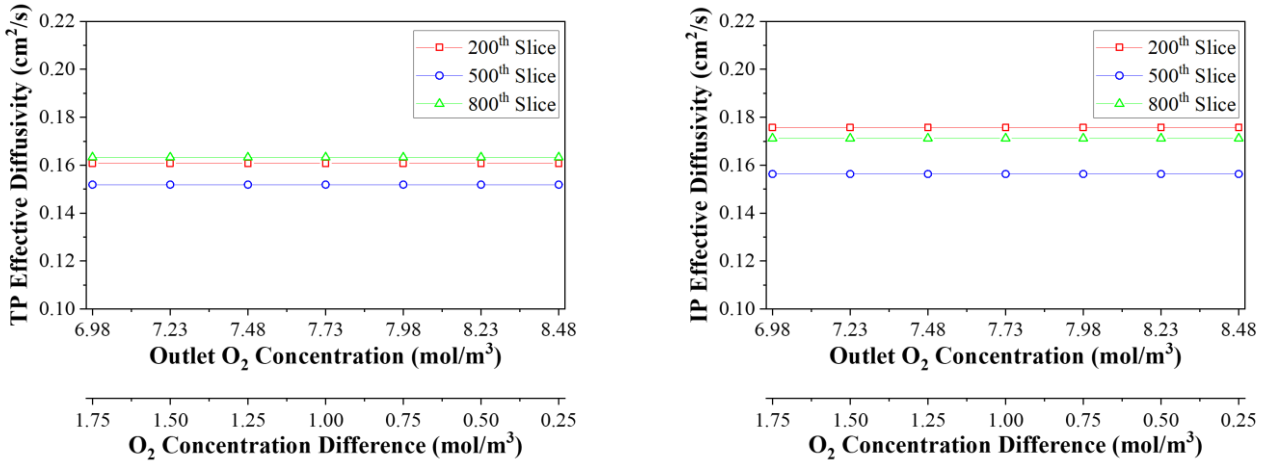

(a) **(b)**

Figure 3.8 – Effective diffusivity of oxygen into nitrogen for (a) through- and (b) in-plane directions for seven different outlet oxygen concentrations (and oxygen concentration differences, ΔC) for the 200th, 500th, and 800th slices.

3.4 RESULTS AND DISCUSSION

Figures 3.9 and 3.10 show the velocity profiles, for the through- and in-plane flow directions, respectively, within one of the modelled CT slices. It is evident that the random position and the size of the ligaments of the foam significantly influence the velocity magnitude and direction within the modelled CT slice, thus resulting in highly non-uniform velocity profiles. Similar profiles were obtained for the other modelled CT slices (not shown). Notably, a slightly more uniform velocity profile is obtained for the in-plane flow compared to the through-plane direction. As will be shown in Section 3.4.2, this could be attributed to the smaller tortuosity values as

demonstrated by the nickel form in the in-plane direction than in the through-plane direction. The following subsections present the computationally-estimated structural and mass transport properties of the nickel foam.

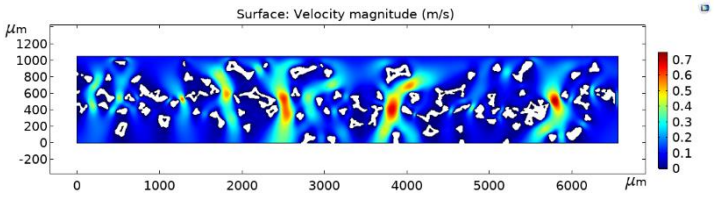

(a)

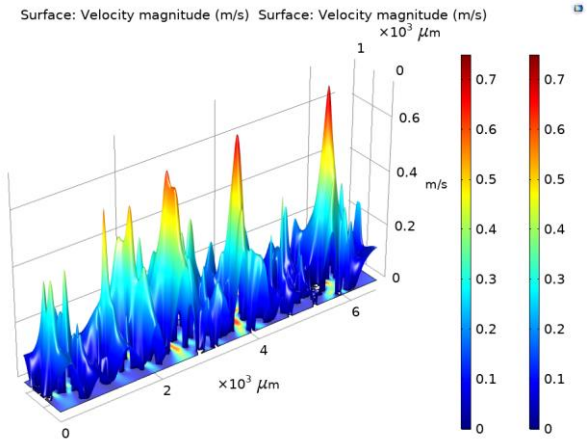

(b)

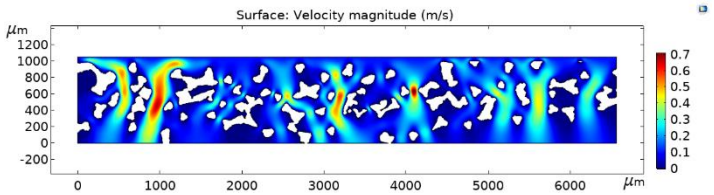

(c)

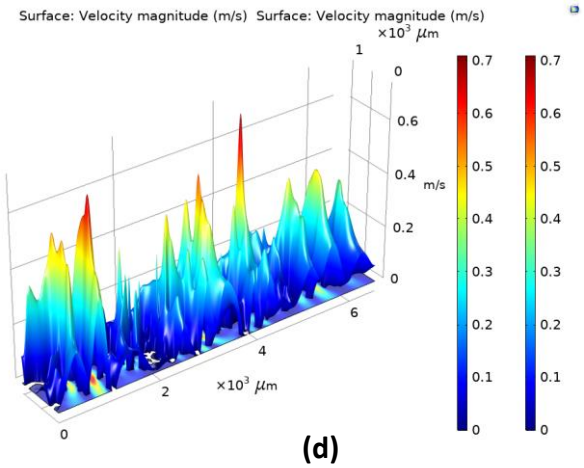

(d)

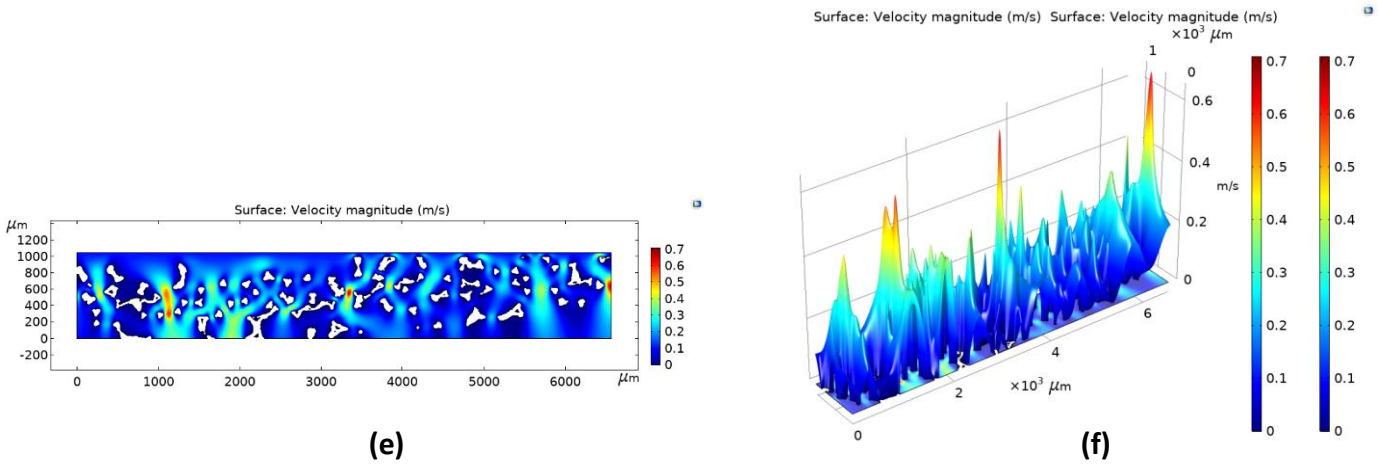

(e) **(f)**

Figure 3.9 – The numerical-estimated velocity profile for the through-plane flows within the modelled CT nickel foam slice 200 (a and b), 500 (c and d) and 800 (e and f).

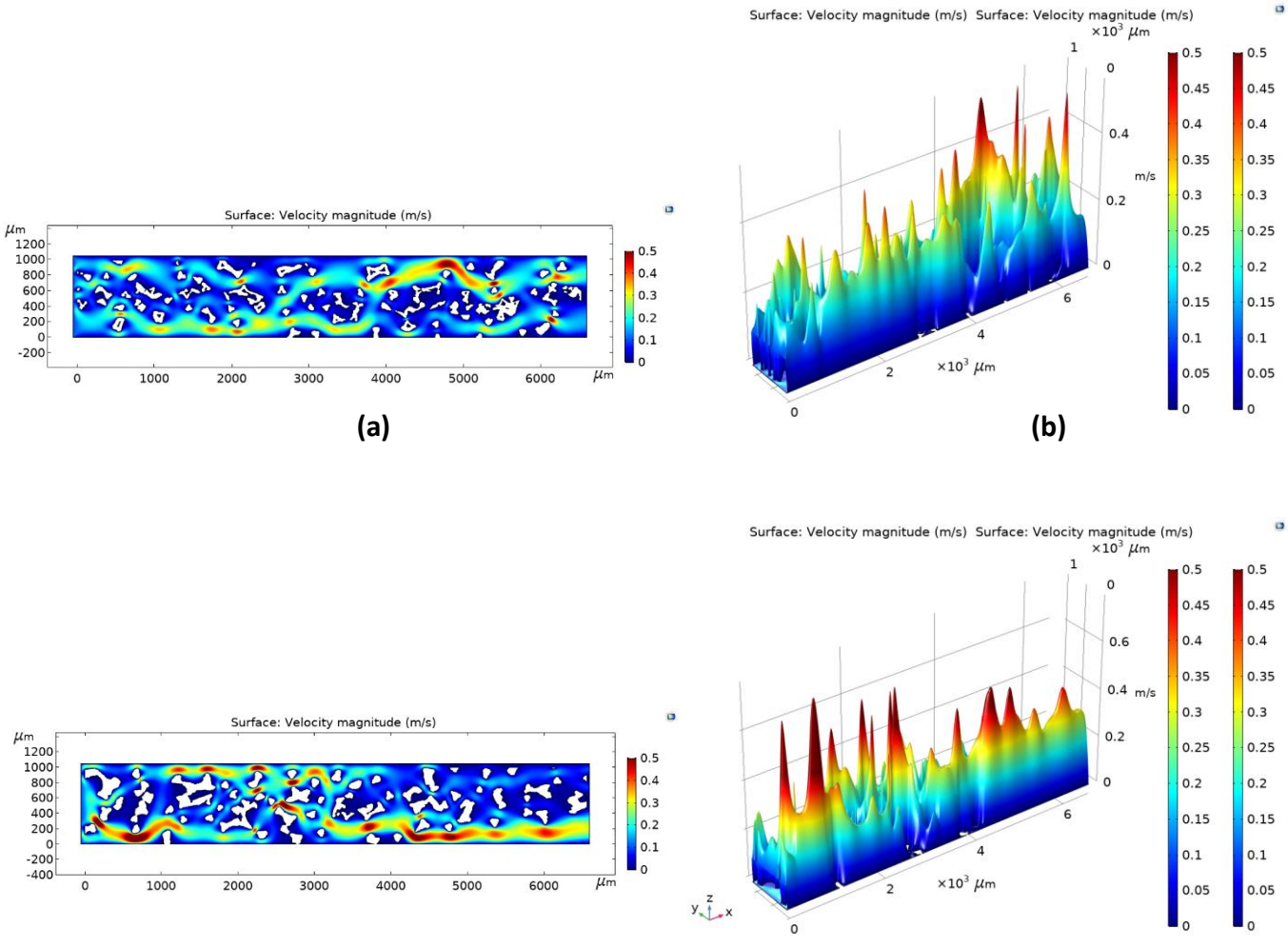

(a) **(b)**

(c) **(d)**

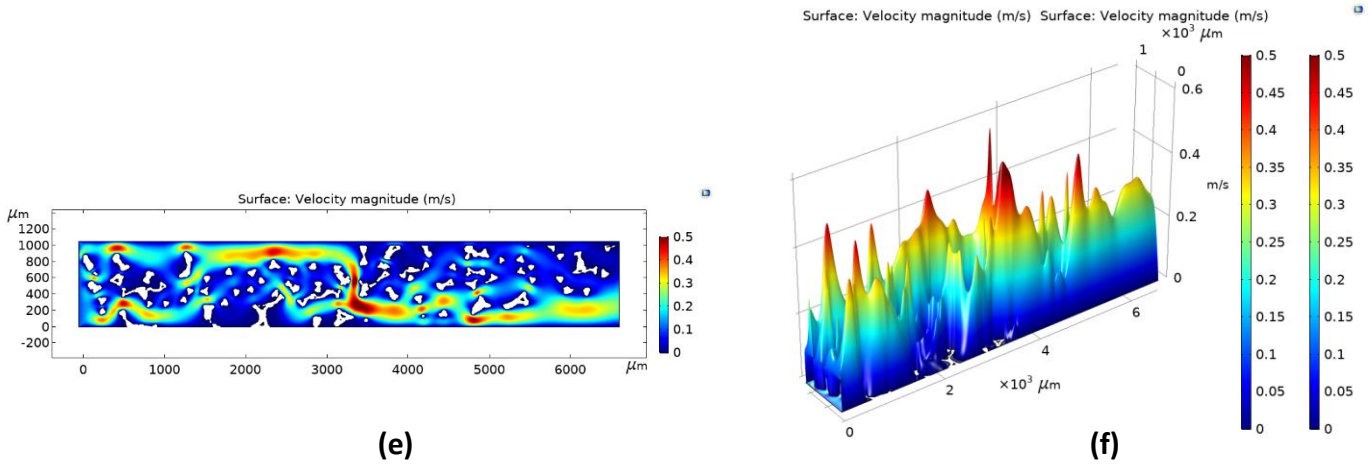

Figure 3.10 – The numerical-estimated velocity profile for the in-plane flows within the modelled CT nickel foam slice 200 (a and b), 500 (c and d) and 800 (e and f).

3.4.1 Porosity

Figure 3.11 shows the porosity values for each of the equally-spaced selected 20 slices. The range of the porosity is from 0.844 to 0.873 and the mean values for the porosity values of all the slices is 0.856 with a 95% confidence interval of ±0.003. These porosity values are in agreement with those reported in the literature [102–107]. For instance, the porosity of the nickel foam was experimentally determined by Oun and Kennedy [104] as 0.88. Also, the porosity of the nickel foam was reported by Khayargoli et al. [105] to be between 0.83 and 0.90, and by Slade [108] to be between 0.85 and 0.97. Moreover, Vicente et al. [107] computed the porosity of some nickel foam samples employing 3D CT images and found that it lies between 0.87 and 0.93. These relatively wide ranges for the porosity values and/or the slight discrepancies between the values/ranges reported by the various research groups could be attributed to the potentially different manufacturing settings used [50]. The

multiple 2D CT images using computational method, unlike the conventional experimental methods and the 3D numerical X-ray CT studies, reveal how uniform the nickel foam is in terms of porosity. This uniformity and the high values of porosity of nickel foams is expected to facilitate mass transport within the PEFCs.

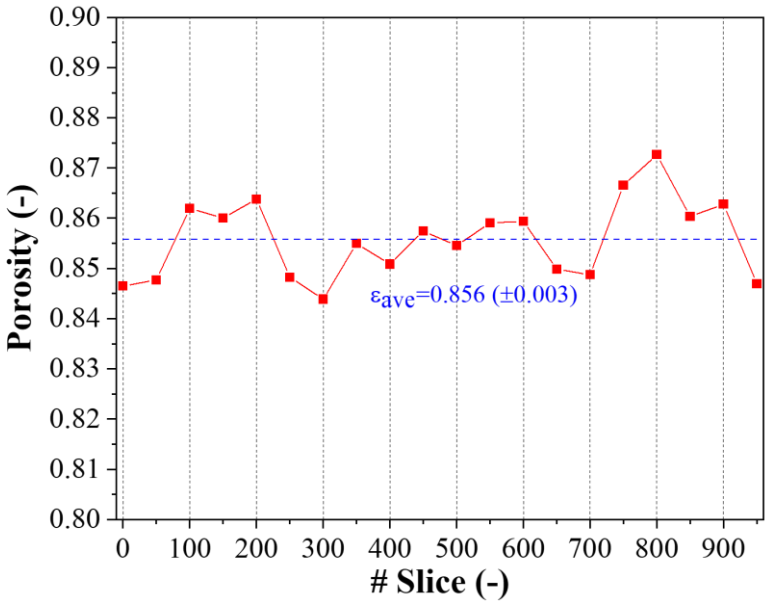

Figure 3.11 – Computationally computed porosity values for 20 equally-spaced CT nickel foam slices.

3.4.2 Tortuosity

The through- and in-plane tortuosity values for the 20 equally-spaced two-dimensional CT slices are presented in Figure 3.12. The average through-plane tortuosity is 1.175, which is between those values reported in the literature by Khayargoli et al. (i.e. 1.15) [105] and Kopanidis et al. (i.e. 1.26) [109]. The average in-plane tortuosity (i.e. 1.124) was found to be slightly less than that in the through-plane direction and in line with those reported in the literature by Brun et al. (i.e. 1.09

– 1.13) [110]. It is noteworthy that the latter authors estimated the tortuosity making use of the X-ray CT images generated for a nickel foam material. The results shows that the tortuosity of the nickel foam are significantly less than those of the conventionally-used carbon substrates; the smallest reported tortuosity for an SGL and Toray carbon substrates were found to be 1.33 and 2.50, respectively [111,112]. This suggests that, compared to the carbon substrates, the reacting gases and/or excess water would flow through more straight pathways when using nickel foams as the GDLs, thus reducing the mass transport resistance and potentially mitigating the water flooding, particularly beneath the ribs of the flow-field plates.

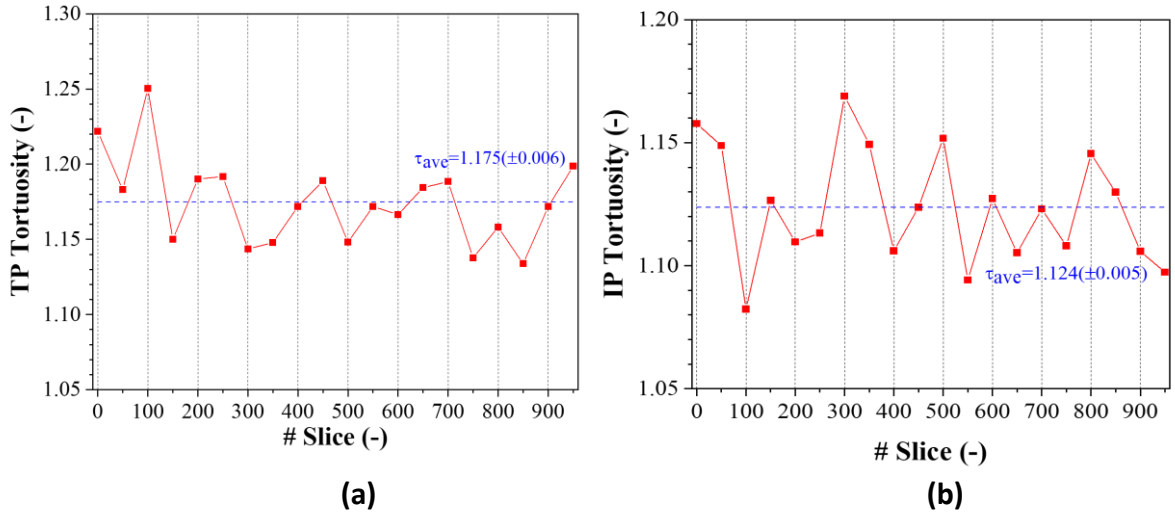

Figure 3.12 – Computationally computed (a) through-plane tortuosity and (b) in-plane tortuosity for 20 equally-spaced CT nickel foam slices.

3.4.3 Pore size distribution

The pore size distribution histograms for 10 CT slices are shown in Figure 3.13. Considering all the slices, the average pore size was calculated to be around 390 (±16) µm and the range of the pore size is between 100 and 750 µm. The above average pore sizes are in line with those reported in the literature. Namely, it lies between that reported by Khayargoli et al. [105], i.e. 360 µm, and that reported by Milazzo et al. [113], Oun and Kennedy [114], and Hellmann et al. [114], i.e. 450 µm. The average pore size of the nickel foam is two orders of magnitude higher than those of the conventional carbon fibre based GDLs [111], which suggests that, as with the tortuosity, that less mass transport resistance is demonstrated by nickel foam based GDLs. It is noteworthy that the nickel foam exhibits a slightly larger pore size compared to other metal foams and this due to the relatively thinner ligament thickness of the former foam [115]. Large pore size in the porous material is beneficial for effective mass transport [116]; Crosnier et al. [117] stated that the larger is the pore diameter, the smaller is the pressure drop and the higher is the permeability. As the pore size of nickel foam decreases, the specific surface area increases which creates an additional flow resistance.

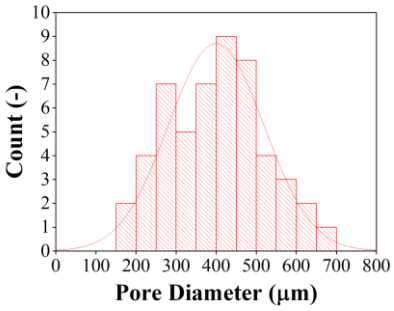
Count (-)
Pore Diameter (µm)

(a)

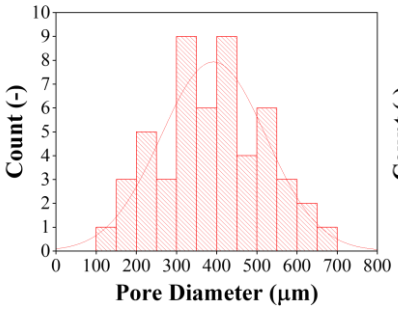
Count (-)
Pore Diameter (µm)

(b)

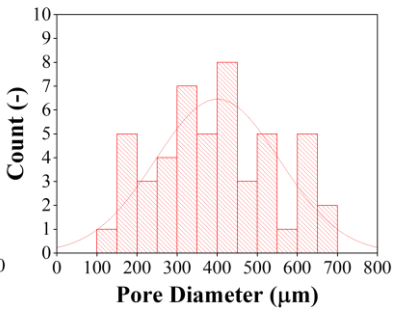
Count (-)
Pore Diameter (µm)

(c)

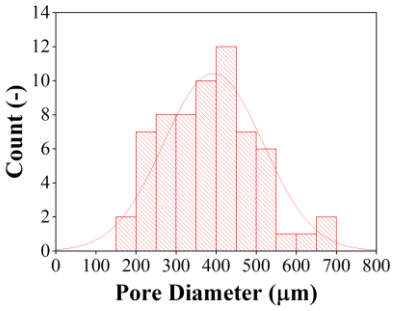
Count (-)
Pore Diameter (µm)

(d)

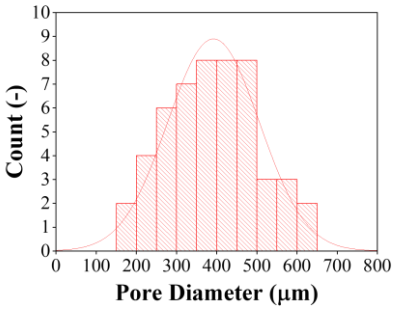
Count (-)
Pore Diameter (µm)

(e)

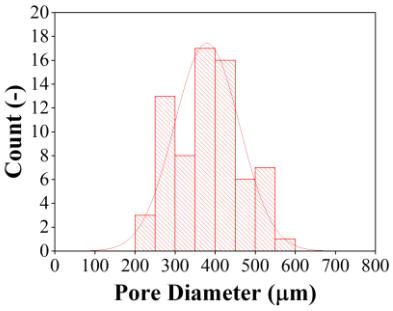
Count (-)
Pore Diameter (µm)

(f)

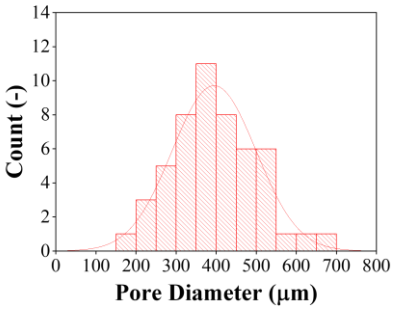
Count (-)
Pore Diameter (µm)

(g)

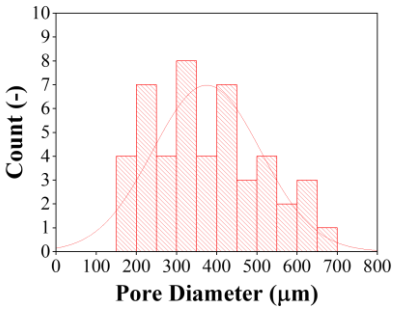
Count (-)
Pore Diameter (µm)

(h)

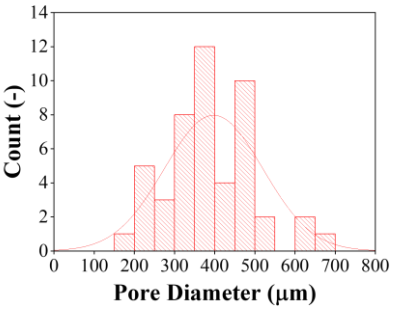
Count (-)
Pore Diameter (µm)

(i)

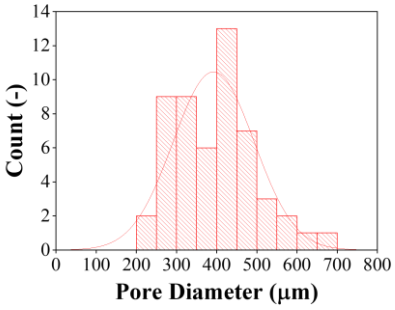
Count (-)
Pore Diameter (µm)

(j)

Figure 3.13 – The pore size distribution for the CT nickel foam slice number: (a) 0, (b) 100, (c) 200, (d) 300, (e) 400, (f) 500, (g) 600, (h) 700, (i) 800, and (j) 900.

3.4.4 Ligament thickness distribution

The ligament thickness distribution histograms for 10 CT slices are shown in Figure 3.14. Considering all of these 10 slices, the average ligament thickness was calculated to be around 99 (±3) µm and the range of the ligament thickness is between 60 and 180 µm. This calculated average ligament thickness is consistent with those reported in the literature. Namely, Tsolas et al. [118] experimentally and numerically evaluated the properties of nickel foams and reported the ligament thickness as 95 µm. Further, Miwa and Revankar [102] experimentally evaluated the structural characteristics of nickel foam and reported an average ligament thickens that is almost identical to that reported in this study, i.e. ~ 99 µm. It should be noted that the average ligament thickness of nickel is significantly larger than the average carbon fibre thickness of the conventionally used GDLs; the carbon-based GDLs fibre diameter has been reported to be between 7 and 10 µm [119,120].

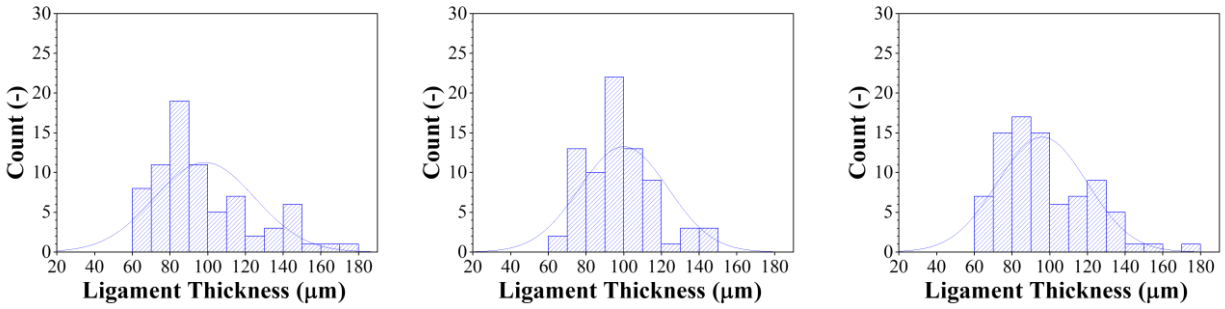

(a) **(b)** **(c)**

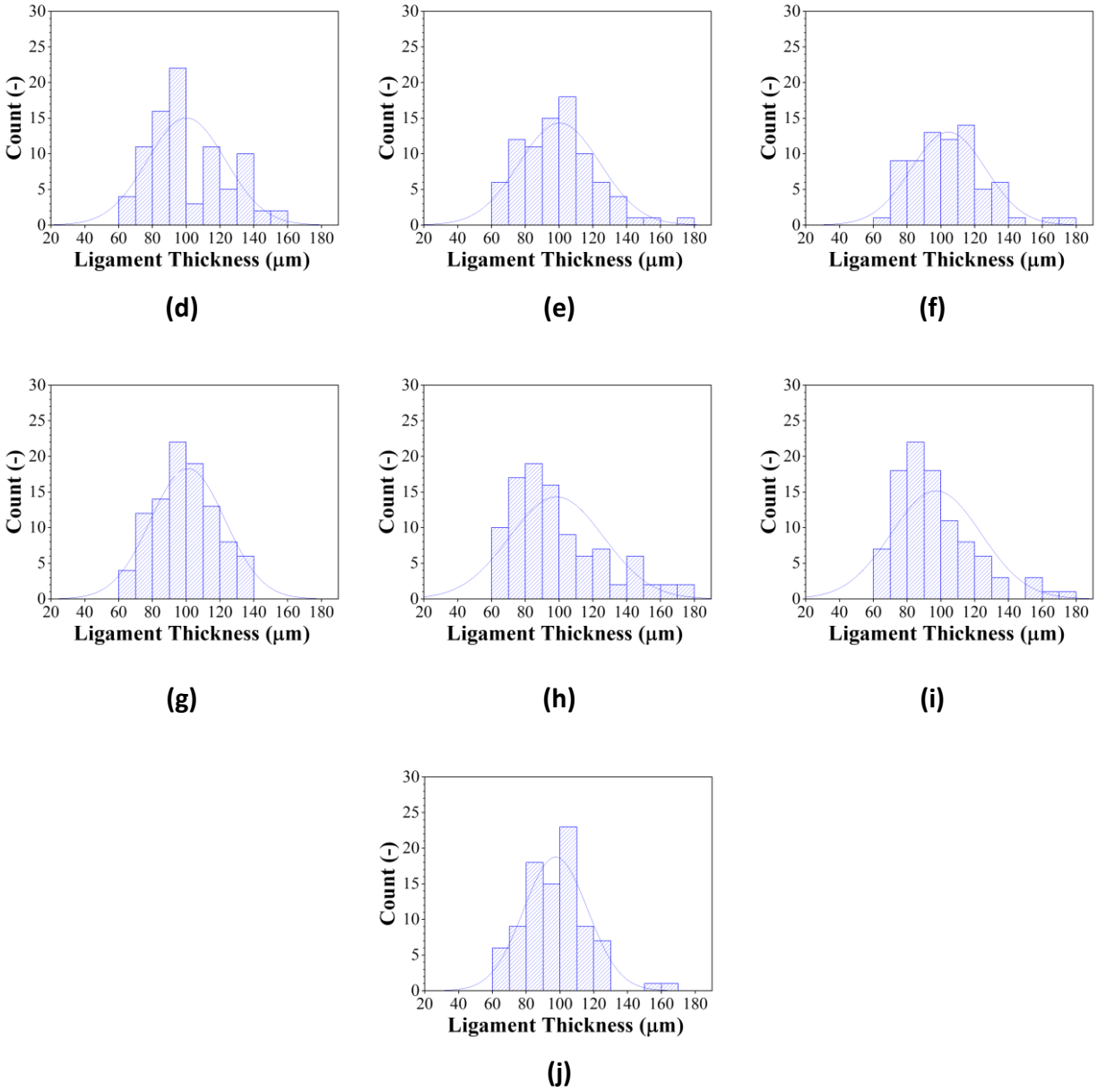

Figure 3.14 – The ligament thickness distribution for the CT nickel foam slice number: (a) 0, (b) 100, (c) 200, (d) 300, (e) 400, (f) 500, (g) 600, (h) 700, (i) 800, and (j) 900.

3.4.5 Specific surface area

Figure 3.15 shows the specific surface area (SSA) for 20 equally-spaced two-dimensional CT slices. As seen from the figure, the range of the SSA is between around 40500 and 46100 m^{-1}. The average SSA for all the slices is around 43560 (±310)

m^{-1} which is in accordance with those reported in the literature. Namely, Yang et al. [121] experimentally investigated nickel foam as a cathode electrode for aluminium-hydrogen peroxide fuel cells and they reported the SSA of the nickel foam as 42800 m^{-1}. Similarly, Langlois and Coeuret [122] experimentally assessed the structural properties of nickel foams and they, using a BET analysis, reported that the SSA of the nickel foam sample to be around 41000 m^{-1}. Compared to the conventionally used carbon substrates, nickel foam possess significantly higher SSA; this implies that they have superior heat and electrical conduction due to the better contact to the flow-field plates [114].

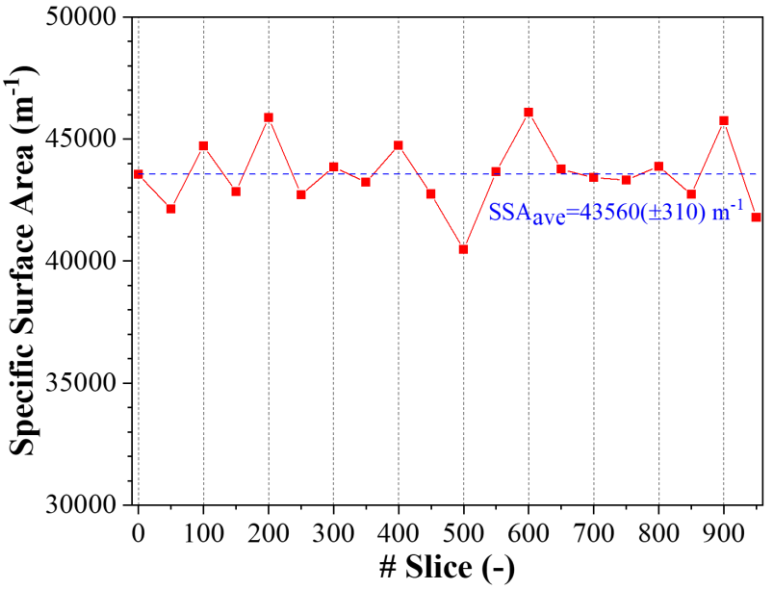

Figure 3.15 – Computationally computed specific surface area values for 20 equally-spaced CT nickel foam slices.

3.4.6 Gas Permeability

The through- and in-plane permeability was calculated as described in Section 3.3.4.1 for all the 20 equally-spaced two-dimensional CT slices; see Figure 3.16. The average

through-plane and in-plane permeability values are, considering the permeability of all the individual modelled slices, 1.26×10^{-9} and 1.39×10^{-9} m^2, respectively. The range is between 9.81×10^{-10} and 1.51×10^{-9} m^2 for the through-plane permeability and is between 8.63×10^{-10} and 1.84×10^{-9} m^2 for the in-plane permeability. The above computationally-estimated through-plane permeability is in very good agreement with those experimentally estimated values using the in-house set-up which is 1.40×10^{-9} m^2. Further, the above average permeability's are in excellent agreement with those reported in the literature. Namely, Khayargoli et al. [105] and Medraj et al. [123] experimentally estimated the through-plane permeability of nickel foam as 1.30×10^{-9} m^2. The average in-plane permeability computed in this study lies between that reported by Hugo et al. (1.38×10^{-9} m^2) [103] and that reported by Miwa and Revankar (1.45×10^{-9} m^2) [124]. Overall, the gas permeability of nickel foam is at least two orders of magnitudes higher than those of the conventionally used carbon fibre based substrates whose values are normally between 10^{-11} and 10^{-12} m^2 [111]. This signifies that nickel foam based GDL would demonstrate significantly higher convective flows than the conventionally used GDLs, thus improving the supply of the reactant gases to the catalyst layers and/or the removal of excess water from the catalyst layers. Another observation is that the gas permeability of nickel foam was found to be more isotropic than that of the commonly used carbon fibre based carbon substrates; the in-plane permeability of the latter material is larger than the through-plane permeability by almost one order of magnitude [12,125].

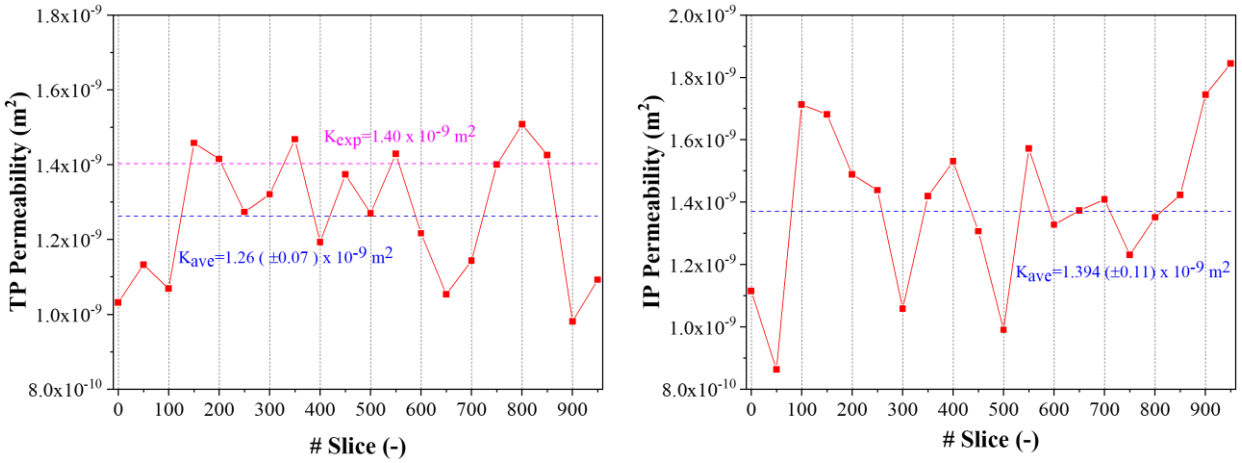

(a) **(b)**

Figure 3.16 – Computationally computed (a) through-plane and (b) in-plane gas permeability for 20 equally-spaced CT nickel foam slices.

3.4.7 Effective Diffusivity

Figure 3.17 shows the through- and in-plane effective diffusivity of oxygen into nitrogen corrected for the structure of the nickel foam for the all the 20 equally-spaced two-dimensional CT slices. The average through- and in-plane effective diffusivity are, considering all the 20 CT slices, 0.154 and 0.166 cm^2/s, respectively. The range is between 0.142 and 0.165 cm^2/s for the through-plane effective diffusivity and is between 0.156 and 0.176 cm^2/s for the in-plane effective diffusivity. As with the gas permeability of nickel foam, the effective diffusivity of nickel foam shows a good degree of isotropy as evidenced from the comparable values for the effective diffusivity in the through- and in-plane directions. This should be compared with the effective diffusivity of the commonly used carbon substrates where the in-plane diffusivity is higher than the through-plane value by a factor of 1.3 to 3 [61,126].

Moreover, the nickel foam-based GDL yields a much higher effective diffusivity for both the through- and in-plane directions than those of the conventional carbon-based GDLs which are typically between 0.066 and 0.120 cm^2/s (for through-plane direction) and 0.085 and 0.124 cm^2/s (for in-plane direction), respectively [127].

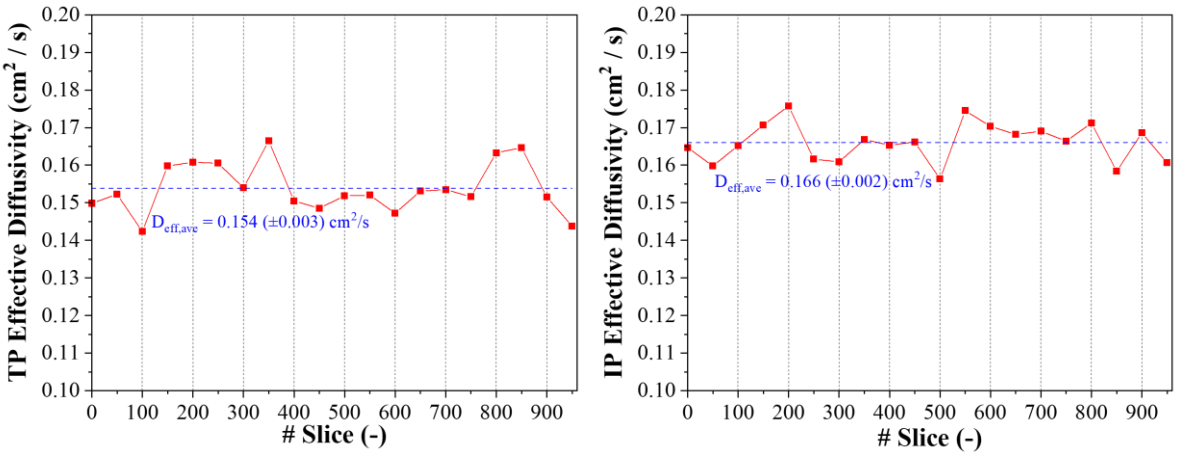

(a) **(b)**

Figure 3.17 – Computationally computed (a) through-plane and (b) in-plane effective diffusivity of oxygen into nitrogen for 20 equally-spaced CT nickel foam slices.

3.5 CONCLUSIONS

Nickel foams have a great potential to be used as gas diffusion layers in polymer electrolyte fuel cells and this is due to their superior structural and transport properties. In this chapter, some key structural (porosity, tortuosity, pore size distribution, ligament thickness distribution, and specific surface area) and mass transport (gas permeability and effective diffusivity) of a typical nickel foam sample have been determined using equally-spaced multiple computationally-efficient two-

dimensional X-ray CT images and/or corresponding numerical models. This is, in addition to saving computational time through not solving computationally expensive three-dimensional images and/or numerical models, performed to check for the multidimensional uniformity of the nickel foam samples. The main findings could be summarised as follows:

- All the computationally-determined properties of the nickel foam, compared to those of the conventionally-used carbon substrates, demonstrate better uniformity in the in-plane and through-plane directions and better isotropy as evidenced from the comparable individual values computed for all the two-dimensional CT slices. Further, all of these computed properties were found to be in agreement with experimental and/or computationally-determined literature data.
- The mean porosity and the mean pore size of the nickel foam sample were computed to be around 0.86 and 390 µm, respectively; these values are, compared to those of the conventionally-used carbon substrates, high; thus facilitating the mass transport of the gases and liquid water to/from the catalysts layers. Likewise, the relatively low through-plane (~1.18) and in-plane (~1.12) tortuosity lowers the mass transport resistance of the chemical species.
- The mean ligament thickness was computed to be around 99 µm which is one order of magnitude higher than the mean carbon fibre diameter of the conventionally-used carbon substrates; thus implying better mechanical support by nickel foam for the delicate membrane electrode assembly of the fuel cell.

- The computed mean through-plane (1.26×10^{-9} m²) and in-plane (1.39×10^{-9} m²) gas permeability was found to be at least one order of magnitude higher than those of the normally-used carbon substrates, signifying higher contribution of convective flow to the mass transport of gases within the nickel foam based GDL. Likewise, the computed mean effective through-plane (0.154 cm^2/s) and in-plane (0.166 cm^2/s) gas diffusivity was found to be higher than those of the carbon substrates by an order of magnitude, meaning more effective diffusive transport to/from the catalyst layer and beneath the ribs of the flow field plates.

3.6 REFERENCES

[1] Tanaka S, Bradfield WW, Legrand C, Malan AG. Numerical and experimental study of the effects of the electrical resistance and diffusivity under clamping pressure on the performance of a metallic gas-diffusion layer in polymer electrolyte fuel cells. J Power Sources 2016;330:273–84. https://doi.org/10.1016/j.jpowsour.2016.08.121.

[2] Barbir F. PEM Fuel Cells - Theory and Practice. 2nd ed. 2012.

[3] Ozden A, Shahgaldi S, Li X, Hamdullahpur F. A review of gas diffusion layers for proton exchange membrane fuel cells—With a focus on characteristics, characterization techniques, materials and designs. Prog Energy Combust Sci 2019;74:50–102. https://doi.org/10.1016/j.pecs.2019.05.002.

[4] Wilberforce T, El-Hassan Z, Khatib FN, Al Makky A, Baroutaji A, Carton JG, et al. Developments of electric cars and fuel cell hydrogen electric cars. Int J Hydrogen Energy 2017;42:25695–734. https://doi.org/10.1016/j.ijhydene.2017.07.054.

[5] Alaefour I, Shahgaldi S, Ozden A, Li X, Hamdullahpur F. The role of flow-field layout on the conditioning of a proton exchange membrane fuel cell. Fuel 2018;230:98–103. https://doi.org/10.1016/j.fuel.2018.05.062.

[6] Carton JG, Olabi AG. Design of experiment study of the parameters that affect performance of three flow plate configurations of a proton exchange membrane fuel cell. Energy 2010;35:2796–806.

https://doi.org/10.1016/j.energy.2010.02.044.

[7] Ismail MS, Borman D, Damjanovic T, Ingham DB, Pourkashanian M. On the through-plane permeability of microporous layer-coated gas diffusion layers used in proton exchange membrane fuel cells. Int J Hydrogen Energy 2011;36:10392–402. https://doi.org/10.1016/j.ijhydene.2010.09.012.

[8] Aldakheel F, Ismail MS, Hughes KJ, Ingham DB, Ma L, Pourkashanian M, et al. Gas permeability, wettability and morphology of gas diffusion layers before and after performing a realistic ex-situ compression test. Renew Energy 2020;151:1082–91. https://doi.org/10.1016/j.renene.2019.11.109.

[9] Hasanpour S, Hoorfar M, Phillion AB. Different methods for determining porosity of gas diffusion layer using X-ray microtomography. Electrochim Acta 2015;185:34–9. https://doi.org/10.1016/j.electacta.2015.10.083.

[10] Dhanushkodi SR, Capitanio F, Biggs T, Mérida W. Understanding flexural, mechanical and physico-chemical properties of gas diffusion layers for polymer membrane fuel cell and electrolyzer systems. Int J Hydrogen Energy 2015;40:16846–59. https://doi.org/10.1016/j.ijhydene.2015.07.033.

[11] Rama P, Liu Y, Chen R, Ostadi H, Jiang K, Gao Y, et al. A numerical study of structural change and anisotropic permeability in compressed carbon cloth polymer electrolyte fuel cell gas diffusion layers. Fuel Cells 2011;11:274–85. https://doi.org/10.1002/fuce.201000037.

[12] Ismail MS, Damjanovic T, Hughes K, Ingham DB, Ma L, Pourkashanian M, et al.

Through-plane permeability for untreated and PTFE-treated gas diffusion layers in proton exchange membrane fuel cells. J Fuel Cell Sci Technol 2010;7:0510161–7. https://doi.org/10.1115/1.4000685.

[13] Ijaodola OS, El- Hassan Z, Ogungbemi E, Khatib FN, Wilberforce T, Thompson J, et al. Energy efficiency improvements by investigating the water flooding management on proton exchange membrane fuel cell (PEMFC). Energy 2019;179:246–67. https://doi.org/10.1016/j.energy.2019.04.074.

[14] Rashapov R, Imami F, Gostick JT. A method for measuring in-plane effective diffusivity in thin porous media. Int J Heat Mass Transf 2015;85:367–74. https://doi.org/10.1016/j.ijheatmasstransfer.2015.01.101.

[15] Ogungbemi E, Ijaodola O, Khatib FN, Wilberforce T, El Hassan Z, Thompson J, et al. Fuel cell membranes – Pros and cons. Energy 2019;172:155–72. https://doi.org/10.1016/j.energy.2019.01.034.

[16] Carton JG, Olabi AG. Three-dimensional proton exchange membrane fuel cell model: Comparison of double channel and open pore cellular foam flow plates. Energy 2017;136:185–95. https://doi.org/10.1016/j.energy.2016.02.010.

[17] Wang Y, Wang CY, Chen KS. Elucidating differences between carbon paper and carbon cloth in polymer electrolyte fuel cells. Electrochim Acta 2007;52:3965–75. https://doi.org/10.1016/j.electacta.2006.11.012.

[18] Han M, Xu JH, Chan SH, Jiang SP. Characterization of gas diffusion layers for PEMFC. Electrochim Acta 2008;53:5361–7.

https://doi.org/10.1016/j.electacta.2008.02.057.

[19] Jayakumar A, Sethu SP, Ramos M, Robertson J, Al-Jumaily A. A technical review on gas diffusion, mechanism and medium of PEM fuel cell. Ionics (Kiel) 2015;21:1–18. https://doi.org/10.1007/s11581-014-1322-x.

[20] Singh Y, White RT, Najm M, Haddow T, Pan V, Orfino FP, et al. Tracking the evolution of mechanical degradation in fuel cell membranes using 4D in situ visualization. J Power Sources 2019;412:224–37. https://doi.org/10.1016/j.jpowsour.2018.11.049.

[21] Park J, Oh H, Ha T, Lee Y Il, Min K. A review of the gas diffusion layer in proton exchange membrane fuel cells: Durability and degradation. Appl Energy 2015;155:866–80. https://doi.org/10.1016/j.apenergy.2015.06.068.

[22] Wu J, Yuan XZ, Martin JJ, Wang H, Zhang J, Shen J, et al. A review of PEM fuel cell durability: Degradation mechanisms and mitigation strategies. J Power Sources 2008;184:104–19. https://doi.org/10.1016/j.jpowsour.2008.06.006.

[23] Dukhan N. Correlations for the pressure drop for flow through metal foam. Exp Fluids 2006;41:665–72. https://doi.org/10.1007/s00348-006-0194-x.

[24] Dukhan N, Ali M. Effect of Confining Wall on Properties of Gas Flow Through Metal Foam: An Experimental Study. Transp Porous Media 2012;91:225–37. https://doi.org/10.1007/s11242-011-9841-7.

[25] Dukhan N, Patel K. Effect of sample's length on flow properties of open-cell metal foam and pressure-drop correlations. J Porous Mater 2011;18:655–65.

https://doi.org/10.1007/s10934-010-9423-z.

[26] Hmad AA, Dukhan N. Cooling design for pem fuel-cell stacks employing air and metal foam: Simulation and experiment. Energies 2021;14. https://doi.org/10.3390/en14092687.

[27] Wang Y, Leung DYC, Xuan J, Wang H. A review on unitized regenerative fuel cell technologies, part B: Unitized regenerative alkaline fuel cell, solid oxide fuel cell, and microfluidic fuel cell. Renew Sustain Energy Rev 2017;75:775–95. https://doi.org/10.1016/j.rser.2016.11.054.

[28] Mukanova A, Nurpeissova A, Urazbayev A, Kim SS, Myronov M, Bakenov Z. Silicon thin film on graphene coated nickel foam as an anode for Li-ion batteries. Electrochim Acta 2017;258:800–6. https://doi.org/10.1016/j.electacta.2017.11.129.

[29] Majasan JO, Iacoviello F, Cho JIS, Maier M, Lu X, Neville TP, et al. Correlative study of microstructure and performance for porous transport layers in polymer electrolyte membrane water electrolysers by X-ray computed tomography and electrochemical characterization. Int J Hydrogen Energy 2019;44:19519–32. https://doi.org/10.1016/j.ijhydene.2019.05.222.

[30] Rybár R, Beer M, Kudelas D, Pandula B. Copper metal foam as an essential construction element of innovative heat exchanger. Metalurgija 2016;55:489–92.

[31] Liang L, Diao YH, Zhao YH, Wang ZY, Bai FW. Numerical and experimental

investigations of latent thermal energy storage device based on a flat micro-heat pipe array–metal foam composite structure. Renew Energy 2020;161:1195–208. https://doi.org/10.1016/j.renene.2020.07.033.

[32] Toghyani S, Afshari E, Baniasadi E. Metal foams as flow distributors in comparison with serpentine and parallel flow fields in proton exchange membrane electrolyzer cells. Electrochim Acta 2018;290:506–19. https://doi.org/10.1016/j.electacta.2018.09.106.

[33] Tan WC, Saw LH, Thiam HS, Xuan J, Cai Z, Yew MC. Overview of porous media/metal foam application in fuel cells and solar power systems. Renew Sustain Energy Rev 2018;96:181–97. https://doi.org/10.1016/j.rser.2018.07.032.

[34] Sim Y, Kwak J, Kim SY, Jo Y, Kim S, Kim SY, et al. Formation of 3D graphene-Ni foam heterostructures with enhanced performance and durability for bipolar plates in a polymer electrolyte membrane fuel cell. J Mater Chem A 2018;6:1504–12. https://doi.org/10.1039/c7ta07598g.

[35] Tseng CJ, Tsai BT, Liu ZS, Cheng TC, Chang WC, Lo SK. A PEM fuel cell with metal foam as flow distributor. Energy Convers Manag 2012;62:14–21. https://doi.org/10.1016/j.enconman.2012.03.018.

[36] Sajid Hossain M, Shabani B. Metal foams application to enhance cooling of open cathode polymer electrolyte membrane fuel cells. J Power Sources 2015;295:275–91. https://doi.org/10.1016/j.jpowsour.2015.07.022.

[37] Tabe Y, Nasu T, Morioka S, Chikahisa T. Performance characteristics and internal phenomena of polymer electrolyte membrane fuel cell with porous flow field. J Power Sources 2013;238:21–8. https://doi.org/10.1016/j.jpowsour.2013.03.047.

[38] Tseng CJ, Heush YJ, Chiang CJ, Lee YH, Lee KR. Application of metal foams to high temperature PEM fuel cells. Int J Hydrogen Energy 2016;41:16196–204. https://doi.org/10.1016/j.ijhydene.2016.06.149.

[39] Tsai BT, Tseng CJ, Liu ZS, Wang CH, Lee CI, Yang CC, et al. Effects of flow field design on the performance of a PEM fuel cell with metal foam as the flow distributor. Int J Hydrogen Energy 2012;37:13060–6. https://doi.org/10.1016/j.ijhydene.2012.05.008.

[40] Baroutaji A, Carton JG, Stokes J, Olabi AG. Application of Open Pore Cellular Foam for air breathing PEM fuel cell. Int J Hydrogen Energy 2017;42:25630–8. https://doi.org/10.1016/j.ijhydene.2017.05.114.

[41] Shin DK, Yoo JH, Kang DG, Kim MS. Effect of cell size in metal foam inserted to the air channel of polymer electrolyte membrane fuel cell for high performance. Renew Energy 2018;115:663–75. https://doi.org/10.1016/j.renene.2017.08.085.

[42] Liu R, Zhou W, Li S, Li F, Ling W. Performance improvement of proton exchange membrane fuel cells with compressed nickel foam as flow field structure. Int J Hydrogen Energy 2020;45:17833–43. https://doi.org/10.1016/j.ijhydene.2020.04.238.

[43] Zamel N, Li X. Effective transport properties for polymer electrolyte membrane fuel cells - With a focus on the gas diffusion layer. Prog Energy Combust Sci 2013;39:111–46. https://doi.org/10.1016/j.pecs.2012.07.002.

[44] Jung S, Sabharwal M, Jarauta A, Wei F, Gingras M, Gostick J, et al. Estimation of Relative Transport Properties in Porous Transport Layers Using Pore-Scale and Pore-Network Simulations. J Electrochem Soc 2021;168:064501. https://doi.org/10.1149/1945-7111/ac03f2.

[45] Fishman Z, Hinebaugh J, Bazylak A. Microscale tomography investigations of heterogeneous porosity distributions of PEMFC GDLs. J Electrochem Soc 2010;157:1643–50. https://doi.org/10.1149/1.3481443.

[46] Zenyuk I V., Parkinson DY, Connolly LG, Weber AZ. Gas-diffusion-layer structural properties under compression via X-ray tomography. J Power Sources 2016;328:364–76. https://doi.org/10.1016/j.jpowsour.2016.08.020.

[47] Chevalier S, Lavielle N, Hatton BD, Bazylak A. Novel electrospun gas diffusion layers for polymer electrolyte membrane fuel cells: Part I. Fabrication, morphological characterization, and in situ performance. J Power Sources 2017;352:272–80. https://doi.org/10.1016/j.jpowsour.2017.03.098.

[48] Obermaier M, Bauer A, Dalkilic M, Rauber M, Scheu C. Gas diffusion layer wettability determination by cyclic voltammetry for automotive fuel cells. Fuel Cells 2021:221–33. https://doi.org/10.1002/fuce.202000184.

[49] Kaushal S, Sahu AK, Rani M, Dhakate SR. Multiwall carbon nanotubes tailored

porous carbon fiber paper-based gas diffusion layer performance in polymer electrolyte membrane fuel cell. Renew Energy 2019;142:604–11. https://doi.org/10.1016/j.renene.2019.04.096.

[50] Çeçen A, Wargo EA, Hanna AC, Turner DM, Kalidindi SR, Kumbur EC. 3-D Microstructure Analysis of Fuel Cell Materials: Spatial Distributions of Tortuosity, Void Size and Diffusivity. J Electrochem Soc 2012;159:B299–307. https://doi.org/10.1149/2.068203jes.

[51] De Chiffre L, Carmignato S, Kruth JP, Schmitt R, Weckenmann A. Industrial applications of computed tomography. CIRP Ann - Manuf Technol 2014;63:655–77. https://doi.org/10.1016/j.cirp.2014.05.011.

[52] Vásárhelyi L, Kónya Z, Kukovecz, Vajtai R. Microcomputed tomography–based characterization of advanced materials: a review. Mater Today Adv 2020;8:1–13. https://doi.org/10.1016/j.mtadv.2020.100084.

[53] Banerjee R, Hinebaugh J, Liu H, Yip R, Ge N, Bazylak A. Heterogeneous porosity distributions of polymer electrolyte membrane fuel cell gas diffusion layer materials with rib-channel compression. Int J Hydrogen Energy 2016;41:14885–96. https://doi.org/10.1016/j.ijhydene.2016.06.147.

[54] Zenyuk I V., Parkinson DY, Connolly LG, Weber AZ. Gas-diffusion-layer structural properties under compression via X-ray tomography. J Power Sources 2016;328:364–76. https://doi.org/10.1016/j.jpowsour.2016.08.020.

[55] Fishman Z, Bazylak A. Heterogeneous Through-Plane Porosity Distributions for

Treated PEMFC GDLs I. PTFE Effect. J Electrochem Soc 2011;158:B841. https://doi.org/10.1149/1.3594578.

[56] Fishman Z, Bazylak A. Heterogeneous Through-Plane Porosity Distributions for Treated PEMFC GDLs. II. Effect of MPL Cracks. J Electrochem Soc 2011;158:B846. https://doi.org/10.1149/1.3594636.

[57] James JP, Choi HW, Pharoah JG. X-ray computed tomography reconstruction and analysis of polymer electrolyte membrane fuel cell porous transport layers. Int J Hydrogen Energy 2012;37:18216–30. https://doi.org/10.1016/j.ijhydene.2012.08.077.

[58] Meyer Q, Ashton S, Boillat P, Cochet M, Engebretsen E, Finegan DP, et al. Effect of gas diffusion layer properties on water distribution across air-cooled, open-cathode polymer electrolyte fuel cells: A combined ex-situ X-ray tomography and in-operando neutron imaging study. Electrochim Acta 2016;211:478–87. https://doi.org/10.1016/j.electacta.2016.06.068.

[59] Meyer Q, Mansor N, Iacoviello F, Cullen PL, Jervis R, Finegan D, et al. Investigation of Hot Pressed Polymer Electrolyte Fuel Cell Assemblies via X-ray Computed Tomography. Electrochim Acta 2017;242:125–36. https://doi.org/10.1016/j.electacta.2017.05.028.

[60] Fazeli M, Hinebaugh J, Fishman Z, Tötzke C, Lehnert W, Manke I, et al. Pore network modeling to explore the effects of compression on multiphase transport in polymer electrolyte membrane fuel cell gas diffusion layers. J Power Sources 2016;335:162–71.

https://doi.org/10.1016/j.jpowsour.2016.10.039.

[61] García-Salaberri PA, Zenyuk I V., Shum AD, Hwang G, Vera M, Weber AZ, et al. Analysis of representative elementary volume and through-plane regional characteristics of carbon-fiber papers: diffusivity, permeability and electrical/thermal conductivity. Int J Heat Mass Transf 2018;127:687–703. https://doi.org/10.1016/j.ijheatmasstransfer.2018.07.030.

[62] Fly A, Butcher D, Meyer Q, Whiteley M, Spencer A, Kim C, et al. Characterisation of the diffusion properties of metal foam hybrid flow-fields for fuel cells using optical flow visualisation and X-ray computed tomography. J Power Sources 2018;395:171–8. https://doi.org/10.1016/j.jpowsour.2018.05.070.

[63] Fly A, Meyer Q, Whiteley M, Iacoviello F, Neville T, Shearing PR, et al. X-ray tomography and modelling study on the mechanical behaviour and performance of metal foam flow-fields for polymer electrolyte fuel cells. Int J Hydrogen Energy 2019;44:7583–95. https://doi.org/10.1016/j.ijhydene.2019.01.206.

[64] Kulkarni N, Meyer Q, Hack J, Jervis R, Iacoviello F, Ronaszegi K, et al. Examining the effect of the secondary flow-field on polymer electrolyte fuel cells using X-ray computed radiography and computational modelling. Int J Hydrogen Energy 2019;44:1139–50. https://doi.org/10.1016/j.ijhydene.2018.11.038.

[65] Wu Y, Cho JIS, Whiteley M, Rasha L, Neville TP, Ziesche R, et al. Characterization of water management in metal foam flow-field based polymer electrolyte fuel cells using in-operando neutron radiography. Int J Hydrogen Energy 2019.

https://doi.org/10.1016/j.ijhydene.2019.11.069.

[66] Ranut P, Nobile E, Mancini L. High resolution X-ray microtomography-based CFD simulation for the characterization of flow permeability and effective thermal conductivity of aluminum metal foams. Exp Therm Fluid Sci 2015;67:30–6. https://doi.org/10.1016/j.expthermflusci.2014.10.018.

[67] Gao Y, Zhang X, Rama P, Liu Y, Chen R, Ostadi H, et al. Calculating the Anisotropic Permeability of Porous Media Using the Lattice Boltzmann Method and X-ray Computed Tomography. Transp Porous Media 2012;92:457–72. https://doi.org/10.1007/s11242-011-9914-7.

[68] Ostadi H, Rama P, Liu Y, Chen R, Zhang XX, Jiang K. Influence of threshold variation on determining the properties of a polymer electrolyte fuel cell gas diffusion layer in X-ray nano-tomography. Chem Eng Sci 2010;65:2213–7. https://doi.org/10.1016/j.ces.2009.12.019.

[69] Espinoza M, Sundén B, Andersson M, Yuan J. Analysis of porosity and tortuosity in a 2D selected region of solid oxide fuel cell cathode using the lattice boltzmann method. ECS Trans 2015;65:59–73. https://doi.org/10.1149/06501.0059ecst.

[70] Mayken Espinoza*,†, Martin Andersson JY and BS. Compress effects on porosity, gas-phase tortuosity, and gas permeability in a simulated PEM gas diffusion layer. Arch Thermodyn 2015;33:23–40. https://doi.org/10.1002/er.

[71] Zamel N, Li X, Becker J, Wiegmann A. Effect of liquid water on transport

properties of the gas diffusion layer of polymer electrolyte membrane fuel cells. Int J Hydrogen Energy 2011;36:5466–78. https://doi.org/10.1016/j.ijhydene.2011.01.146.

[72] Kandlikar SG, Garofalo ML, Lu Z. Water management in a PEMFC: Water transport mechanism and material degradation in gas diffusion layers. Fuel Cells 2011;11:814–23. https://doi.org/10.1002/fuce.201000172.

[73] Poserin V, Marcuson S, Shu J, Wilkinson DS. CVD technique for Inco nickel foam production. Adv Eng Mater 2004;6:454–9. https://doi.org/10.1002/adem.200405142.

[74] Tamayol A, McGregor F, Bahrami M. Single phase through-plane permeability of carbon paper gas diffusion layers. J Power Sources 2012;204:94–9. https://doi.org/10.1016/j.jpowsour.2011.11.084.

[75] Liu J, Wang Y, Song R. A Pore Scale Flow Simulation of Reconstructed Model Based on the Micro Seepage Experiment. Geofluids 2017;2017. https://doi.org/10.1155/2017/7459346.

[76] Nabovati A, Hinebaugh J, Bazylak A, Amon CH. Effect of porosity heterogeneity on the permeability and tortuosity of gas diffusion layers in polymer electrolyte membrane fuel cells. J Power Sources 2014;248:83–90. https://doi.org/10.1016/j.jpowsour.2013.09.061.

[77] ImageJ/Fiji. https://imagej.net/software/fiji/ n.d.

[78] Wohlleben W, Mielke J, Bianchin A, Ghanem A, Freiberger H, Rauscher H, et al.

Reliable nanomaterial classification of powders using the volume-specific surface area method. J Nanoparticle Res 2017;19. https://doi.org/10.1007/s11051-017-3741-x.

[79] Duan DL, Zhang RL, Ding XJ, Li S. Calculation of specific surface area of foam metals using dodecahedron model. Mater Sci Technol 2006;22:1364–8. https://doi.org/10.1179/174328406X111138.

[80] Huo S, Cooper NJ, Smith TL, Park JW, Jiao K. Experimental investigation on PEM fuel cell cold start behavior containing porous metal foam as cathode flow distributor. Appl Energy 2017;203:101–14. https://doi.org/10.1016/j.apenergy.2017.06.028.

[81] August A, Nestler B. About the surface area to volume relations of open cell foams. Eng Res Express 2020;2:15021. https://doi.org/10.1088/2631-8695/ab6ac6.

[82] Ozmat B, Leyda B, Benson B. Thermal applications of open-cell metal foams. Mater Manuf Process 2004;19:839–62. https://doi.org/10.1081/AMP-200030568.

[83] Allioux FM, Merhebi S, Tang J, Idrus-Saidi SA, Abbasi R, Saborio MG, et al. Catalytic Metal Foam by Chemical Melting and Sintering of Liquid Metal Nanoparticles. Adv Funct Mater 2020;30:1–13. https://doi.org/10.1002/adfm.201907879.

[84] Liu PS. A new method for calculating the specific surface area of porous metal

foams. Philos Mag Lett 2010;90:447–53. https://doi.org/10.1080/09500831003745571.

[85] Chen J, Zhang X, Li C, Zhang X, Ren Y, He J, et al. Calculation Method of Specific Surface Area of Foam Metal Based on an Ideal Tetradecahedron Model for Lithium Ion Battery. Int J Photoenergy 2020;2020. https://doi.org/10.1155/2020/2478579.

[86] Okonkwo PC, Otor C. A review of gas diffusion layer properties and water management in proton exchange membrane fuel cell system. Int J Energy Res 2021;45:3780–800. https://doi.org/10.1002/er.6227.

[87] Ahmed DH, Sung HJ, Bae J. Effect of GDL permeability on water and thermal management in PEMFCs-I. Isotropic and anisotropic permeability. Int J Hydrogen Energy 2008;33:3767–85. https://doi.org/10.1016/j.ijhydene.2008.04.024.

[88] Ahmed DH, Sung HJ, Bae J. Effect of GDL permeability on water and thermal management in PEMFCs-II. Clamping force. Int J Hydrogen Energy 2008;33:3786–800. https://doi.org/10.1016/j.ijhydene.2008.04.023.

[89] Cindrella L, Kannan AM, Lin JF, Saminathan K, Ho Y, Lin CW, et al. Gas diffusion layer for proton exchange membrane fuel cells-A review. J Power Sources 2009;194:146–60. https://doi.org/10.1016/j.jpowsour.2009.04.005.

[90] Reshetenko T V., St-Pierre J, Rocheleau R. Effects of local gas diffusion layer gas permeability variations on spatial proton exchange membrane fuel cells

performance. J Power Sources 2013;241:597–607. https://doi.org/10.1016/j.jpowsour.2013.04.131.

[91] Williams M V., Kunz HR, Fenton JM. Influence of Convection Through Gas-Diffusion Layers on Limiting Current in PEM FCs Using a Serpentine Flow Field. J Electrochem Soc 2004;151:A1617. https://doi.org/10.1149/1.1789791.

[92] Gurau V, Bluemle MJ, De Castro ES, Tsou YM, Zawodzinski TA, Mann JA. Characterization of transport properties in gas diffusion layers for proton exchange membrane fuel cells. 2. Absolute permeability. J Power Sources 2007;165:793–802. https://doi.org/10.1016/j.jpowsour.2006.12.068.

[93] Orogbemi OM, Ingham DB, Ismail MS, Hughes KJ, Ma L, Pourkashanian M. On the gas permeability of the microporous layer used in polymer electrolyte fuel cells. J Energy Inst 2018;91:894–901. https://doi.org/10.1016/j.joei.2017.09.006.

[94] Orogbemi OM, Ingham DB, Ismail MS, Hughes KJ, Ma L, Pourkashanian M. Through-plane gas permeability of gas diffusion layers and microporous layer: Effects of carbon loading and sintering. J Energy Inst 2018;91:270–8. https://doi.org/10.1016/j.joei.2016.11.008.

[95] Aldakheel F, Ismail MS, Hughes KJ, Ingham DB, Ma L, Pourkashanian M. Effects of compression on mechanical integrity, gas permeability and thermal stability of gas diffusion layers with/without sealing gaskets. Int J Hydrogen Energy 2021;46:22907–19. https://doi.org/10.1016/j.ijhydene.2021.04.087.

[96] Ismail MS, Hughes KJ, Ingham DB, Ma L, Pourkashanian M. Effects of anisotropic permeability and electrical conductivity of gas diffusion layers on the performance of proton exchange membrane fuel cells. Appl Energy 2012;95:50–63. https://doi.org/10.1016/j.apenergy.2012.02.003.

[97] Neehall ND, Ismail MS, Hughes KJ, Pourkashanian M. Effect of composition and structure of gas diffusion layer and microporous layer on the through-plane gas permeability of PEFC porous media. Int J Energy Res 2021;45:20988–1005. https://doi.org/10.1002/er.7158.

[98] Lee FC, Ismail MS, Ingham DB, Hughes KJ, Ma L, Lyth SM, et al. Alternative architectures and materials for PEMFC gas diffusion layers: A review and outlook. Renew Sustain Energy Rev 2022;166:112640. https://doi.org/10.1016/j.rser.2022.112640.

[99] Orogbemi OM, Ingham DB, Ismail MS, Hughes KJ, Ma L, Pourkashanian M. The effects of the composition of microporous layers on the permeability of gas diffusion layers used in polymer electrolyte fuel cells. Int J Hydrogen Energy 2016;41:21345–51. https://doi.org/10.1016/j.ijhydene.2016.09.160.

[100] Holman JP. Heat Transfer. 10th Ed.,. McGraw-Hill; 2010.

[101] Ismail M. On the Transport Properties of Gas Diffusion Layers used in Proton Exchange Membrane Fuel Cells 2011:34–61.

[102] Miwa S, Revankar ST. Hydrodynamic characterization of nickel metal foameffects of pore structure and permeability. Heat Transf Eng 2012;33:800–

8. https://doi.org/10.1080/01457632.2012.646872.

[103] Hugo J-M, Brun E, Topi F. Metal Foam Effective Transport Properties. Evaporation, Condens Heat Transf 2011. https://doi.org/10.5772/21321.

[104] Oun H, Kennedy A. Experimental investigation of pressure-drop characteristics across multi-layer porous metal structures. J Porous Mater 2014;21:1133–41. https://doi.org/10.1007/s10934-014-9863-y.

[105] Khayargoli P, Loya V, Lefebvre LP, Medraj M. The impact of microstructure on the permeability of metal foams. CSME 2004 Forum 2004;2004:220–8.

[106] Brun E, Vicente J, Topin F, Occelli R, Clifton MJ. Microstructure and transport properties of cellular materials: Representative volume element. Adv Eng Mater 2009;11:805–10. https://doi.org/10.1002/adem.200900131.

[107] Vicente J, Topin F, Daurelle JV. Open celled material structural properties measurement: From morphology to transport properties. Mater Trans 2006;47:2195–202. https://doi.org/10.2320/matertrans.47.2195.

[108] Slade PG. Electrical contacts: principles and applications. CRC press; 2017.

[109] Kopanidis A, Theodorakakos A, Gavaises E, Bouris D. 3D numerical simulation of flow and conjugate heat transfer through a pore scale model of high porosity open cell metal foam. Int J Heat Mass Transf 2010;53:2539–50. https://doi.org/10.1016/j.ijheatmasstransfer.2009.12.067.

[110] Brun E, Vicente J, Topin F, Occelli R. Geometrical measurement of real foams from 3D images. MetFoam 2007 - Proc 5th Int Conf Porous Met Met Foam

2008:425–8.

[111] El-Kharouf A, Mason TJ, Brett DJL, Pollet BG. Ex-situ characterisation of gas diffusion layers for proton exchange membrane fuel cells. J Power Sources 2012;218:393–404. https://doi.org/10.1016/j.jpowsour.2012.06.099.

[112] Lamanna JM, Kandlikar SG. Determination of effective water vapor diffusion coefficient in pemfc gas diffusion layers. Int J Hydrogen Energy 2011;36:5021–9. https://doi.org/10.1016/j.ijhydene.2011.01.036.

[113] Milazzo RG, Privitera SMS, Scalese S, Lombardo SA. Effect of morphology and mechanical stability of nanometric platinum layer on nickel foam for hydrogen evolution reaction. Energies 2019;12. https://doi.org/10.3390/en12163116.

[114] Hellmann A, Pitz M, Schmidt K, Haller F, Ripperger S. Characterization of an open-pored nickel foam with respect to aerosol filtration efficiency by means of measurement and simulation. Aerosol Sci Technol 2015;49:16–23. https://doi.org/10.1080/02786826.2014.990555.

[115] Zhang C, Zhou W, Wang Q, Wang H, Tang Y, Hui KS. Comparison of static contact angle of various metal foams and porous copper fiber sintered sheet. Appl Surf Sci 2013;276:377–82. https://doi.org/10.1016/j.apsusc.2013.03.101.

[116] Serov A, Workman MJ, Artyushkova K, Atanassov P, McCool G, McKinney S, et al. Highly stable precious metal-free cathode catalyst for fuel cell application. J Power Sources 2016;327:557–64. https://doi.org/10.1016/j.jpowsour.2016.07.087.

[117] S. Crosnier, R. Rivam, B. Bador VB. Modeling of gas flow through metallic foams, 1st European Hydrogen Energy Conference, September 2–5, Grenobel, France: 2003, p. 1–15.

[118] Tsolas N, Chandra S. Forced convection heat transfer in spray formed copper and nickel foam heat exchanger tubes. J Heat Transfer 2012;134:1–10. https://doi.org/10.1115/1.4006015.

[119] Gostick JT, Fowler MW, Pritzker MD, Ioannidis MA, Behra LM. In-plane and through-plane gas permeability of carbon fiber electrode backing layers. J Power Sources 2006;162:228–38. https://doi.org/10.1016/j.jpowsour.2006.06.096.

[120] Martínez-Rodríguez MJ, Cui T, Shimpalee S, Seraphin S, Duong B, Van Zee JW. Effect of microporous layer on MacMullin number of carbon paper gas diffusion layer. J Power Sources 2012;207:91–100. https://doi.org/10.1016/j.jpowsour.2012.01.132.

[121] Yang W, Yang S, Sun W, Sun G, Xin Q. Nanostructured silver catalyzed nickel foam cathode for an aluminum-hydrogen peroxide fuel cell. J Power Sources 2006;160:1420–4. https://doi.org/10.1016/j.jpowsour.2006.02.015.

[122] Langlois S, Coeuret F. Flow-through and flow-by porous electrodes of nickel foam. II. Diffusion-convective mass transfer between the electrolyte and the foam. J Appl Electrochem 1989;19:51–60. https://doi.org/10.1007/BF01039389.

[123] Medraj M, Baril E, Loya V, Lefebvre LP. The effect of microstructure on the permeability of metallic foams. J Mater Sci 2007;42:4372–83. https://doi.org/10.1007/s10853-006-0602-x.

[124] Miwa S, Revankar ST. Hydrodynamic Characterization of Nickel Metal Foam, Part 2: Effects of Pore Structure and Permeability. Transp Porous Media 2011;89:323–36. https://doi.org/10.1007/s11242-011-9773-2.

[125] Ismail MS, Damjanovic T, Ingham DB, Ma L, Pourkashanian M. Effect of polytetrafluoroethylene-treatment and microporous layer-coating on the in-plane permeability of gas diffusion layers used in proton exchange membrane fuel cells. J Power Sources 2010;195:6619–28. https://doi.org/10.1016/j.jpowsour.2010.04.036.

[126] Holzer L, Pecho O, Schumacher J, Marmet P, Stenzel O, Büchi FN, et al. Microstructure-property relationships in a gas diffusion layer (GDL) for Polymer Electrolyte Fuel Cells, Part I: effect of compression and anisotropy of dry GDL. Electrochim Acta 2017;227:419–34. https://doi.org/10.1016/j.electacta.2017.01.030.

[127] Flückiger R, Freunberger SA, Kramer D, Wokaun A, Scherer GG, Büchi FN. Anisotropic, effective diffusivity of porous gas diffusion layer materials for PEFC. Electrochim Acta 2008;54:551–9. https://doi.org/10.1016/j.electacta.2008.07.034.

Chapter 4

X-ray CT-based Numerical Investigation of Nickel Foam-based GDLs under Compression

4.1 SUMMARY

Nickel foams feature superior structural and transport characteristics and are therefore strong candidates to be used as gas diffusion layers (GDLs) in polymer electrolyte fuel cells (PEFCs). In this chapter, the impact of compression on the key structural and transport properties has been investigated, including employing a specially-designed compression apparatus and X-ray computed tomography. Namely, 20 equally-spaced two-dimensional CT based images and numerical models have been used/developed to investigate the sensitivity of the key properties of nickel foams (porosity, tortuosity, pore size, ligament thickness, specific surface area, gas permeability and effective diffusivity) to realistic compressions normally experienced in PEFCs. Wherever

applicable, the anisotropy in the property has been investigated. One of the notable findings is that, unlike porosity and ligament thickness, the mean pore size was found to decrease significantly with compression. Further, unlike the effective diffusivity, the gas permeability was shown to be highly anisotropic with compression; this fact is of particular importance for PEFC modelling where the properties of GDLs are often assumed isotropic. In addition, all the computationally-estimated properties have been presented, validated and discussed in this chapter.

4.2 INTRODUCTION

The polymer electrolyte fuel cell (PEFC) is an electrochemical device that directly converts chemical energy into electrical energy [1–4]. The PEFC is a highly promising technology that could be utilised in the automotive industry due to its higher efficiency, quiet operation, fast refuelling and zero-emission at the point of use [5–10]. Consequently, in recent decades, PEFC-powered vehicles have attracted much attention from researchers and industries [11–15]. Despite the early deployment stage of the PEFC technology, many technical barriers concerning the performance, reliability, durability and low cost need to be addressed [16–18].

A wet-proof, porous layer between the flow-field plate and catalyst layer is termed as the gas diffusion layer (GDL). The GDL plays a prominent role inside the PEFC in terms of being the exchange medium of mass, charge and heat between the catalyst layer and the flow channels grooved in the flow-field plate. The GDL should ideally: (i) provide sufficient air/oxygen gases to the active areas in the catalyst layers, (ii) ease the removal

of the excess water, (iii) facilitate charge and heat transfer between the catalyst layer and flow-field plate and (iv) mechanically support the membrane [19–26]. The most commonly-used GDLs are prevalently of carbon paper or carbon cloth forms [27–30]. However, these traditional GDLs, particularly those used at the cathode side, are in general vulnerable to various types of degradation including: mechanical degradation (due to the clamping pressure), thermal degradation (due to freeze/thaw cycles), carbon dissolution and erosion [31–34]. These degradations negatively affect the PEFC performance and the durability. Mechanical degradation is the most commonly type of degradation the GDL is subject to as its carbon fibres experience breakage, cracks and permanent deformation as a result of the assembly compression, thus leading to potential deterioration of the structural integrity of the GDL and reduced transport properties [35–39]. Hence, many researchers have been seeking alternative materials for the GDLs.

Metal foams have attracted a good deal of attention as promising materials used in various components in a multitude of energy engineering applications [40–42]. Recent studies have reported that nickel foam is a propitious material for cathode flow field plates (FFP) and/or GDLs due to its superior properties such as: high porosity, excellent electrical and thermal conductivity, high cost-effectiveness, low weight-to-volume ratio and robust architecture. Hence, there have been only a few demonstrations in which the performance of the fuel cell equipped with nickel foam FFP has been compared to that of the conventional graphite FFP [43–51]. For instance, Tseng et al. [44] experimentally reported that the PEFC running with the nickel foam FFPs outperformed

that running with the conventional FFPs and this is due to their superior mass transport properties of the former FFPs. Similarly, Liu et al. [49] experimentally showed that the fuel cell with a compressed nickel foam-based cathode FFP has a higher peak power density than that with a conventional graphite FFP, thus proposing nickel foam as a replacement material to graphite for FFPs. Furthermore, Tabe et al. [50] experimentally investigated the nickel foam-based FFP and their results indicated that nickel foam-based cathode FFP has, compared to the conventional FFPs, superior drainage ability and the fuel cell operating with it featured more stable operation at the higher current densities.

The performance of a PEFC is directly related to the structural and effective transport properties of the GDL materials. Thus, it has become indispensable to accurately determine these GDL properties and understand how they impact the operation behaviour of the PEFC under various operational conditions [52–55]. Moreover, the anisotropic nature of the GDLs must be assessed while the structural and transport properties are evaluated [36,56,57]. The structural and transport properties of the GDL might considerably differ between the through-plane and in-plane directions owing to the interior architecture of the material. To this end, numerous ex-situ methods are used to determine the structural properties of GDLs. For example, mercury intrusion porosimetry (MIP) is widely used to estimate the porosity and the pore size distribution of the GDLs [1,56,58]. Furthermore, the scanning electron microscope (SEM) is used to image the surface of the GDL to measure, for example, the fibre thickness [19]. The Brunauer-Emmett-Teller (BET) absorption technique is used to determine the specific

surface area of the GDL [59,60]. Most of the above characterisation techniques are either destructive (e.g. focused ion beam) or do not provide insights into the interior structure of the GDLs. To illustrate, SEM typically provides high-resolution images; however, these images are only two-dimensional and superficial [40].

X-ray computed tomography (CT) is a highly versatile technique to provide detailed insight into the nano- or micro-scale morphological and transport characteristics of the PEFC components, including GDLs. The main advantages of X-ray CT are that it is: (i) non-destructive, (ii) relatively fast and accurate, (iii) cost-effective, (iv) available for a wide variety of sample sizes and (v) allowing for investigation under the realistic operation conditions [61–63]. The commercial carbon-based GDLs have been widely investigated using the X-ray CT method to resolve the interior structure of the GDL [64–70]. This method has also been employed to understand the GDL structural properties under realistic fuel cell compression. For example, Zenyuk et al. [71] comprehensively investigated the morphological structures of various types of carbon-based GDLs (TGP, SGL, MRC and Freudenberg) by using X-ray CT tomography under compression. They evaluated the porosity, tortuosity, and pore size distribution under varying compression ratios; the researchers can then use these morphological into their numerical PEFC models. Similarly, Je et al. [72] investigated a Toray GDL using a compression apparatus hosted in an X-ray CT system. The porosity of the uncompressed GDL was found to decrease 0.79 by about 30% to be 0.56 with about 52% compression ratio. In addition, X-ray CT has been used to investigate the impact of compression on the nickel foam-based flow field fields used in PEFCs. For instance, Fly et al. [73] examined nickel foam

as a flow field plate under different compression ratios using X-ray CT and finite element analysis. They showed that the fuel cell peak power density increased by 42% when increasing the compression from 20% to 70%. This improvement is because the penetration of nickel foam ligaments into the GDL increases with compression, thus allowing for more convective flow to reach the catalyst layer and better electrical contact between the nickel foam FFP and each of the GDL and the stainless-steel plate. Likewise, Wu et al. [74] investigated the nickel foam-based flow field plates under compression using X-ray CT. Their findings showed that the mean pore size decreased considerably with increasing compression ratios (6%, 37%, and 69%), while the porosity decreased insignificantly. Moreover, it was shown that the increased compression caused a higher pressure drop, higher airflow through the nickel foam and subsequently better removal of excess liquid water. In addition, the peak power density was found to be maximum with 37% compression ratio (853 mW/cm^2) and minimum with 6% compression (568 mW/cm^2).

To the best of my knowledge, there have been no studies investigating the impact of compression (that is normally encountered in operating PEFCs) on the structural and transport properties of nickel foam based using a non-distractive technique of X-ray CT. The above mentioned conventional characterisation techniques (e.g. SEM and MIP) cannot be used to determine the properties of the GDL under compression [71]. Ercelik et al. [75] investigated the potential use of nickel foam as a GDL for PEFCs using X-ray CT. They developed computationally-economic X-ray CT image-based two-dimensional models to determinate the key structural and transport properties of the nickel foam-

based GDL. As a valuable and important extension to this investigation, the objective of the present study is to evaluate the structural (the porosity, tortuosity, pore size distribution, ligament thickness distribution, and the specific surface area) and transport (gas permeability and effective diffusivity) of nickel foam based GDLs under compression ratios normally encountered in operating PEFCs. Furthermore, the anisotropic nature of the nickel foam-based GDL under compression is evaluated. To achieve this, a specially designed compression apparatus was manufactured through 3D printing and used in an X-ray CT chamber to image the compressed nickel foam. The X-ray CT-based images are then used to create computationally-economic 2D models.

4.3 METHODOLOGY

4.3.1 Compression Apparatus

A special compression apparatus was designed, manufactured and used inside an X-ray CT chamber (Figure 4.1) in order to investigate the structural and transport properties of the nickel foam based GDL under compressions that the GDL is subject to inside the PEFC. The apparatus parts were designed using SolidWorks® 2015 and manufactured using Ultimaker 2+ Extended® 3D printer (Ultimaker, Cambridge, MA, US). The material for 3D printing was polylactic acid (PLA) which possesses high X-ray radiolucent characteristic. Likewise, nylon M5 bolts, nuts and washers were employed owing to their X-ray transparency properties.

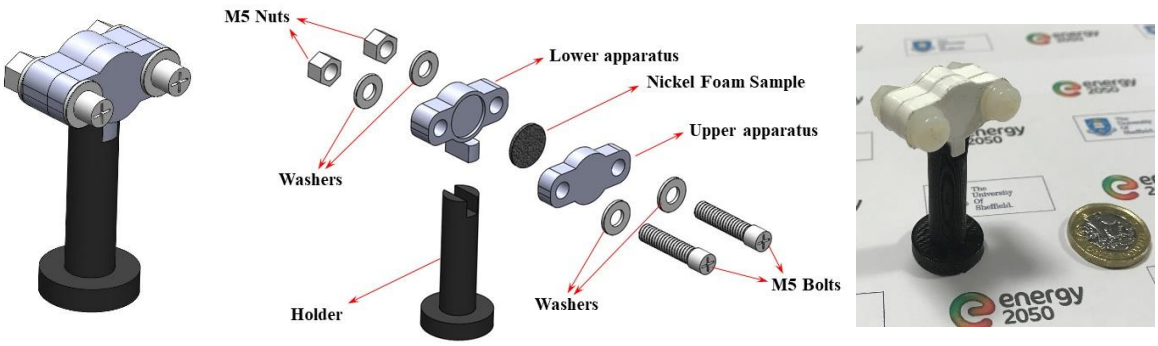

(a) **(b)** **(c)**

Figure 4.1 – (a) The designed compression apparatus, (b) the exploded view and the main components of the apparatus and (c) the manufactured compression apparatus.

4.3.2 X-ray CT and Image Processing

SKYSCAN 1172 (Bruker US) X-ray microscopy system was employed during the X-ray CT imaging process. This system consists of an X-ray source, a detector and a rotational stage where the compression apparatus is fixed. The emitted X-ray from the source traversed through the sample and the detector captured the X-rays weakened due to solid ligaments. Figure 4.2 shows the main components of the X-ray CT system. A commercially available nickel foam sheet with 99.5% purity (Goodfellow, Cambridge Ltd., UK) was punched to create a 12.7 mm diameter sample. The sample was carefully located in the compression apparatus and the apparatus was then fixed on the rotational stage. The scanning processes were performed every time the stage was rotated by 0.7° until the full 180° rotation was reached. The exposure time was 0.885

second and 1025 projections were collected for each scanning. The source voltage was 80 kV, and the beam current was 124 µA. The image resolution was 7 µm per pixel. The compression of the apparatus was increased step by step after each scanning.

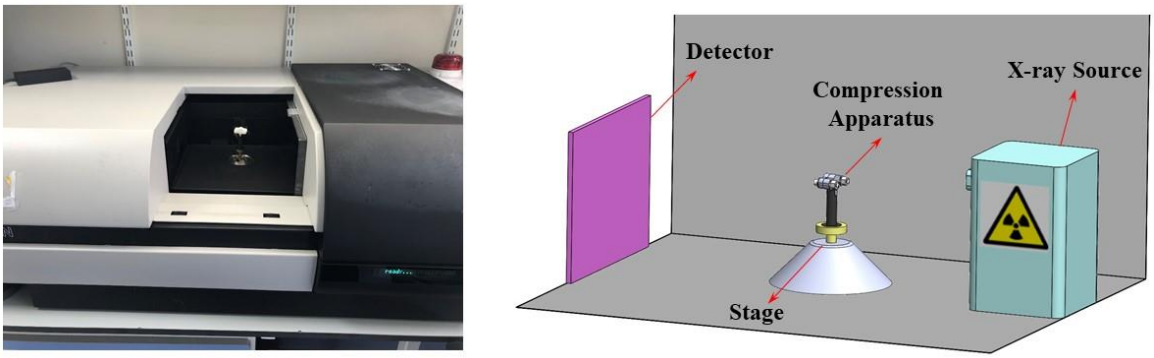

Figure 4.2 – (a) SKYSCAN X-ray CT system and (b) its main components.

The 2D shadow images were obtained and processed using the NRecon Reconstruction software (SKYSCAN, Belgium) to reconstruct the cross-sectional images from the X-ray CT projection images. The images were then processed using Bruker CTan Micro-CT where Otsu's thresholding method was employed to separate the solid and void phases. Finally, the processed images were imported to COMSOL Multiphysics® 5.5 using MATLAB® and LiveLink™ for MATLAB®.

4.3.3 Numerical modelling

The continuity and momentum conservation equations were solved within COMSOL Multiphysics® 5.5 for 20 equally-spaced X-ray CT slices with a 350 µm distance for each compression level of nickel foam. It is noteworthy that the effect of the number of slices (from a range that starts with 5 slices and ends with 30 slides) on the structural and

transport properties of the nickel foam was investigated in the Appendix – IV; see Figures A4.1 to A4.7. It was shown that the values of the structural and transport properties of the nickel foam starts to saturate with 10 equally-spaced X-ray CT slices. Therefore, the selected number of equally-spaced X-ray CT slices (i.e. 20) should be highly representative of the nickel foam material. The length of each slice was 6.65 mm and the height changed depending on the compression applied. Namely, the heights were 1.05, 0.84 and 0.63 mm for 0, 20 and 40% compressions respectively; the 3D X-ray CT-based representations of the nickel foam under the abovementioned compressions are shown in Figure 4.3.

The flow regime in the computational domains was assumed to be steady-state, incompressible (Mach numbers << 0.3) and laminar (Reynolds numbers << 2300). Thereby, the continuity and momentum conservation equations can be given as follows:

$$\nabla \cdot (\rho \boldsymbol{u}) = 0 \qquad \textbf{(4.1)}$$

where ∇ is the operator ($i\frac{\partial}{\partial x} + j\frac{\partial}{\partial y}$), ρ is the fluid density (kg/m^3) and $\boldsymbol{u}$ is the velocity vector.

$$\rho(\boldsymbol{u} \cdot \nabla)\boldsymbol{u} = \nabla \cdot \left[-p\boldsymbol{I} + \mu(\nabla \boldsymbol{u} + (\nabla \boldsymbol{u})^T) - \frac{2}{3}\mu(\nabla \cdot \boldsymbol{u})\boldsymbol{I}\right] \qquad \textbf{(4.2)}$$

where p is the pressure, I is the identity matrix and μ is the dynamic viscosity (Pa·s). The conservation of chemical species, which is oxygen in our case, is expressed as follows:

$$\nabla \cdot (-D_{O2} \nabla C_{O2}) = R \qquad \textbf{(4.3)}$$

where D_{O2} is the oxygen diffusion coefficient (m^2/s), C_{O2} is the oxygen concentration (mol/m^3), and R is the source term which is zero in our case (there is no reaction taking place within the GDL).

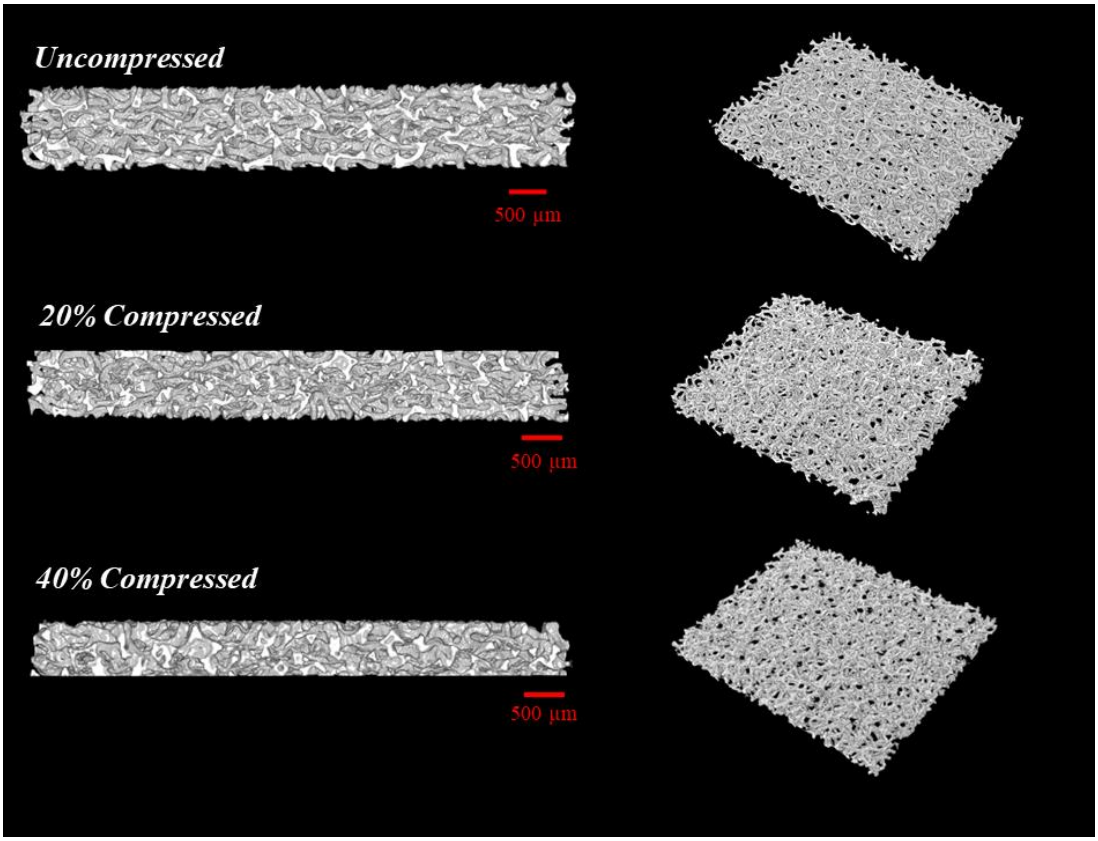

Figure 4.3 – The three-dimensional X-ray CT representations of the nickel foam at 0, 20 and 40% compressions.

The 20 CT slices were meshed within COMSOL Multiphysics® 5.5 at each level of compression. All the computational domains were checked for mesh-independent solutions. Figure 4.4 exhibits how the through- and in-plane gas permeability's (and the corresponding computation time) change with the number of element numbers for an arbitrarily selected 20% compressed slice (the 200th Slice). The computed permeability values were shown to be almost insensitive to the number of elements beyond around

550,000 elements and the corresponding computation times were found to be relatively short: around 100 seconds. Overall, the mesh-independent solutions for all the 20 computational domains were found to be between 400,000 and 700,000; Figure 4.5 shows a typical meshed computational domain along with the boundary conditions used to solve the models.

The gas flowing through the nickel foam was assumed to be air which is the normally-used oxidant at the cathode of the PEFCs. As for the gas permeability investigation, the inlet air velocity and outlet pressure were arbitrarily set as 0.1 m/s and 0 Pa, respectively. Notably, under relatively low flow rates (Darcy's regime), the pressure gradient linearly changes with the inlet air velocity and as such the gas permeability, which is an intrinsic property of the material, evidently does not change with velocity as demonstrated in Figures 4.6 and 4.7 in Section 4.3.5.1. Moving to the effective diffusivity investigation, the inlet air (molar fraction-wise) consists of 21% oxygen and 79% nitrogen. Hence, the inlet concentration of oxygen (C_{in}) is 8.73 mol/m^3 at 20°C and 1 atm whereas the outlet concentration was assumed to be 7.73 mol/m^3. It should be noted that there is no impact of the concentration difference on the estimated effective oxygen diffusivity since the molar flux of oxygen proportionally changes with the concentration difference; see Figure 4.8, and Tables A5.1 and A5.2 in the Appendix-V. The bulk oxygen diffusivity coefficient is 0.219 cm^2/s at 20°C and 1 atm. Equations (4.2) and (4.3) are solved independently for each direction (i.e. through- and in-plane directions) to estimate the gas permeability and effective oxygen diffusivity for each direction.

The boundary conditions used for the models are shown in Figure 4.5. Namely, the top edge was defined as an inlet while the bottom was set as an outlet for the through-plane direction analyses. In addition, the right and the left edges were prescribed as symmetry boundary conditions. On the other hand, the left and the right edges were defined as an inlet and an outlet for the in-plane direction analyses, respectively, whereas the top and the bottom edges were set as walls. Furthermore, the borders surrounding the ligaments were defined as no-slip boundary conditions. It should be noted that the numerical simulations were conducted assuming that the inlet temperature is 20°C. The models were numerically solved using a small-scale workstation (Inter® Xenon® CPU E3-1246 v3@ 3.50 GHz, 16 GB installed RAM), and the computational time for each modelled CT slice was found to be between 100 and 200 s.

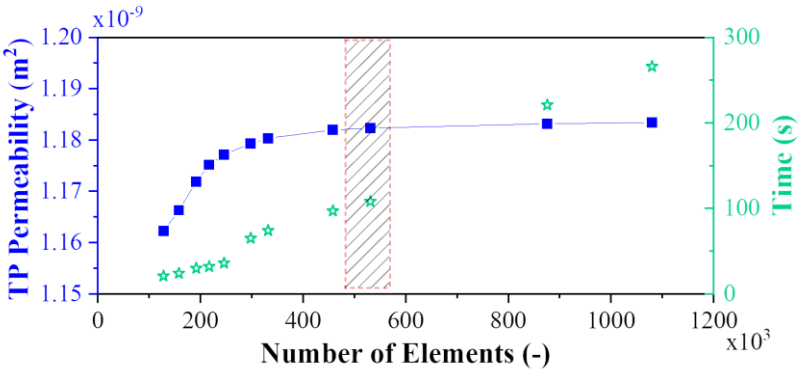

(a)

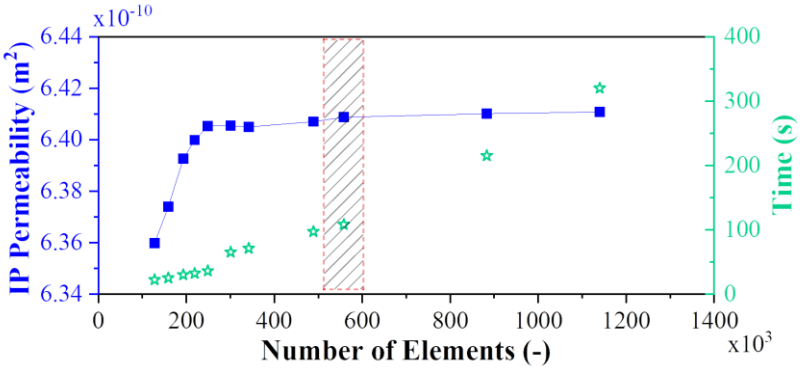

(b)

Figure 4.4 – (a) The through-plane and (a) in-plane permeability's (and the corresponding computation time) as they change with number of elements for a 20% compressed CT slice (the 200th slice). The shaded areas highlights the number of elements with which the mesh-independent solutions are realised.

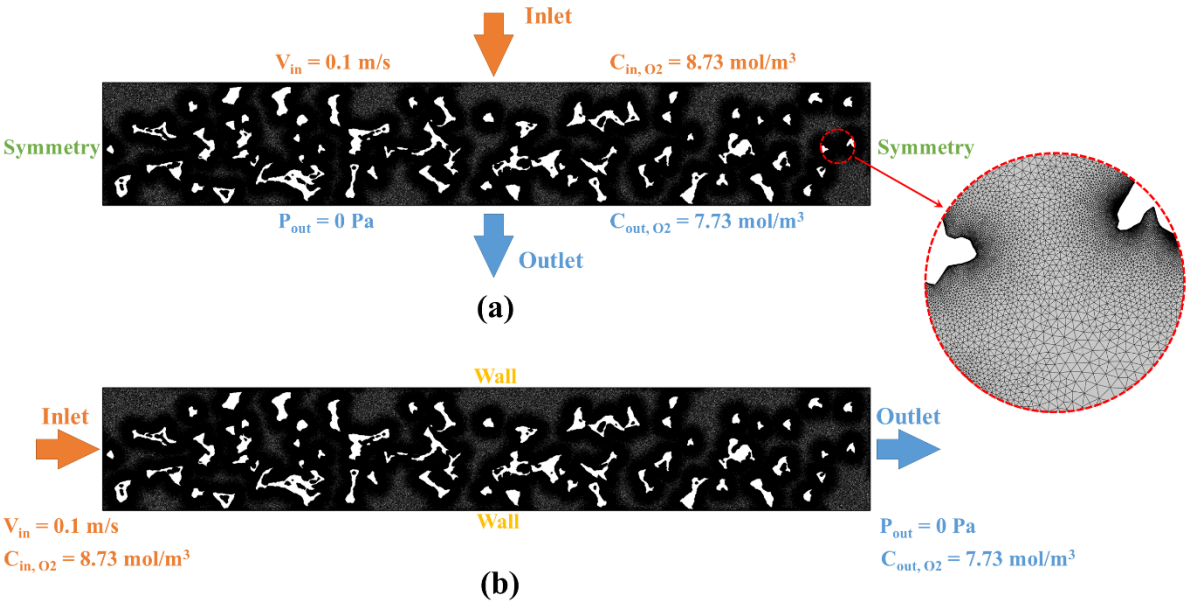

Figure 4.5 – The boundary conditions and the meshed computational domain for (a) through-plane and (b) in-plane directions. The white areas are the solid phase (i.e. the ligaments of the nickel foam).

4.3.4 Structural properties

4.3.4.1 *Porosity*

The porosity (ε) is a structural property of the medium that represents the ratio between the volume of the void and the total volume of that material. The transport properties (e.g. gas permeability and effective diffusivity) strongly depend on the porosity and typically decline with decreasing porosity. On the other hand, the electrical and thermal conductivities are inversely proportional to the GDL porosity. Many experimental methods, such as mercury intrusion porosimetry (MIP) or other standard porosimetry techniques, are normally used to measure the GDL porosity. These methods, nevertheless, may not provide accurate and/or detailed results and this is mainly due the compressible and inhomogeneous structure of the GDL material [71]. Therefore, these techniques are mainly used to measure the GDL porosity for the uncompressed situation; however, the operational fuel cells are assembled with the assistance of a clamping force [71]. On the other hand, the X-ray CT provides insight into the interior structure and inhomogeneity of the GDL with/without realistic compressions. The maximum reported porosity of an uncompressed carbon fibre-based GDL is about 0.90 [1,76], whereas the maximum reported porosity of an uncompressed nickel foam porosity is 0.98 [77]. Evidently, increasing the compression on the GDL decreases its porosity. In this study, the porosity values for a nickel foam-based GDL under three compression ratios were determined for 20 equally-spaced X-ray CT slices using the COMSOL Multiphysics® 5.5. This was achieved

through measuring and summing the areas for each of the void and the solid phases and then dividing the total area of the void phase by the total area of the slice:

$$\varepsilon = \frac{Total\ area\ of\ void\ phases}{Total\ area\ of\ slice} \quad \textbf{(4.4)}$$

For comparison purposes, the porosity was also theoretically calculated using the following equation:

$$\varepsilon_{theo} = \frac{\varepsilon_0 - X_{comp}}{1 - X_{comp}} \quad \textbf{(4.5)}$$

where ε_{theo} is theoretical porosity, ε_0 is the uncompressed porosity, and X_{comp} is the compression ratio of the compressed nickel foam. It should be noted that, in Equation (4.5), it is assumed that only the void that decreases with compression [73].

4.3.4.2 Tortuosity

Tortuosity is a structural characteristic that denotes the ratio of the actual length of the flow path to the straight path between the two ends of that path [78]. In other words, tortuosity equals to unity if the flow path is straight and tortuosity more than unity mean that the flow needs to travel longer distance than that of the fictitious straight path of the flow. Furthermore, the tortuosity provides information on how the pores are interconnected within the porous medium. The tortuosity values for through- and in-plane directions within a two-dimensional CT slice can be obtained using the following equations [79]:

$$\tau_{Through-plane} = \frac{u_{mag}}{u_y} \quad \textbf{(4.6)}$$

$$\tau_{In-plane} = \frac{u_{mag}}{u_x} \qquad \textbf{(4.7)}$$

where u_{mag} is the velocity magnitude averaged over the computational domain, and u_y and u_x are the velocity components in the through- and in-plane directions, respectively.

4.3.4.3 Pore size distribution

The pore size distribution of the nickel foam-based GDL considerably affects the transport properties of reactant gases and liquid water. Large pores within the foam ease the transverse of fluids from one cell to another. The pore size distributions for all the compression cases for all the 20 CT slices were determined using an open-source ImageJ/Fiji software [80]. Unlike SEM images, which only show the superficial morphology, three-dimensional or multiple two-dimensional CT images allow for the access to the interior structure of the compressed/uncompressed porous material.

4.3.4.4 Ligament thickness distribution

Ligaments (or struts) are the solid metal rods that constitute the cellular web-like structure of the nickel foam. The structures and thicknesses of the ligaments could significantly affect the electrical and thermal conductivity and the mechanical integrity of the foam. As with the pore size distribution, the ligament thickness distribution for the all the 20 CT slices under all the investigated three compression ratios were determined using the ImageJ/Fiji software [80].

4.3.4.5 Specific surface area

The specific surface area (SSA) can be defined as the surface area per the volume unit. As with all the structural properties, the specific surface area of the nickel foam impacts the mass, heat and charge transport within it [81,82]. The nickel foam typically possesses a high specific surface area due to its web-like cellular architecture. However, this property expectedly increases with increasing compression [83]. The total length of the borders of the solid phase and its areas were measured for all the 20 CT slices under the three investigated compression ratios using COMSOL Multiphysics®.

4.3.5 Mass transport properties

4.3.5.1 Gas Permeability

The gas permeability represents how permeable the porous media is. It is an important GDL property particularly at the cathode side. High gas permeability leads to lower pressure gradients within the GDL and subsequently lower water saturation, thus mitigating the water flooding phenomena [84–86]. Furthermore, high gas permeability enhances the convective flow from the flow channels to the catalyst layer, the availability of reactant gases and, therefore, the PEFC performance [1,87–89]. The GDLs within the fuel cell are under compression and therefore the transport properties should be quantified under that compression to obtain more accurate values for these transport properties. For this purpose, the through- and in-plane gas permeability for nickel foam under a realistic set of compression ratios were obtained

through solving Equations (4.1) and (4.2) that were applied to the two-dimensional CT-based computational domains. For low velocities, the viscous resistance is dominant and the inertial resistance is negligible. Therefore, the linear Darcy's Law (rather than the quadratic Forchheimer equation) was used to estimate the permeability values of the porous medium:

$$\frac{\Delta P}{L} = \frac{\mu}{K} u \quad \textbf{(4.8)}$$

where ΔP denotes the pressure difference between the inlet and outlet boundaries, L is the length of the GDL material across the flow length, μ is the dynamic viscosity of the flowing fluid (air), K is the gas permeability of the porous medium and u is the inlet gas velocity. L represents the length of the nickel foam GDL (i.e. 6.65 mm) for in-plane gas permeability simulations and represents its thickness (i.e. 1.05, 0.84 and 0.63 mm for 0, 20 and 40% compression ratios) for the through-plane gas permeability simulations. The dynamic viscosity of air (μ) at 20°C and 1 atm is 1.751 x 10^{-5} Pa.s [90]. The inlet velocity of the computational domain (u) has been set as 0.1 m/s for each compression ratio. It is noteworthy that the sensitivity of gas permeability to relatively low inlet gas velocities are almost negligible, as shown in Figure 4.6; this figure shows that the pressure gradient scales linearly with the inlet velocity under different compression ratios. Similarly, Figure 4.7 demonstrates that the gas permeability negligibly changes with inlet velocity under different compression ratios.

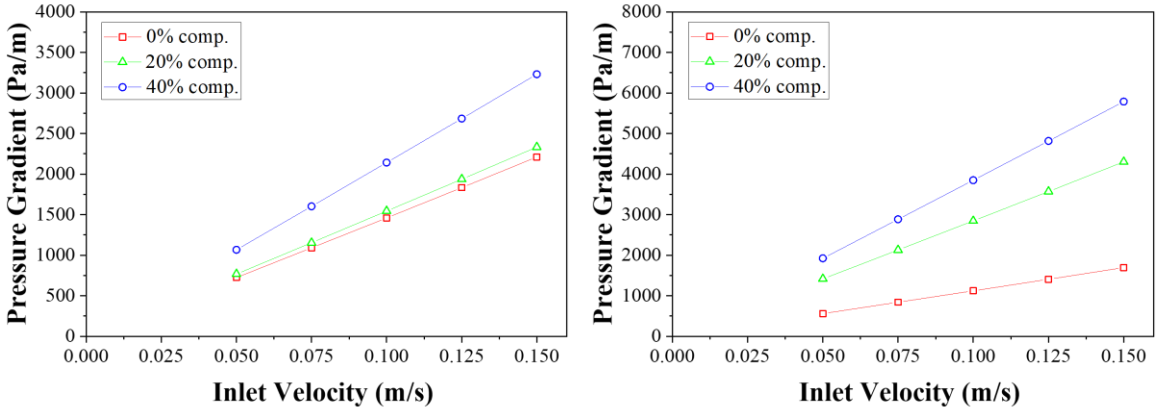

Figure 4.6 – Pressure gradient versus inlet velocity for (a) through-plane and (b) in-plane directions for 0, 20 and 40% compression ratios for the 200th CT slice.

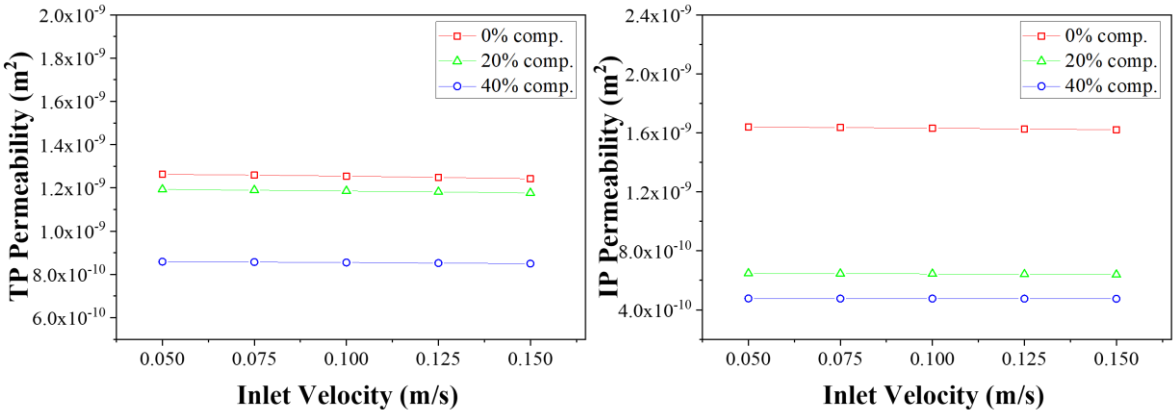

Figure 4.7 – Gas permeability versus inlet velocity for (a) through-plane and (b) in-plane directions for 0, 20 and 40% compression ratios for the 200th CT slice.

4.3.5.2 Effective Diffusivity

Diffusion within the GDL plays a significant role in transporting reactant gases between the flow channel and the catalyst layer; this role is more profound for the conventional carbon fibre-based based GDLs and this is due to their low gas permeability values [20–22,28,88,91,92]. The effective diffusivity represents how chemical species diffuse into each other within a porous medium. The effective diffusivity of oxygen into nitrogen in a porous GDL can be estimated by Fick's Law:

$$J = D_{O2,N2}^{eff} \frac{\Delta C}{L} \quad \textbf{(4.9)}$$

where J is the oxygen molar flux (mol/(m^2·s)), ΔC is the oxygen concentration difference between the inlet and outlet across the thickness (for through-plane diffusivity simulations) or length (for in-plane diffusivity simulations) of the GDL. As with the gas permeability simulations, L is the length of the nickel foam GDL (6.65 mm) for the in-plane diffusivity simulations and is the GDL thickens (i.e. 1.05, 0.84 and 0.63 mm for 0, 20 and 40% compression ratios) for the through-plane diffusivity simulations. The oxygen concentration difference (ΔC) is assumed to be 1 mol/m^3 for each compression scenario. It is noteworthy that (as shown in Table 4.1, Table 4.2, and Figure 4.8) the oxygen concentration difference does not impact the effective diffusivity since the oxygen molar flux changes proportionally with the concentration difference of oxygen.

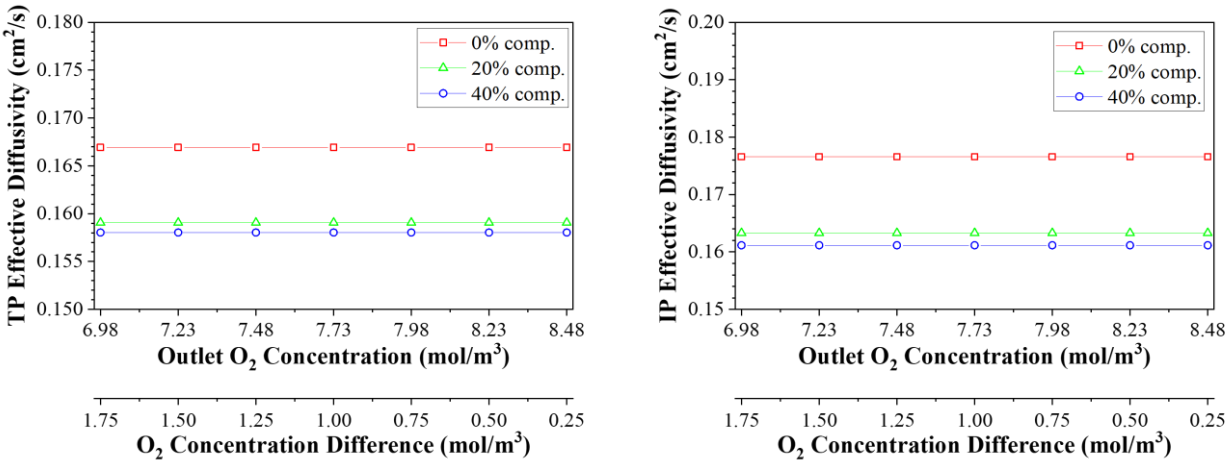

(a) **(b)**

Figure 4.8 – Effective diffusivity of oxygen into nitrogen for (a) through- and (b) in-plane directions for seven different outlet oxygen concentrations (and oxygen concentration differences, ΔC) for 0, 20 and 40% compression ratios for the 200th CT slice.

4.4 RESULTS AND DISCUSSION

The velocity profiles of the flowing air through the uncompressed, 20% compressed, and 40% compressed nickel foam-based GDL are shown in Figures (4.9) and (4.10) for the through- and in-plane directions, respectively. In general, the position and the thickness of the ligaments considerably affect the magnitude of the air velocity and the direction of the flow, resulting in relatively high non-uniform velocity profiles. It is evident from Figures (4.9) and (4.10) that the velocity magnitudes, in either the through- or in-plane directions, become higher as the compression ratio increases. This is understandable due to the fact that the voids between the ligaments are closed up due to the compression resulting in smaller flow openings and subsequently higher local velocities for a given boundary flow rate.

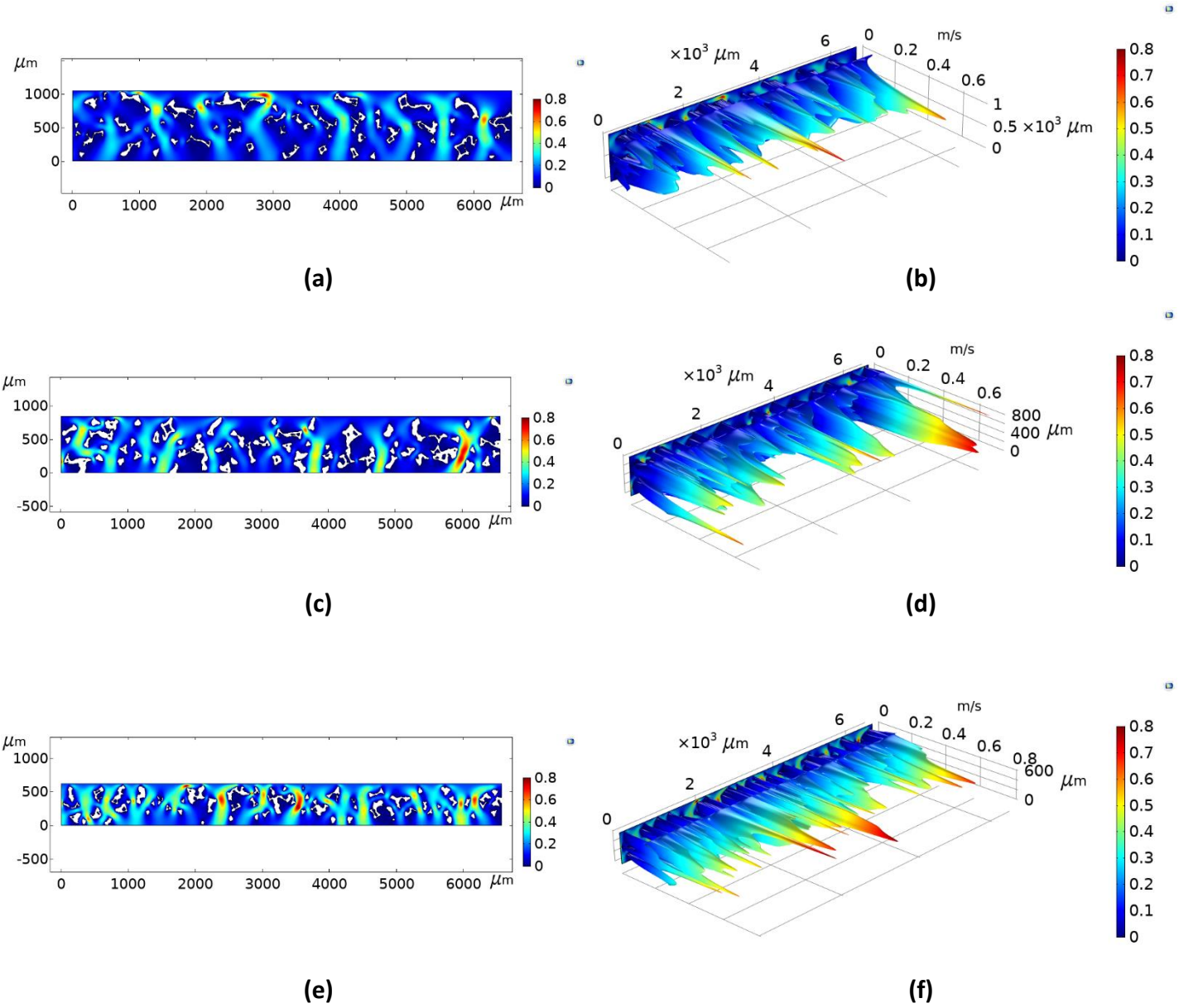

Figure 4.9 – The through-plane velocity profiles for the 100th slice under uncompressed (a and b), 20% compressed (c and d), and 40% compressed (e and f) situations.

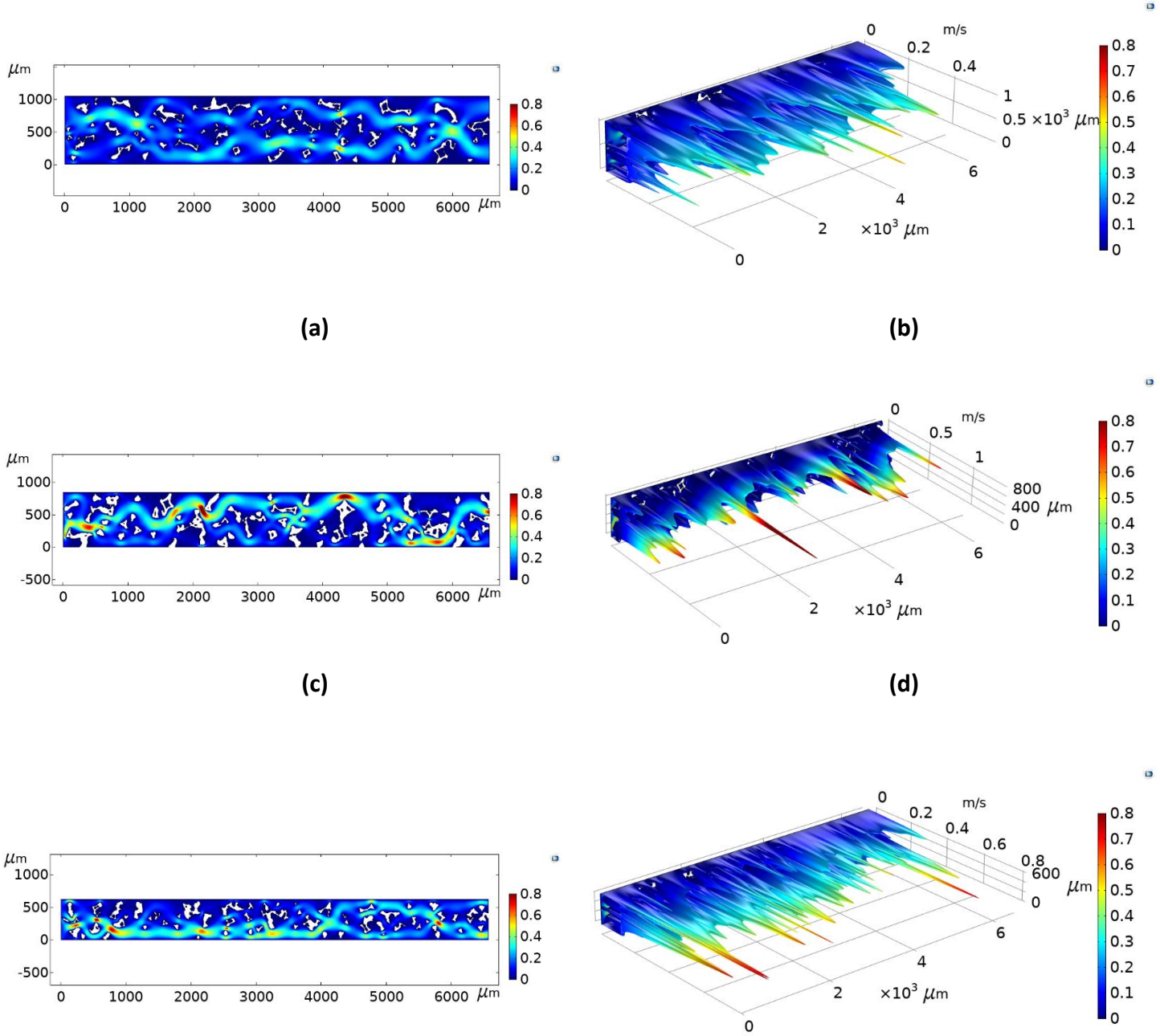

Figure 4.10 – The in-plane velocity profiles for the 100th slice under uncompressed (a and b), 20% compressed (c and d), and 40% compressed (e and f) situations.

4.4.1 Porosity

The porosity values for all the 20 equally-spaced X-ray CT slices are shown in Figure 4.11(a) for three different compression ratios. The mean porosity value for the uncompressed sample is 0.894±0.008 and it varies between 0.861 and 0.921. This value is highly consistent with the experimental results reported in the literature for nickel foam material. For instance, Oun and Kennedy [83] experimentally estimated the porosity of uncompressed nickel foams and found it to be 0.88. The range of porosity for uncompressed nickel foams was investigated utilising 3D X-ray CT imaging by Vicente et al. [93] and was reported to be between 0.87 to 0.92. Clearly, as the compression increases, the porosity of the metal foam decreases. The mean porosity range for 20 % compressed nickel foam is 0.866±0.007 and it varies between 0.84 and 0.90. The porosity continues to slightly decrease with 40% compression and becomes 0.842±0.011 and it varies between 0.799 and 0.883. As with the uncompressed nickel foam case, the results are highly consistent with the porosity values reported in the literature. For example, Fly et al. [73] investigated the nickel foam flow field plates using 3D X-ray CT imaging and reported the porosity for uncompressed, 17% compressed and 35% compressed nickel foams as 0.892, 0.875, and 0.834, respectively.

Furthermore, the actual (obtained from the new X-ray CT-based method) and the theoretical (obtained from Equation (4.5)) porosity of the nickel foam sample are shown in Figure 4.11 (b). It is clear that there is a very good agreement between the actual and the calculated values of the porosity for the uncompressed and 20%

compressed nickel foam cases. However, the theoretical porosity is slightly less than the actual porosity at 40% compression. The reason behind this discrepancy is that Equation (4.5) assumes that the volume reduction of the void only takes place in the open spaces between the ligaments. However, there exists isolated voids between the ligaments that are normally created as a result of the corresponding manufacturing process. The reduction in volume of these isolated voids are not included in Equation (4.5), thus resulting in the underestimation of the porosity of the nickel foam subject to the relatively high compression (i.e. 40%).

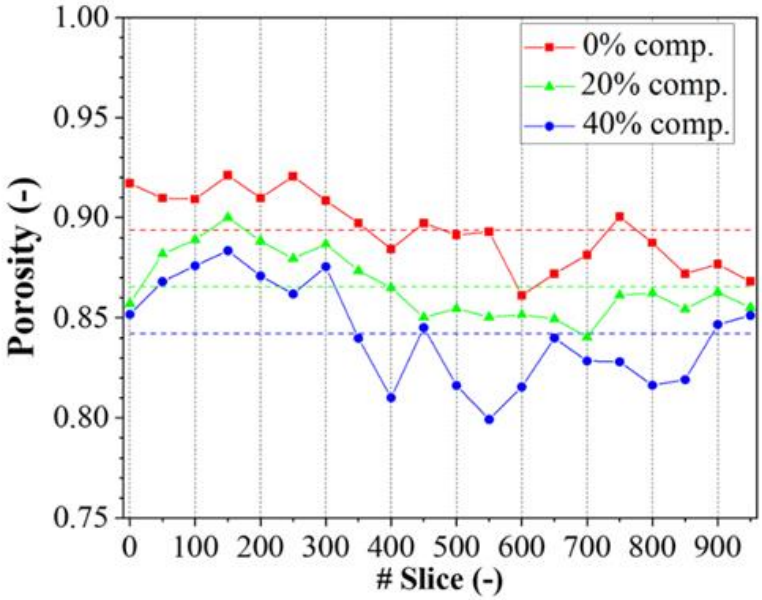

(a)

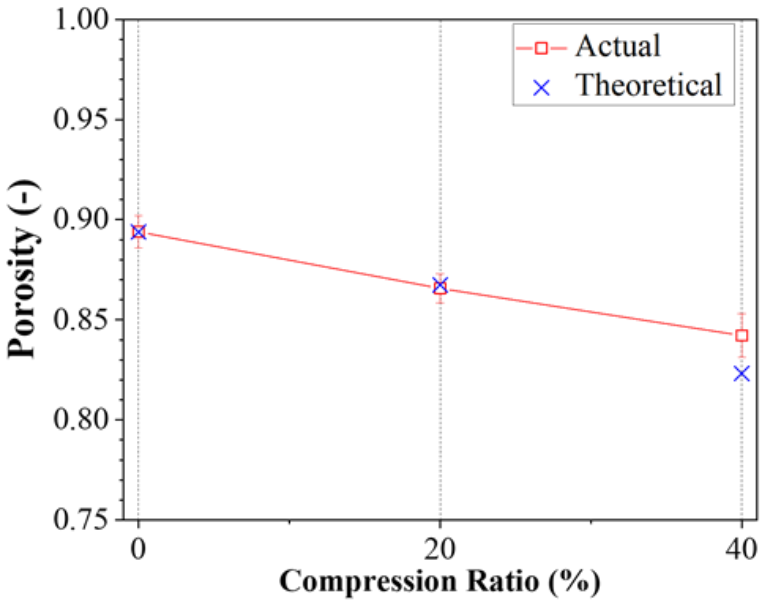

(b)

Figure 4.11 – (a) Porosity values for the uncompressed, 20% compressed, and 40% compressed CT nickel foam slices and (b) the actual and theoretical porosity of nickel foam. Note that the error bars represent 95% confidence intervals.

4.4.2 Tortuosity

The tortuosity in the through- and in-plane directions for all the 20 CT slices are shown in Figure 4.12 for the three investigated compression ratios. The mean through-plane tortuosity for the uncompressed situation is 1.179±0.011. This value is in very good agreement with those reported in the literature: Khayargoli et al. (i.e. 1.15) [94], Ercelik et al. (i.e. 1.175) [75] and Langlois and Coeuret (i.e 1.15±0.10) [95]. The in-plane tortuosity of the uncompressed nickel foam is 1.138±0.011 and therefore is slightly lower than that of the through-plane direction. As with the through-plane tortuosity, the computed in-plane tortuosity of the uncompressed nickel foam is in very good consistence with those reported in the literature, which

were found to be between 1.09 and 1.13 [96]. It should be noted that the tortuosity values of the conventional carbon fibre-based GDLs are considerably higher than those of the nickel foam. For example, the minimum tortuosity values for the SGL and Toray GDLs were reported to be 1.33 and 2.50, respectively [19]. With 20% compression ratio, the mean through- and in-plane tortuosity values, compared to those of the uncompressed foam, increase to 1.20±0.022 and 1.168±0.022, respectively. It is evident that the voids between the ligaments are closed up with increasing compression, thus leading to more tortuous paths throughout the foam. As the compression increases to 40%, the mean values of the through- and in-plane tortuosity become closer to each other: they are 1.184±0.017 and 1.189±0.014, respectively. One may notice that the in-plane tortuosity increases as the compression increases from 0 to 40%; however, the through-plane tortuosity was found to increase as the compression increases from 0 to 20% and then decrease as the compression increases from 20 to 40%. This could be attributed to the observation that the structure of the nickel foam is more or less “nest-like” and therefore the “entanglement” of the ligaments, which is mainly in the in-plane directions, increases with increasing compression. On the other hand, the through-plane pathways appear to straighten after a certain threshold compression.

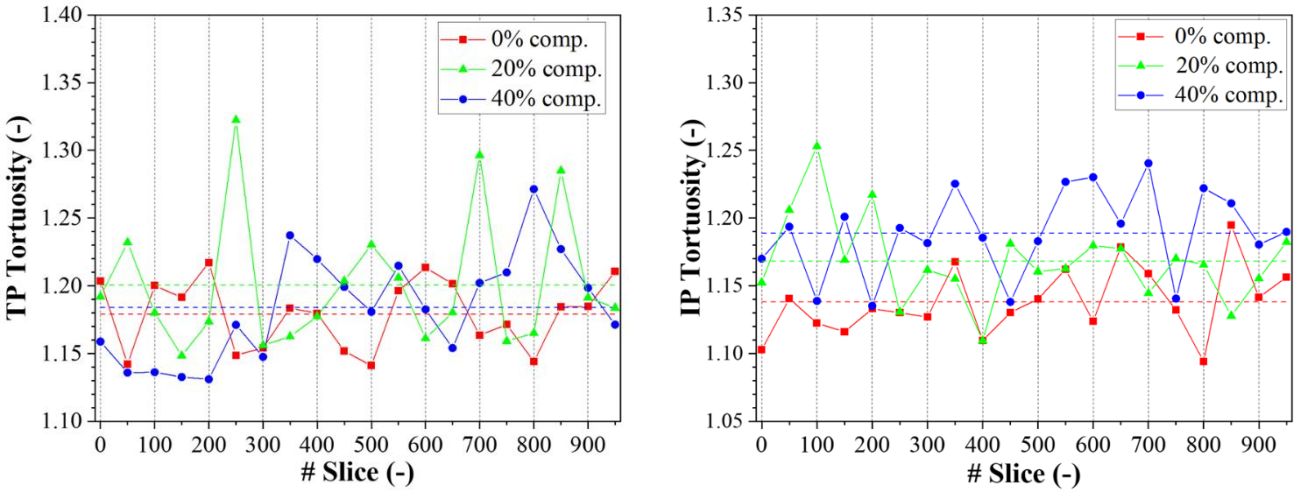

(a) **(b)**

Figure 4.12 – (a) Through-plane and (b) in-plane tortuosity values for the uncompressed, 20% compressed, and 40% compressed CT nickel foam slices.

4.4.3 Pore size distribution

The pore size values for all the 20 CT nickel foam slices are shown in Figure 4.13 for the uncompressed, 20% compressed, and 40% compressed cases. The pore size histograms of all the cases (60 cases representing 20 CT slices and 3 compression ratios) are shown in Figures 4.14 to 4.16. The mean pore size value of the uncompressed nickel foam is 175±5 µm and the range of pore sizes is between 151 and 217 µm. The mean pore size of the uncompressed nickel foam is in very good agreement with those reported in the literature; for example Miwa and Ravankar [97] reported the mean pore size of some nickel foam samples as a range of from 172 µm to 182 µm while Milazzo et al. [98] measured it as 230 µm. The mean pore size and the lower and the upper limits of its range expectedly decrease with increasing compression due to reduction in the volume of voids of the nickel foam. Namely, the

mean pore size, with 20% compression, decrease to 110±4 µm for and the limits of the range decrease to 92 and 119 µm. Likewise, the mean pore size decrease to 71±2 µm and the limits of its range decrease to 55 and 81 µm with 40% compression.

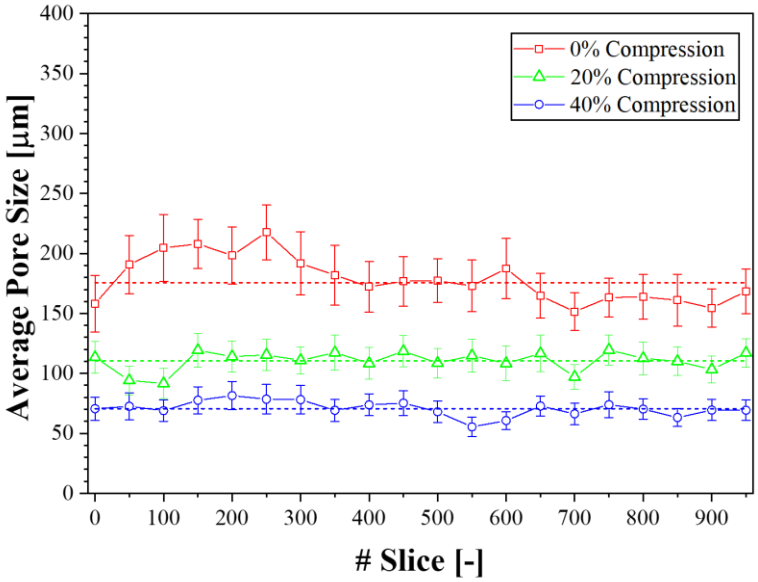

Figure 4.13 – Mean pore size for the uncompressed, 20% compressed, and 40% compressed CT nickel foam slices. Note that the error bars represent 95% confidence intervals.

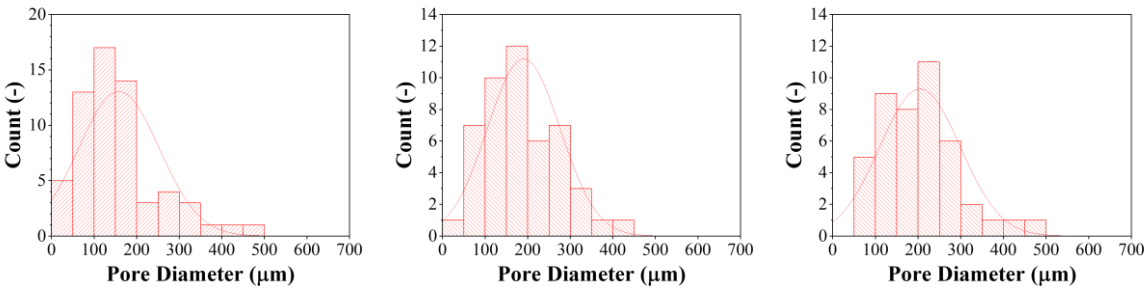

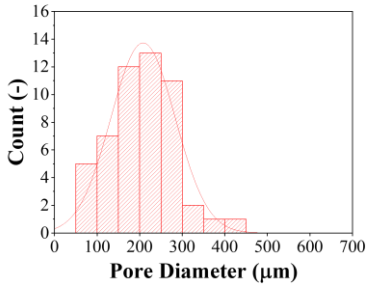

(d)

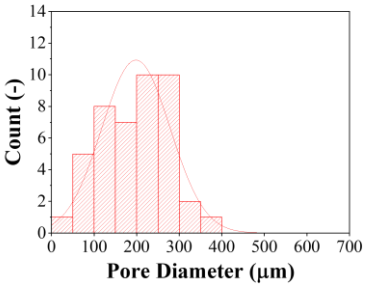

(e)

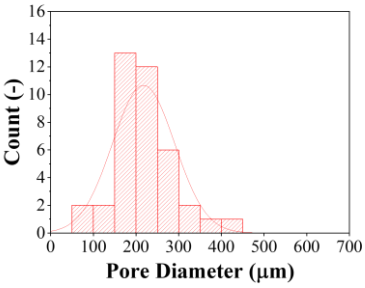

(f)

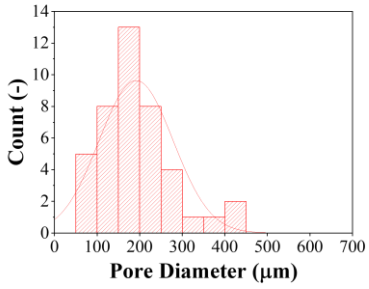

(g)

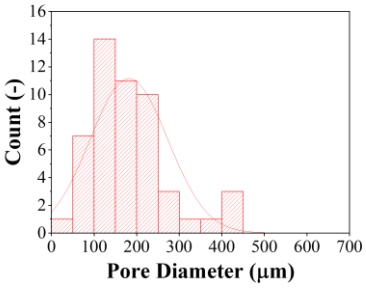

(h)

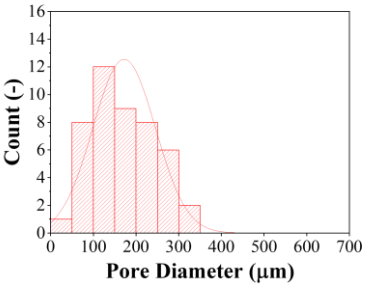

(i)

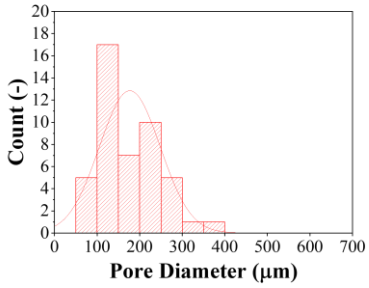

(j)

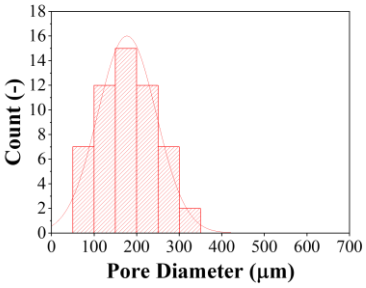

(k)

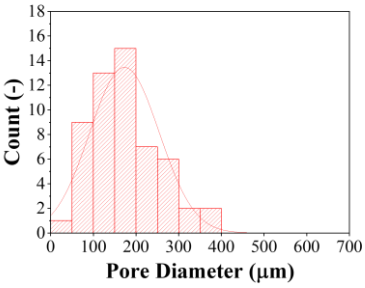

(l)

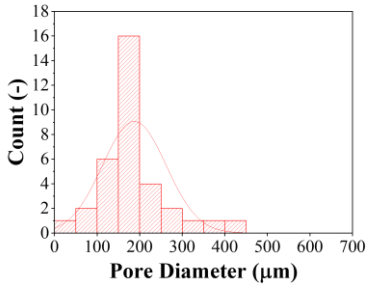

(m)

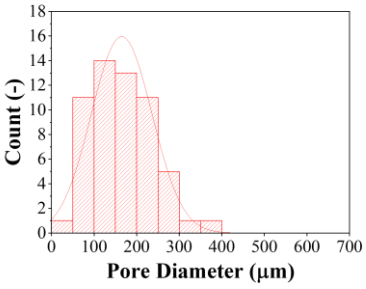

(n)

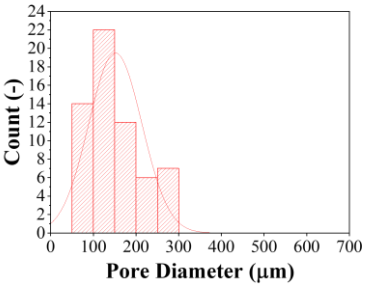

(o)

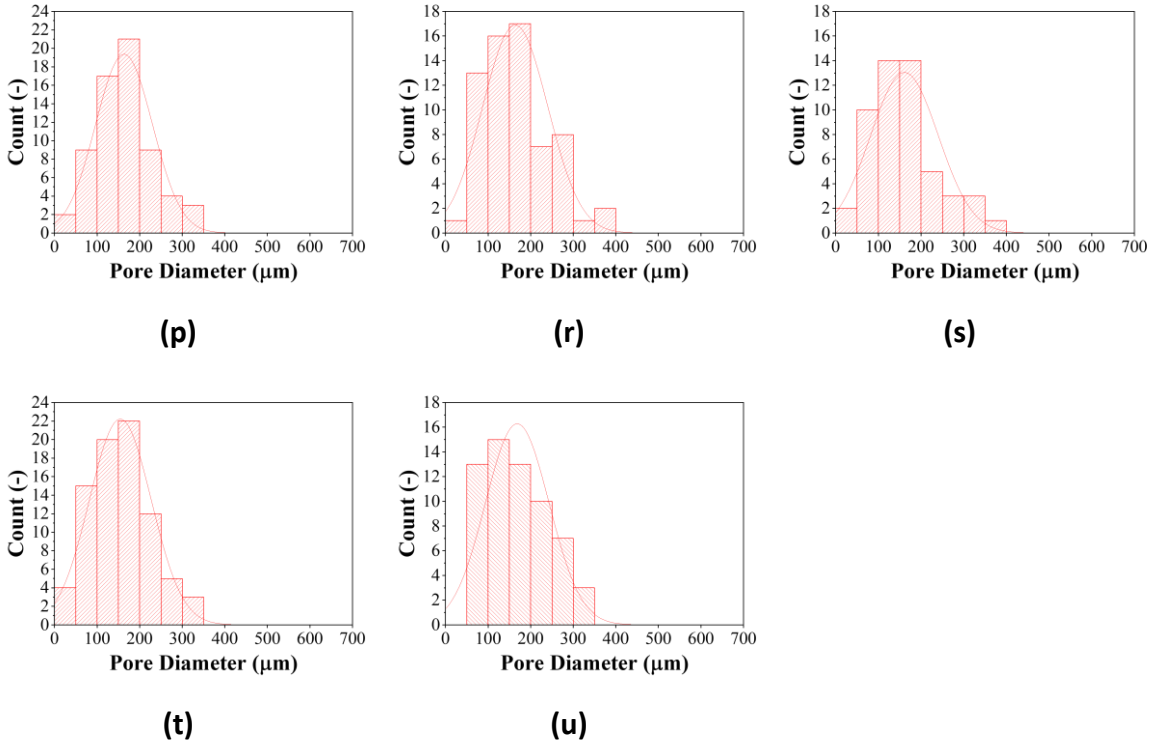

Figure 4.14 – The pore size distribution for the uncompressed nickel foam CT slices numbered as: (a) 0, (b) 50, (c) 100, (d) 150, (e) 200, (f) 250, (g) 300, (h) 350, (i) 400, (j) 450, (k) 500, (l) 550, (m) 600, (n) 650, (o) 700, (p) 750, (r) 800, (s) 850, (t) 900 and (u) 950.

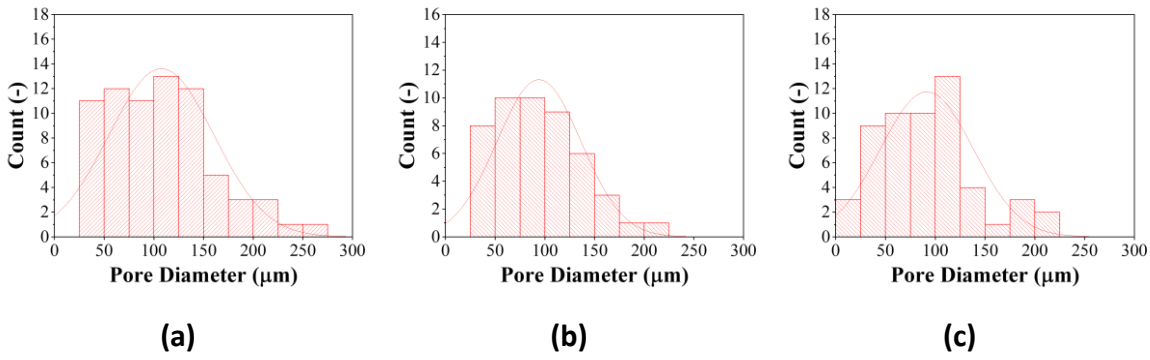

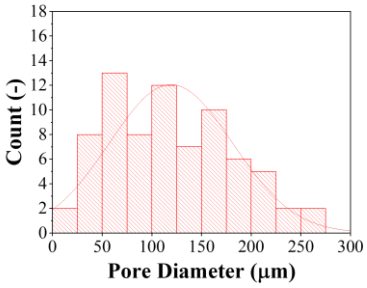

(d)

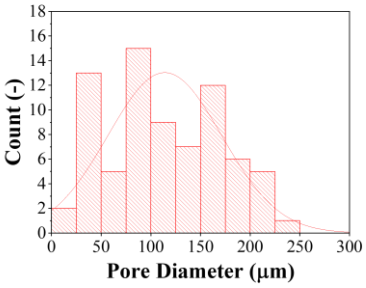

(e)

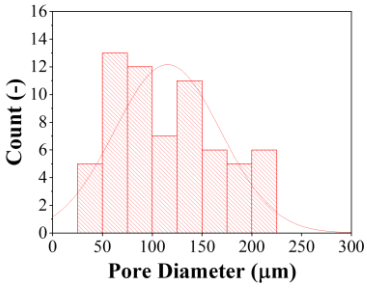

(f)

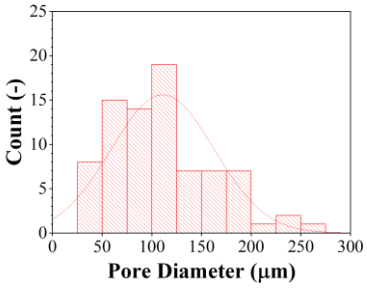

(g)

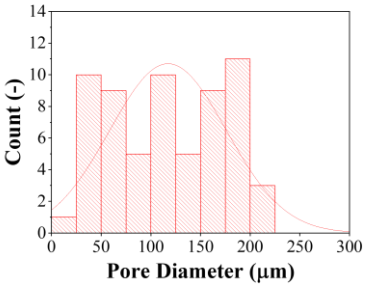

(h)

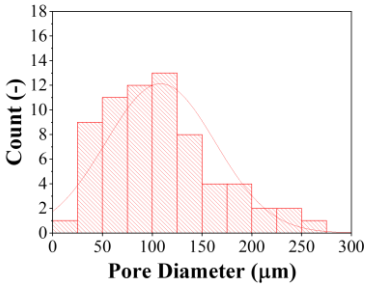

(i)

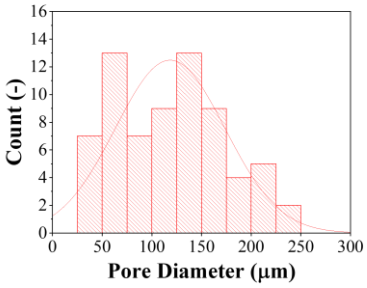

(j)

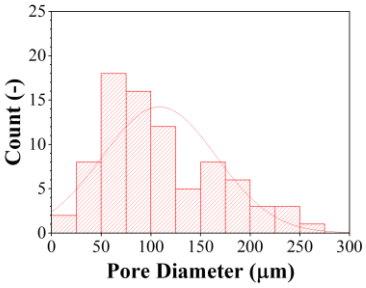

(k)

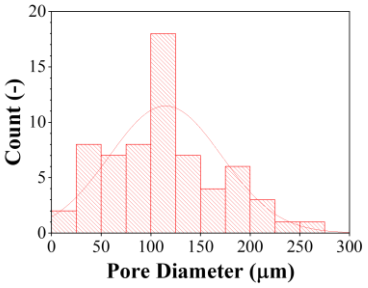

(l)

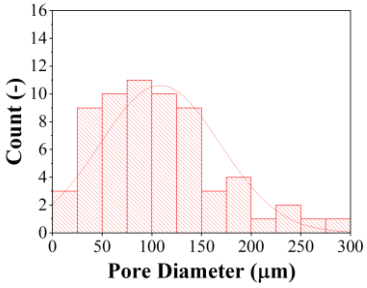

(m)

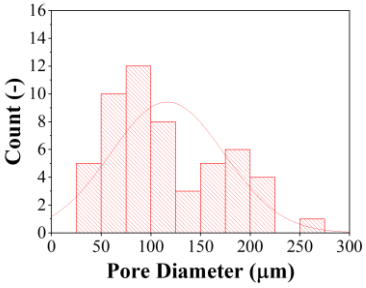

(n)

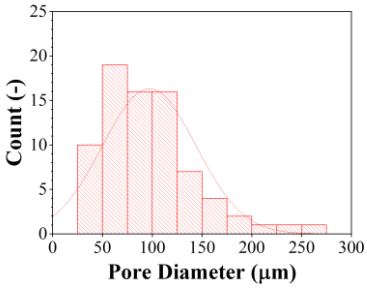

(o)

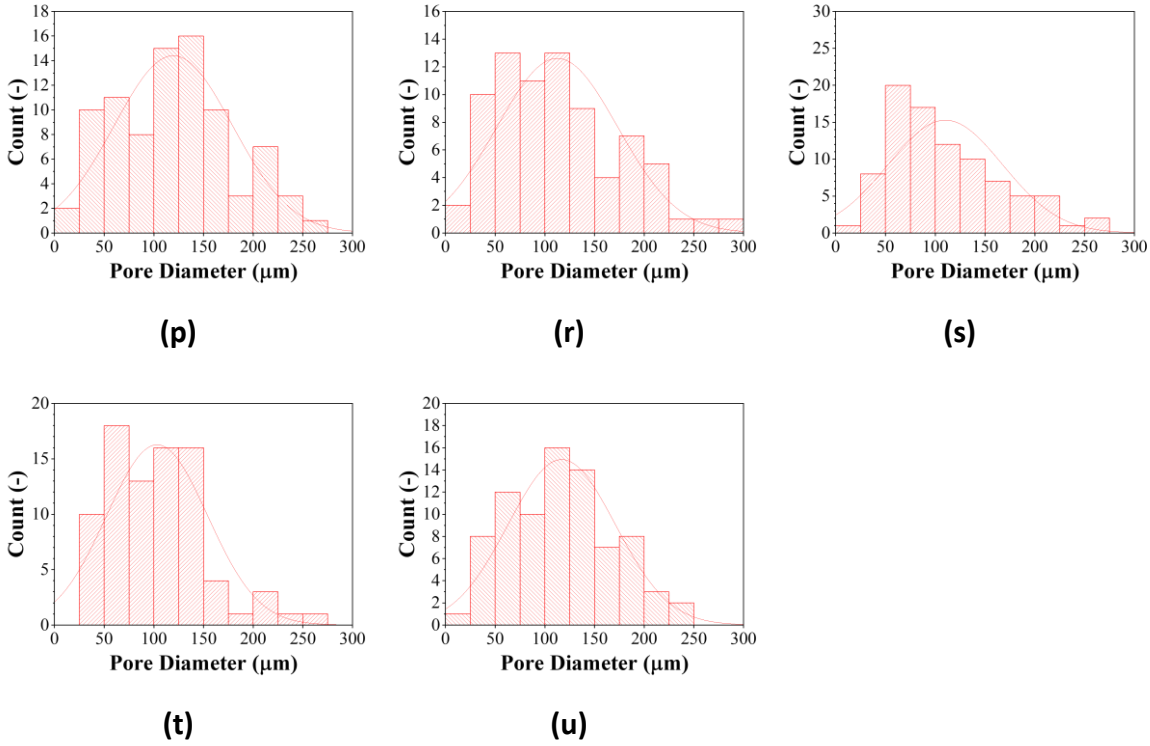

Figure 4.15 – The pore size distribution for the 20% compressed nickel foam CT slices numbered as: (a) 0, (b) 50, (c) 100, (d) 150, (e) 200, (f) 250, (g) 300, (h) 350, (i) 400, (j) 450, (k) 500, (l) 550, (m) 600, (n) 650, (o) 700, (p) 750, (r) 800, (s) 850, (t) 900 and (u) 950.

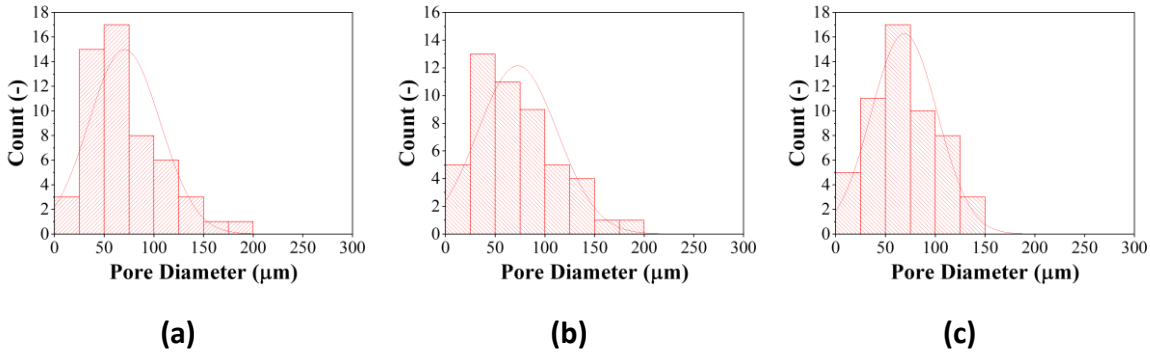

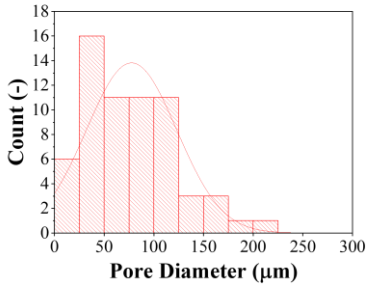

(d)

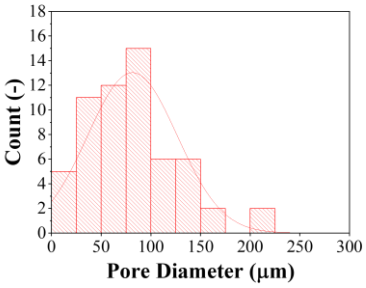

(e)

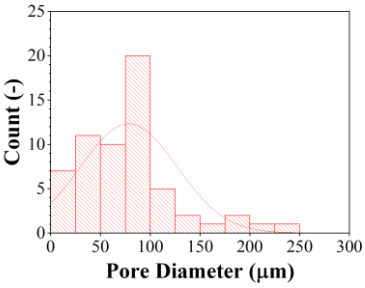

(f)

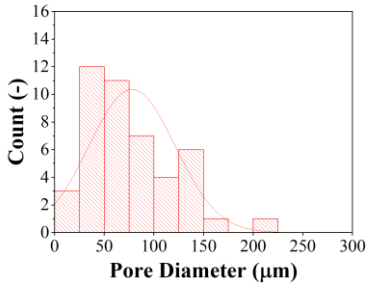

(g)

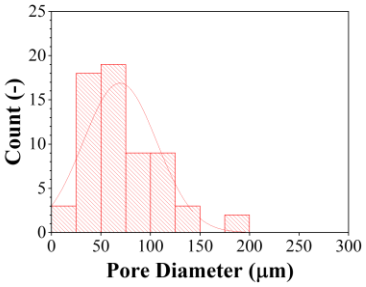

(h)

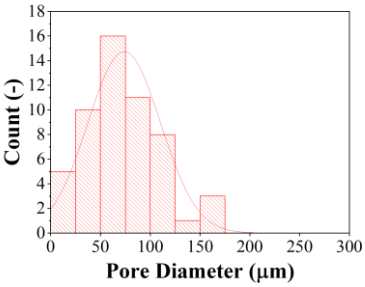

(i)

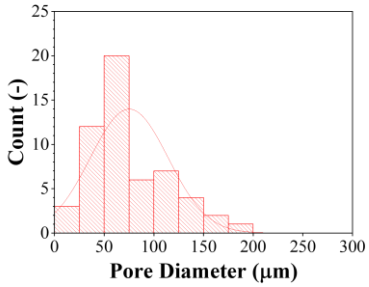

(j)

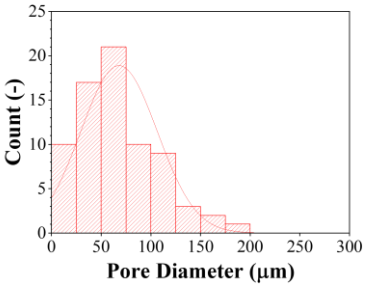

(k)

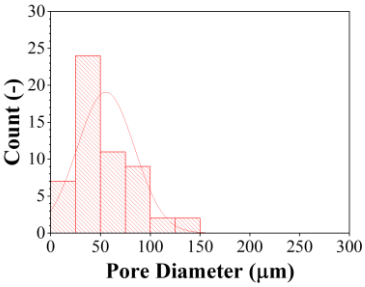

(l)

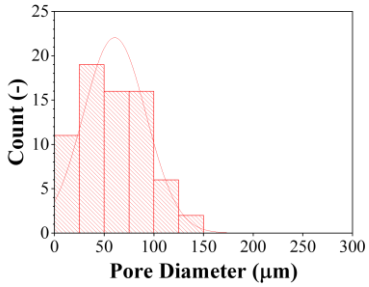

(m)

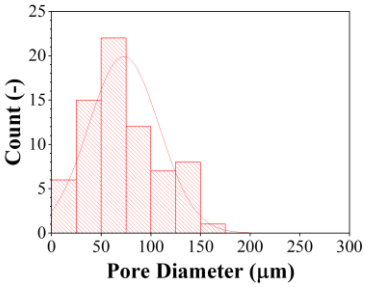

(n)

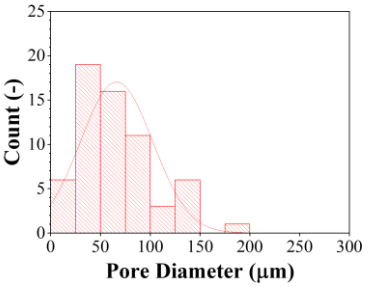

(o)

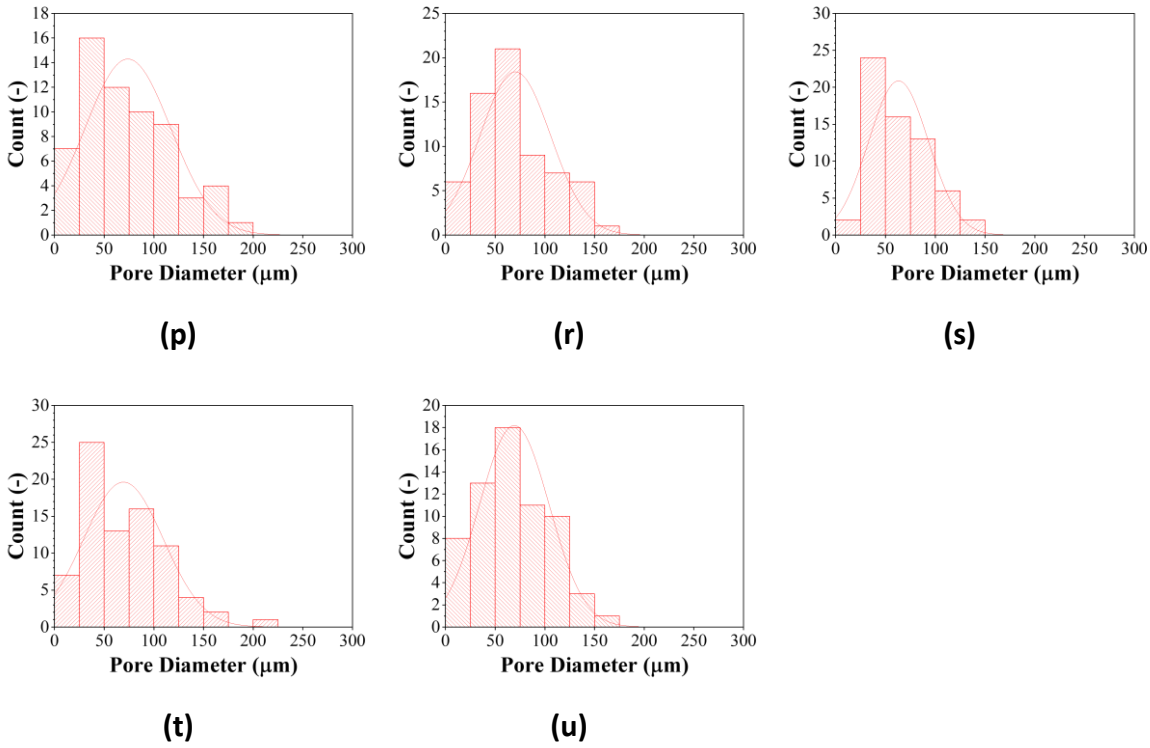

Figure 4.16 – The pore size distribution for the 40% compressed nickel foam CT slices numbered as: (a) 0, (b) 50, (c) 100, (d) 150, (e) 200, (f) 250, (g) 300, (h) 350, (i) 400, (j) 450, (k) 500, (l) 550, (m) 600, (n) 650, (o) 700, (p) 750, (r) 800, (s) 850, (t) 900 and (u) 950.

4.4.4 Ligament thickness distribution

The ligament thickness values for all the 20 CT nickel foam slices are presented in Figure 4.17 for the uncompressed, 20% compressed, and 40% compressed cases. The histograms of the ligament thickness distribution are shown in Figures 4.18 to 4.20. The mean ligament thickness is 100±1 μm for the uncompressed nickel foam, which is in very good agreement with those reported in the literature. For instance, Miwa and Revankar [97] found that the mean ligament thickness of nickel foam is between

99 and 107 µm. Interestingly, the ligament thicknesses were found to significantly decrease with increasing compression; the mean ligament thickness decreases to 96±1 with 20% compression and to 90±1 µm with 40% compression. This is primarily due to the fact that the ligaments are not entirely solid and they enclose some of the void that shrinks as the compression increases.

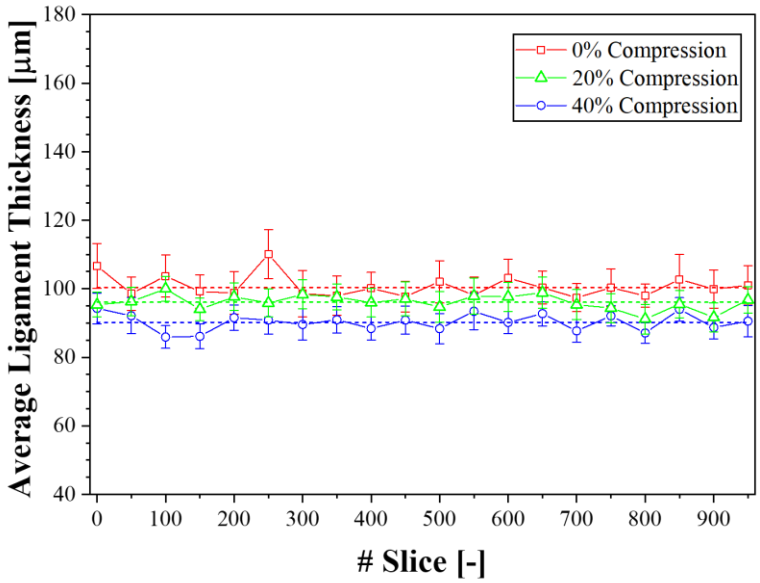

Figure 4.17 – Mean ligament thickness for the uncompressed, 20% compressed, and 40% compressed CT nickel foam slices. Note that the error bars represent 95% confidence intervals.

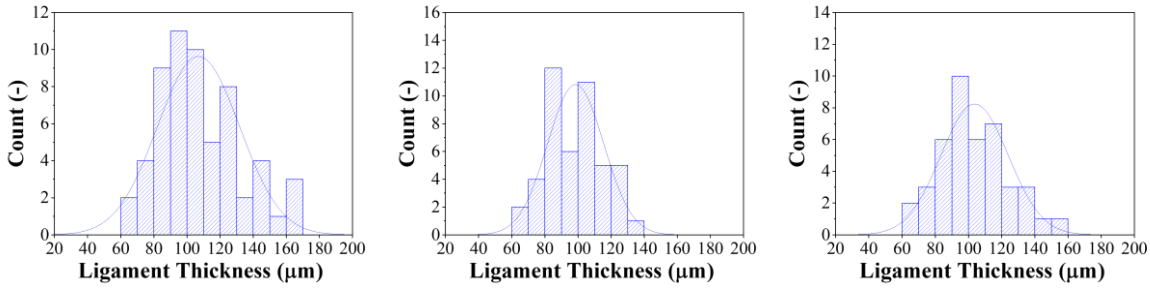

(a) **(b)** **(c)**

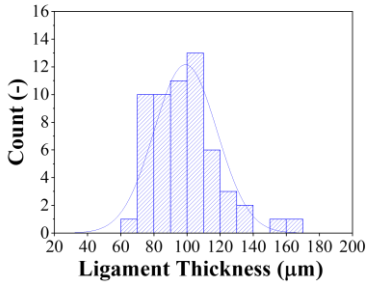

(d)

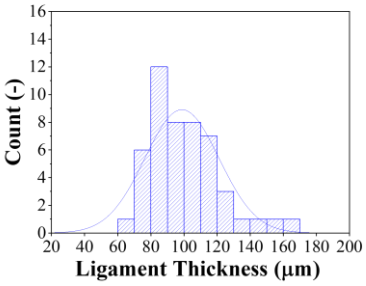

(e)

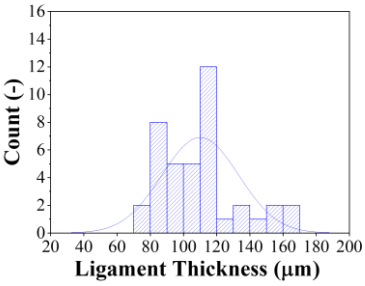

(f)

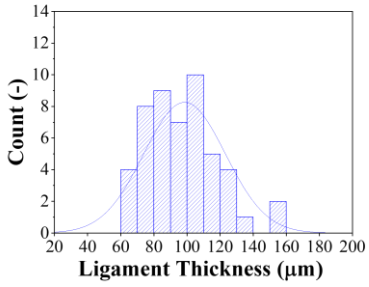

(g)

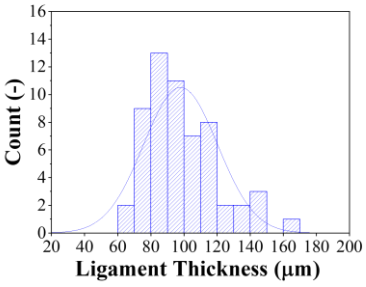

(h)

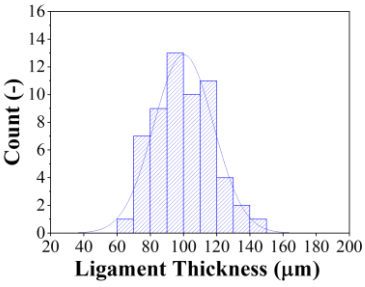

(i)

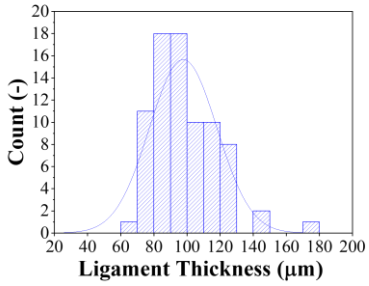

(j)

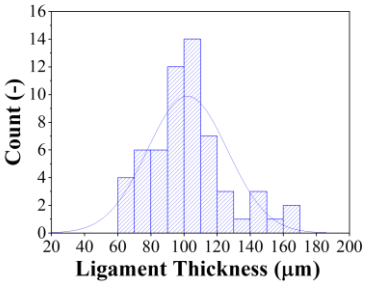

(k)

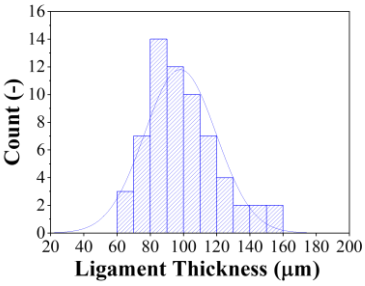

(l)

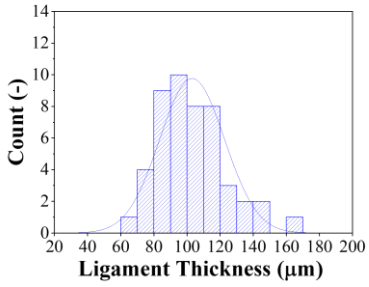

(m)

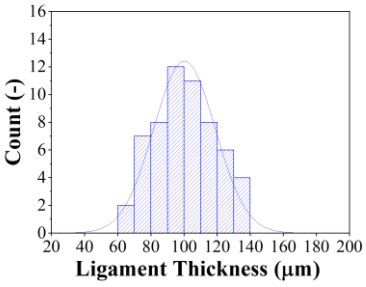

(n)

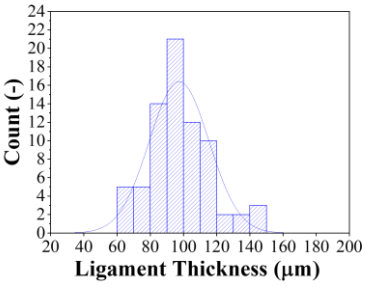

(o)

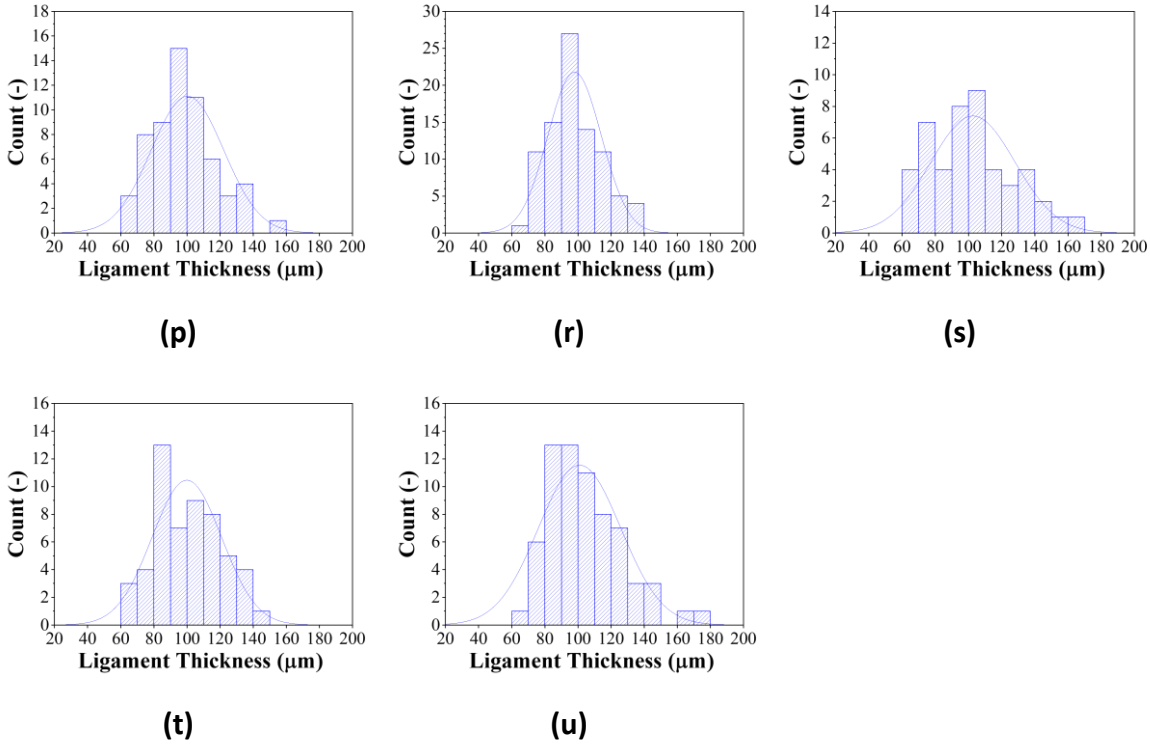

Figure 4.18 – The ligament thickness distribution for <u>the uncompressed</u> nickel foam CT slices numbered as: (a) 0, (b) 50, (c) 100, (d) 150, (e) 200, (f) 250, (g) 300, (h) 350, (i) 400, (j) 450, (k) 500, (l) 550, (m) 600, (n) 650, (o) 700, (p) 750, (r) 800, (s) 850, (t) 900 and (u) 950.

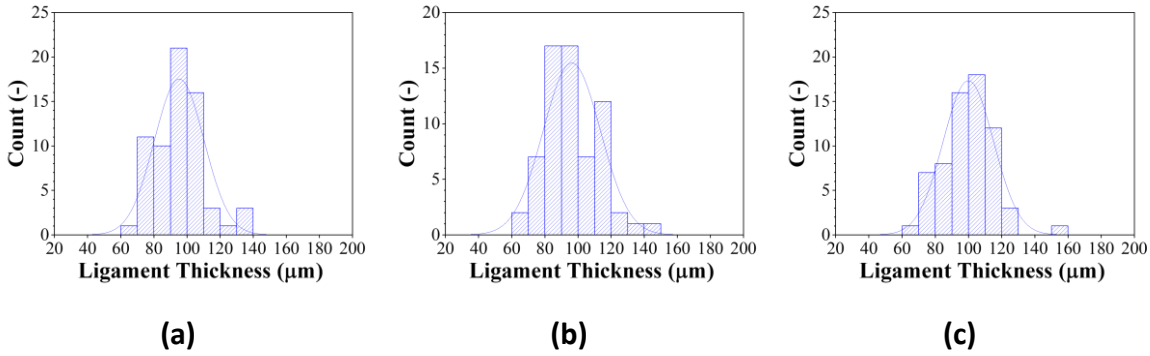

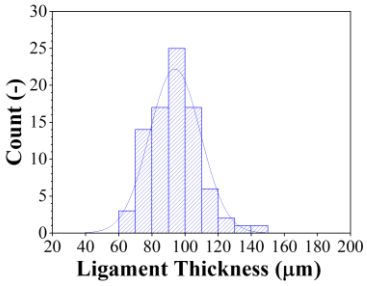

(d)

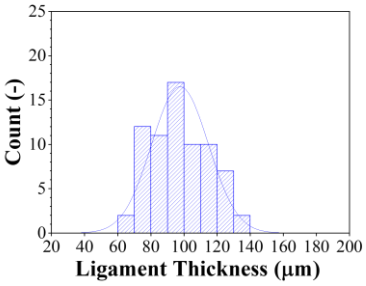

(e)

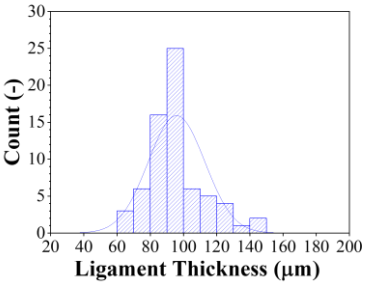

(f)

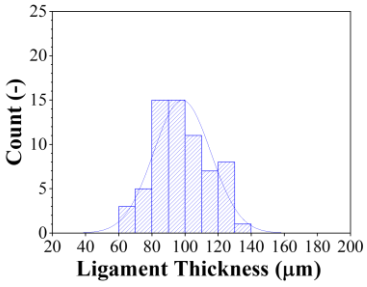

(g)

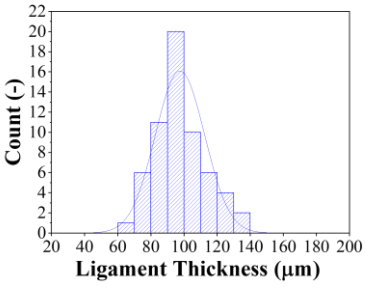

(h)

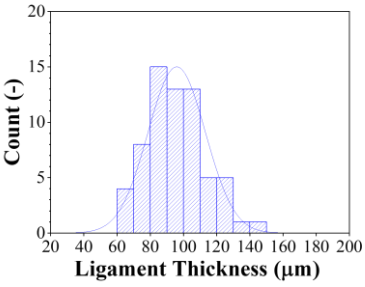

(i)

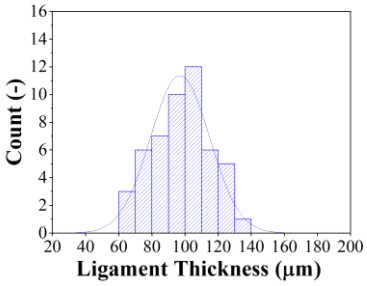

(j)

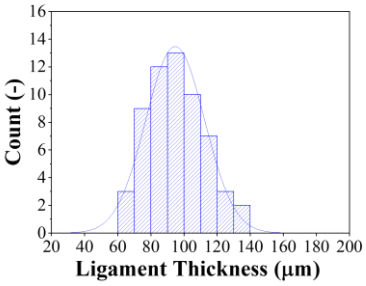

(k)

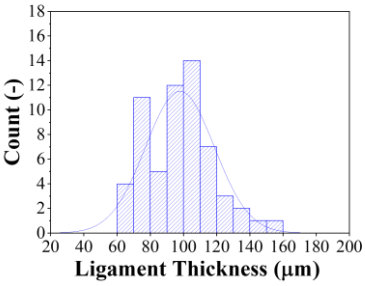

(l)

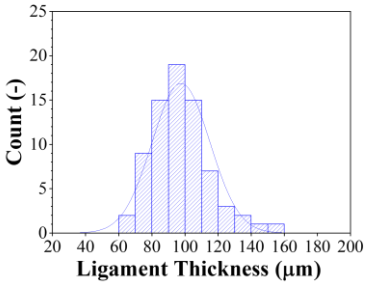

(m)

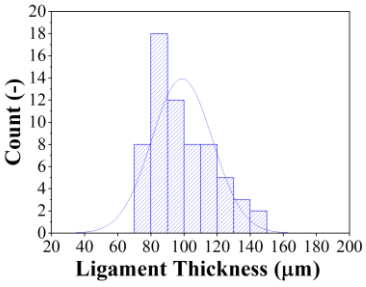

(n)

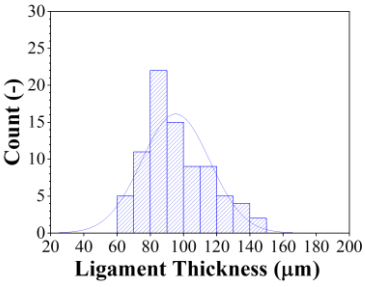

(o)

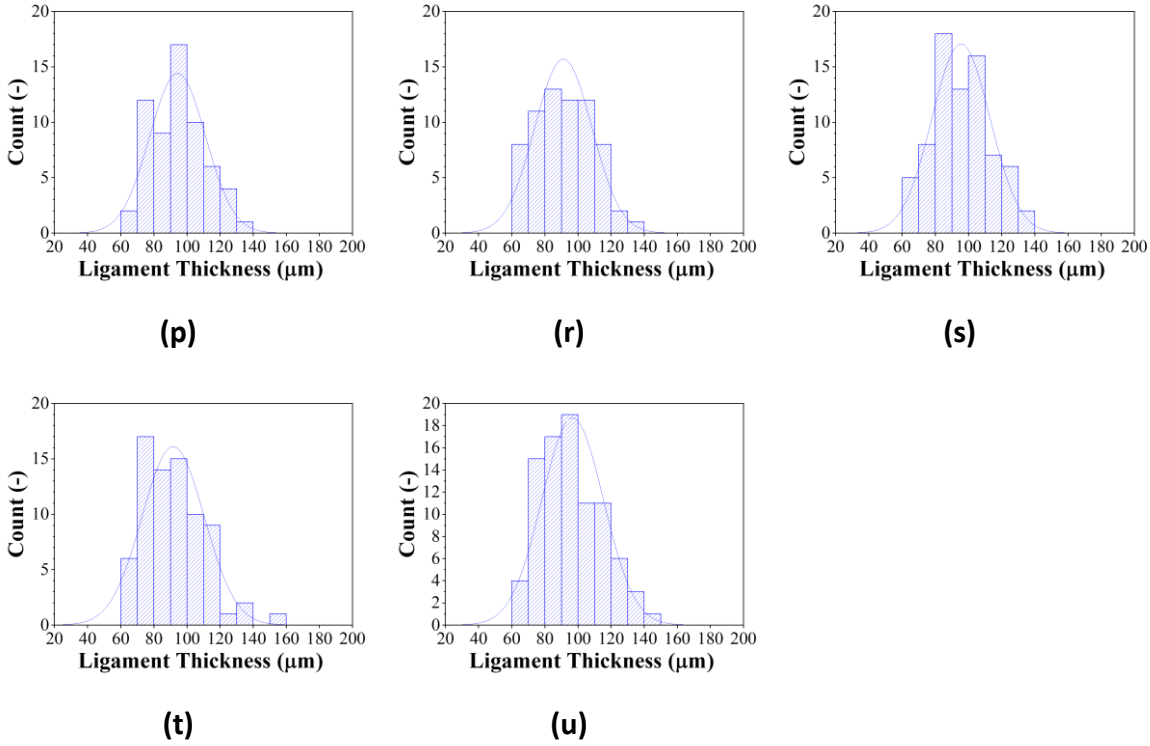

Figure 4.19 – The ligament thickness distribution for <u>the 20% compressed</u> nickel foam CT slices numbered as: (a) 0, (b) 50, (c) 100, (d) 150, (e) 200, (f) 250, (g) 300, (h) 350, (i) 400, (j) 450, (k) 500, (l) 550, (m) 600, (n) 650, (o) 700, (p) 750, (r) 800, (s) 850, (t) 900 and (u) 950.

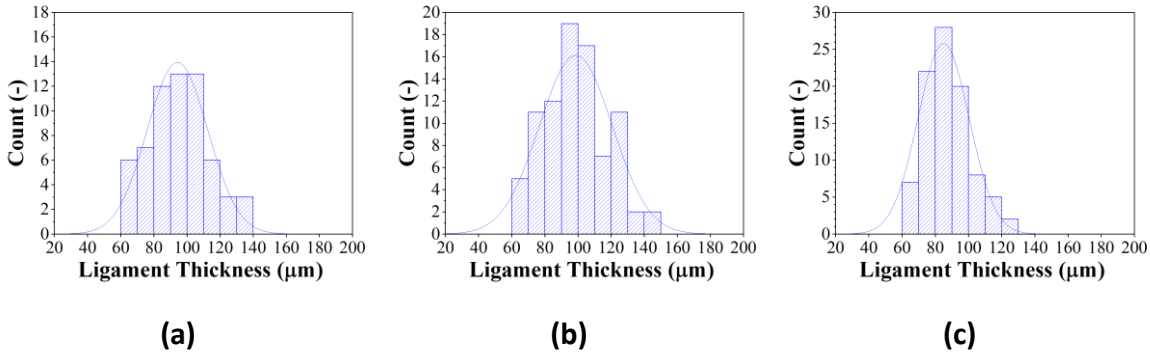

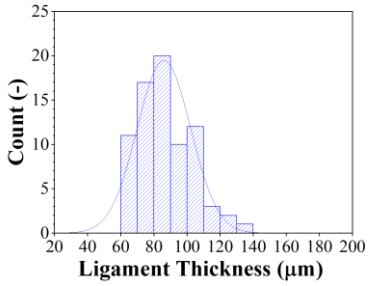

(d)

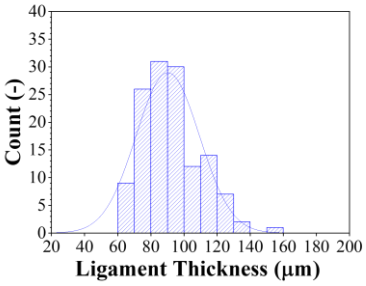

(e)

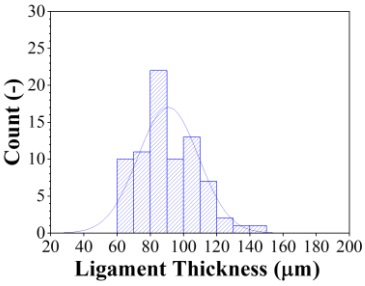

(f)

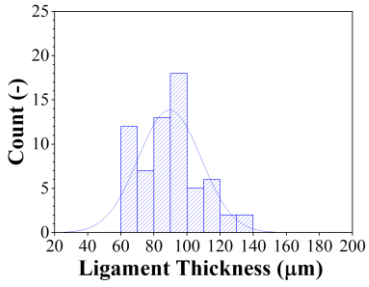

(g)

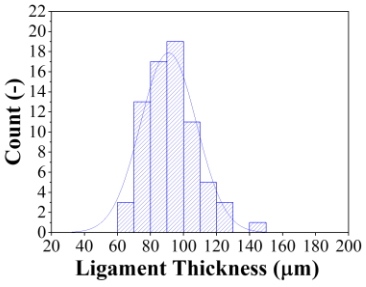

(h)

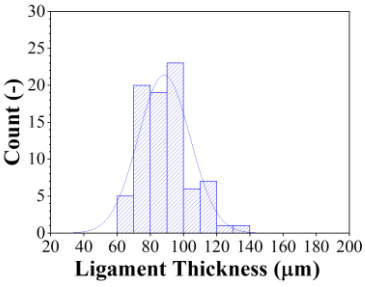

(i)

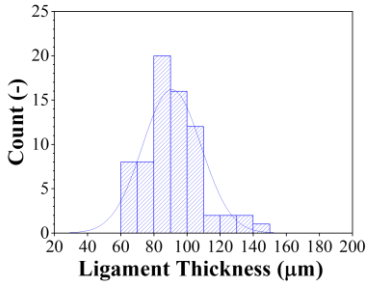

(j)

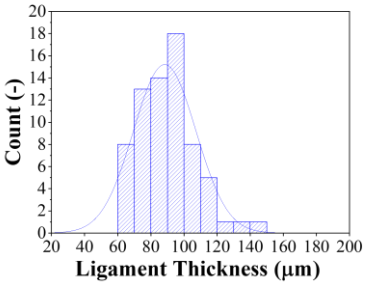

(k)

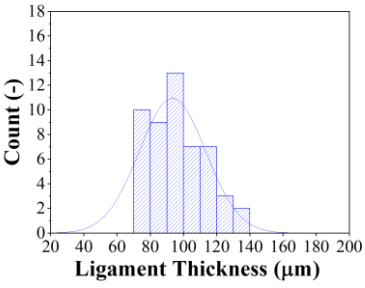

(l)

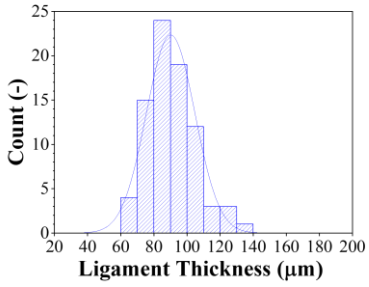

(m)

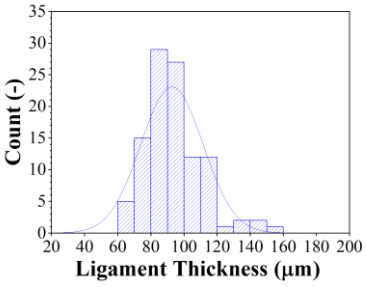

(n)

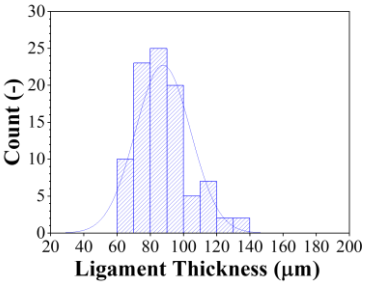

(o)

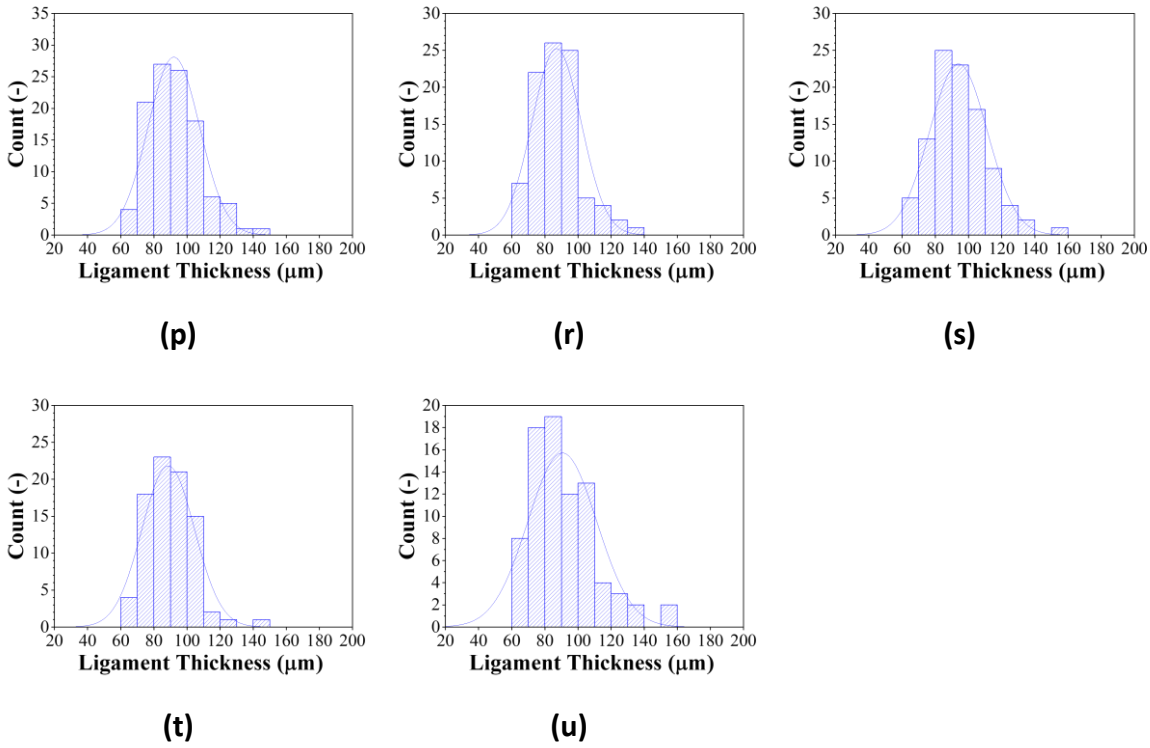

Figure 4.20 – The ligament thickness distribution for the 40% compressed nickel foam CT slices numbered as: (a) 0, (b) 50, (c) 100, (d) 150, (e) 200, (f) 250, (g) 300, (h) 350, (i) 400, (j) 450, (k) 500, (l) 550, (m) 600, (n) 650, (o) 700, (p) 750, (r) 800, (s) 850, (t) 900 and (u) 950.

4.4.5 Specific surface area

Figure 4.21 displays the specific surface area (SSA) for all the 20 CT nickel foam slices for the uncompressed, 20% compressed, and 40% compressed cases. The mean specific surface area of the uncompressed nickel foam is 55700±2700 m^{-1}. The specific surface area increase with increasing compression (due to the evident volumetric decrease); it increases to 57100±2800 m^{-1} with 20% compression ratio and to 61000±2900 m^{-1} with 40% compression ratio. These results are in accordance with

the findings reported in the literature that shows that the specific surface are of nickel foams increase with increasing compression [99–101]. High specific surface area is expected to increase mass transport resistance; this will be touched on in the following section. On the other hand, high specific area areas are favourable for the electrical and the thermal conductivity as well as the electrical contact with either the catalyst layer or the flow-field plate [102,103].

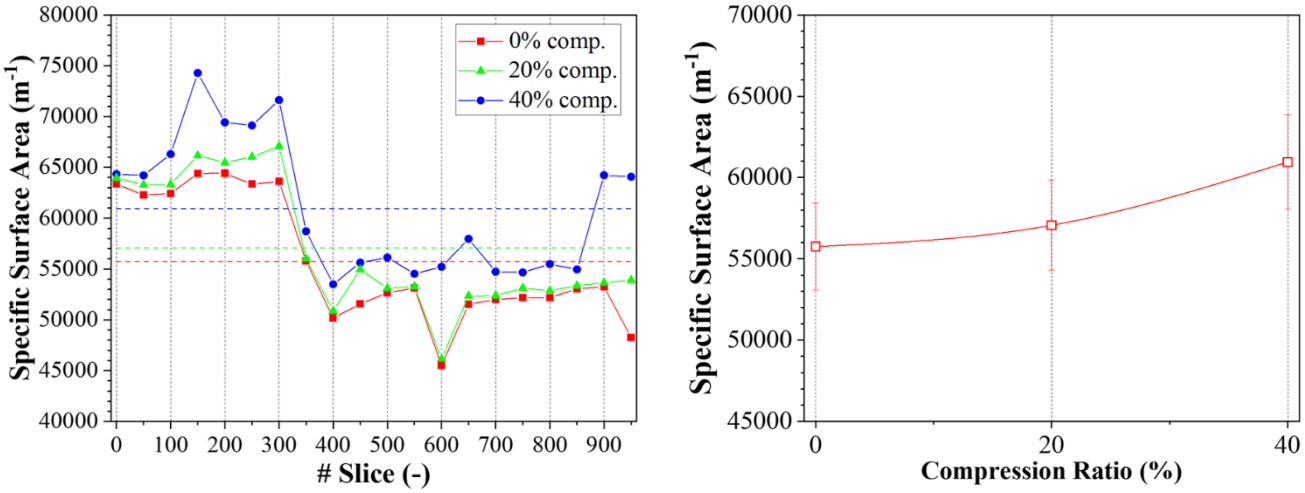

(a) **(b)**

Figure 4.21 – (a) Specific surface area values for the uncompressed, 20% compressed, and 40% compressed CT nickel foam slices and (b) the mean specific surface area as a function of the compression ratio. Note that the error bars represent 95% confidence intervals.

4.4.6 Gas Permeability

The gas permeability values for all the 20 CT nickel foam slices were computationally estimated under the three compression ratios: 0, 20 and 40%; see Figure 4.22. The average through- and in-plane permeability values were respectively computed to be

1.63×10^{-9} and 1.64×10^{-9} m^2 for the uncompressed nickel foam. The mean through-plane and in-plane permeability values are very close to each other and this signifies the high isotropy of the uncompressed nickel foam; the anisotropy ratio (which is the ratio between the through- and the in-plane transport properties) is almost one. Figure 4.22 shows that the through-plane permeability of the CT nickel slices vary between 1.02×10^{-9} and 2.17×10^{-9} m^2. Likewise, the corresponding in-plane permeability varies between 1.12×10^{-9} and 2.31×10^{-9} m^2. These permeability values are in very good agreement with those reported in the literature. For instance, Khayargoli et al. [94] and Medraj et al. [104] experimentally estimated the through-plane permeability to be around 1.30×10^{-9} m^2. Gerbaux et al. [105] experimentally estimated the in-plane permeability of nickel foam as 1.94×10^{-9} m^2. Likewise, Topin et al. [106], Hugo et al. [107], and Bonnet et al. [41] measured the in-plane permeability as 1.38×10^{-9}, 1.38×10^{-9} and 1.85×10^{-9} m^2, respectively. It is noteworthy that the gas permeability of the uncompressed nickel foam-based GDL is at least two orders of magnitude higher than the conventional carbon fibre based GDLs [19]. The permeability is evidently decrease with compression; see Figure 4.22. The mean through- and in-plane permeability of the 20% compressed nickel foam are respectively 9.96×10^{-10} and 6.89×10^{-10} m^2, and the lower and the upper limits are 1.39×10^{-10} and 6.48×10^{-10} m^2 for the through-plane permeability and 5.09×10^{-10} m^2 and 1.08×10^{-9} m^2 for the in-plane permeability. Clearly, as shown in Sections 4.4.1 and 4.4.3, compression decreases the pores between the ligaments and, subsequently, the porosity of the foam. It is well-known that gas permeability decreases with decreasing porosity as evident from Carman-Kozeny equation [108].

With 40% compression ratio, the mean through- and in-plane permeability values further reduce to 5.57×10^{-10} and 3.51×10^{-10} m^2 respectively, and the lower and upper limits decrease to 3.07×10^{-10} and 8.69×10^{-10} m^2 for the through-plane permeability and to 1.21×10^{-10} and 6.68×10^{-10} m^2 for the in-plane permeability. Notably, the permeability in the in-plane direction is more sensitive to compression than that in the through-plane direction as compression increases to 20; this is more evident in Figure 4.22. This is most likely due to the fact that the ligaments are mainly oriented in the in-plane directions and therefore there would be less resistance to compressive forces to close up the gaps parallel to these ligaments than those normal to them.

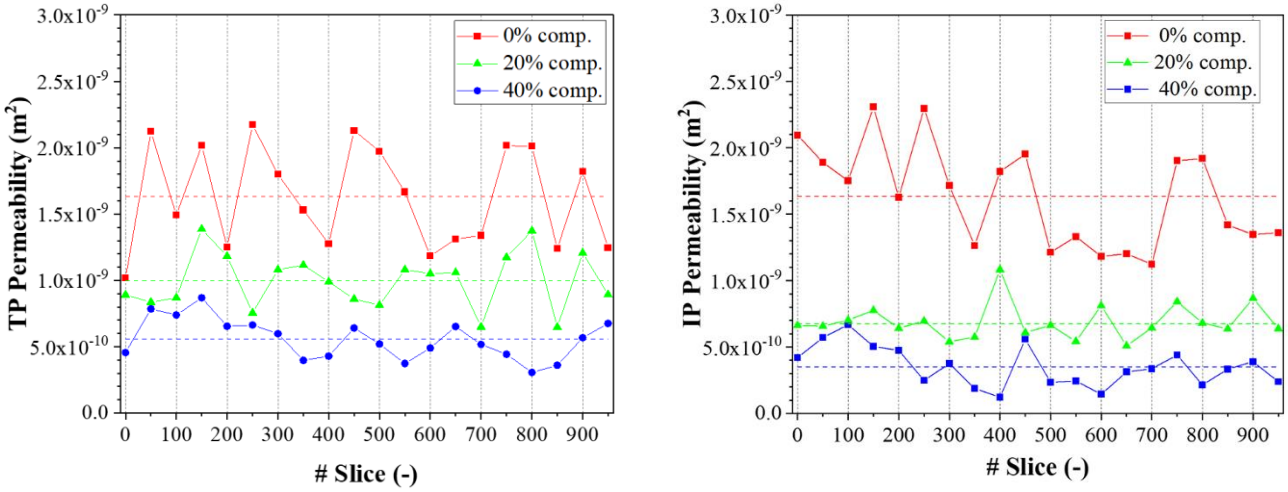

(a) **(b)**

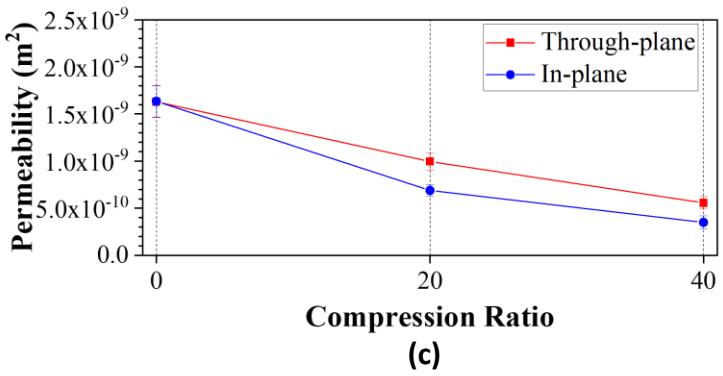

(c)

Figure 4.22 – (a) Through-plane and (b) in-plane permeability values and (c) the mean permeability values for the uncompressed, 20%, and 40% compressed CT nickel foam slices. Note that the error bars represent 95% confidence intervals. Note that the error bars represent 95% confidence intervals.

The average through- and in-plane permeability values are almost the same for the uncompressed nickel foam signifying the high isotropy of this material; the anisotropy ratio was calculated as 1.04 with 0% compression ratio (Figure 4.23). This value is in good agreement with those reported in the literature for the anisotropy ratio of the nickel foam [109–111]. Interestingly, the anisotropic ratio starts to increase to around 1.48 with 20% compression ratio and to around 1.82 with 40% compression ratio. As mentioned earlier, this is due to the gas permeability being more sensitive to the compression in the in-plane direction than the through-plane direction. Therefore, when using nickel foam as GDLs, the validity of the assumption that the nickel foam GDL is isotropic in the PEFC models needs to be carefully examined.

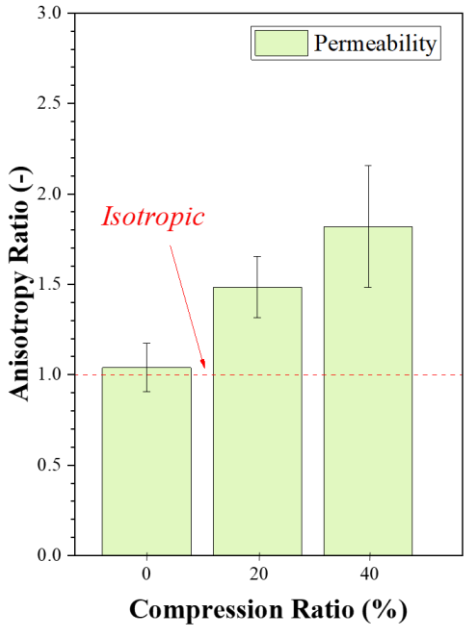

Figure 4.23 – The anisotropy ratios of the gas permeability of nickel foam under different compression ratios. Note that the error bars represent 95% confidence intervals.

4.4.7 Effective Diffusivity

The effective diffusivity of oxygen into nitrogen in both the through- and in-plane directions were computationally estimated for all the 20 CT nickel foam slices; see Figure 4.24. The mean effective diffusivity values in the through- and in-plane directions for the uncompressed nickel foam are 0.161 and 0.170 cm^2/s, respectively. As with the permeability, the effective diffusivity is expected to decrease with compression. The through-plane and the in-plane effective diffusivity values become 0.152 and 0.154 cm^2/s with 20% compression ratio, and 0.145 and 0.143 cm^2/s with 40% compression ratio. These effective diffusivity values are notably higher than

those of the conventional carbon fibres based GDLs. For example, the through-plane effective diffusivity for the uncoated SGL GDL was reported to be between 0.153 and 0.08 cm^2/s and for Toray GDL to be between 0.081 and 0.033 cm^2/s [71,112]. Similarly, the in-plane effective diffusivity of Toray GDL was found to vary between 0.78 and 0.02 cm^2/s. It should be noted that the above lower limits are for the compressed GDLs while the upper limits are for the uncompressed GDLs. Unlike the gas permeability of compressed nickel foam, the effective diffusivity of the nickel foam was found to be highly isotropic even with high compression ratios. Namely, the anisotropic ratio of the effective diffusivity is 1.05 with 0% compression ratio, 1.03 with 20% compression ratio and 1.01 with 40% compression ratio; see Figure 4.25.

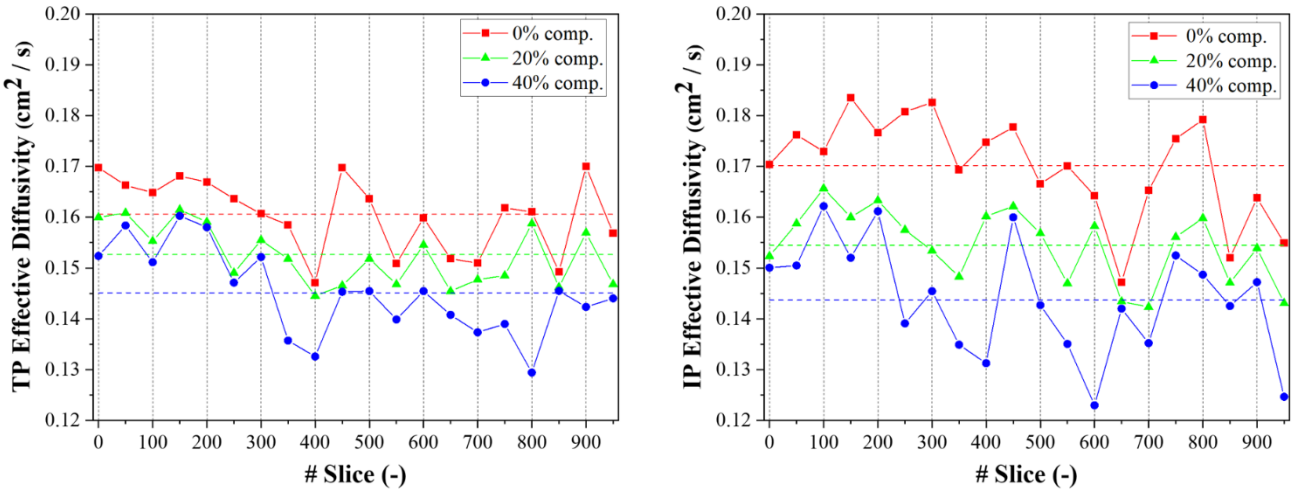

(a) **(b)**

Figure 4.24 – (a) The through-plane and (b) the in-plane effective diffusivity values for the uncompressed, 20% compressed, and 40% CT nickel foam slices.

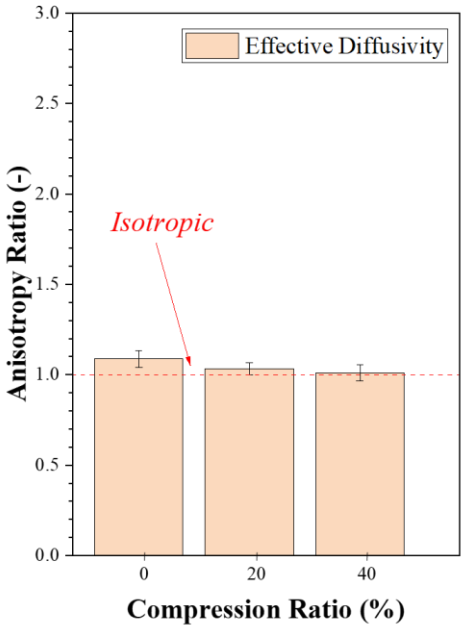

Figure 4.25 – The anisotropy ratios of the effective diffusivity of nickel foam under different compression ratios. Note that the error bars represent 95% confidence intervals.

4.5 CONCLUSIONS

Nickel foam is a serious candidate for gas diffusion layers in polymer electrolyte fuel cells and this is due to their superior structural and transport properties. In this work, the impact of realistic compression (mimicking those applied to the PEFCs) on some of the key structural and transport properties has been investigated using computationally-efficient two-dimensional X-ray CT based images and numerical models. These investigated structural and transport properties are: porosity, tortuosity, pore size distribution, ligament thickness distribution, and specific surface area, gas permeability and effective diffusivity. The following are the main findings of this chapter:

- The porosity of nickel foam was found to decrease slightly with realistic compressions. Namely, the mean porosity of nickel foam (~ 0.89) decreased by less 6% (0.84) when compressed by 40%. These values are higher than those demonstrated by the conventional carbon substrates under similar compressions; this implies less mass transport resistance when using nickel foam as GDLs.
- The pore size was shown to considerably decrease with compression; the mean pore size of nickel foam (~ 175 μm) decreased by around 60% (71 μm) when nickel foam was compressed by 40%. Interestingly, the ligament thickness was found to decrease by around 10% when compressing nickel foam by 40%; the ligament thickness decreased from ~ 100 μm to ~ 90 μm with 40% compression ratio and this is due to the fact that the ligaments encapsulate some small pores. On the other hand, the specific surface area was shown to increase with compression; it increases from 55700 m^{-1} (uncompressed nickel foam) to 61000 m^{-1} with 40% compression ratio.
- The in-plane tortuosity of nickel foam increases with compression; it increased from ~ 1.14 to 1.19 with 40% compression ratio. On the other hand, its through-plane tortuosity (~ 1.18) was found to increase with 20% compression (~ 1.20) and then decrease (~ 1.18) with 40% compression. This is most likely due to the observation that the ligaments are mainly oriented in the in-plane directions and therefore the pores parallel to these ligaments are closed up with compression; thus creating more in-plane tortuous flow paths. However, a compression beyond a certain value appear to straighten the pathways in the through-plane directions.

- The gas permeability of nickel foam significantly decreases with compression particularly in the in-plane direction; the mean through-plane permeability (1.63×10^{-9} m^2) decreased by around 65% (5.57×10^{-10} m^2) and mean the in-plane permeability (1.64×10^{-9} m^2) by around 80% (3.51×10^{-10} m^2) with 40% compression ratio. The numbers show that gas permeability of the uncompressed nickel foam is highly isotropic; the anisotropic ratio (which is the ratio between the through-plane and in-plane gas permeability) is around unity. However, this factor increases significantly with compression; it increased to around 1.5 with 20% compression ratio and to around 1.8 with 40% compression ratio. This is mainly due to the ligaments being mainly oriented in the in-plane direction, thus allowing for easier closing up of the gaps between them compared to those normal to the ligaments.
- Unlike the gas permeability, the effective diffusivity of oxygen into nitrogen was found to be highly isotropic and less sensitive to compression. Namely, the through-plane effective diffusivity (0.161 cm^2/s) decreased by around 10% (0.145 cm^2/s) and the in-plane effective diffusivity (0.170 cm^2/s) decreased by around 15% (0.143 cm^2/s) with 40% compression ratio. Interestingly, the isotropy of the effective diffusivity was found to slightly decrease with compression; the anisotropic ratio decreased from 1.05 to 1.01 with 40% compression ratio.

4.6 REFERENCES

[1] Ozden A, Shahgaldi S, Li X, Hamdullahpur F. A review of gas diffusion layers for proton exchange membrane fuel cells—With a focus on characteristics, characterization techniques, materials and designs. Prog Energy Combust Sci 2019;74:50–102. https://doi.org/10.1016/j.pecs.2019.05.002.

[2] Pang Y, Hao L, Wang Y. Convolutional neural network analysis of radiography images for rapid water quantification in PEM fuel cell. Appl Energy 2022;321:119352. https://doi.org/10.1016/j.apenergy.2022.119352.

[3] Kahveci EE, Taymaz I. Assessment of single-serpentine PEM fuel cell model developed by computational fluid dynamics. Fuel 2018;217:51–8. https://doi.org/10.1016/j.fuel.2017.12.073.

[4] Kahveci EE, Taymaz I. Experimental study on performance evaluation of PEM fuel cell by coating bipolar plate with materials having different contact angle. Fuel 2019;253:1274–81. https://doi.org/10.1016/j.fuel.2019.05.110.

[5] Wang Y, Ruiz Diaz DF, Chen KS, Wang Z, Adroher XC. Materials, technological status, and fundamentals of PEM fuel cells – A review. Mater Today 2020;32:178–203. https://doi.org/10.1016/j.mattod.2019.06.005.

[6] Arvay A, Yli-Rantala E, Liu CH, Peng XH, Koski P, Cindrella L, et al. Characterization techniques for gas diffusion layers for proton exchange membrane fuel cells - A review. J Power Sources 2012;213:317–37. https://doi.org/10.1016/j.jpowsour.2012.04.026.

[7] Lee S, Tam J, Li W, Yu B, Cho HJ, Samei J, et al. Multi-scale morphological characterization of Ni foams with directional pores. Mater Charact 2019;158. https://doi.org/10.1016/j.matchar.2019.109939.

[8] Meyer Q, Liu S, Ching K, Da Y, Zhao C. Operando monitoring of the evolution of triple-phase boundaries in proton exchange membrane fuel cells. J Power Sources 2023;557:232539. https://doi.org/10.1016/j.jpowsour.2022.232539.

[9] Alaefour I, Shahgaldi S, Ozden A, Li X, Hamdullahpur F. The role of flow-field layout on the conditioning of a proton exchange membrane fuel cell. Fuel 2018;230:98–103. https://doi.org/10.1016/j.fuel.2018.05.062.

[10] Thanasilp S, Hunsom M. Effect of MEA fabrication techniques on the cell performance of Pt-Pd/C electrocatalyst for oxygen reduction in PEM fuel cell. Fuel 2010;89:3847–52. https://doi.org/10.1016/j.fuel.2010.07.008.

[11] Wilberforce T, El-Hassan Z, Khatib FN, Al Makky A, Baroutaji A, Carton JG, et al. Developments of electric cars and fuel cell hydrogen electric cars. Int J Hydrogen Energy 2017;42:25695–734. https://doi.org/10.1016/j.ijhydene.2017.07.054.

[12] Das HS, Tan CW, Yatim AHM. Fuel cell hybrid electric vehicles: A review on power conditioning units and topologies. Renew Sustain Energy Rev 2017;76:268–91. https://doi.org/10.1016/j.rser.2017.03.056.

[13] Chen X, Liu B, Sun C, Xia X. Effects of microscopic morphology of ligament and porous parameter on spectral radiative properties of nickel foams. Infrared

Phys Technol 2022;123:104208. https://doi.org/10.1016/j.infrared.2022.104208.

[14] Taner T. The novel and innovative design with using H2 fuel of PEM fuel cell: Efficiency of thermodynamic analyze. Fuel 2021;302:121109. https://doi.org/10.1016/j.fuel.2021.121109.

[15] Bahari M, Rostami M, Entezari A, Ghahremani S, Etminan M. Performance evaluation and multi-objective optimization of a novel UAV propulsion system based on PEM fuel cell. Fuel 2022;311:122554. https://doi.org/10.1016/j.fuel.2021.122554.

[16] Ozden A, Shahgaldi S, Zhao J, Li X, Hamdullahpur F. Assessment of graphene as an alternative microporous layer material for proton exchange membrane fuel cells. Fuel 2018;215:726–34. https://doi.org/10.1016/j.fuel.2017.11.109.

[17] Ozden A, Alaefour IE, Shahgaldi S, Li X, Colpan CO, Hamdullahpur F. Gas Diffusion Layers for PEM Fuel Cells: Ex- and In-Situ Characterization. Elsevier; 2018. https://doi.org/10.1016/B978-0-12-813734-5.00040-8.

[18] Sánchez M, Pierna AR, Lorenzo A, Del Val JJ. Effect of cocatalyst and composition on catalytic performance of amorphous alloys for ethanol electrooxidation and PEMFCs. Int J Hydrogen Energy 2016;41:19749–55. https://doi.org/10.1016/j.ijhydene.2016.06.064.

[19] El-Kharouf A, Mason TJ, Brett DJL, Pollet BG. Ex-situ characterisation of gas diffusion layers for proton exchange membrane fuel cells. J Power Sources 2012;218:393–404. https://doi.org/10.1016/j.jpowsour.2012.06.099.

[20] Aldakheel F, Ismail MS, Hughes KJ, Ingham DB, Ma L, Pourkashanian M. Effects of compression on mechanical integrity, gas permeability and thermal stability of gas diffusion layers with/without sealing gaskets. Int J Hydrogen Energy 2021;46:22907–19. https://doi.org/10.1016/j.ijhydene.2021.04.087.

[21] Ismail MS, Damjanovic T, Ingham DB, Pourkashanian M, Westwood A. Effect of polytetrafluoroethylene-treatment and microporous layer-coating on the electrical conductivity of gas diffusion layers used in proton exchange membrane fuel cells. J Power Sources 2010;195:2700–8. https://doi.org/10.1016/j.jpowsour.2009.11.069.

[22] Ismail MS, Damjanovic T, Hughes K, Ingham DB, Ma L, Pourkashanian M, et al. Through-plane permeability for untreated and PTFE-treated gas diffusion layers in proton exchange membrane fuel cells. J Fuel Cell Sci Technol 2010;7:0510161–7. https://doi.org/10.1115/1.4000685.

[23] Ismail MS, Hassanpour A, Ingham DB, Ma L, Pourkashanian M. On the compressibility of gas diffusion layers in proton exchange membrane fuel cells. Fuel Cells 2012;12:391–7. https://doi.org/10.1002/fuce.201100054.

[24] Okereke IC, Ismail MS, Ingham D, Hughes KJ, Ma L, Pourkashanian M. The effects of GDL anisotropic transport properties on the PEFC performance. Int J

Numer Methods Heat Fluid Flow 2022. https://doi.org/10.1108/hff-05-2022-0284.

[25] Park S, Popov BN. Effect of a GDL based on carbon paper or carbon cloth on PEM fuel cell performance. Fuel 2011;90:436–40. https://doi.org/10.1016/j.fuel.2010.09.003.

[26] Turkmen AC, Celik C. The effect of different gas diffusion layer porosity on proton exchange membrane fuel cells. Fuel 2018;222:465–74. https://doi.org/10.1016/j.fuel.2018.02.058.

[27] Jayakumar A, Sethu SP, Ramos M, Robertson J, Al-Jumaily A. A technical review on gas diffusion, mechanism and medium of PEM fuel cell. Ionics (Kiel) 2015;21:1–18. https://doi.org/10.1007/s11581-014-1322-x.

[28] Ismail MS, Borman D, Damjanovic T, Ingham DB, Pourkashanian M. On the through-plane permeability of microporous layer-coated gas diffusion layers used in proton exchange membrane fuel cells. Int J Hydrogen Energy 2011;36:10392–402. https://doi.org/10.1016/j.ijhydene.2010.09.012.

[29] Ye L, Qiu D, Peng L, Lai X. Microstructures and electrical conductivity properties of compressed gas diffusion layers using X-ray tomography. Appl Energy 2022;326:119934. https://doi.org/10.1016/j.apenergy.2022.119934.

[30] Zhao J, Shahgaldi S, Ozden A, Alaefour IE, Li X, Hamdullahpur F. Effect of catalyst deposition on electrode structure, mass transport and performance of polymer

electrolyte membrane fuel cells. Appl Energy 2019;255:113802. https://doi.org/10.1016/j.apenergy.2019.113802.

[31] Park J, Oh H, Ha T, Lee Y Il, Min K. A review of the gas diffusion layer in proton exchange membrane fuel cells: Durability and degradation. Appl Energy 2015;155:866–80. https://doi.org/10.1016/j.apenergy.2015.06.068.

[32] Pan Y, Wang H, Brandon NP. Gas diffusion layer degradation in proton exchange membrane fuel cells: Mechanisms, characterization techniques and modelling approaches. J Power Sources 2021;513:230560. https://doi.org/10.1016/j.jpowsour.2021.230560.

[33] Ozden A, Shahgaldi S, Zhao J, Li X, Hamdullahpur F. Degradations in porous components of a proton exchange membrane fuel cell under freeze-thaw cycles: Morphology and microstructure effects. Int J Hydrogen Energy 2020;45:3618–31. https://doi.org/10.1016/j.ijhydene.2018.10.209.

[34] Bose AB, Zhu X. Design of stable and durable polymer electrolyte membrane fuel cells by embedding hydrophobic cage-structured material in cell components. Fuel 2019;235:954–61. https://doi.org/10.1016/j.fuel.2018.08.051.

[35] El-kharouf A, Pollet BG. Gas Diffusion Media and Their Degradation. Elsevier Inc.; 2012. https://doi.org/10.1016/B978-0-12-386936-4.10004-1.

[36] Bosomoiu M, Tsotridis G, Bednarek T. Study of effective transport properties of fresh and aged gas diffusion layers. J Power Sources 2015;285:568–79. https://doi.org/10.1016/j.jpowsour.2015.03.132.

[37] Nitta I, Hottinen T, Himanen O, Mikkola M. Inhomogeneous compression of PEMFC gas diffusion layer. Part I. Experimental. J Power Sources 2007;171:26–36. https://doi.org/10.1016/j.jpowsour.2006.11.018.

[38] Ozden A, Shahgaldi S, Li X, Hamdullahpur F. The impact of ionomer type on the morphological and microstructural degradations of proton exchange membrane fuel cell electrodes under freeze-thaw cycles. Appl Energy 2019;238:1048–59. https://doi.org/10.1016/j.apenergy.2019.01.136.

[39] Yan X, Lin C, Zheng Z, Chen J, Wei G, Zhang J. Effect of clamping pressure on liquid-cooled PEMFC stack performance considering inhomogeneous gas diffusion layer compression. Appl Energy 2020;258:114073. https://doi.org/10.1016/j.apenergy.2019.114073.

[40] Tan WC, Saw LH, Thiam HS, Xuan J, Cai Z, Yew MC. Overview of porous media/metal foam application in fuel cells and solar power systems. Renew Sustain Energy Rev 2018;96:181–97. https://doi.org/10.1016/j.rser.2018.07.032.

[41] Bonnet JP, Topin F, Tadrist L. Flow laws in metal foams: Compressibility and pore size effects. Transp Porous Media 2008;73:233–54. https://doi.org/10.1007/s11242-007-9169-5.

[42] Awin Y, Dukhan N. Experimental performance assessment of metal-foam flow fields for proton exchange membrane fuel cells. Appl Energy 2019;252:113458. https://doi.org/10.1016/j.apenergy.2019.113458.

[43] Zhang G, Bao Z, Xie B, Wang Y, Jiao K. Three-dimensional multi-phase simulation of PEM fuel cell considering the full morphology of metal foam flow field. Int J Hydrogen Energy 2021;46:2978–89. https://doi.org/10.1016/j.ijhydene.2020.05.263.

[44] Tseng CJ, Tsai BT, Liu ZS, Cheng TC, Chang WC, Lo SK. A PEM fuel cell with metal foam as flow distributor. Energy Convers Manag 2012;62:14–21. https://doi.org/10.1016/j.enconman.2012.03.018.

[45] Tsai BT, Tseng CJ, Liu ZS, Wang CH, Lee CI, Yang CC, et al. Effects of flow field design on the performance of a PEM fuel cell with metal foam as the flow distributor. Int J Hydrogen Energy 2012;37:13060–6. https://doi.org/10.1016/j.ijhydene.2012.05.008.

[46] Baroutaji A, Carton JG, Stokes J, Olabi AG. Application of Open Pore Cellular Foam for air breathing PEM fuel cell. Int J Hydrogen Energy 2017;42:25630–8. https://doi.org/10.1016/j.ijhydene.2017.05.114.

[47] Shin DK, Yoo JH, Kang DG, Kim MS. Effect of cell size in metal foam inserted to the air channel of polymer electrolyte membrane fuel cell for high performance. Renew Energy 2018;115:663–75. https://doi.org/10.1016/j.renene.2017.08.085.

[48] Zheng W, Liu M, Lee LYS. Best Practices in Using Foam-Type Electrodes for Electrocatalytic Performance Benchmark. ACS Energy Lett 2020;5:3260–4. https://doi.org/10.1021/acsenergylett.0c01958.

[49] Liu R, Zhou W, Li S, Li F, Ling W. Performance improvement of proton exchange membrane fuel cells with compressed nickel foam as flow field structure. Int J Hydrogen Energy 2020;45:17833–43. https://doi.org/10.1016/j.ijhydene.2020.04.238.

[50] Tabe Y, Nasu T, Morioka S, Chikahisa T. Performance characteristics and internal phenomena of polymer electrolyte membrane fuel cell with porous flow field. J Power Sources 2013;238:21–8. https://doi.org/10.1016/j.jpowsour.2013.03.047.

[51] Chen X, Yang C, Sun Y, Liu Q, Wan Z, Kong X, et al. Water management and structure optimization study of nickel metal foam as flow distributors in proton exchange membrane fuel cell. Appl Energy 2022;309:118448. https://doi.org/10.1016/j.apenergy.2021.118448.

[52] Zamel N, Li X. Effective transport properties for polymer electrolyte membrane fuel cells - With a focus on the gas diffusion layer. Prog Energy Combust Sci 2013;39:111–46. https://doi.org/10.1016/j.pecs.2012.07.002.

[53] Jankovic J, Zhang S, Putz A, Saha MS, Susac D. Multiscale imaging and transport modeling for fuel cell electrodes. J Mater Res 2019;34:579–91. https://doi.org/10.1557/jmr.2018.458.

[54] Rosén T, Eller J, Kang J, Prasianakis NI, Mantzaras J, Büchi FN. Saturation Dependent Effective Transport Properties of PEFC Gas Diffusion Layers. J Electrochem Soc 2012;159:F536–44. https://doi.org/10.1149/2.005209jes.

[55] Bao Z, Li Y, Zhou X, Gao F, Du Q, Jiao K. Transport properties of gas diffusion layer of proton exchange membrane fuel cells: Effects of compression. Int J Heat Mass Transf 2021;178:121608. https://doi.org/10.1016/j.ijheatmasstransfer.2021.121608.

[56] Gostick JT, Fowler MW, Pritzker MD, Ioannidis MA, Behra LM. In-plane and through-plane gas permeability of carbon fiber electrode backing layers. J Power Sources 2006;162:228–38. https://doi.org/10.1016/j.jpowsour.2006.06.096.

[57] García-Salaberri PA, Zenyuk I V., Shum AD, Hwang G, Vera M, Weber AZ, et al. Analysis of representative elementary volume and through-plane regional characteristics of carbon-fiber papers: diffusivity, permeability and electrical/thermal conductivity. Int J Heat Mass Transf 2018;127:687–703. https://doi.org/10.1016/j.ijheatmasstransfer.2018.07.030.

[58] Fishman Z, Hinebaugh J, Bazylak A. Microscale tomography investigations of heterogeneous porosity distributions of PEMFC GDLs. J Electrochem Soc 2010;157:1643–50. https://doi.org/10.1149/1.3481443.

[59] Obermaier M, Bauer A, Dalkilic M, Rauber M, Scheu C. Gas diffusion layer wettability determination by cyclic voltammetry for automotive fuel cells. Fuel Cells 2021:221–33. https://doi.org/10.1002/fuce.202000184.

[60] Kaushal S, Sahu AK, Rani M, Dhakate SR. Multiwall carbon nanotubes tailored porous carbon fiber paper-based gas diffusion layer performance in polymer electrolyte membrane fuel cell. Renew Energy 2019;142:604–11. https://doi.org/10.1016/j.renene.2019.04.096.

[61] Vásárhelyi L, Kónya Z, Kukovecz, Vajtai R. Microcomputed tomography–based characterization of advanced materials: a review. Mater Today Adv 2020;8:1–13. https://doi.org/10.1016/j.mtadv.2020.100084.

[62] De Chiffre L, Carmignato S, Kruth JP, Schmitt R, Weckenmann A. Industrial applications of computed tomography. CIRP Ann - Manuf Technol 2014;63:655–77. https://doi.org/10.1016/j.cirp.2014.05.011.

[63] Kou X, Li X Sen, Wang Y, Zhang Y, Chen ZY. Distribution and reformation characteristics of gas hydrate during hydrate dissociation by thermal stimulation and depressurization methods. Appl Energy 2020;277:115575. https://doi.org/10.1016/j.apenergy.2020.115575.

[64] Fishman Z, Bazylak A. Heterogeneous Through-Plane Porosity Distributions for Treated PEMFC GDLs I. PTFE Effect. J Electrochem Soc 2011;158:B841. https://doi.org/10.1149/1.3594578.

[65] Fishman Z, Bazylak A. Heterogeneous Through-Plane Porosity Distributions for Treated PEMFC GDLs. II. Effect of MPL Cracks. J Electrochem Soc 2011;158:B846. https://doi.org/10.1149/1.3594636.

[66] Banerjee R, Hinebaugh J, Liu H, Yip R, Ge N, Bazylak A. Heterogeneous porosity distributions of polymer electrolyte membrane fuel cell gas diffusion layer materials with rib-channel compression. Int J Hydrogen Energy 2016;41:14885–96. https://doi.org/10.1016/j.ijhydene.2016.06.147.

[67] Meyer Q, Ashton S, Boillat P, Cochet M, Engebretsen E, Finegan DP, et al. Effect of gas diffusion layer properties on water distribution across air-cooled, open-cathode polymer electrolyte fuel cells: A combined ex-situ X-ray tomography and in-operando neutron imaging study. Electrochim Acta 2016;211:478–87. https://doi.org/10.1016/j.electacta.2016.06.068.

[68] Meyer Q, Mansor N, Iacoviello F, Cullen PL, Jervis R, Finegan D, et al. Investigation of Hot Pressed Polymer Electrolyte Fuel Cell Assemblies via X-ray Computed Tomography. Electrochim Acta 2017;242:125–36. https://doi.org/10.1016/j.electacta.2017.05.028.

[69] Holzer L, Pecho O, Schumacher J, Marmet P, Stenzel O, Büchi FN, et al. Microstructure-property relationships in a gas diffusion layer (GDL) for Polymer Electrolyte Fuel Cells, Part I: effect of compression and anisotropy of dry GDL. Electrochim Acta 2017;227:419–34. https://doi.org/10.1016/j.electacta.2017.01.030.

[70] Ma J, Zhang X, Jiang Z, Ostadi H, Jiang K, Chen R. Flow properties of an intact MPL from nano-tomography and pore network modelling. Fuel 2014;136:307–15. https://doi.org/10.1016/j.fuel.2014.07.040.

[71] Zenyuk I V., Parkinson DY, Connolly LG, Weber AZ. Gas-diffusion-layer structural properties under compression via X-ray tomography. J Power Sources 2016;328:364–76. https://doi.org/10.1016/j.jpowsour.2016.08.020.

[72] Je J, Doh S, Kim J, Kim MH. Heterogeneous Porosity Distribution Under Compression of Gas Diffusion Layer Using Synchrotron X-Ray Tomography. ECS Meet Abstr 2012;MA2012-02:1494–1494. https://doi.org/10.1149/ma2012-02/13/1494.

[73] Fly A, Meyer Q, Whiteley M, Iacoviello F, Neville T, Shearing PR, et al. X-ray tomography and modelling study on the mechanical behaviour and performance of metal foam flow-fields for polymer electrolyte fuel cells. Int J Hydrogen Energy 2019;44:7583–95. https://doi.org/10.1016/j.ijhydene.2019.01.206.

[74] Wu Y, Lu X, Cho JIS, Rasha L, Whiteley M, Neville TP, et al. Multi-length scale characterization of compression on metal foam flow-field based fuel cells using X-ray computed tomography and neutron radiography. Energy Convers Manag 2021;230:1–10. https://doi.org/10.1016/j.enconman.2020.113785.

[75] Ercelik M, Ismail MS, Ingham DB, Hughes KJ, Ma L. Efficient X-ray CT-based numerical computations of structural and mass transport properties of nickel foam-based GDLs for PEFCs. Energy 2023;262:125531. https://doi.org/10.1016/j.energy.2022.125531.

[76] Tamayol A, McGregor F, Bahrami M. Single phase through-plane permeability of carbon paper gas diffusion layers. J Power Sources 2012;204:94–9. https://doi.org/10.1016/j.jpowsour.2011.11.084.

[77] Poserin V, Marcuson S, Shu J, Wilkinson DS. CVD technique for Inco nickel foam production. Adv Eng Mater 2004;6:454–9. https://doi.org/10.1002/adem.200405142.

[78] Kia A, Wong HS, Cheeseman CR. Clogging in permeable concrete: A review. J Environ Manage 2017;193:221–33. https://doi.org/10.1016/j.jenvman.2017.02.018.

[79] Nabovati A, Hinebaugh J, Bazylak A, Amon CH. Effect of porosity heterogeneity on the permeability and tortuosity of gas diffusion layers in polymer electrolyte membrane fuel cells. J Power Sources 2014;248:83–90. https://doi.org/10.1016/j.jpowsour.2013.09.061.

[80] ImageJ/Fiji. https://imagej.net/software/fiji/ n.d.

[81] Huo S, Shi WY, Wang RF, Lu BB, Wang Y, Jiao K, et al. Elucidating the operating behavior of PEM fuel cell with nickel foam as cathode flow field. Sci China Technol Sci 2021;64:1041–56. https://doi.org/10.1007/s11431-020-1767-5.

[82] Duan DL, Zhang RL, Ding XJ, Li S. Calculation of specific surface area of foam metals using dodecahedron model. Mater Sci Technol 2006;22:1364–8. https://doi.org/10.1179/174328406X111138.

[83] Oun H, Kennedy A. Experimental investigation of pressure-drop characteristics across multi-layer porous metal structures. J Porous Mater 2014;21:1133–41. https://doi.org/10.1007/s10934-014-9863-y.

[84] Han M, Xu JH, Chan SH, Jiang SP. Characterization of gas diffusion layers for PEMFC. Electrochim Acta 2008;53:5361–7. https://doi.org/10.1016/j.electacta.2008.02.057.

[85] Ahmed DH, Sung HJ, Bae J. Effect of GDL permeability on water and thermal management in PEMFCs-I. Isotropic and anisotropic permeability. Int J Hydrogen Energy 2008;33:3767–85. https://doi.org/10.1016/j.ijhydene.2008.04.024.

[86] Ahmed DH, Sung HJ, Bae J. Effect of GDL permeability on water and thermal management in PEMFCs-II. Clamping force. Int J Hydrogen Energy 2008;33:3786–800. https://doi.org/10.1016/j.ijhydene.2008.04.023.

[87] Lee FC, Ismail MS, Ingham DB, Hughes KJ, Ma L, Lyth SM, et al. Alternative architectures and materials for PEMFC gas diffusion layers: A review and outlook. Renew Sustain Energy Rev 2022;166:112640. https://doi.org/10.1016/j.rser.2022.112640.

[88] Ismail MS, Hughes KJ, Ingham DB, Ma L, Pourkashanian M. Effects of anisotropic permeability and electrical conductivity of gas diffusion layers on the performance of proton exchange membrane fuel cells. Appl Energy 2012;95:50–63. https://doi.org/10.1016/j.apenergy.2012.02.003.

[89] Neehall ND, Ismail MS, Hughes KJ, Pourkashanian M. Effect of composition and structure of gas diffusion layer and microporous layer on the through-plane gas permeability of PEFC porous media. Int J Energy Res 2021;45:20988–1005. https://doi.org/10.1002/er.7158.

[90] Holman JP. Heat Transfer. 10th Ed.,. McGraw-Hill; 2010.

[91] Ismail MS, Ingham DB, Hughes KJ, Ma L, Pourkashanian M. Effective diffusivity of polymer electrolyte fuel cell gas diffusion layers: An overview and numerical study. Int J Hydrogen Energy 2015;40:10994–1010. https://doi.org/10.1016/j.ijhydene.2015.06.073.

[92] Orogbemi OM, Ingham DB, Ismail MS, Hughes KJ, Ma L, Pourkashanian M. The effects of the composition of microporous layers on the permeability of gas diffusion layers used in polymer electrolyte fuel cells. Int J Hydrogen Energy 2016;41:21345–51. https://doi.org/10.1016/j.ijhydene.2016.09.160.

[93] Vicente J, Topin F, Daurelle JV. Open celled material structural properties measurement: From morphology to transport properties. Mater Trans 2006;47:2195–202. https://doi.org/10.2320/matertrans.47.2195.

[94] Khayargoli P, Loya V, Lefebvre LP, Medraj M. The impact of microstructure on the permeability of metal foams. CSME 2004 Forum 2004;2004:220–8.

[95] Langlois S, Coeuret F. Flow-through and flow-by porous electrodes of nickel foam. I. Material characterization. J Appl Electrochem 1989;19:43–50. https://doi.org/10.1007/BF01039388.

[96] Brun E, Vicente J, Topin F, Occelli R. Geometrical measurement of real foams from 3D images. MetFoam 2007 - Proc 5th Int Conf Porous Met Met Foam 2008:425–8.

[97] Miwa S, Revankar ST. Hydrodynamic characterization of nickel metal foameffects of pore structure and permeability. Heat Transf Eng 2012;33:800–8. https://doi.org/10.1080/01457632.2012.646872.

[98] Milazzo RG, Privitera SMS, Scalese S, Lombardo SA. Effect of morphology and mechanical stability of nanometric platinum layer on nickel foam for hydrogen evolution reaction. Energies 2019;12. https://doi.org/10.3390/en12163116.

[99] Dukhan N, Patel P. Equivalent particle diameter and length scale for pressure drop in porous metals. Exp Therm Fluid Sci 2008;32:1059–67. https://doi.org/10.1016/j.expthermflusci.2007.12.001.

[100] Dukhan N. Correlations for the pressure drop for flow through metal foam. Exp Fluids 2006;41:665–72. https://doi.org/10.1007/s00348-006-0194-x.

[101] Boomsma K, Poulikakos D, Zwick F. Metal foams as compact high performance heat exchangers. Mech Mater 2003;35:1161–76. https://doi.org/10.1016/j.mechmat.2003.02.001.

[102] Flitsanov Y, Kribus A. A cooler for dense-array CPV receivers based on metal foam. Sol Energy 2018;160:25–31. https://doi.org/10.1016/j.solener.2017.12.002.

[103] Kang DG, Lee DK, Choi JM, Shin DK, Kim MS. Study on the metal foam flow field with porosity gradient in the polymer electrolyte membrane fuel cell. Renew Energy 2020;156:931–41. https://doi.org/10.1016/j.renene.2020.04.142.

[104] Medraj M, Baril E, Loya V, Lefebvre LP. The effect of microstructure on the permeability of metallic foams. J Mater Sci 2007;42:4372–83. https://doi.org/10.1007/s10853-006-0602-x.

[105] Gerbaux O, Vercueil T, Memponteil A, Bador B. Experimental characterization of single and two-phase flow through nickel foams. Chem Eng Sci 2009;64:4186–95. https://doi.org/10.1016/j.ces.2009.06.056.

[106] Topin F, Bonnet JP, Madani B, Tadrist L. Experimental analysis of multiphase flow in metallic foam: Flow laws, heat transfer and convective boiling. Adv Eng Mater 2006;8:890–9. https://doi.org/10.1002/adem.200600102.

[107] Hugo J-M, Brun E, Topi F. Metal Foam Effective Transport Properties. Evaporation, Condens Heat Transf 2011. https://doi.org/10.5772/21321.

[108] Ismail MS, Hughes KJ, Ingham DB, Ma L, Pourkashanian M. Effect of PTFE loading of gas diffusion layers on the performance of proton exchange membrane fuel cells running at high-efficiency operating conditions. Int J Energy Res 2013;37:1592–9. https://doi.org/10.1002/er.2968.

[109] Banhart J. Manufacture, characterisation and application of cellular metals and metal foams. Prog Mater Sci 2001;46:559–632. https://doi.org/10.1016/S0079-6425(00)00002-5.

[110] Montillet A, Comiti J, Legrand J. Determination of structural parameters of metallic foams from permeametry measurements. J Mater Sci 1992;27:4460–4. https://doi.org/10.1007/BF00541579.

[111] Jadhav PH, Gnanasekaran N, Perumal DA. Numerical consideration of LTNE and darcy extended forchheimer models for the analysis of forced convection in a horizontal pipe in the presence of metal foam. J Heat Transfer 2021;143:1–16. https://doi.org/10.1115/1.4048622.

[112] Becker J, Flückiger R, Reum M, Büchi FN, Marone F, Stampanoni M. Determination of Material Properties of Gas Diffusion Layers: Experiments and Simulations Using Phase Contrast Tomographic Microscopy. J Electrochem Soc 2009;156:B1175. https://doi.org/10.1149/1.3176876.

Chapter 5

Polymer Electrolyte Fuel Cell Operating with Nickel Foam-based Gas Diffusion Layers

5.1 SUMMARY

Due to their outstanding structural, transport and electrical characteristics, nickel foams serve as excellent candidate materials for gas diffusion layers (GDLs) in polymer electrolyte fuel cells (PEFCs). In this work, a new three-dimensional PEFC model was developed to explore the local and global fuel cell performance with nickel foam-based GDLs. The fuel cell operating with nickel foam GDL was shown to have, due to its superior mass and charge transport properties, higher oxygen and water concentration and current density compared to that operating with the conventional carbon fibre-based GDLs. The results show that the pumping power should be taken into account when optimising the dimensions of the flow channels and as such the net power density must be the criterion for optimisation. The optimal dimensions of

the flow channels for the fuel cell operating with nickel foam based GDLs were found to be 0.25 mm for the channel height and 1 mm for the channel width; the maximum net power density with these dimensions was around 0.95 W/cm^2 which is two times higher than that operating with carbon fibre based GDLs. All the results have been presented and critically discussed.

5.2 INTRODUCTION

The polymer electrolyte fuel cell (PEFC) is a promising clean energy conversion technology that directly converts the chemical energy stored in hydrogen to electrical energy without producing greenhouse gases [1,2]. The PEFC technology has been employed for transportation applications due to its favourable features: high power density and efficiency, zero-emission, low operating temperature, and compact design [3–6]. A standard PEFC is composed of several key components: (i) a proton-conductive polymeric membrane electrolyte, (ii) anode and cathode catalyst layers where half electrochemical reactions take place, (iii) anode and cathode gas diffusion layers, and (iv) anode and cathode flow field plates.

The gas diffusion layer (GDL) is a wet-proof porous medium that is positioned between the catalyst layer and the flow field plate. The properties of the GDL significantly affect the transport of mass, heat, and electrons between the catalyst layer and the flow field plate [7,8]. A GDL should ideally fulfil the following functions: (i) supply sufficient oxygen/hydrogen to the catalyst layers, (ii) ease the removal of excess water, (iii) enable fast charge and heat transfer between catalyst layers and

flow field plates, and (iv) mechanically support the membrane [9,10]. The most used form of GDL is carbon paper [11,12]. Nevertheless, the carbon paper-based GDLs are generally susceptible to various forms of degradation including: mechanical degradation, thermal degradation, carbon dissolution, and erosion [13–15]. These degradations detrimentally affect the PEFC performance and lifespan. As a result, more robust GDL materials are required to be developed for PEFC applications.

Metal foams have recently gained significant attention as a prospective GDL material for PEFC applications. This interest stems from their outstanding advantages surpassing conventional carbon fibre-based GDLs. Nickel foam is a promising material for PEFC applications as a GDL and/or flow field plate (FFP) due to its superior electrical and thermal conductivity, high specific surface area, and porous structure. Shin et al. [16] experimentally compared the nickel foam-based cathode FFP to conventional graphite cathode FFP with serpentine channels. They showed that the nickel foam-based FFP exhibits approximately 50% higher fuel cell performance and more stable operation. Similarly, Tseng et al. [17] evaluated the nickel foam-based cathode FFP in PEFCs. Their results indicated that the nickel foam-based FFP performed better than the conventional graphite-based FFPs. The maximum power density with carbon-based FFP was 0.95 W/cm^2 at 0.5 V, whereas it was 1.35 W/cm^2 with nickel foam-based FFP. This is due to the superior mass transport characteristics of nickel foam-based FFP. Likewise, Tabe et al. [18] conducted an experimental investigation on the nickel foam-based FFP as an alternative to the conventional graphite-based FFPs. Their results showed that the nickel foam-based FFP exhibited

better water drainage capability and higher stability than the conventional graphite-based FFPs. Ercelik et al. [19] investigated the structural and transport characteristics of the nickel foam-based GDL using X-ray computed tomography. Their findings revealed that the nickel foam-based GDLs have superior porosity, specific surface area, gas permeability, and effective diffusivity compared to carbon fibre-based GDLs. The same research group [20] evaluated the nickel foam-based GDL under realistic fuel cell compression. They reported that, compared to the almost isotropic uncompressed sample, the anisotropy of the nickel foam becomes significantly more profound with increasing compression. Furthermore, their findings indicated that as the compression increased, the mass transport properties decrease and the specific surface area increases.

Adequate water management is crucial for PEFCs to achieve high performance and extended lifetime [21,22]. Water is produced at the cathode catalyst layer as a results of the oxygen oxidation reaction (ORR). Furthermore, the reactant and oxidant gases are normally humidified to ensure that the membrane is adequately hydrated, particularly at the start of the fuel cell operation. A portion of the water produced at the cathode may transport to the anode through the membrane due to concentration difference [23]. This mode of transport for dissolved water through the membrane is normally referred to as back diffusion. On the other hand, water at the anode is transported to the cathode through electro-osmotic drag; this may lead to dehydration of the anode side of the membrane. Excess water, particularly at the cathode side, normally leads to water flooding that prevents the supply of the

reactant gases to the catalyst layer, thereby degrading. The design of the flow channels was, amongst other factors, found to be crucial in removing excess water and maintaining high fuel cell performance [24–27]. The flow channels are grooved into the flow field plates which are conventionally made from graphite. However, metallic flow field plates have been increasingly employed in PEFCs and this is due to the low manufacturing cost, high mechanical strength, being lightweight, and high electrical and thermal conductivity [28].

When designing flow channels, it is vital to optimise both the mass and charge transports. Evidently, wider flow channels allow for better mass transport to/from the catalyst layers, whereas broader ribs enhance electrical conduction between the FFPs and the catalyst layers. Conventional FFPs normally host rectangular cross-section flow channels [29]. However, there have been numerous studies investigating the impact of the design of the flow channel on the fuel cell performance. For example, Khazaee and Sabadbafan [30] numerically investigated three different cross-section designs (rectangular, triangular, and elliptical) for flow channels and they reported that the rectangular cross-section exhibited slightly higher performance at the lower cell voltages. Moreover, for all three cross-section designs, the fuel cell performance was found to significantly improve when the cross-sections increased from 1 to 2 mm^2. Similarly, Tian et al. [31] investigated the impact of three different flow channel cross-section designs: rectangular, trapezoidal, and hybrid that involves a rectangular inlet and a trapezoidal outlet. They found that the hybrid design demonstrated a higher performance as the gas velocity within the channel

increases with this design, thus supplying higher amounts of reactant gases to the catalyst layers through convection. Carcedea et al. [32] created a multiphase and non-isothermal three-dimensional model aiming to assess how the rectangular channel size impacts the PEFC performance. Expectedly, they found that as the channel height or width decrease, the cell performance improves. For instance, when the channel width was reduced from 3 mm to 0.5 mm, there was an 11% increase in the maximum cell power. Higier and Liu [33] experimentally investigated the current density distribution beneath the channel and rib regions and they found that the best-performing FFP channel configuration is that with narrower channels. Their outcome showed that the current density at 0.4 V was approximately 0.6 A/cm^2 for 2 mm channel width, while it was 0.8 A/cm^2 for 1 mm channel width. Likewise, Yoon et al. [34] carried out an experimental study to investigate the effects of channel and rib dimensions. The dimensions of the ribs were varied between 0.5 and 3 mm while keeping the channel width at 1 mm. They found that the fuel cell performance becomes better as the ratio between the areas of the channel and the rib increases. Scholta et al. [35] experimentally found that the ideal width for both the channel and the rib ranged between 0.7 and 1 mm. They also reported that very small channel dimensions are technically challenging and costly. Moreover, very narrow or shallow flow channels may be clogged with water droplets. On the other hand, a channel height of more than 1.5 mm was found to cause a considerable amount of wasted oxygen. Carcedea et al. [36] numerically and experimentally evaluated the influence of the channel dimensions of a large-active-area (200 cm^2) PEFC. They observed an improvement of up to 7% in the fuel cell peak power density with the smallest

channel height (i.e. 0.25 mm); this was attributed to the enhanced removal of excess liquid water.

Kerkoub et al. [37] numerically investigated parallel, serpentine and interdigitated flow configurations with different channel widths (0.4 - 1.4 mm). They showed that, for all the configurations, the fuel cell performance improves with decreasing channel width (and increasing rib width). As the channel width decreases, the convective flow beneath the ribs increases, leading to higher reactant velocity beneath these ribs and supplying more reactant gases to the catalyst layer. Similar findings were reported by Liu et al. [38]. Kaplan [39] developed a 3D PEFC numerical model to evaluate the effect of the dimensions of rectangular channels on the cell performance. Their results showed that the maximum current density was achieved with a 0.2 mm channel width and a 1 mm channel height due to reduced contact resistance and enhanced oxygen consumption. Chowdhury et al. [40] developed a 3D PEFC isothermal model. They showed that, for a given channel height, the fuel cell performance improves with decreasing channel width. They also highlighted that channel height and width are equally important for the cell performance. In addition, they emphasised that the pumping power must be taken into the account when optimising the dimensions of the channel dimension. Considering both the peak power density and pumping power requirements, the optimal dimensions of the channel were found to be 1 mm for the channel width and 1 mm for the rib width. Heidary et al. [41] introduced baffles within the channels to boost mass transport and mitigate water flooding at high current densities. The cell performance was improved

by 28% when these baffles were arranged in a staggered configuration rather than in-line configuration. Likewise, Chen et al. [42] developed a two-dimensional numerical model to examine the impact of baffled flow channels on the PEFC performance. They found that the baffles in the channels improved the mass transport and cell performance; however, these baffles caused an increase in the required pumping power. To optimise cell performance and minimise pumping power, they proposed introducing small baffles at the start of the channels and transitioning to larger baffles towards the end of the channels. Cooper et al. [43] conducted a comprehensive experimental study to optimise the channel dimensions within a range of 0.25 – 1 mm. They emphasised the importance of accounting for the required pumping power when optimising these dimensions. They found that, for the parallel FFP, the peak power density was achieved by a 0.25 mm channel height and a 0.25 mm channel width. However, when the required pumping power was taken into consideration, the highest net output power was obtained with a 0.5 mm channel height and a 0.5 mm channel width.

The above literature survey underscores the crucial role of the channel dimensions in attaining high performance. Due to its superior interior characteristics, nickel foam emerges as a promising material for GDLs in PEFCs; however, there have been no comprehensive PEFC modelling studies focusing on the use of nickel foam as a GDL. This work aims at assessing the performance of PEFC equipped with conventional and nickel foam GDLs. The pressure drop and pumping power required were taken into

account when optimising the dimensions of the flow channels. To this end, a three-dimensional PEFC was created to identify these optimal dimensions.

5.3 METHODOLOGY

The geometrical models were constructed using the COMSOL Multiphysics® 6.0 software. Figure 5.1 depicts the computational domain for the baseline case, where both the channel height and width are set as 1 mm. As shown in the figure, a single straight flow channel has been modelled to save computational time and resources. The following assumptions and considerations were taken into account when developing the current model:

- The operation of the fuel cell is steady state.
- The flow in the channels is laminar (Re << 2300) and incompressible (Ma << 0.3).
- The gas mixtures are treated as ideal gases.
- The catalyst layers and membrane are assumed to be isotropic, whereas gas diffusion layers are anisotropic.
- The membrane is impermeable to gases.
- The gas diffusion layer intrusion into the channel is considered.
- The interfacial contact resistances between components are negligible.

In this study, the channel dimensions were optimised for two different GDL materials: carbon fibre-based and nickel foam-based. A total of 32 scenarios were investigated in this study. The gas diffusion layers were considered 20% compressed under the channel area and 40% compressed under the rib area. The inlet volumetric flow rates

on the anode and cathode sides were 0.1 L/min and 0.5 L/min, respectively. The outlet pressure of both anode and cathode flow channels was set to be zero gauge pressure. The symmetrical boundary conditions were defined as shown in Figure 5.1. Table 5.1 shows the parameters used in the numerical model.

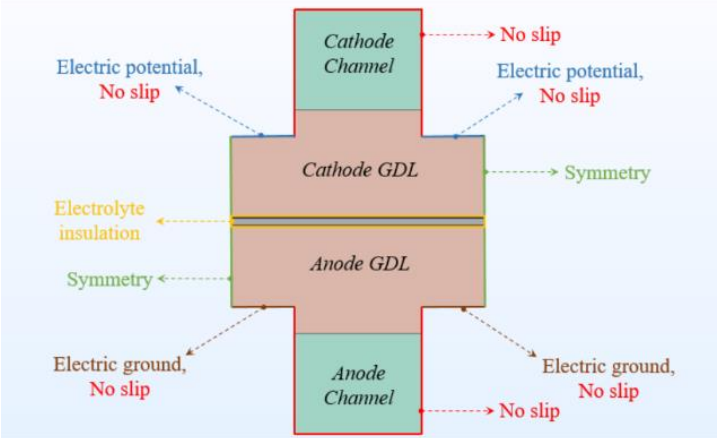

(a)

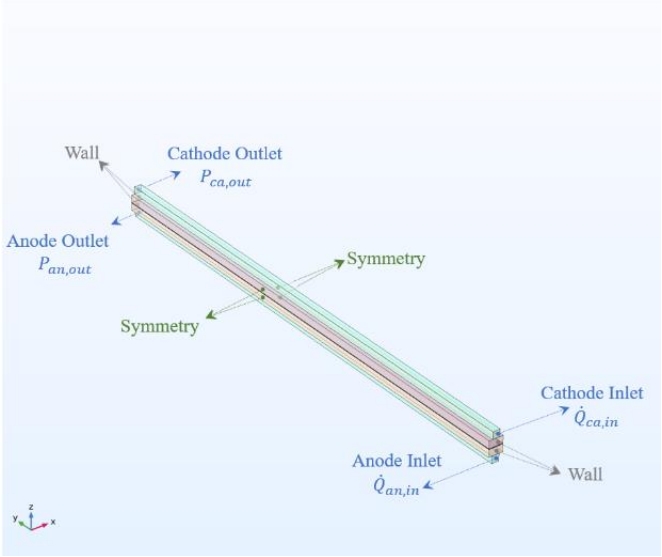

(b)

Figure 5.1 – The PEFC computational domain and the associated boundary conditions: (a) the cross-section and (b) the isometric views.

Table 5.1 – Parameters used in the model [20,43–53]

Parameter	Value	Unit
Channel length (L)	70	mm
Channel height (h)	1 – 0.25	mm
Channel width (w)	1 – 0.25	mm
Carbon fibre-based GDL height under rib	0.191	mm
Carbon fibre-based GDL height under channel	0.254	mm
Nickel foam-based GDL height under rib	0.63	mm
Nickel foam-based GDL height under channel	0.84	mm
Catalyst layer thickness	0.014	mm
Membrane thickness	0.051	mm
Carbon fibre-based GDL porosity under rib	0.6	-
Carbon fibre-based GDL porosity under channel	0.7	-
Nickel foam-based GDL porosity under rib	0.842	-
Nickel foam-based GDL porosity under channel	0.866	-
Catalyst layer porosity	0.4	-
Carbon fibre-based GDL permeability under rib (through-plane)	7×10^{-13}	m^2
Carbon fibre-based GDL permeability under rib (in-plane)	3×10^{-13}	m^2
Carbon fibre-based GDL permeability under channel (through-plane)	2×10^{-12}	m^2
Carbon fibre-based GDL permeability under channel (in-plane)	5×10^{-13}	m^2

Nickel foam-based GDL permeability under rib (through-plane)	5.6×10^{-10}	m^2
Nickel foam-based GDL permeability under rib (in-plane)	3.4×10^{-10}	m^2
Nickel foam-based GDL permeability under channel (through-plane)	9.7×10^{-10}	m^2
Nickel foam-based GDL permeability under channel (in-plane)	6.9×10^{-10}	m^2
Catalyst layer permeability	1×10^{-12}	m^2
Carbon fibre-based GDL electrical conductivity under rib (through-plane)	600	S/m
Carbon fibre-based GDL electrical conductivity under rib (in-plane)	5000	S/m
Carbon fibre-based GDL electrical conductivity under channel (through-plane)	53	S/m
Carbon fibre-based GDL electrical conductivity under channel (in-plane)	4000	S/m
Nickel foam-based GDL electrical conductivity under rib (through-plane)	500000	S/m
Nickel foam-based GDL electrical conductivity under rib (in-plane)	500000	S/m
Nickel foam-based GDL electrical conductivity under channel (through-plane)	470000	S/m
Nickel foam-based GDL electrical conductivity under channel (in-plane)	470000	S/m
Catalyst layer electrical conductivity	53	S/m

Membrane conductivity	10	S/m
Carbon fibre-based GDL thermal conductivity under rib (through-plane)	2	W/(m·K)
Carbon fibre-based GDL thermal conductivity under rib (in-plane)	33	W/(m·K)
Carbon fibre-based GDL thermal conductivity under channel (through-plane)	1.27	W/(m·K)
Carbon fibre-based GDL thermal conductivity under channel (in-plane)	21	W/(m·K)
Nickel foam-based GDL thermal conductivity under rib (through-plane)	95	W/(m·K)
Nickel foam-based GDL thermal conductivity under rib (in-plane)	95	W/(m·K)
Nickel foam-based GDL thermal conductivity under channel (through-plane)	91	W/(m·K)
Nickel foam-based GDL thermal conductivity under channel (in-plane)	91	W/(m·K)
Catalyst layer thermal conductivity	0.3	W/(m·K)
Nickel foam-based GDL effective diffusivity under rib (through-plane)	0.145	cm^2/s
Nickel foam-based GDL effective diffusivity under rib (in-plane)	0.143	cm^2/s
Nickel foam-based GDL effective diffusivity under channel (through-plane)	0.152	cm^2/s
Nickel foam-based GDL effective diffusivity under channel (in-plane)	0.154	cm^2/s

Diffusivity of oxygen in nitrogen	2.19×10^{-5}	m^2/s
Anode catalyst coefficient	0.5	-
Cathode catalyst coefficient	1	-
Relative humidity of inlet gases	90	%
Oxygen molar ratio in air	0.21	-
Nitrogen molar ratio in air	0.79	-
Cell temperature, T	60	°C
Atmospheric pressure	101325	Pa
Reference exchange current density at cathode	0.004	A/m^2
Reference exchange current density at anode	30	A/m^2
Specific surface area of catalyst layer	1×10^7	m^2/m^3
Anode volumetric flow rate	0.1	L/min
Cathode volumetric flow rate	0.5	L/min
Faraday's constant, F	96485	C/mol
Universal gas constant, R	8.314	J/(mol·K)
Isobaric specific heat capacity of air, cp	1008	J/(kg·K)
Specific heat ratio of air, k	1.401	-
Efficiency of compressor, η_{comp}	70	%

The following set of conservation equations were used in the model [30,54,55]. The conservation of mass is expressed as follows:

$$\nabla (\rho \cdot \boldsymbol{u}) = S_m \quad \textbf{(5.1)}$$

where ∇ is the operator $\left(\boldsymbol{i}\frac{\partial}{\partial x}+\boldsymbol{j}\frac{\partial}{\partial y}+\boldsymbol{k}\frac{\partial}{\partial z}\right)$, ρ is fluid density (kg/m^3), $\boldsymbol{u}$ is the velocity vector, and S_m is the source term. Below is the conservation of momentum equation:

$$\nabla\cdot\left(\frac{\rho\,\boldsymbol{u}\,\boldsymbol{u}}{\varepsilon^2}\right)=-\nabla P+\ \nabla\cdot\mu\left[\left(\nabla\left(\frac{\boldsymbol{u}}{\varepsilon}\right)+\nabla\left(\frac{\boldsymbol{u}}{\varepsilon}\right)^T\right)-\frac{2}{3}\nabla\frac{\boldsymbol{u}}{\varepsilon}\mathbf{I}\right]+S_u \qquad \textbf{(5.2)}$$

$$S_u=\ -\frac{\mu}{K}\boldsymbol{u} \qquad \textbf{(5.3)}$$

where ε is porosity of porous medium, P means the pressure, $\mathbf{I}$ is the identity matrix, μ is the dynamic viscosity (Pa·s), and K is the permeability (m^2) of the porous media and S_u is the momentum source term which represent Darcy's law in this case. The porosity of the flow channels is evidently unity. The conservation of species equation is given as:

$$\nabla\cdot(\rho\,\boldsymbol{u}\,X_k)=\nabla\left(\rho\,D_k^{eff}\,X_k\right)+\ S_k \qquad k=O_2,H_2O,H_2 \qquad \textbf{(5.4)}$$

where D_k^{eff} is effective mass diffusivity of the species k, X_k is mass fraction of k, and S_k is the source term of the species k. The effective diffusivity values of carbon fibre-based GDLs and catalyst layers are calculated using the Bruggeman correlation:

$$D_k^{eff}=\ \varepsilon^{1.5}\,D_k \qquad \textbf{(5.5)}$$

where ε and D_k are the porosity of the porous medium and the bulk diffusion coefficient of species k, respectively. It should be noted that the effective diffusivities of nickel foam were taken from the literature [20]. The source terms of species are only applicable in the catalyst layers:

$$S_{H_2}=\ \frac{-M_{H_2}\,i_a\,a_a}{2F} \qquad \textbf{(5.6)}$$

$$S_{O_2} = \frac{-M_{O_2}\, i_c\, a_c}{4F} \qquad \textbf{(5.7)}$$

$$S_{H_2O} = \frac{-M_{H_2O}\, i_c\, a_c}{2F} \qquad \textbf{(5.8)}$$

where M_k is molecular weight of species k (kg·mol^{-1}) and F is Faraday's constant (96485 C/mol). i_a and i_c are the anode and cathode volumetric current densities, respectively. a_a and a_c are the anode and cathode specific surface areas, respectively. The conservation of charge is represented by the following equations:

$$\nabla \cdot (-\sigma_s\, \nabla \phi_s) = S_s \qquad \textbf{(5.9)}$$

$$\nabla \cdot (-\sigma_l\, \nabla \phi_l) = S_l \qquad \textbf{(5.10)}$$

where σ_s and σ_l are electrical conductivities of solid and membrane phases, respectively. ϕ_s and ϕ_l represent the solid and membrane phase potentials, respectively. S_s and S_l are the charge source terms which are equal to the volumetric transfer current densities at the anode or cathode electrodes. These current densities are obtained from the Butler-Volmer equations:

$$i_a a_a = i_a^{ref} a_a \left(\frac{X_{H_2}}{X_{H_2}^{ref}}\right)^{0.5} \left[exp\left(\frac{\alpha_{a,a}F}{RT}\eta_{act,a}\right) - exp\left(-\frac{\alpha_{a,c}F}{RT}\eta_{act,c}\right)\right] \textbf{(5.11)}$$

$$i_c a_c = i_c^{ref} a_c \left(\frac{X_{O_2}}{X_{O_2}^{ref}}\right) \left[exp\left(\frac{\alpha_{c,a}F}{RT}\eta_{act,c}\right) - exp\left(-\frac{\alpha_{c,c}F}{RT}\eta_{act,c}\right)\right] \qquad \textbf{(5.12)}$$

where i_a^{ref} and i_c^{ref} are the reference current densities at the anode and the cathode, respectively. a_a and a_c are the anode and cathode specific surface areas, respectively. $X_{H_2}^{ref}$ and $X_{O_2}^{ref}$ represents the hydrogen and oxygen mass fraction at

reference conditions (25°C and 1 atm). $\alpha_{a,a}$ and $\alpha_{a,c}$ are anodic and cathodic charge transport coefficient at anode electrode. Likewise, $\alpha_{c,a}$ and $\alpha_{c,c}$ are anodic and cathodic charge transport coefficient at cathode electrode. R is the universal gas constant (8.314 J/(mol·K)) and T is the temperature. $\eta_{act,a}$ and $\eta_{act,c}$ are anodic and cathodic activation overpotentials:

$$\eta_{act,a} = \phi_s - \phi_l \qquad \textbf{(5.13)}$$

$$\eta_{act,c} = \phi_s - \phi_l - V_0 \qquad \textbf{(5.14)}$$

where V_0 is the equilibrium cell potential and could be obtained using the following equation [56]:

$$V_0 = 1.482 - 8.45 \times 10^{-4}\, T + 4.31 \times 10^{-5}\, T \ln\left(P_{H_2}\, P_{O_2}^{0.5}\right) \qquad \textbf{(5.15)}$$

The conservation of energy equation is given by:

$$\nabla \cdot \left(\rho c_p \boldsymbol{u} T\right) = \nabla \cdot (\lambda \nabla T) + S_T \qquad \textbf{(5.16)}$$

where c_p is specific heat capacity (J/(kg·K)), λ is thermal conductivity (W/m·K), and S_T is the heat source term which takes the following forms in the catalyst layer and the membrane, respectively:

$$S_{T,CL} = n\, i + \left(\frac{T\Delta S}{n\, F}\right) i \qquad \textbf{(5.17)}$$

$$S_{T,mem} = \frac{i^2}{\sigma_{mem}} \qquad \textbf{(5.18)}$$

The power required for pumping should be taken into account when computing the net output power needed for the optimisation study, and the cell power density is given by:

$$E_{cell} = i \cdot V \qquad \textbf{(5.19)}$$

and the pumping power density (E_{pump}) is related to the pressure drop along the flow channel [57]:

$$E_{pump} = \frac{\dot{m}_{air} \cdot c_P \cdot T}{A \cdot \eta_{comp}} \left(\left(\frac{P_{inlet}}{P_{atm}} \right)^{\frac{k-1}{k}} - 1 \right) \qquad \textbf{(5.20)}$$

where $\dot{m}_{air}$ is the air mass flow rate (kg/s), c_P is the isobaric specific heat capacity of air (J/(kg·K)), T is the temperature of air (K), A is the cell active area (cm^2), η_{comp} is the efficiency of compressor, P_{inlet} cathode inlet pressure (Pa), P_{atm} is atmospheric pressure (Pa), and k is the specific heat ratio of air. The required pumping power is directly related to the pressure drop through the flow channel [57]. Therefore, the net power density (E_{Net}) is given by:

$$E_{Net} = E_{Cell} - E_{Pump} \qquad \textbf{(5.21)}$$

To ascertain mesh-independent results, the element number has been systematically changed for the base case (h = 1 mm and w = 1 mm) of nickel foam-based GDL analyses. Figure 5.2 exhibits the meshed geometry of the base case with nickel foam based GDL. Figure 5.3 shows the current density values at cell voltages of 0.3, 0.4, and 0.5 V and the corresponding computation time as they change with the number of elements. The figure shows that, to achieve a mesh-independent solution, the

required number of elements is ~80,000 with a computation time of approximately 1,800 s. All the numerical simulations were run on a workstation (Intel® Xeon® CPU E5-1650 v4 @ 3.60GHz) with 192 GB of installed RAM.

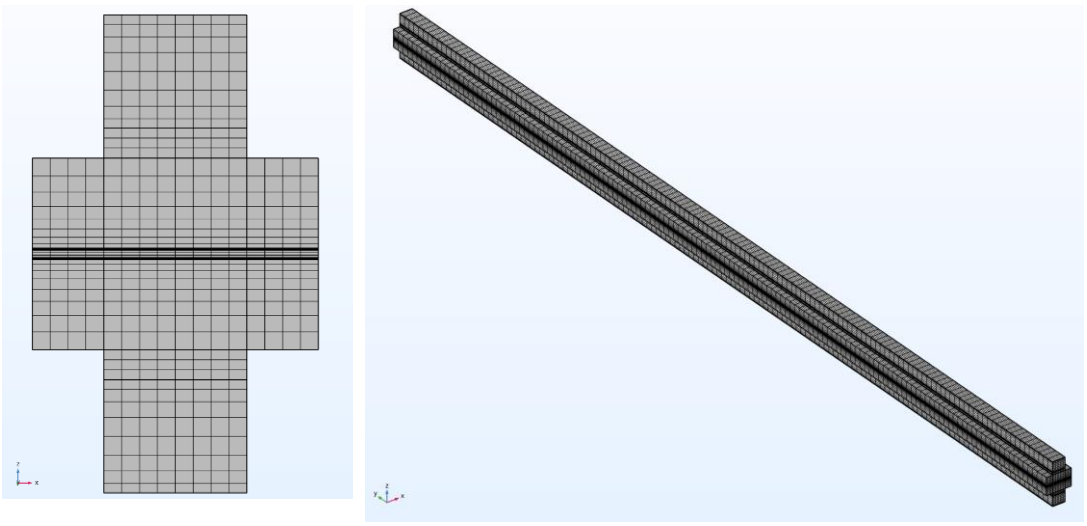

(a) **(b)**

Figure 5.2 – Nickel foam-based PEFC meshed geometry. (a) The cross section of the meshed geometry and (b) the 3D view of the meshed geometry.

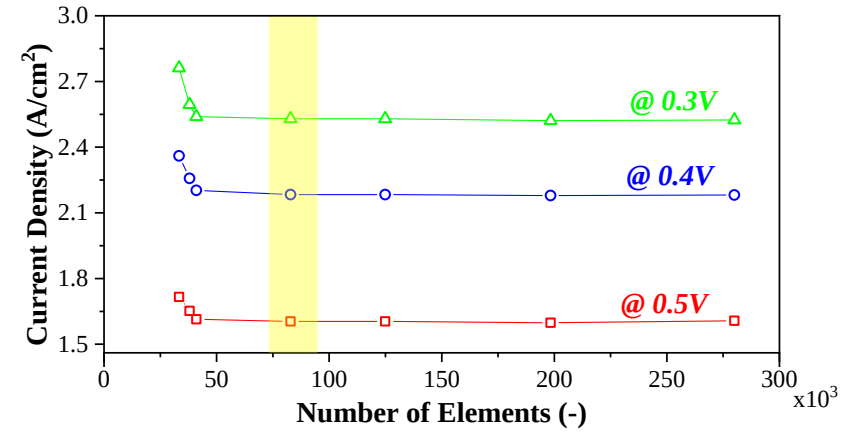

(a)

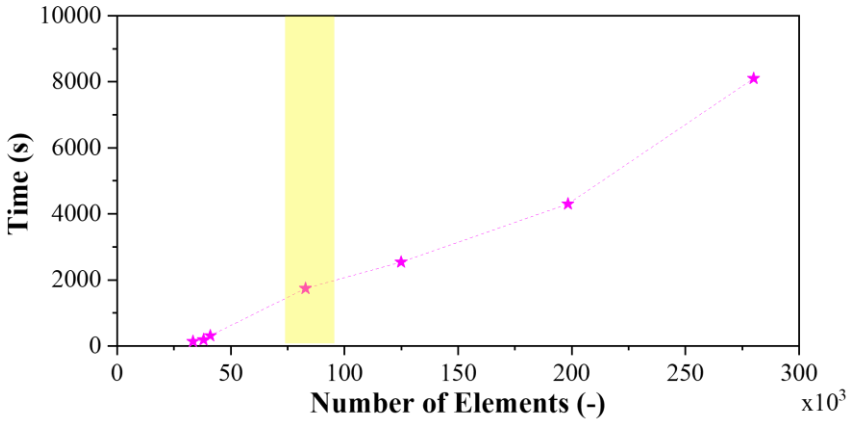

(b)

Figure 5.3 – The grid independency test of the modelled PEFC with nickel foam-based GDLs (h = 1mm, w = 1mm): (a) the current densities at three different cell voltages and (b) the equivalent computation times. The shaded yellow box shows the selected element numbers.

5.4 RESULTS AND DISCUSSION

In order to validate the model's accuracy for carbon fibre based PEFC, the results of the base case channel dimensions, h = 1 mm and w = 1 mm, were compared to the experimental results obtained by Wang et al [53], as shown in Figure 5.4. As observed in the figure, the simulated numerical polarisation curve is in good agreement with the experimental results.

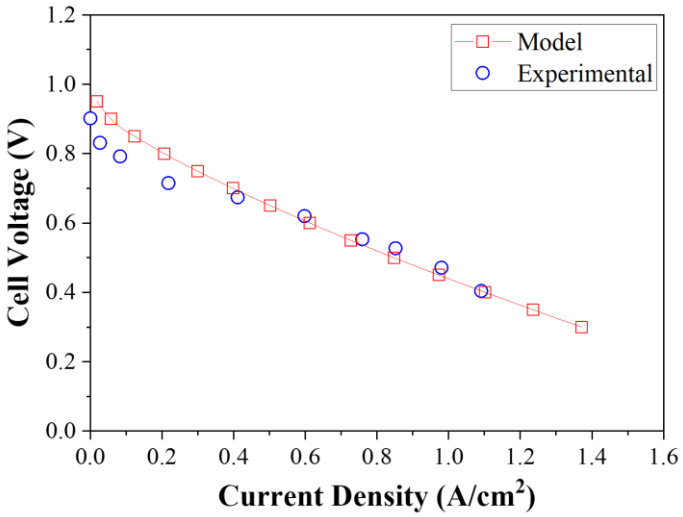

Figure 5.4 – The simulated polarisation curve for the base as compared with the experimental polarisation curve reported in [53].

5.4.1 Local distributions

A series of numerical simulations were carried out for different channel dimensions ranging from 0.25 to 1 mm to for carbon fibre-based and nickel foam-based PEFCs. Figures 5.5 show the mole fraction distributions at the cathode catalyst layer/GDL interface for carbon fibre-based PEFC taken near the inlet (y = 10 mm) and the outlet (y = 60 mm) for various channel widths at 0.4 V cell voltage for two channel heights: 0.25 and 1 mm. Figures A6.1 to A6.5 in the Appendix – VI display the oxygen and

water mole fractions for carbon fibre-based GDLs across all channel heights and widths. As expected, for all the cases, the maximum oxygen concentration and minimum water concentration coincide with the centre of the cathode flow channel. The oxygen concentration diminishes from the centre of the cathode flow channel to the midpoint of the rib, reaching a minimum level; the concentration of water exhibits an opposite trend. Oxygen concentration expectedly decreases from the inlet to the outlet as it is consumed at the catalyst layer, while water concentration increases as it is produced at the catalyst layer. For example, for a channel with width and height both 1 mm (Figure 5.5a and e), the oxygen mole fraction drops from 0.136 (at y = 10 mm) to 0.119 (at y = 60 mm), and water mole fraction increases from 0.242 to 0.267 at the corresponding locations. Another notable observation is the rise in oxygen concentration and the decline in water concentration with a decrease in channel height. This is, for a given flow rate, evidently attributed to the increased convective flow within the GDL. Similar trends are maintained for the channel widths 0.75, 0.50 and 0.25 mm. However, the uniformity of oxygen concentration decreases as the channel width decreases. For example, for 1 mm channel width and 1 mm channel height (Figure 5.5 a and e), moving from the centre of the flow channel to the centre of the rib, the mole fraction of oxygen decreases by 48%. On the other hand, for 0.25 mm channel width and 1 mm channel height (Figure 5.5d and h), moving from the centre of flow channel to the centre of the rib, the mole fraction of oxygen decreases by 98%. This is attributed to the widening of the rib as the channel width reduces. Likewise, for all the channel heights, the concentration of oxygen expectedly decreases with decreasing channel width.

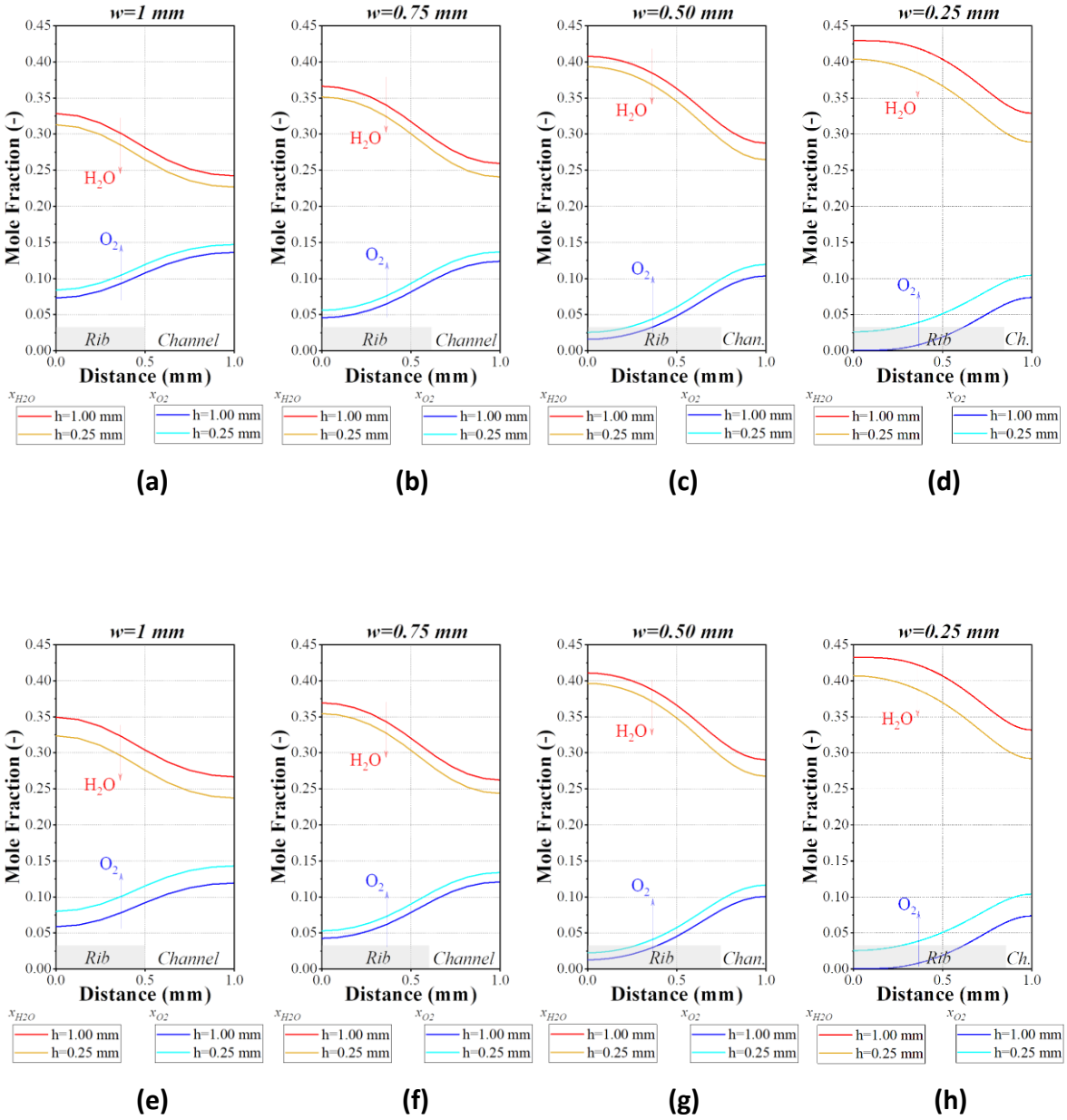

Figure 5.5 – Water and oxygen mole fractions at 0.4 V at the interface between the cathode carbon fibre-based GDL and the cathode catalyst layer near: (a-d) the inlet (y=10 mm) and (e-h) the outlet (y=60 mm) for channel heights 0.25 and 1 mm.

Figure 5.6 shows the oxygen and water mole fractions at the interface between the cathode catalyst layer and GDL for the nickel foam-based PEFC for the cases where the channel heights are 0.25 and 1 mm. Figures A6.6 to A6.10 in the Appendix – VI

display the oxygen and water mole fractions for nickel foam-based GDLs across all channel heights and widths. Notably, for all the cases, the uniformity of oxygen and water concentrations across the flow channel and rib improves with nickel foam based GDLs compared to carbon fibre-based GDLs (this is more profound with shallow flow channels); this is attributed to superior mass transport properties of the former GDLs [19, 20]. For example, near the inlet (y = 10 mm), using nickel foam as a GDL for the case where the channel width is 1 mm and channel height is 0.25 mm, the oxygen mole fraction decreases only by 9% moving from the centre of the channel to the centre of the rib. On the other hand, for the same setting, using carbon fibre-based GDL results in a decrease of 45%. This better uniformity with nickel foam based GDLs is beneficial as it mitigates local oxidant starvation and eases water transport beneath the ribs. One more notable observation is that, compared to the carbon fibre-based GDL, as the channel width decreases, the oxygen concentration increases and water concentration decreases within the cathode GDL. For example, near the outlet (y = 60 mm), for a channel height of 0.25 mm, the oxygen mole fraction under the middle of the rib increases from 0.107 to 0.121 with nickel foam based GDLs when the channel width decreases from 1 to 0.25 mm; however, for the same settings it decreases from 0.812 to 0.003 with carbon fibre-based GDLs. This is due to the flow being more dominated by convection in the case of nickel foam (which has superior gas permeability compared to the conversional GDL [19, 20]) as a result of the nickel foam's significant intrusion into the channels; the intrusion of nickel foam (210 μ) into the channels is over three times higher than that of carbon fibre-based GDL (60 μ).

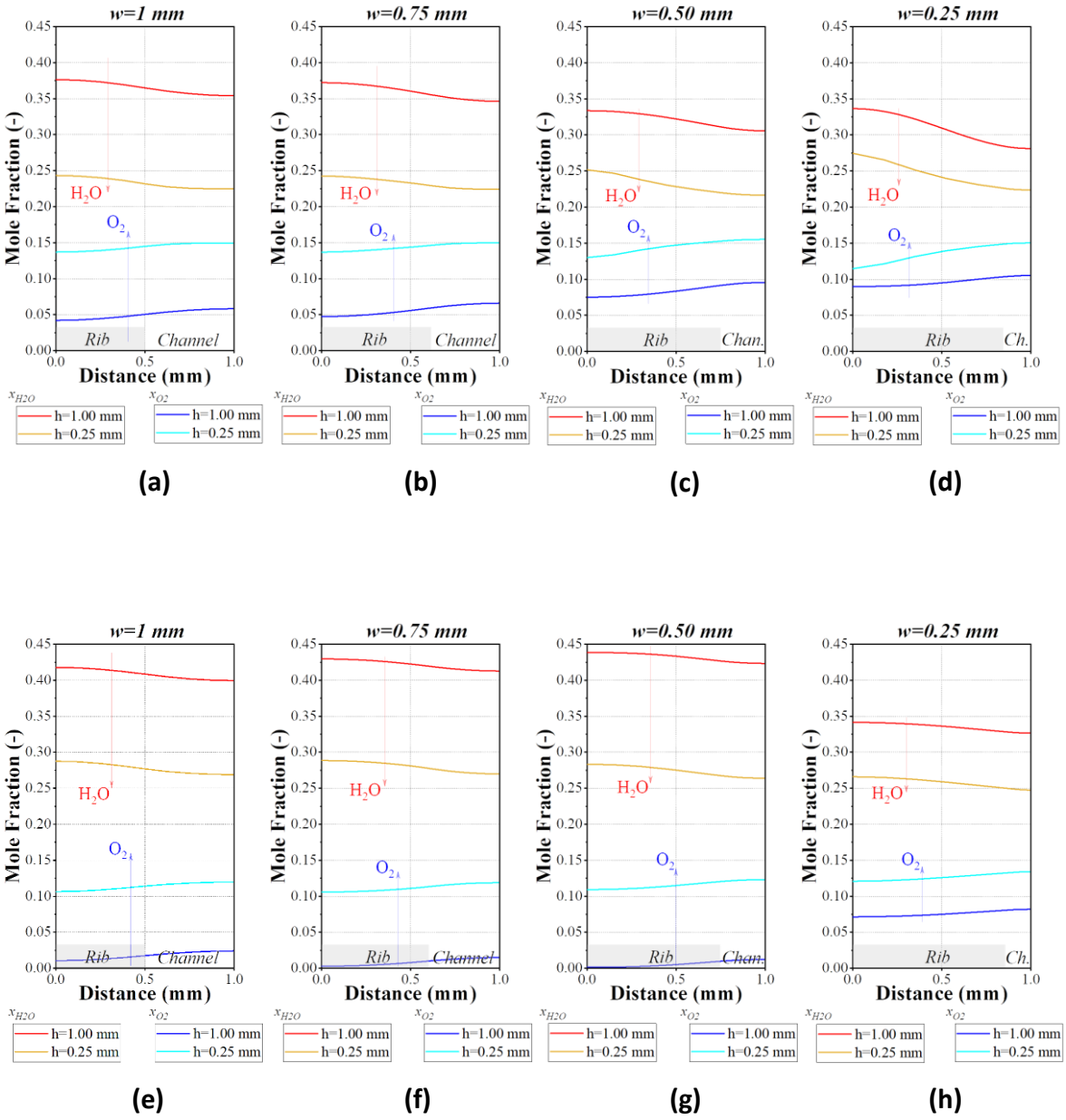

Figure 5.6 – Water and oxygen mole fractions at 0.4 V at the interface between the cathode nickel foam-based GDL and the cathode catalyst layer near: (a-d) the inlet (y=10 mm) and (e-h) the outlet (y=60 mm) for channel heights 0.25 and 1 mm.

Figures 5.7 and 5.8 show the local current density across the flow channel and the ribs. The first evident observation is that the current density decreases from the inlet to the outlet; this is due to the decreased concentration of oxygen from the inlet to the outlet as a result of its consumption at the catalyst layer. Further, the figure shows that, for all the cases, the current density is a maximum near the edge between the flow channel and the rib as this place is optimal for the combined supply of both the reactant gas and the electrons [56,58]. The figures also show that, for a given channel height, the non-uniformity of current density increases with increasing channel width. This is attributed to the electrons having to travel longer distances to reach the area beneath the centre of the flow channel as the channel width increases. Another observation is that, as the channel height decreases, the uniformity of the current density improves for nickel foam based GDL. This is attributed to the increased convective flows. As with oxygen and water concentrations, Figures 5.7 and 5.8 also show that, for all the cases, the current density is more uniform with a nickel foam based GDL compared to a carbon fibre-based GDL and this is evidently due to the superior mass and charge transport properties of the former GDL [19,20,47].

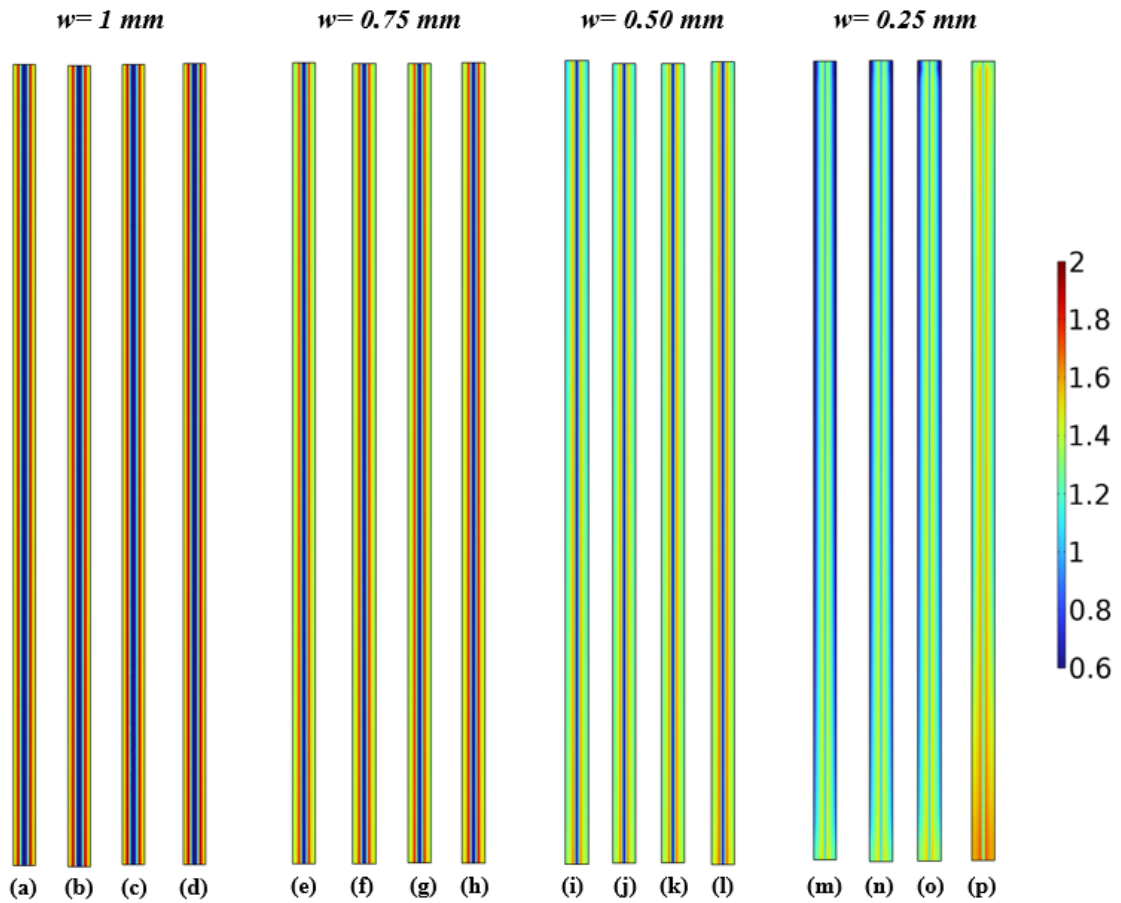

Figure 5.7 – Local current density distributions at the mid-cathode GDL in the carbon fibre-based PEFC at 0.4 V. The distributions are shown for different channel heights: (a, e, i, m) for h=1 mm; (b, f, j, n) for h=0.75 mm; (c, g, k, o) for h=0.5 mm; and (d, h, l, p) for h=0.25 mm. Note that the inlets are at the bottom of the domains.

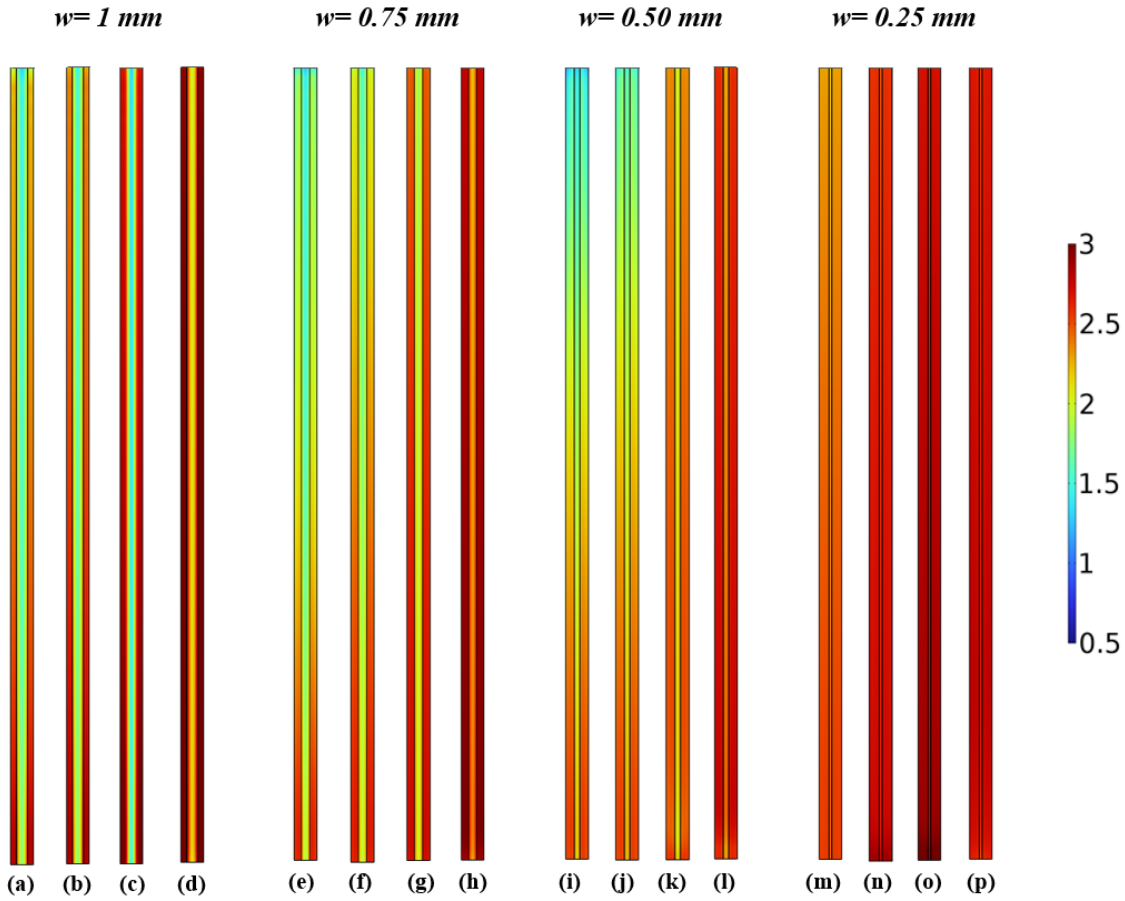

Figure 5.8 – Local current density distributions at the mid-cathode GDL in the nickel foam-based PEFC at 0.4 V. The distributions are shown for different channel heights: (a, e, i, m) for h=1 mm; (b, f, j, n) for h=0.75 mm; (c, g, k, o) for h=0.5 mm; and (d, h, l, p) for h=0.25 mm. Note that the inlets are at the bottom of the domains.

5.4.2 Polarisation curves

Figure 5.9 displays the polarisation curves of the various cases for the fuel cell operating with carbon fibre-based GDLs. The results show that for most of the cases there are optimal channel dimensions that ensure sufficient mass and charge transport and subsequently maximise fuel cell performance. Specifically, a channel

width of 0.50 mm proves to be optimal for most of the channel heights: 1 mm, 0.75 mm, and 0.5 mm. Clearly, this channel width (and the corresponding rib width) ensure adequate mass and charge transport for the above channel heights. However, this is not the case when the channel height is only 0.25 mm as the fuel cell was found to perform better for most of the key regions of the polarisation curve with the minimum channel width: 0.25 mm. This is clearly due to the fact that, for a given flow rate, these small channel dimensions, compared to other configurations, increase the convective flow within the cathode GDL and subsequently ensure supply of adequate amount of oxygen to the catalyst layer.

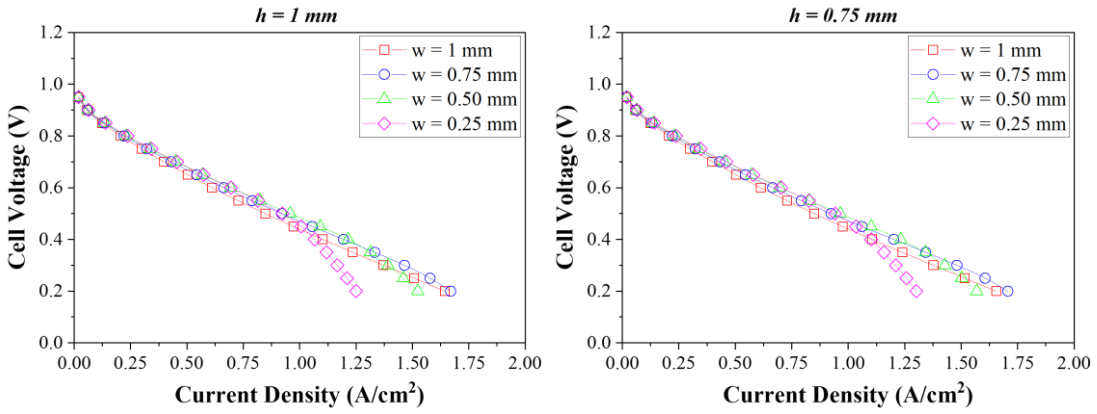

(a) **(b)**

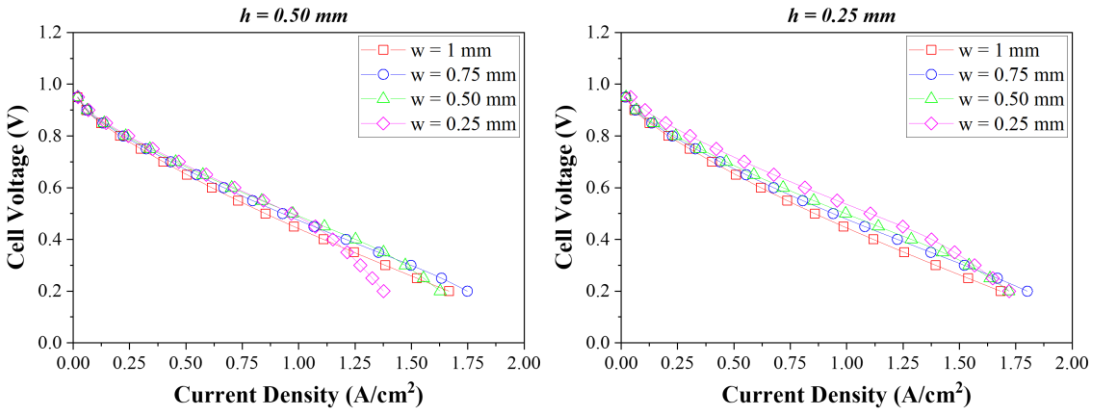

(c) **(d)**

Figure 5.9 – The polarisation curves of the carbon fibre-based GDL for four different channel widths (w) for (a) 1 mm, (b) 0.75 mm, (c) 0.5 mm, and (d) 0.25 mm channel heights (h).

Figure 5.10 shows the polarisation curves of the various cases for the fuel cell operating with nickel foam based GDLs. The first observation is that, for all the cases, the fuel cell with nickel foam based GDLs preform considerably better than with carbon fibre-based GDLs; this is due to the superior mass and charge transport properties demonstrated by the former GDLs [19,20,47]. For example, for the case where the channel width and height are both 1 mm, the limiting current density with carbon fibre-based GDLs is 1.64 A/cm^2 while it is 2.49 A/cm^2 with nickel foam based GDLs. The second observation is that the cases where the channel width is 0.25 mm perform better than other cases for most of the channel heights particularly for the channel height of 1 mm. The enhancement in fuel cell performance observed with the 0.25 mm channel width is attributed to the increased convective flow resulting from the reduced cross-sectional area of the channel. Notably, for the 1 mm channel height, the fuel cell with a 1 mm channel width outperforms those with 0.75 mm and 0.50 mm channel widths. The cross-sections of the flow channels with 0.75 mm and 0.50 mm channel widths appear to be not small enough to generate adequately high gas velocities within the nickel foam GDL. The final observation is that, at the smallest channel height (0.25 mm), the fuel cell performance becomes insensitive to channel width. Under this channel height, the cross-sections of the flow channels are

sufficiently small to generate sufficient convective flow, thus supplying abundant oxygen to the catalyst layer.

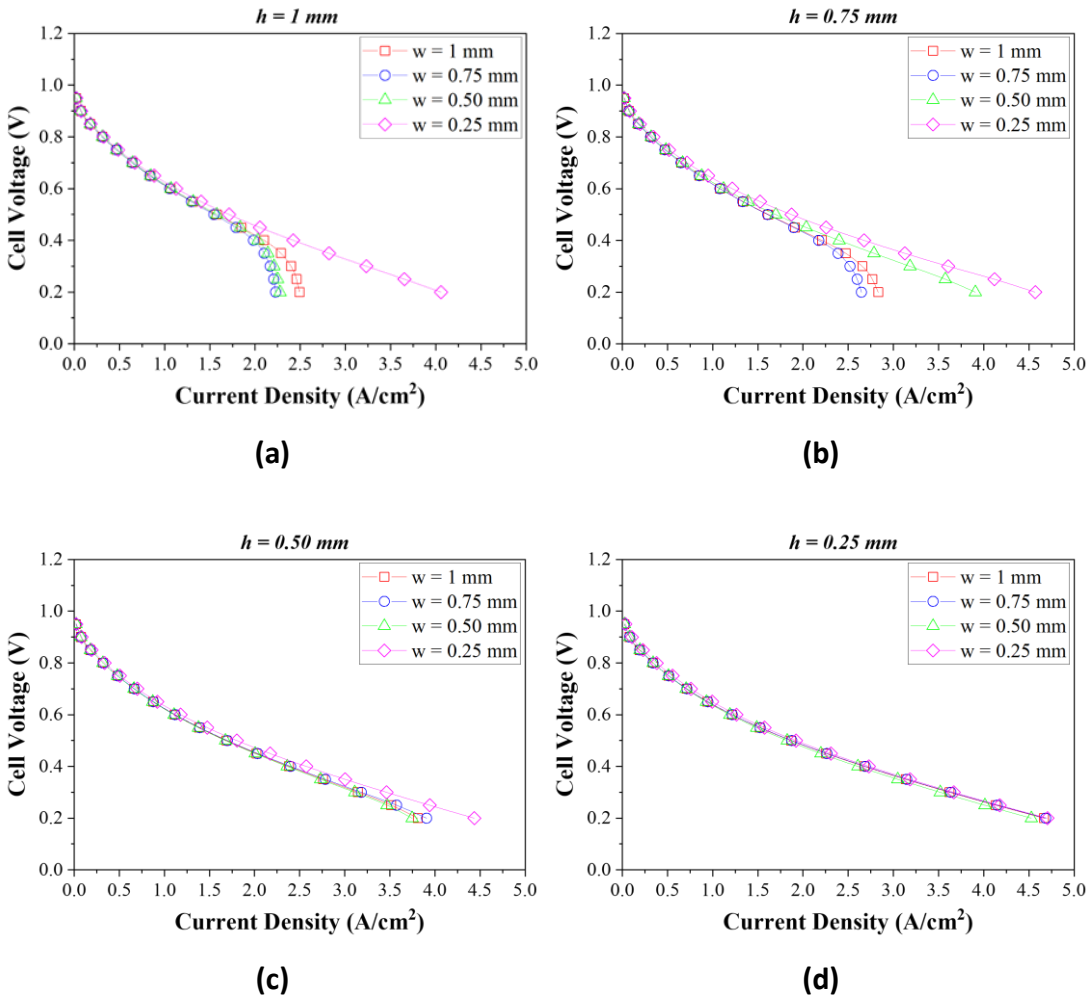

Figure 5.10 – The polarisation curves of the nickel foam-based GDL for four different channel widths (w) for (a) 1 mm, (b) 0.75 mm, (c) 0.5 mm, and (d) 0.25 mm channel heights (h).

5.4.3 Net power output

Optimising the fuel cell flow channels involves more than just maximising the fuel cell output power. It is crucial to also take into account the pumping power required to

drive the reactant gases through the flow channels during this optimisation process. Figure 5.11 presents both the cell power and pumping power densities for the set of channel dimensions investigated in this study for the fuel cell operating with carbon fibre-based GDLs. For most of the cases, the peak cell power density was found to be at 0.4 V. Apart from the cases where the channel height is 0.25 mm, the channel width at which the cell power density is a maximum is 0.5 mm and this is due optimal transport of mass and charge with this setting. However, with 0.25 mm channel height, the cell power density was found to increase with decreasing width channel and this is, for a given flow rate, due to increased convective flow within the GDL. However, for this channel height (0.25 mm), the pumping power density increases significantly with decreasing channel width; the pumping power density was found to increase from 0.091 W/cm^2 with 1 mm channel width to 1.373 W/cm^2 with 0.25 mm channel width. On the other hand, the pumping power is minimal with larger channel dimensions. For example, it is only 0.003 W/cm^2 with a channel width and height both set at 1 mm.

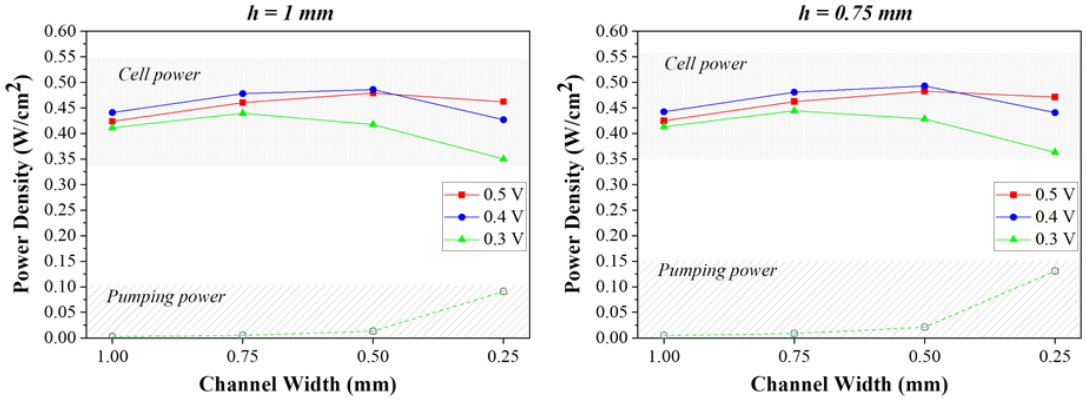

(a) **(b)**

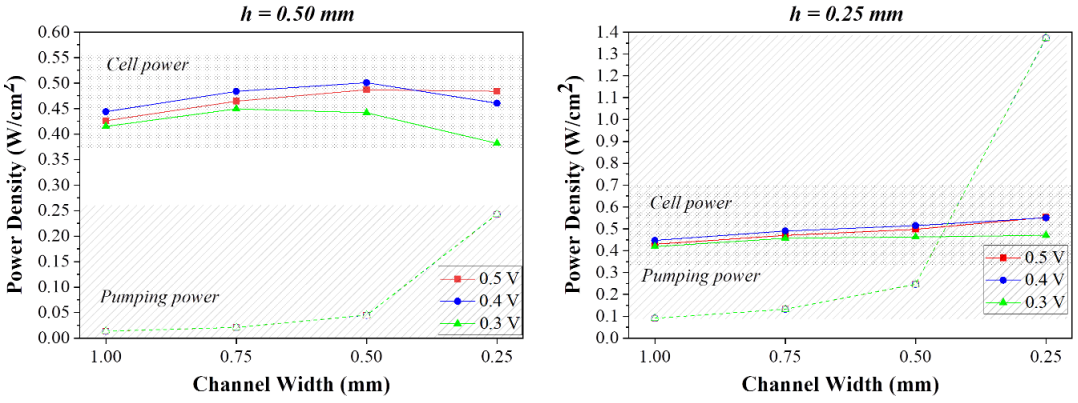

(c) **(d)**

Figure 5.11 – The cell power density and the pumping power density for the fuel cell equipped with carbon fibre-based GDLs as a function of channel heights ((a) 1 mm, (b) 0.75 mm, (c) 0.5 mm and (d) 0.25 mm) and channel widths.

Figure 5.12 exhibits the net power density, which is the difference between the cell power density and the pumping power density, for all the above cases. The maximum net power density for the fuel cell equipped with carbon fibre-based GDLs is attained at 0.4 V when the channel height is 1 or 0.75 mm and channel width is 0.75 or 0.5 mm, which is around 0.475 W/cm^2. The pumping power density for these settings is always below 0.05 W/cm^2. On the other hand, we have negative net power densities for the cases where the channel height is 0.25 mm and the channel width is 0.25 mm. This indicates that the power generated from the fuel cell is not sufficiently high to meet alone the increased pressure drop along the channels and that the pump or the compressor needs an external power source to drive the air through these small cross-sections.

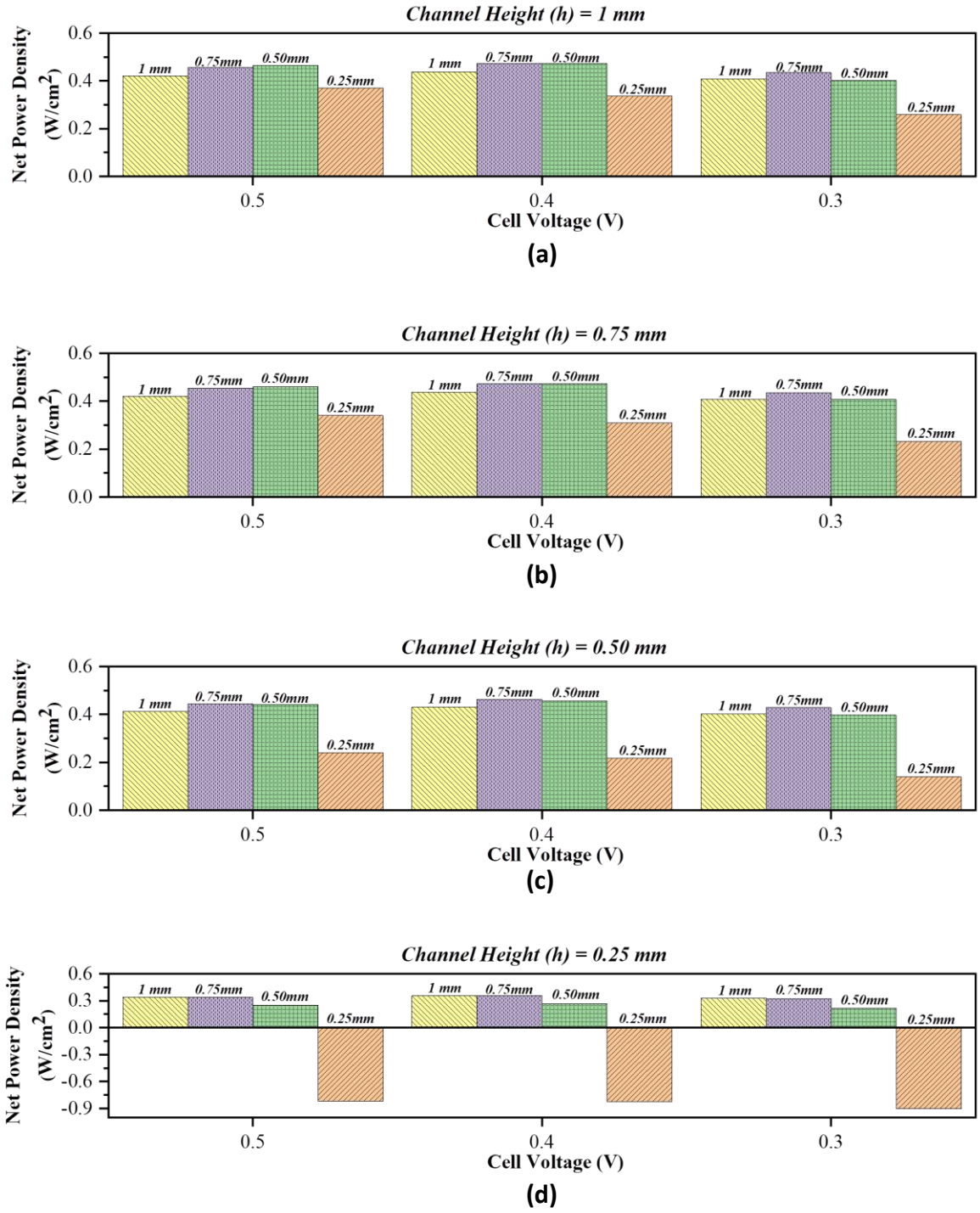

Figure 5.12 – The net power density for the fuel cell equipped with carbon fibre-based GDLs as a function of channel heights ((a) 1 mm, (b) 0.75 mm, (c) 0.5 mm and (d) 0.25 mm) and channel widths.

Figure 5.13 shows the cell and pumping power densities for the set of channel dimensions investigated in this study for the fuel cell operating with nickel foam based GDLs. As with the fuel cell equipped with the conventional carbon fibre-based GDL, the peak power density for all the cases are attained at 0.4 V cell voltage. The cell power density was, for all the channel heights, found to increase with decreasing channel width. For example, for 1 mm channel height, the cell power density increases by 0.13 W/cm^2 when decreasing the channel width from 1 mm to 0.25 mm. This can be attributed to the superior gas permeability of the nickel foam-based GDLs, leading to increased convective flows within the nickel foam-based GDLs as the flow channel cross-section decreases. The pumping power increases, but to a lesser extent compared to the carbon fibre-based GDLs, as the channel dimensions decrease. For example, the pumping power density increases from 0.004 W/cm^2 with both channel height and width set at 1 mm to 0.660 W/cm^2 with both channel height and width set at 0.25 mm.

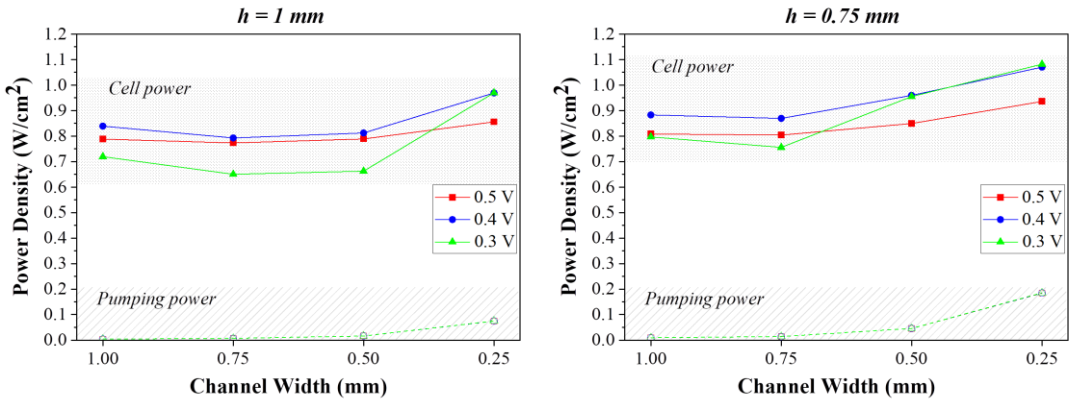

(a) **(b)**

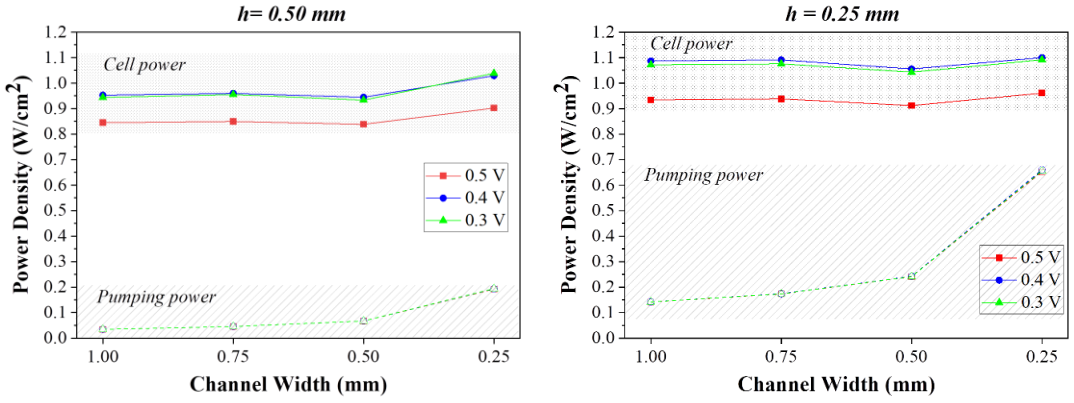

Figure 5.13 – The cell power density and the pumping power density for the fuel cell equipped with nickel foam-based GDLs as a function of channel heights ((a) 1 mm, (b) 0.75 mm, (c) 0.5 mm and (d) 0.25 mm) and channel widths.

Figure 5.14 displays the net power density for the nickel foam based GDL cases. The maximum net power density, 0.945 W/cm^2, is achieved at 0.4 V with a channel height of 0.25 mm and a channel width of 1 mm. Under this channel height, the channel width is adequately high, eliminating the need for significant pumping power. Notably, unlike cases involving carbon fibre-based GDLs, the net power density of the smallest cross-section has not been negative. This is clearly attributed to the superior mass transport properties exhibited by the nickel foam-based GDLs.

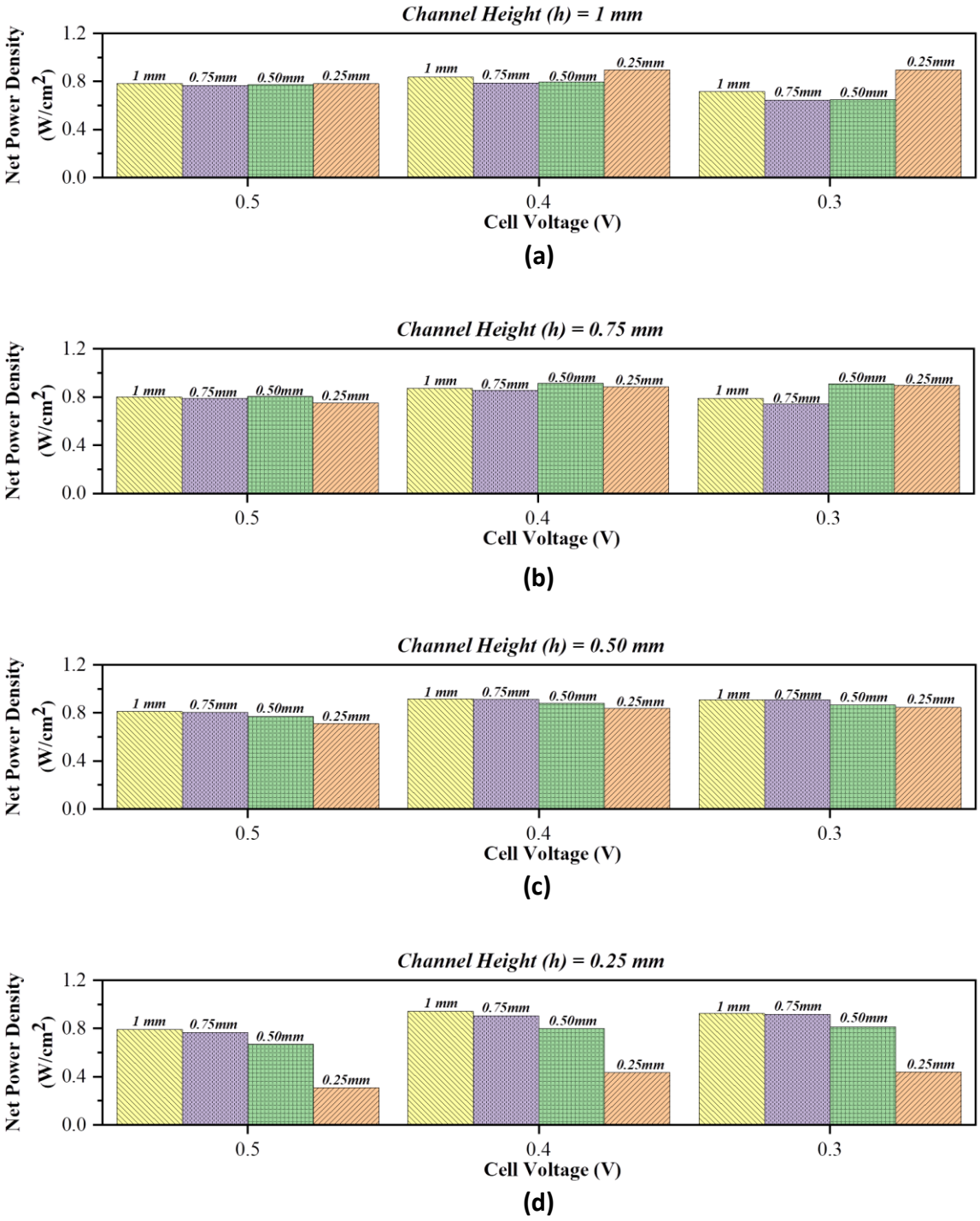

Figure 5.14 – The net power density for the fuel cell equipped with nickel foam-based GDLs as a function of channel heights ((a) 1 mm, (b) 0.75 mm, (c) 0.5 mm and (d) 0.25 mm) and channel widths.

5.5 CONCLUSIONS

Nickel foam emerges as a compelling candidate for gas diffusion layers in polymer electrolyte fuel cells due to its superior structural and transport properties. To investigate the performance gain with nickel foam based GDLs, we have developed a three-dimensional PEFC model and simulated different scenarios in which the dimensions of the flow channel were realistically changed with either carbon fibre-based or nickel foam-based GDLs. The following are the main findings of the study:

- The concentrations of oxygen and water as well as current density within the GDL are higher and significantly more uniform with nickel foam GDLs compared to the conventional carbon fibre GDLs and this is due to superior mass and charge transport properties of the nickel foam GDLs. Notably, for all the cases, the maximum current density is near the interface between the flow channel and the rib as this is the location for the shortest pathways for both the reactant gas and the electronic charge.
- The pumping power should be taken into account when optimising the dimensions of the flow channels. The flow channels with the smallest dimension (0.25 mm height and 0.25 mm width) were shown to demonstrate the best fuel cell power density owing to the increased convective flow within the GDL. However, these channels require higher pumping power to overcome the increased pressure drop along the flow channels. For example, for the fuel cell operating with carbon fibre based GDLs, the highest fuel cell power density (0.55 W/cm^2) was observed for flow channel with 0.25 mm

height and 0.25 mm width. However, the pumping power density was extremely high with these channels (1.373 W/cm^2), meaning that the net power density is negative and external power source is required to drive the flow along the channel.

- Taking the pumping power into account, the optimal flow channel dimensions that maximises the net power density (~0.475 W/cm^2) were found to be between 0.75 and 1 mm for the channel height and between 0.5 and 0.75 mm for the channel width for the fuel cell with carbon fibre based GDLs. On the other hand, the maximum net power density optimal flow channel dimensions that maximises the net power density (0.945 W/cm^2) were found to be 1 mm for the channel width and 0.25 mm for the channel height for the fuel cell operating with the nickel foam based GDLs. The superior net power density demonstrated with the nickel foam GDLs underscores the superiority of its mass and charge transport properties.

5.6 REFERENCES

[1] Sánchez M, Pierna AR, Lorenzo A, Del Val JJ. Effect of cocatalyst and composition on catalytic performance of amorphous alloys for ethanol electrooxidation and PEMFCs. Int J Hydrogen Energy 2016;41:19749–55. https://doi.org/10.1016/j.ijhydene.2016.06.064.

[2] Aldakheel F, Ismail MS, Hughes KJ, Ingham DB, Ma L, Pourkashanian M. Effects of compression on mechanical integrity, gas permeability and thermal stability of gas diffusion layers with/without sealing gaskets. Int J Hydrogen Energy 2021;46:22907–19. https://doi.org/10.1016/j.ijhydene.2021.04.087.

[3] Alaswad A, Baroutaji A, Achour H, Carton J, Al Makky A, Olabi AG. Developments in fuel cell technologies in the transport sector. Int J Hydrogen Energy 2016;41:16499–508. https://doi.org/10.1016/j.ijhydene.2016.03.164.

[4] Wang Y, Ruiz Diaz DF, Chen KS, Wang Z, Adroher XC. Materials, technological status, and fundamentals of PEM fuel cells – A review. Materials Today 2020;32:178–203. https://doi.org/10.1016/j.mattod.2019.06.005.

[5] Liu Y, Tu Z, Chan SH. Applications of ejectors in proton exchange membrane fuel cells: A review. Fuel Processing Technology 2021;214:106683. https://doi.org/10.1016/j.fuproc.2020.106683.

[6] Orogbemi OM, Ingham DB, Ismail MS, Hughes KJ, Ma L, Pourkashanian M. The effects of the composition of microporous layers on the permeability of gas

diffusion layers used in polymer electrolyte fuel cells. Int J Hydrogen Energy 2016;41:21345–51. https://doi.org/10.1016/j.ijhydene.2016.09.160.

[7] Zamel N, Li X. Effective transport properties for polymer electrolyte membrane fuel cells - With a focus on the gas diffusion layer. Prog Energy Combust Sci 2013;39:111–46. https://doi.org/10.1016/j.pecs.2012.07.002.

[8] Neehall ND, Ismail MS, Hughes KJ, Pourkashanian M. Effect of composition and structure of gas diffusion layer and microporous layer on the through-plane gas permeability of PEFC porous media. Int J Energy Res 2021;45:20988–1005. https://doi.org/10.1002/er.7158.

[9] Zenyuk I V., Parkinson DY, Connolly LG, Weber AZ. Gas-diffusion-layer structural properties under compression via X-ray tomography. J Power Sources 2016;328:364–76. https://doi.org/10.1016/j.jpowsour.2016.08.020.

[10] Colpan CO, Nalbant Y, Ercelik M. Fundamentals of Fuel Cell Technologies. Comprehensive Energy Systems 2018;4–5:1107–30. https://doi.org/10.1016/B978-0-12-809597-3.00446-6.

[11] Zhao J, Shahgaldi S, Ozden A, Alaefour IE, Li X, Hamdullahpur F. Effect of catalyst deposition on electrode structure, mass transport and performance of polymer electrolyte membrane fuel cells. Appl Energy 2019;255:113802. https://doi.org/10.1016/j.apenergy.2019.113802.

[12] Lee FC, Ismail MS, Ingham DB, Hughes KJ, Ma L, Lyth SM, et al. Alternative architectures and materials for PEMFC gas diffusion layers: A review and

outlook. Renewable and Sustainable Energy Reviews 2022;166. https://doi.org/10.1016/j.rser.2022.112640.

[13] Park J, Oh H, Ha T, Lee Y Il, Min K. A review of the gas diffusion layer in proton exchange membrane fuel cells: Durability and degradation. Appl Energy 2015;155:866–80. https://doi.org/10.1016/j.apenergy.2015.06.068.

[14] Pan Y, Wang H, Brandon NP. Gas diffusion layer degradation in proton exchange membrane fuel cells: Mechanisms, characterization techniques and modelling approaches. J Power Sources 2021;513:230560. https://doi.org/10.1016/j.jpowsour.2021.230560.

[15] Ozden A, Shahgaldi S, Zhao J, Li X, Hamdullahpur F. Degradations in porous components of a proton exchange membrane fuel cell under freeze-thaw cycles: Morphology and microstructure effects. Int J Hydrogen Energy 2020;45:3618–31. https://doi.org/10.1016/j.ijhydene.2018.10.209.

[16] Shin DK, Yoo JH, Kang DG, Kim MS. Effect of cell size in metal foam inserted to the air channel of polymer electrolyte membrane fuel cell for high performance. Renew Energy 2018;115:663–75. https://doi.org/10.1016/j.renene.2017.08.085.

[17] Tseng CJ, Tsai BT, Liu ZS, Cheng TC, Chang WC, Lo SK. A PEM fuel cell with metal foam as flow distributor. Energy Convers Manag 2012;62:14–21. https://doi.org/10.1016/j.enconman.2012.03.018.

[18] Tabe Y, Nasu T, Morioka S, Chikahisa T. Performance characteristics and internal phenomena of polymer electrolyte membrane fuel cell with porous flow field. J Power Sources 2013;238:21–8. https://doi.org/10.1016/j.jpowsour.2013.03.047.

[19] Ercelik M, Ismail MS, Ingham DB, Hughes KJ, Ma L. Efficient X-ray CT-based numerical computations of structural and mass transport properties of nickel foam-based GDLs for PEFCs. Energy 2023;262:125531. https://doi.org/10.1016/j.energy.2022.125531.

[20] Ercelik M, Ismail MS, Hughes KJ, Ingham DB, Ma L, Pourkashanian M. X-ray CT-based numerical investigation of nickel foam-based GDLs under compression. Int J Hydrogen Energy 2023:1–20. https://doi.org/10.1016/j.ijhydene.2023.07.001.

[21] Okonkwo PC, Otor C. A review of gas diffusion layer properties and water management in proton exchange membrane fuel cell system. Int J Energy Res 2021;45:3780–800. https://doi.org/10.1002/er.6227.

[22] Lee FC, Ismail MS, Zhang K, Ingham DB, Aldakheel F, Hughes KJ, et al. Optimisation and characterisation of graphene-based microporous layers for polymer electrolyte membrane fuel cells. Int J Hydrogen Energy 2023. https://doi.org/10.1016/j.ijhydene.2023.05.003.

[23] Ozden A, Shahgaldi S, Li X, Hamdullahpur F. A review of gas diffusion layers for proton exchange membrane fuel cells—With a focus on characteristics, characterization techniques, materials and designs. Prog Energy Combust Sci 2019;74:50–102. https://doi.org/10.1016/j.pecs.2019.05.002.

[24] Ozden A, Ercelik M, Ouellette D, Colpan CO, Ganjehsarabi H, Hamdullahpur F. Designing, modeling and performance investigation of bio-inspired flow field based DMFCs. Int J Hydrogen Energy 2017;42:21546–58. https://doi.org/10.1016/j.ijhydene.2017.01.007.

[25] Ouellette D, Ozden A, Ercelik M, Colpan CO, Ganjehsarabi H, Li X, et al. Assessment of different bio-inspired flow fields for direct methanol fuel cells through 3D modeling and experimental studies. Int J Hydrogen Energy 2018;43:1152–70. https://doi.org/10.1016/j.ijhydene.2017.06.073.

[26] Tang Y, Yuan W, Pan M, Wan Z. Feasibility study of porous copper fiber sintered felt: A novel porous flow field in proton exchange membrane fuel cells. Int J Hydrogen Energy 2010;35:9661–77. https://doi.org/10.1016/j.ijhydene.2010.06.101.

[27] Ismail MS, Berber MR, Alrowaili ZA, Pourkashanian M. Fully-developed laminar flow in trapezoidal ducts with rounded corners: a numerical solution and case study. Int J Numer Methods Heat Fluid Flow 2022;32:2682–99. https://doi.org/10.1108/HFF-09-2021-0620.

[28] Wilberforce T, Ijaodola O, Baroutaji A, Ogungbemi E, Olabi AG. Effect of Bipolar Plate Material on Proton Exchange Membrane Fuel Cell Performance. Energies (Basel) 2022;15:1–15. https://doi.org/10.3390/en15051886.

[29] Kumar A, Reddy RG. Modeling of polymer electrolyte membrane fuel cell with metal foam in the flow-field of the bipolar/end plates. J Power Sources 2003;114:54–62. https://doi.org/10.1016/S0378-7753(02)00540-2.

[30] Khazaee I, Sabadbafan H. Numerical study of changing the geometry of the flow field of a PEM fuel cell. Heat and Mass Transfer/Waerme- Und Stoffuebertragung 2016;52:993–1003. https://doi.org/10.1007/s00231-015-1621-4.

[31] Tian J, Ismail MS, Ingham D, Hughes KJ, Ma L, Pourkashanian M. Multiphase, three-dimensional PEM fuel cell numerical model with a variable cross-sectional area flow channel. Int J Numer Methods Heat Fluid Flow 2023;33:2778–99. https://doi.org/10.1108/HFF-02-2023-0075.

[32] Carcadea E, Varlam M, Ingham DB, Ismail MS, Patularu L, Marinoiu A, et al. The effects of cathode flow channel size and operating conditions on PEM fuel performance: A CFD modelling study and experimental demonstration. Int J Energy Res 2018;42:2789–804. https://doi.org/10.1002/er.4068.

[33] Higier A, Liu H. Optimization of PEM fuel cell flow field via local current density measurement. Int J Hydrogen Energy 2010;35:2144–50. https://doi.org/10.1016/j.ijhydene.2009.12.116.

[34] Yoon YG, Lee WY, Park GG, Yang TH, Kim CS. Effects of channel and rib widths of flow field plates on the performance of a PEMFC. Int J Hydrogen Energy 2005;30:1363–6. https://doi.org/10.1016/j.ijhydene.2005.04.008.

[35] Scholta J, Escher G, Zhang W, Küppers L, Jörissen L, Lehnert W. Investigation on the influence of channel geometries on PEMFC performance. J Power Sources 2006;155:66–71. https://doi.org/10.1016/j.jpowsour.2005.05.099.

[36] Carcadea E, Ismail MS, Ingham D Bin, Patularu L, Schitea D, Marinoiu A, et al. Effects of geometrical dimensions of flow channels of a large-active-area PEM fuel cell: A CFD study. Int J Hydrogen Energy 2021;46:13572–82. https://doi.org/10.1016/j.ijhydene.2020.08.150.

[37] Kerkoub Y, Benzaoui A, Haddad F, Ziari YK. Channel to rib width ratio influence with various flow field designs on performance of PEM fuel cell. Energy Convers Manag 2018;174:260–75. https://doi.org/10.1016/j.enconman.2018.08.041.

[38] Liu H, Li P, Wang K. Optimization of PEM fuel cell flow channel dimensions - Mathematic modeling analysis and experimental verification. Int J Hydrogen Energy 2013;38:9835–46. https://doi.org/10.1016/j.ijhydene.2013.05.159.

[39] Kaplan M. Numerical investigation of influence of cross-sectional dimensions of flow channels on pem fuel cell performance. Journal of Energy Systems 2021;5:137–48. https://doi.org/10.30521/jes.871018.

[40] Chowdhury MZ, Genc O, Toros S. Numerical optimization of channel to land width ratio for PEM fuel cell. Int J Hydrogen Energy 2018;43:10798–809. https://doi.org/10.1016/j.ijhydene.2017.12.149.

[41] Heidary H, Kermani MJ, Advani SG, Prasad AK. Experimental investigation of in-line and staggered blockages in parallel flowfield channels of PEM fuel cells. Int J Hydrogen Energy 2016;41:6885–93. https://doi.org/10.1016/j.ijhydene.2016.03.028.

[42] Chen H, Guo H, Ye F, Ma CF, Liao Q, Zhu X. Mass transfer in proton exchange membrane fuel cells with baffled flow channels and a porous-blocked baffled flow channel design. Int J Energy Res 2019;43:2910–29. https://doi.org/10.1002/er.4461.

[43] Cooper NJ, Smith T, Santamaria AD, Park JW. Experimental optimization of parallel and interdigitated PEMFC flow-field channel geometry. Int J Hydrogen Energy 2016;41:1213–23. https://doi.org/10.1016/j.ijhydene.2015.11.153.

[44] Zenyuk I V., Parkinson DY, Connolly LG, Weber AZ. Gas-diffusion-layer structural properties under compression via X-ray tomography. J Power Sources 2016;328:364–76. https://doi.org/10.1016/j.jpowsour.2016.08.020.

[45] Mahmoudimehr J, Daryadel A. Influences of feeding conditions and objective function on the optimal design of gas flow channel of a PEM fuel cell. Int J Hydrogen Energy 2017;42:23141–59. https://doi.org/10.1016/j.ijhydene.2017.07.196.

[46] Mahmoudimehr J, Darbandi A. Technical study of a PEM fuel cell on the Psychrometric chart. Int J Hydrogen Energy 2016;41:607–13. https://doi.org/10.1016/j.ijhydene.2015.10.123.

[47] Poserin V, Marcuson S, Shu J, Wilkinson DS. CVD technique for Inco nickel foam production. Adv Eng Mater 2004;6:454–9. https://doi.org/10.1002/adem.200405142.

[48] Akbari MH, Rismanchi B. Numerical investigation of flow field configuration and contact resistance for PEM fuel cell performance. Renew Energy 2008;33:1775–83. https://doi.org/10.1016/j.renene.2007.10.009.

[49] Taira H, Liu H. In-situ measurements of GDL effective permeability and under-land cross-flow in a PEM fuel cell. Int J Hydrogen Energy 2012;37:13725–30. https://doi.org/10.1016/j.ijhydene.2012.03.030.

[50] Son J, Um S, Kim YB. Numerical analysis of the effect of anisotropic gas diffusion layer permeability on polymer electrolyte membrane fuel cell performance with various channel types. Fuel 2021;289:119888. https://doi.org/10.1016/j.fuel.2020.119888.

[51] Nitta I, Hottinen T, Himanen O, Mikkola M. Inhomogeneous compression of PEMFC gas diffusion layer. Part I. Experimental. J Power Sources 2007;171:26–36. https://doi.org/10.1016/j.jpowsour.2006.11.018.

[52] He G, Yamazaki Y, Abudula A. A three-dimensional analysis of the effect of anisotropic gas diffusion layer(GDL) thermal conductivity on the heat transfer and two-phase behavior in a proton exchange membrane fuel cell(PEMFC). J Power Sources 2010;195:1551–60. https://doi.org/10.1016/j.jpowsour.2009.09.059.

[53] Wang L, Husar A, Zhou T, Liu H. A parametric study of PEM fuel cell performances. Int J Hydrogen Energy 2003;28:1263–72. https://doi.org/10.1016/S0360-3199(02)00284-7.

[54] Azarafza A, Ismail MS, Rezakazemi M, Pourkashanian M. Comparative study of conventional and unconventional designs of cathode flow fields in PEM fuel cell. Renewable and Sustainable Energy Reviews 2019;116:109420. https://doi.org/10.1016/j.rser.2019.109420.

[55] Kwon OJ, Shin HS, Cheon SH, Oh BS. A study of numerical analysis for PEMFC using a multiphysics program and statistical method. Int J Hydrogen Energy, vol. 40, Elsevier Ltd; 2015, p. 11577–86. https://doi.org/10.1016/j.ijhydene.2015.03.163.

[56] Ismail MS, Hughes KJ, Ingham DB, Ma L, Pourkashanian M. Effects of anisotropic permeability and electrical conductivity of gas diffusion layers on the performance of proton exchange membrane fuel cells. Appl Energy 2012;95:50–63. https://doi.org/10.1016/j.apenergy.2012.02.003.

[57] Wang Y. Porous-Media Flow Fields for Polymer Electrolyte Fuel Cells. J Electrochem Soc 2009;156:B1124. https://doi.org/10.1149/1.3183781.

[58] Wang J, Zhang H, Cai W, Ye W, Tong Y, Cheng H. Effect of varying rib area portions on the performance of PEM fuel cells: Insights into design and optimization. Renew Energy 2023;217:119185. https://doi.org/10.1016/j.renene.2023.119185.

Chapter 6

Conclusions and Future Works

6.1 CONCLUSIONS

With their advanced structural and transport properties, nickel foams are increasingly being recognized as potential candidates for gas diffusion layers (GDLs) in polymer electrolyte fuel cells (PEFCs). In this thesis, an efficient X-ray CT based modelling framework has been created, designed for evaluating the essential structural and mass transport properties, as well as assessing the multi-dimensional consistency and/or isotropy of these characteristics (Chapter 3). In particular, a combination of two-dimensional X-ray CT images and numerical models have been employed to accurately compute various attributes of a typical nickel foam sample. These include its porosity, tortuosity, pore size distribution, ligament thickness,

specific surface area, gas permeability, and effective diffusivity. Similarly, the X-ray CT-based numerical models were used to investigate these structural and transport properties under the fuel cell compression conditions (Chapter 4). Finally, a comprehensive 3D COMSOL Multiphysics® PEFC model was developed to compare the conventional carbon-based and nickel foam-based GDLs with various channel dimensions (Chapter 5). The determination of the optimized channel height and width was guided by criteria that encompassed the maximization of both the fuel cell power output and net power output, ensuring a holistic approach to performance enhancement. The following key insights have been extracted from the comprehensive analyses presented within the technical chapters of this thesis, specifically Chapters 3, 4, and 5:

- The computational analysis reveals that nickel foam possesses enhanced uniformity and isotropy in both the in-plane and through-plane dimensions, surpassing the attributes of conventionally used carbon substrates. This assertion is substantiated by the consistent values obtained from two-dimensional CT slices, which align harmoniously with the existing experimental and theoretical literature data, attesting to the precision and reliability of the computational evaluations conducted.
- The nickel foam GDL is characterized by a higher mean porosity and larger mean pore size compared to conventionally used carbon substrates. This distinction facilitates enhanced mass transport of gases and liquid water to and from the catalyst layers. Concurrently, the nickel foam displays reduced

tortuosity in both in-plane and through-plane directions, resulting in decreased mass transport resistance for chemical species.

- The ligament thickness of nickel foam is significantly greater than the carbon fibre diameter of traditional carbon substrates, suggesting that nickel foam provides enhanced mechanical support for the delicate membrane electrode assembly (MEA).
- The gas permeability and effective gas diffusivity of nickel foam are significantly higher than those of conventional carbon substrates. This indicates a superior convective flow and more efficient diffusive transport of gases within the nickel foam-based gas diffusion layer, optimizing the transport to and from the catalyst layer and beneath the flow field plates' ribs.
- The porosity of nickel foam slightly decreases with compression, yet it still retains a higher porosity compared to conventional carbon substrates, showcasing its potential for reduced mass transport resistance.
- While compression results in a significant reduction in pore size, it concurrently leads to an increase in the specific surface area of nickel foam.
- The in-plane tortuosity of nickel foam increases with compression, whereas through-plane tortuosity initially increases and then decreases, a pattern attributed to the ligaments' orientation and the effects of compression.
- The gas permeability of nickel foam decreases significantly with compression, especially in the in-plane direction. While uncompressed nickel foam exhibits high isotropy in gas permeability, compression increases the anisotropic ratio

due to the orientation of the ligaments. These ligaments, primarily aligned in the in-plane direction, facilitate the closing of gaps between them when compressed, altering the permeability characteristics significantly.

- The effective diffusivity of oxygen into nitrogen in nickel foam is highly isotropic and shows minimal sensitivity to compression, contrasting with gas permeability. With compression, there is a modest reduction in both through-plane and in-plane effective diffusivities. The isotropy of effective diffusivity slightly decreases under compression, evidenced by a small reduction in the anisotropic ratio.
- The mole fraction of oxygen is lowest beneath the middle-rib area while the water mole fraction is at its peak. Oxygen mole fraction decreases, and water mole fraction increases along the flow direction, and this trend is amplified with reduced channel height and width. Nickel foam-based GDLs exhibit more uniform mole fraction distributions compared to conventional carbon-based GDLs.
- The local current density decreased beneath the mid-rib area but peaked near the channel. The local current density typically reduces from the inlet to the outlet. The region beneath the rib area, adjacent to the flow channel, exhibits the highest local current density. This phenomenon can be attributed to the electrons in the mid-channel taking longer paths to reach the rib surface, combined with increased species transport in this area. While carbon-based PEFCs show uneven local current density distributions, nickel foam-based

PEFCs offer a more uniform distribution due to enhanced electrical conductivity and transport properties.

- In both the carbon fibre-based and the nickel foam-based PEFC, the highest cell power density was observed at the smallest channel dimensions. However, these dimensions also required a significant pumping power, leading to a negative net power. The optimal net power density was achieved with larger channel dimensions and that optimal net power was found to be higher for the PEFC operating with nickel foam based GDLs.
- Shallower channel dimensions offer promising avenues for future research aimed at creating more compact, cheaper and high-efficiency PEFC stacks that leverage nickel foam-based GDLs. Upcoming investigations will prioritize exploring the innovative potentials of these nickel foam-based GDLs within PEFC contexts.

Overall, this study sheds light on the potential applications of the nickel foam-based GDLs for PEFCs. X-ray CT technique and numerical simulations provide insight into the superior interior structure and transport properties of the nickel foam-based GDLs compared to the carbon-based counterpart. Especially, under fuel cell assembly compression conditions, the key structural (such as porosity, tortuosity, ligament thickness, pore size, specific surface area) and transport (permeability and effective diffusivity) properties were thoroughly investigated. In the final stage, the comprehensive rib/channel compressed numerical model showed the species distribution, local current distribution, cell performance, required pumping power

density and net power output for different channel heights and widths for both conventional carbon-based and nickel foam-based PEFCs. The nickel foam-based PEFCs exhibits more uniform species and local current density, alongside the higher cell performance and net power output. Further, the optimal channel dimensions have been ascertained for both types of PEFCs. Notably, the nickel foam-based PEFCs require shallower channels (0.25mm) for achieving maximum net power output, enabling manufacturers to design more compact fuel cell channels and stacks. Furthermore, the nickel foam-based GDLs could pave the way for the employment of metal materials in flow field plates. These materials, which offer more durability and a more cost-effective grooving process, are viable due to the considerably lower electrical and thermal resistances. Thus, the commercialisation of high performance nickel foam-based PEFCs will be encouraged for further development.

6.2 RECOMMENDATIONS AND FUTURE WORKS

This thesis mainly highlights the utilisation of nickel foam as an innovative GDL material in PEFC applications. The key structural and transport properties were determined for three compression levels using X-ray CT technique and computationally efficient numerical models. Further, the optimised channel geometries for nickel foam-based PEFC were established via 3D COMSOL Multiphysics® simulations, drawing comparisons with the conventional carbon-based counterparts. Despite the comprehensive insights offered, the research presented in this thesis can be extended to further understand on experimental output of both

carbon-based and nickel foam-based PEFCs. The future work for this study can be summarised as follows:

- Embarking on experimental single cell tests for nickel foam-based PEFC with different channel dimensions. This experimental approach is anticipated to shed lights on the cell performance and pressure drop through the channels for nickel foam-based PEFCs.
- The implementation of a thin microporous layer on both carbon-based and nickel foam-based GDLs on numerical analyses and further experimental studies. This additional layer is anticipated to facilitate improved transport of mass, heat, and electricity. This additional layer is also likely to enhance the reactant and oxidant distribution on the catalyst layer and reduce the interfacial electrical resistance of the catalyst layer and GDL.
- Even though the current study evaluated channel height and width for the highest net power output, future research will focus on the comprehensive flow-field pattern designs. This channel optimisation research employed a single channel model to conserve computational resources. Future studies could extend to both numerical and potentially experimental single cell analyses investigating various channel designs such as single channel serpentine, multi-channel serpentine, parallel, pin-shape, interdigitated, and bio-inspired configurations. It should be noted that these designs will also require further optimisation concerning channel dimensions, overall design parameters, manifold dimension and position optimisation.

- Further, the metallic flow field plates are gaining attention due to their potentially high cell performance and simplified channel grooving process. Thus, they would be numerically and experimentally coupled with nickel foam-based GDLs. This strategy is projected to significantly mitigate contact resistance while simultaneously increasing electrical and thermal conductivity. The synergy of these metallic components could be promising for not only higher PEFC performance but also lower manufacturing costs which leads to the commercialisation of PEFC technology.

- To advance the practical application of nickel foam-based GDLs, it is essential to investigate a small-scale, high-efficiency PEFC stack made from this material. Numerical analyses of the nickel foam-based stack would provide insights into hydrogen and oxygen utilisation, water management, heat distribution, local current density distribution, and pressure drop through the channels. Constructing a stack prototype will provide experimental data to validate the numerical results and will guide the researchers in further development and refinement of this promising technology.

- In the light of the findings, nickel foam stands out as a considerably promising GDL material for further FCEV applications. Its potential to enhance fuel cell performance and enable the development of more compact fuel cell stacks is likely to attract significant attention from both industrial specialists and academic researchers.

APPENDIX – I

X-ray CT Scanning Procedure

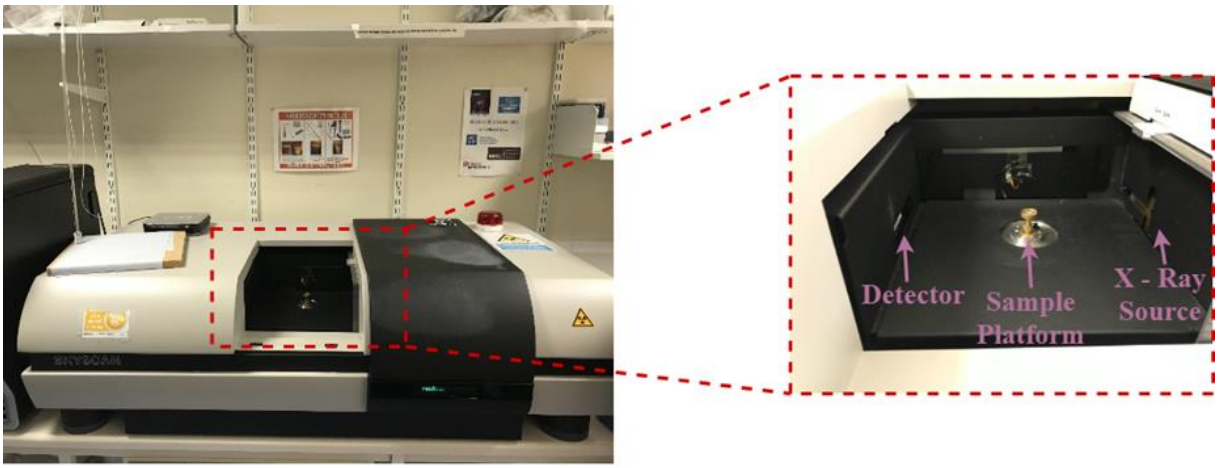

(a) **(b)**

Figure A.1.1. – (a) Bruker SkyScan 1172 µ X-ray computed tomography system and (b) its components.

- Wearing nitrile gloves during cleaning process, sample preparing, and scanning.
- Wipe the surfaces with 70% alcohol solution (do not spray directly on the surface) – Make sure the scanner door is shut and device is switch off before cleaning.
- Open the computer (BRU-1) screen and create a new file.
- To start the X-ray CT device (shown in Figure A.1.1), insert the key and twist to the “Start” position and return to the “ON” position.
- Start the Skyscan 1172 – MicroCT software on the desktop and wait for a while.

Figure A.1.2. – Plastic tube, nylon foil, and different size chucks (sample holders).

- A plastic tube and nylon foil can be used to fix nickel foam sample (or glue might be used) (Figure A.1.2). The sample is carefully wrapped by the transparent nylon foil and fixed on the chuck without any glue. The tube must be double-checked whether it moves or not.

- Click the #1 icon button () on the software interface (demonstrated in Figure A.1.3) to automatically open the system's door.

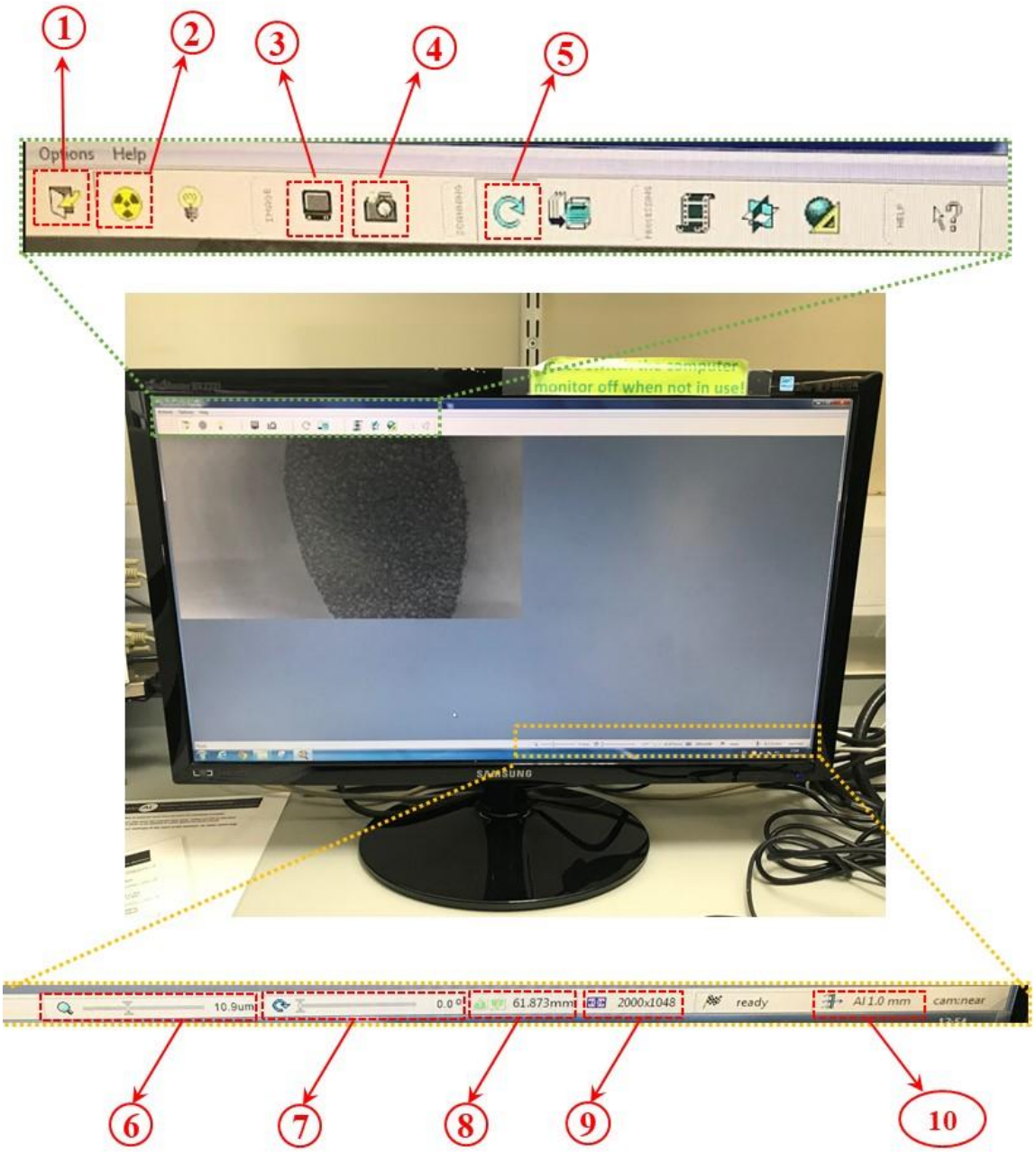

Figure A.1.3. – The Skyscan 1172 MicroCT software interface and the icon buttons.

- Locate the sample attached chuck on the sample platform (Figure A.1.4). Notably, the bolt must be strongly screwed up. Double-check the bolt and chunk is properly attached to the sample holder using your finger.

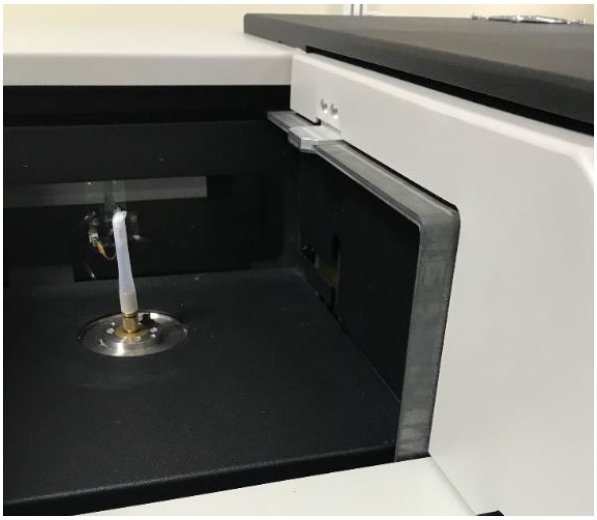

Figure A.1.4. – Fixed chuck and the sample on the sample holder.

- When the sample is fixed, click #1 icon button ( ) to close the door.
- Click to the #2 icon button ( ) to activate X-ray source. If you are the user of the day, the “ageing in progress” window will appear and it will take approximately 15-20 minutes to warm up. If the other users have been previously to the session, aging process should be skipped.
- Click the #3 icon button ( ) to refresh the camera. Wait for a while because it might take time.
- The sample’s location and position can be seen and controlled by using a video camera in the chamber. For this aim, the #4 icon button ( ) should be clicked.
- Arrange the sample’s position by using #6 and #7 bars and #8 icon button at the bottom of the screen. It should be noted that you should be patient because it might take time.

- Click the resolution section (#9 icon button) and set the resolution. Notably, for the medium image size 2000 pixel should be used; however, for the larger image size it should be chosen as 4000.
- Click the filter option (#10 icon button) on the right hand side and select “Al-1.00 mm” option for metal samples.
- Double click the right-hand-side bars and change the source voltage from 100 kV to 80 kV manually. Wait for a short time and press “apply”.
- Click on the pixel size option at the bottom of the screen. Type the pixel size (7 µm) and press apply.
- Rotate the sample by using the adjustable degree options (#7 bar) at the bottom of the screen. So you can be sure the widest face fits on the screen. Manually try the values like 90° or 135°.
- Click the #5 icon button to set up to scan.
- Choose your file location (where the images recorded).
- Enter the rotation step (0.7° per scan), rotation (180°), and averaging value as 2.
- The software will show the estimating scanning time.
- Start the scanning process.
- When the scanning process is finished, Turn off the radiation source (#2 icon button, ).
- Open the door (#1 icon button, ) and carefully remove the chunk from the sample holder.
- Disassemble the chuck
- Close the Skyscan 1172-MicroCT software by clicking “Actions > Exit” on Actions menu.

- Turning the key to “OFF” position and remove the key and return to shelf above the scanner.
- Backup the image files to external hard drive as soon as possible.
- Remove the files from internal hard drive. If they are left on the internal hard drive they are most likely to be deleted to make space for other scanning processes.

NRecon Software Procedure

- Copy the files from the scanner’s PC (BRU-1) to the construction PC.
- Click the “open dataset” icon and select one of the sample images.

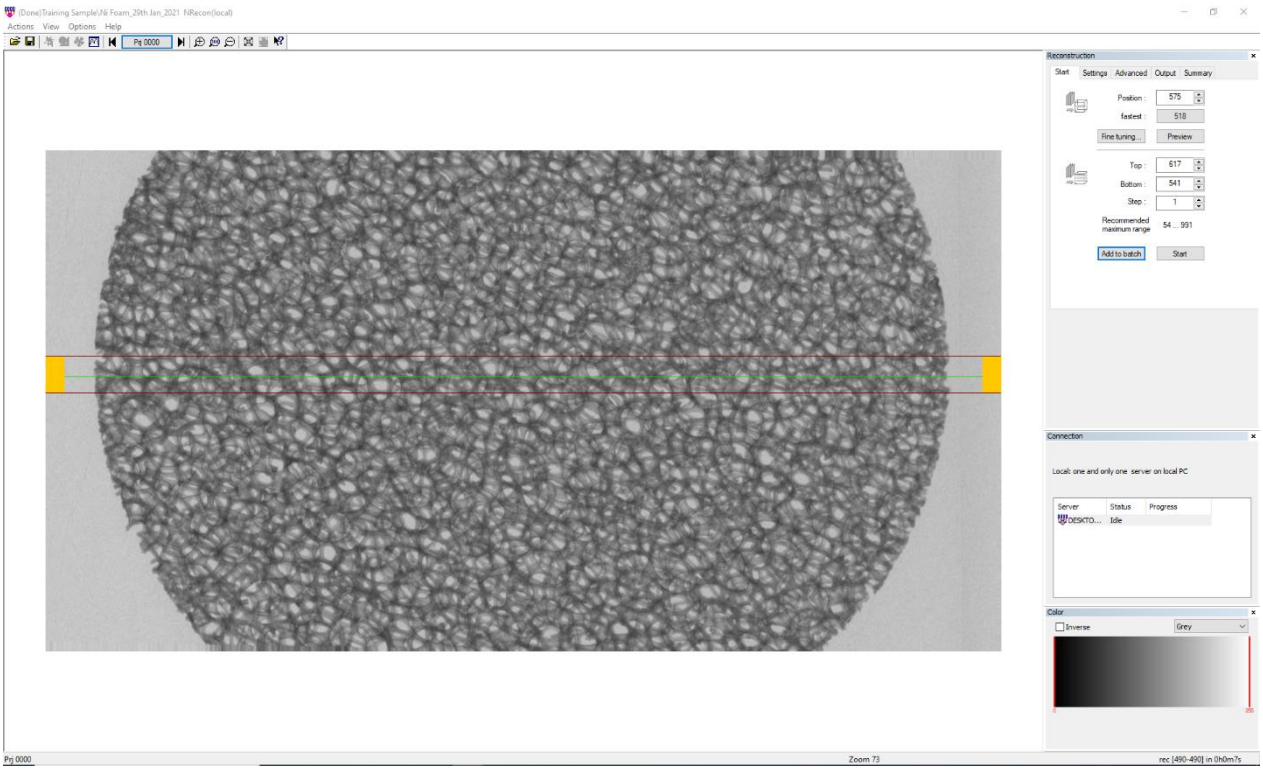

Figure A.1.5. – Interface of the NRecon software.

- The red lines indicate the higher and lower borders and the green line is to preview the slice (shown in Figure A.1.5).
- Arrange the contrast form outlet option “0.0 – 0.38” (Figure A.1.6.).
- Choose “Scales = ON”.
- Create a new folder in the document and add the destination (Figure A.1.6.).
- Choose the file format (Figure A.1.6.).

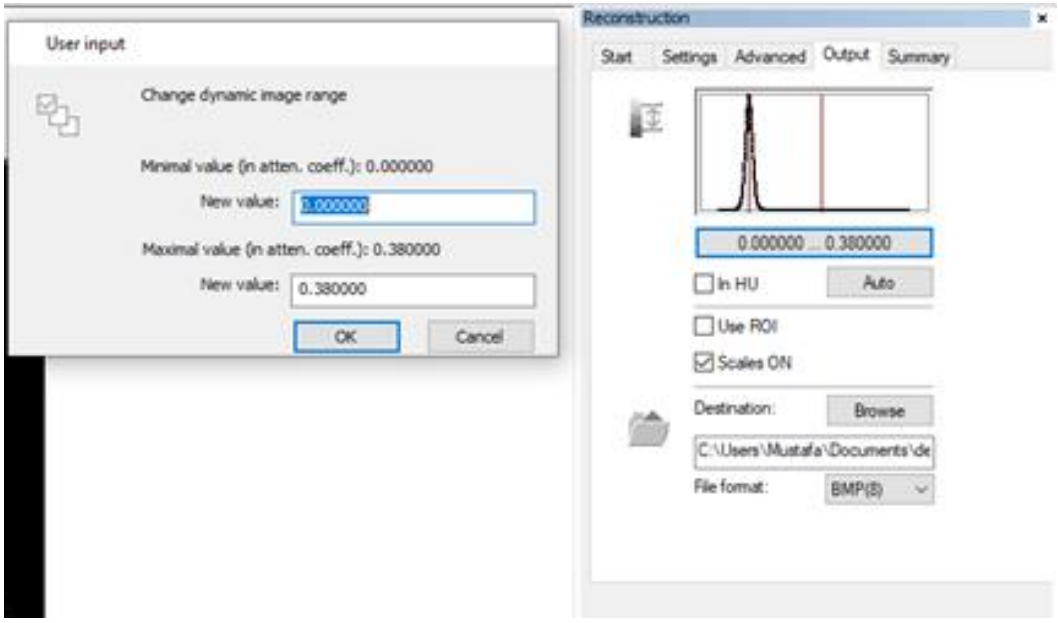

Figure A.1.6. – Contrast arrangement in NRecon software.

- As can be seen in Figure A.1.7, in the setting option;
  - Inactivate the smoothing (off),
  - Ring artifacts reduction is 10,
  - Beam-hardening correction is 35% for the metallic sample,

- CS static rotation is 0°.

- Create a new file.
- Click the start button in the “start” menu.

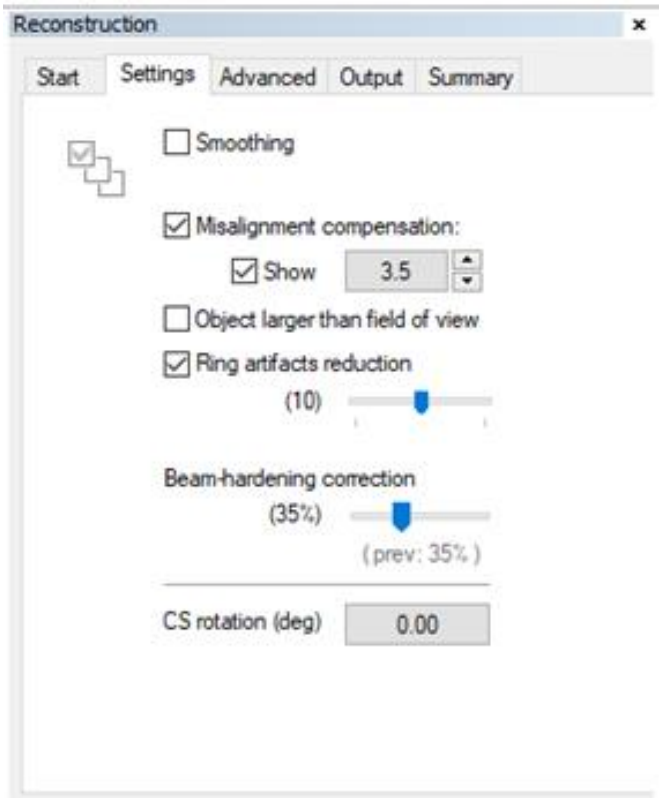

Figure A.1.7. – Settings for nickel foam sample in NRecon software.

CTan Software Procedure

- Click the “open image or dataset” icon and select one of the images (Figure A.1.8)
- Select “Region of interest” (Figure A.1.8)
- Select the area (rectangular or polygonal)

- Be aware that you could not delete it so you should cut it.

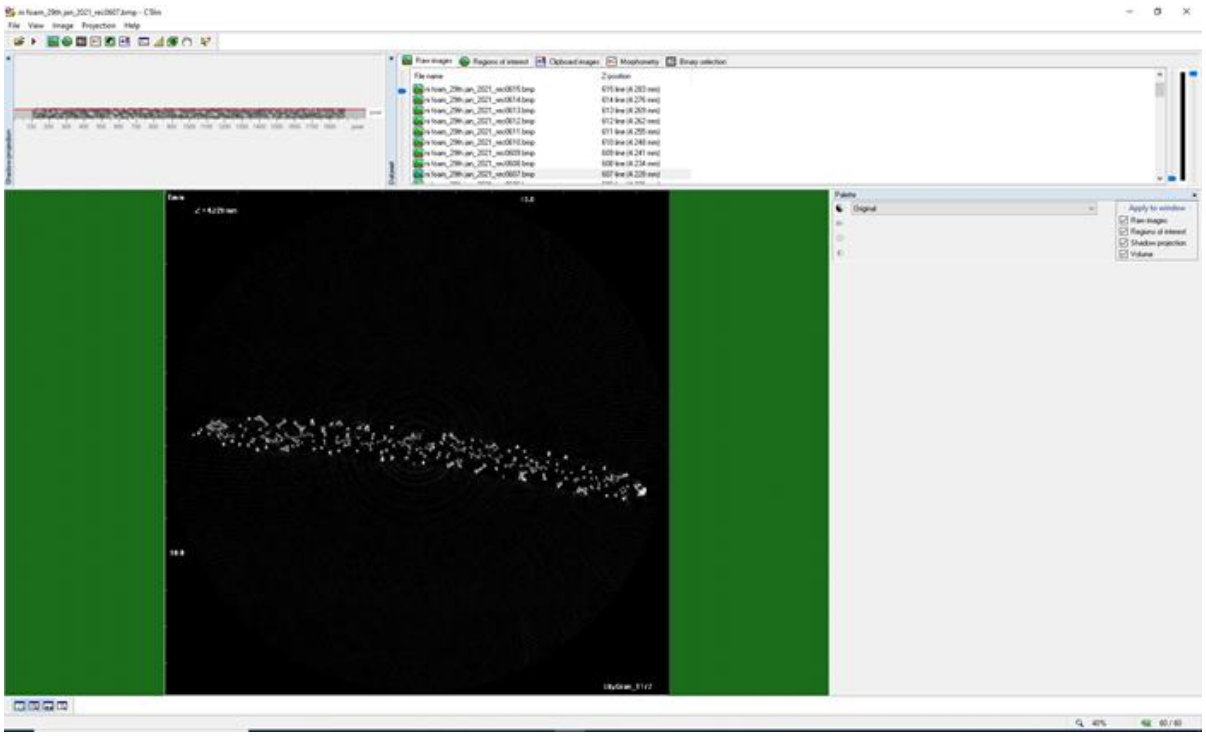

Figure A.1.8. – Interface of CTan software.

- Binary Selection > Histogram > From dataset (Figure A.1.9 and A.1.10)
    - Binary selection is basically referring the thresholding process
    - Max=255, min is you should arrange it manually (It is 62 for nickel foam samples)

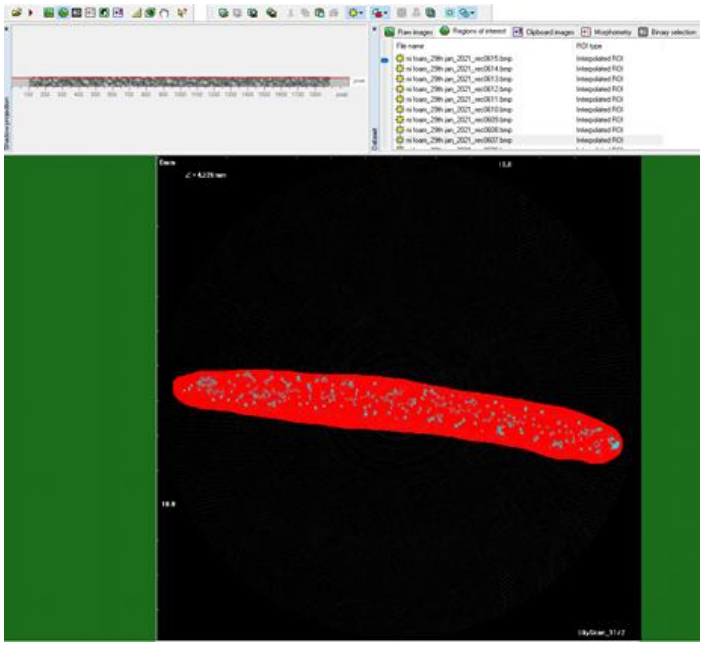

Figure A.1.9. – Region of interest.

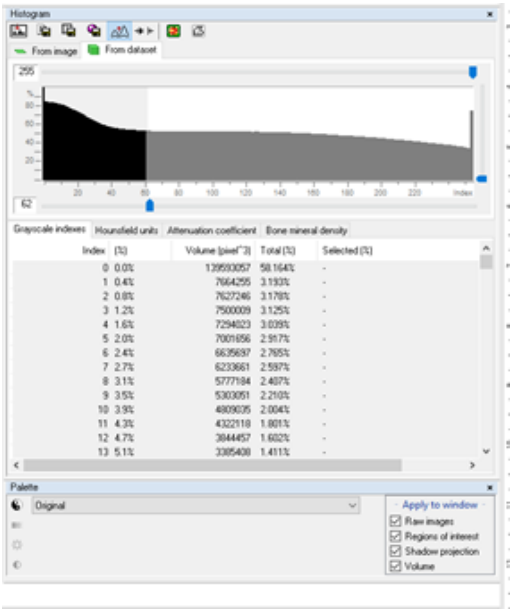

Figure A.1.10. – Histogram option.

- Custom processing > Task List (Figure A.1.11)
    - Filtering (Filter: Gaussian blur, 3D space, radius: 0.65, kernel: square)

- Thresholding (Global, Image, default levels: on)
- Despeckle
- 3D analysis (Basic values: on, Additional values: on, choose all of them, save results as → choose the file direction)
    - Copy a .csv file to the file direction and delete the data inside (therefore it can be save new data as .csv)
- 3D model

- The first 3 processes (Filtering, Thresholding, Despeckle) must be in the sequence. You can add new processes.
- Click the blue play button. Filtering and Thresholding take much more time. Be patient.
- The 3D model is automatically created in the direction as a .stl file.
- For the porosity values : Morphometry > Analysis

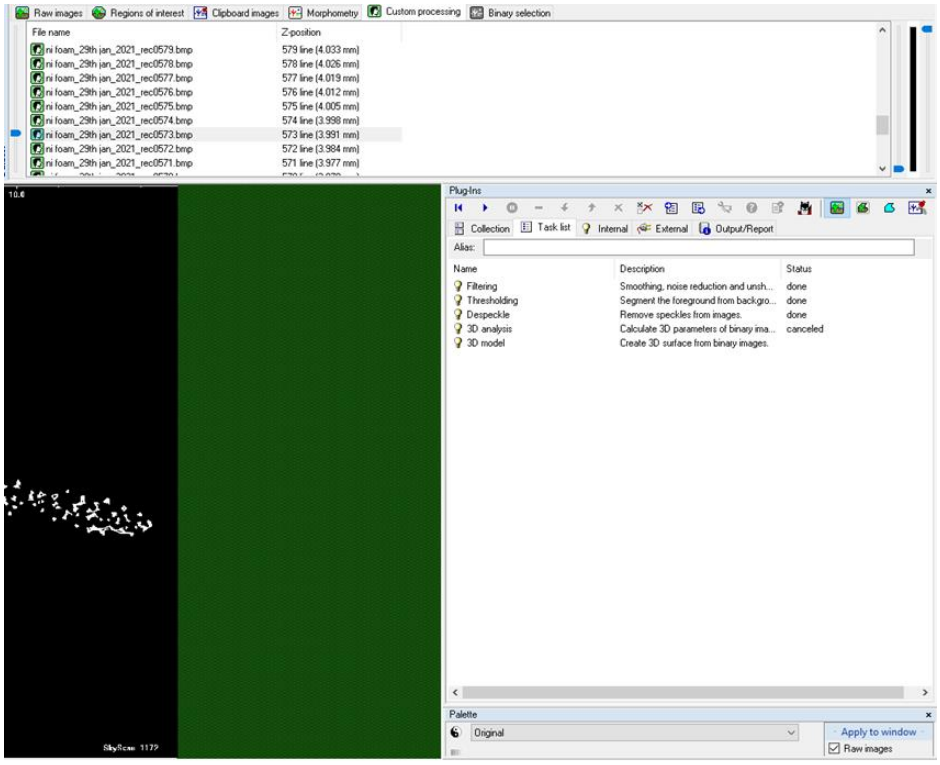

Figure A.1.11. – Custom processing.

APPENDIX – II

Calculation of the Oxygen Inlet Concentration

The following calculations show how the oxygen inlet concentration (which has been used as a boundary condition to solve Eq. (3.3) shown in Section 3.3.2) has calculated. Assuming standard temperature (293.15 K) and pressure (1.0133 x 10^5 Pa), the total concentration is calculated as follows:

$$C_{total} = \frac{P_{atm}}{R\,.T} \quad \text{(A.2.1)}$$

$$C_{total} = \frac{1.013\ x\ 10^5\ Pa}{8.31446\ \mathrm{m^3\ Pa\ K^{-1}mol^{-1}}\ .\ 293.15\ K}$$

$$C_{total} = 41.571\ mol/m^3$$

where R is the universal gas constant (8.31446 m^3Pa $K^{-1}$$mol^{-1}$). Considering that the oxidant used is air (where the molar fraction of oxygen is typically 21%), the molar concentration of oxygen is given as follows:

$$C_{O2} = 0.21\ C_{total} \quad \text{(A.2.2)}$$

$$C_{O2} = 8.73\ mol/m^3$$

APPENDIX – III

The Impact of Outlet Oxygen Concentration on the Molar Flux and Effective Diffusivity

Table A.3.1 – The effect of outlet oxygen concentration on the through-plane molar flux and the through-plane effective diffusivity of oxygen into nitrogen for 3 CT nickel foam slices.

Number of Slice [-]	Inlet Oxygen Concentration (C_{in},O_2), [mol/m^3]	Outlet Oxygen Concentration (C_{out},O_2) [mol/m^3]	Oxygen Concentration difference (ΔC) [mol/m^3]	Molar Flux (J) [mol/(m^2 s)]	The Effective Diffusivity of Oxygen into Nitrogen (D_{eff}) [cm^2/s]
200	8.73	8.48	0.25	0.0038286	0.1608
200	8.73	8.23	0.5	0.0076572	0.1608
200	8.73	7.98	0.75	0.011486	0.1608
200	8.73	7.73	1	0.015314	0.1608
200	8.73	7.48	1.25	0.019143	0.1608
200	8.73	7.23	1.5	0.022972	0.1608
200	8.73	6.98	1.75	0.0268	0.1608
500	8.73	8.48	0.25	0.003616	0.1519
500	8.73	8.23	0.5	0.007232	0.1519
500	8.73	7.98	0.75	0.010848	0.1519
500	8.73	7.73	1	0.014464	0.1519
500	8.73	7.48	1.25	0.01808	0.1519

500	8.73	7.23	1.5	0.021696	0.1519
500	8.73	6.98	1.75	0.025312	0.1519
800	8.73	8.48	0.25	0.003888	0.1633
800	8.73	8.23	0.5	0.007775	0.1633
800	8.73	7.98	0.75	0.011662	0.1633
800	8.73	7.73	1	0.01555	0.1633
800	8.73	7.48	1.25	0.019437	0.1633
800	8.73	7.23	1.5	0.023325	0.1633
800	8.73	6.98	1.75	0.027212	0.1633

Table A.3.2 – The effect of outlet oxygen concentration on the in-plane molar flux and the in-plane effective diffusivity of oxygen into nitrogen for 3 CT nickel foam slices.

Number of Slice [-]	Inlet Oxygen Concentration (C_{in},O_2), [mol/m^3]	Outlet Oxygen Concentration (C_{out},O_2) [mol/m^3]	Oxygen Concentration difference (ΔC) [mol/m^3]	Molar Flux (J) [mol/(m^2 s)]	The Effective Diffusivity of Oxygen into Nitrogen (D_{eff}) [cm^2/s]
200	8.73	8.48	0.25	6.61E-04	0.1757
200	8.73	8.23	0.5	0.0013211	0.1757
200	8.73	7.98	0.75	0.0019817	0.1757
200	8.73	7.73	1	0.0026423	0.1757
200	8.73	7.48	1.25	0.0033028	0.1757
200	8.73	7.23	1.5	0.0039634	0.1757

200	8.73	6.98	1.75	0.004624	0.1757
500	8.73	8.48	0.25	5.88E-04	0.1563
500	8.73	8.23	0.5	0.001175	0.1563
500	8.73	7.98	0.75	0.001763	0.1563
500	8.73	7.73	1	0.002351	0.1563
500	8.73	7.48	1.25	0.002938	0.1563
500	8.73	7.23	1.5	0.003526	0.1563
500	8.73	6.98	1.75	0.004114	0.1563
800	8.73	8.48	0.25	6.44E-04	0.1712
800	8.73	8.23	0.5	0.001287	0.1712
800	8.73	7.98	0.75	0.001931	0.1712
800	8.73	7.73	1	0.002574	0.1712
800	8.73	7.48	1.25	0.003218	0.1712
800	8.73	7.23	1.5	0.003862	0.1712
800	8.73	6.98	1.75	0.004505	0.1712

APPENDIX – IV

Selection of Representative Slice Number

The sensitivity of the computed key structural and mass transport properties of the nickel foam sample, as well as the anisotropy of gas permeability and effective diffusivity, to the number of the CT slices was evaluated as shown in Figures A.4.1 – A.4.7. Evidently, the 20 CT slices (shaded in yellow in the latter figures) were found to be sufficient to accurately compute all the structural and transport properties and the anisotropy related to gas permeability and effective diffusivity.

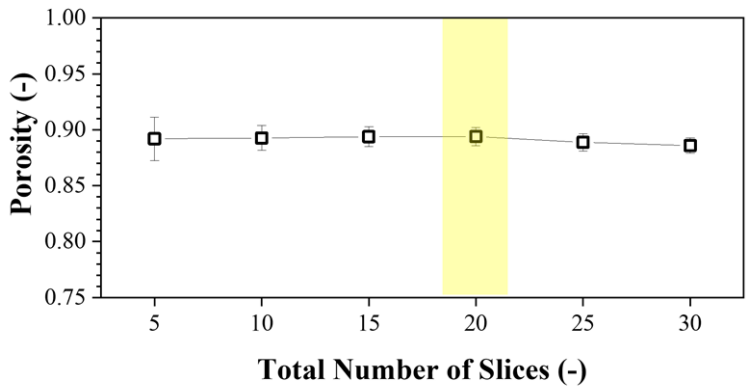

Figure A.4.1 – Porosity of nickel foam as it changes with number of CT slices.

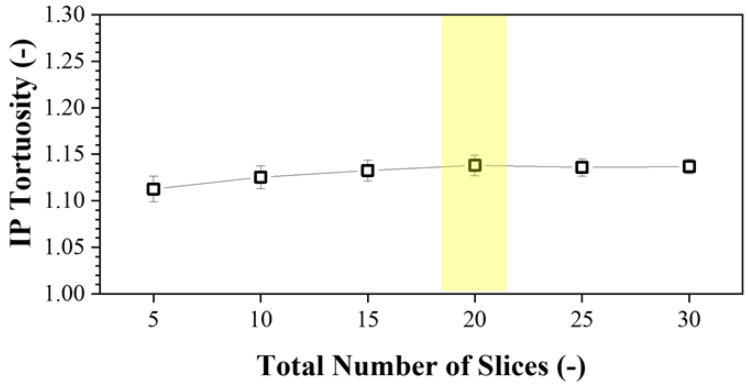

(a)

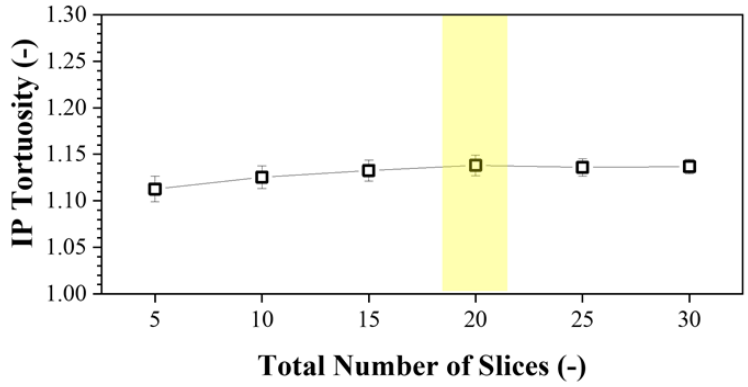

(b)

Figure A.4.2 – (a) Through-plane and (b) in-plane tortuosity of nickel foam as they change with number of CT slices.

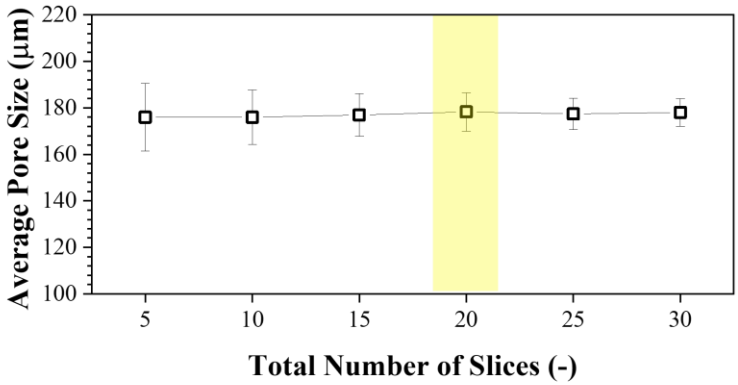

Figure A.4.3 – Pore size of nickel foam as it changes with number of CT slices.

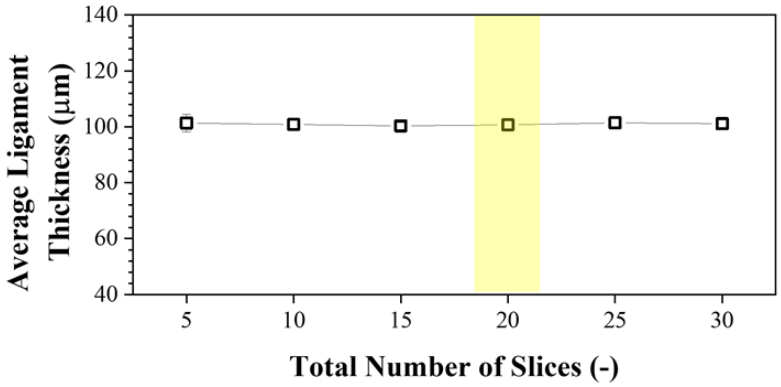

Figure A.4.4 – Ligament thickness of nickel foam as it changes with number of CT slices.

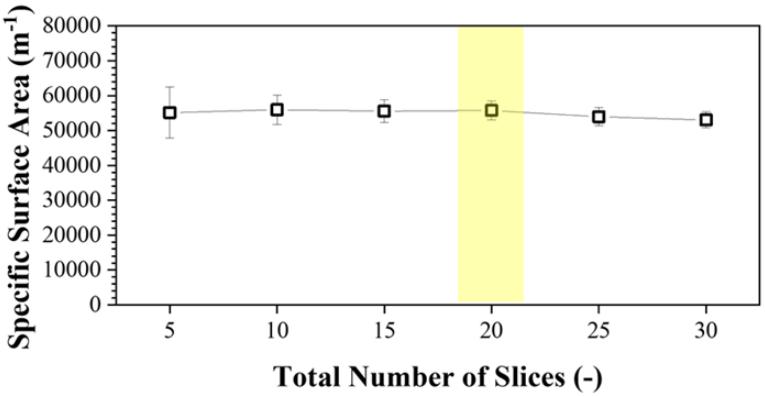

Figure A.4.5 – Specific surface area of nickel foam as it changes with number of CT slices.

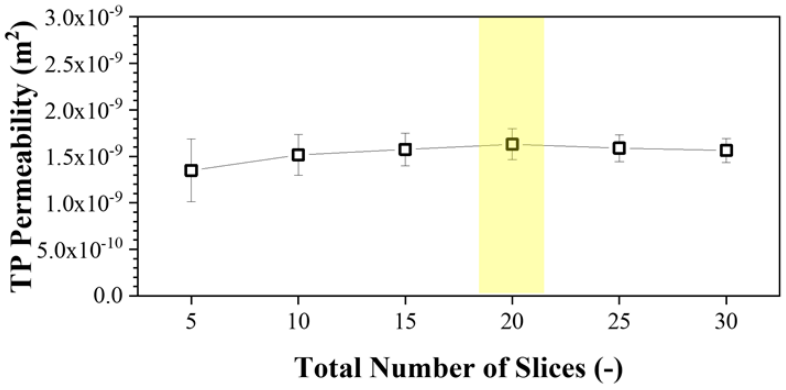

(a)

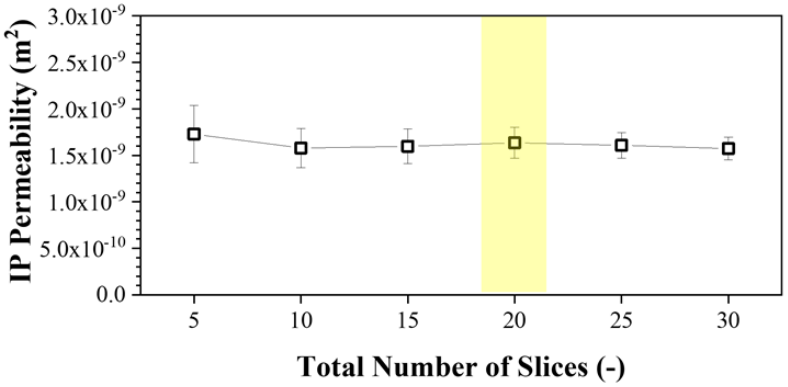

(b)

Figure A.4.6 – (a) Through-plane and (b) in-plane gas permeability of nickel foam as they change with number of CT slices.

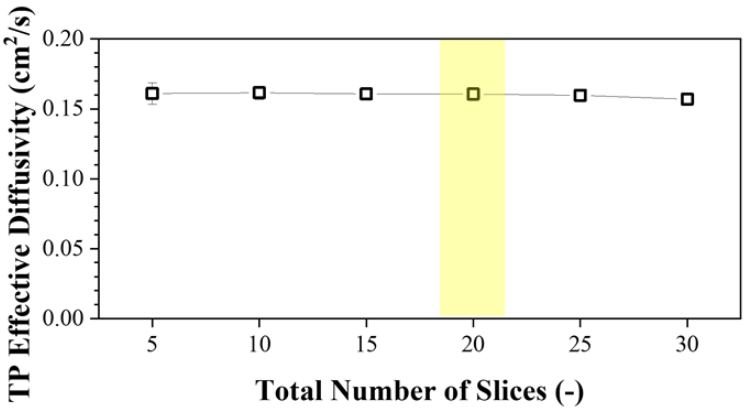

(a)

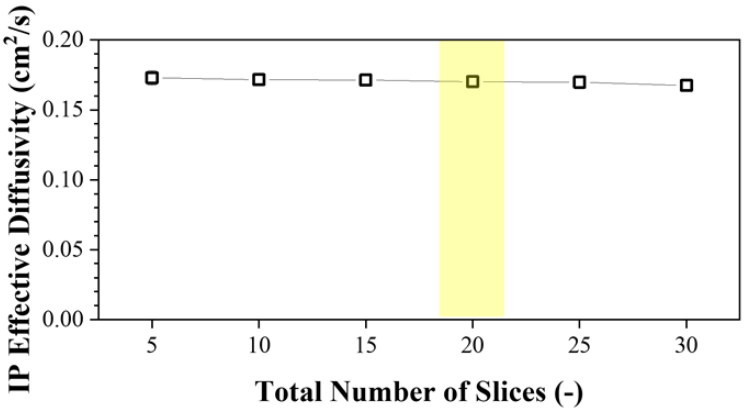

(b)

Figure A.4.7 – (a) Through-plane and (b) in-plane effective oxygen diffusivity of nickel foam as they change with number of CT slices.

APPENDIX – V

The Impact of Outlet Oxygen Concentration on the Molar Flux and Effective Diffusivity under Various Compression Ratios

Table A.5.1 – The effect of outlet oxygen concentration on the through-plane molar flux and the through-plane effective diffusivity of oxygen into nitrogen under 0, 20 and 40% compression ratios for the 200th CT slice.

Compression Ratio (%)	Inlet Oxygen Concentration (C_{in},O_2), [mol/m^3]	Outlet Oxygen Concentration (C_{out},O_2) [mol/m^3]	Oxygen Concentration difference (ΔC) [mol/m^3]	Molar Flux (J) [mol/(m^2 s)]	The Effective Diffusivity of Oxygen into Nitrogen (D_{eff}) [cm^2/s]
0	8.73	8.48	0.25	0.0039743	0.1669
0	8.73	8.23	0.5	0.0079486	0.1669
0	8.73	7.98	0.75	0.0119229	0.1669
0	8.73	7.73	1	0.0158971	0.1669
0	8.73	7.48	1.25	0.0198714	0.1669
0	8.73	7.23	1.5	0.0238457	0.1669
0	8.73	6.98	1.75	0.02782	0.1669
20	8.73	8.48	0.25	0.004734	0.1591
20	8.73	8.23	0.5	0.009467	0.1591
20	8.73	7.98	0.75	0.014201	0.1591
20	8.73	7.73	1	0.018935	0.1591
20	8.73	7.48	1.25	0.023668	0.1591

20	8.73	7.23	1.5	0.028402	0.1591
20	8.73	6.98	1.75	0.033135	0.1591
40	8.73	8.48	0.25	0.006372	0.1580
40	8.73	8.23	0.5	0.012744	0.1580
40	8.73	7.98	0.75	0.019117	0.1580
40	8.73	7.73	1	0.025489	0.1580
40	8.73	7.48	1.25	0.031861	0.1580
40	8.73	7.23	1.5	0.038233	0.1580
40	8.73	6.98	1.75	0.044605	0.1580

Table A.5.2 – The effect of outlet oxygen concentration on the in-plane molar flux and the in-plane effective diffusivity of oxygen into nitrogen under 0, 20 and 40% compression ratios for the 200th CT slice.

Compression Ratio (%)	Inlet Oxygen Concentration (C_{in},O_2), [mol/m^3]	Outlet Oxygen Concentration (C_{out},O_2) [mol/m^3]	Oxygen Concentration difference (ΔC) [mol/m^3]	Molar Flux (J) [mol/(m^2 s)]	The Effective Diffusivity of Oxygen into Nitrogen (D_{eff}) [cm^2/s]
0	8.73	8.48	0.25	0.0006639	0.1766
0	8.73	8.23	0.5	0.0013277	0.1766
0	8.73	7.98	0.75	0.0019916	0.1766
0	8.73	7.73	1	0.0026555	0.1766
0	8.73	7.48	1.25	0.0033194	0.1766
0	8.73	7.23	1.5	0.0039832	0.1766

0	8.73	6.98	1.75	0.0046471	0.1766
20	8.73	8.48	0.25	0.000614	0.1633
20	8.73	8.23	0.5	0.001228	0.1633
20	8.73	7.98	0.75	0.001842	0.1633
20	8.73	7.73	1	0.002455	0.1633
20	8.73	7.48	1.25	0.003069	0.1633
20	8.73	7.23	1.5	0.003683	0.1633
20	8.73	6.98	1.75	0.004297	0.1633
40	8.73	8.48	0.25	0.000606	0.1612
40	8.73	8.23	0.5	0.001212	0.1612
40	8.73	7.98	0.75	0.001818	0.1612
40	8.73	7.73	1	0.002423	0.1612
40	8.73	7.48	1.25	0.003029	0.1612
40	8.73	7.23	1.5	0.003635	0.1612
40	8.73	6.98	1.75	0.004241	0.1612

APPENDIX – VI

Oxygen and Water Mole Fraction Distribution

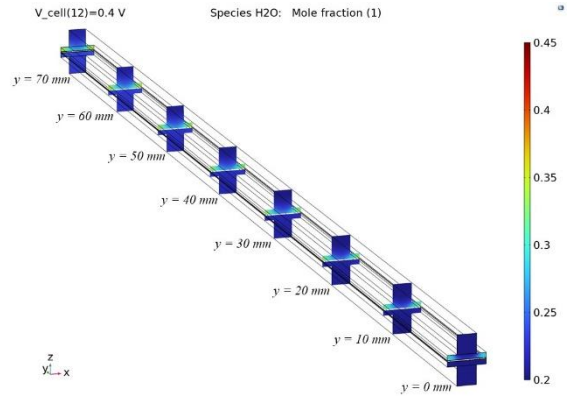

(a)

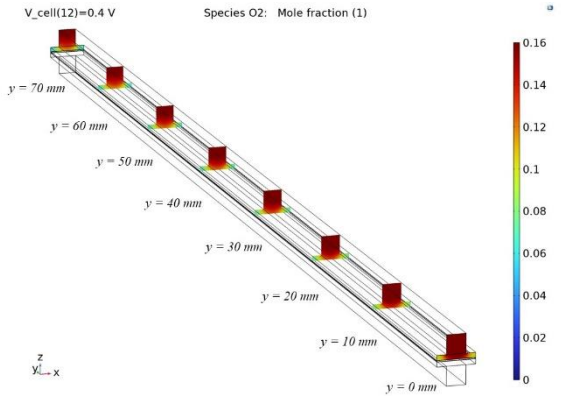

(b)

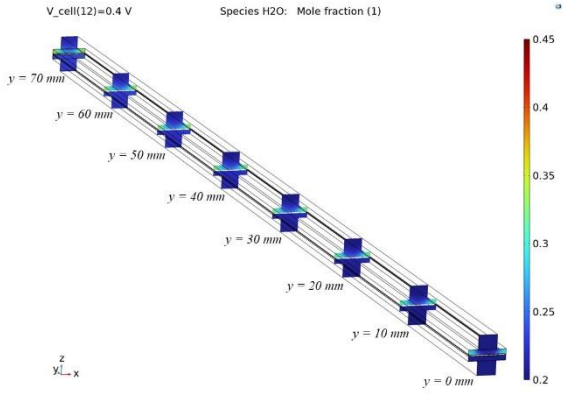

(c)

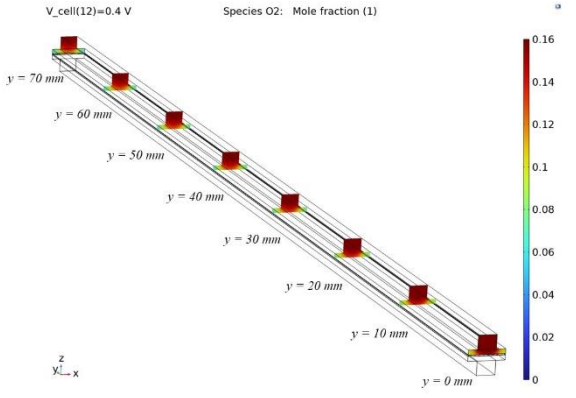

(d)

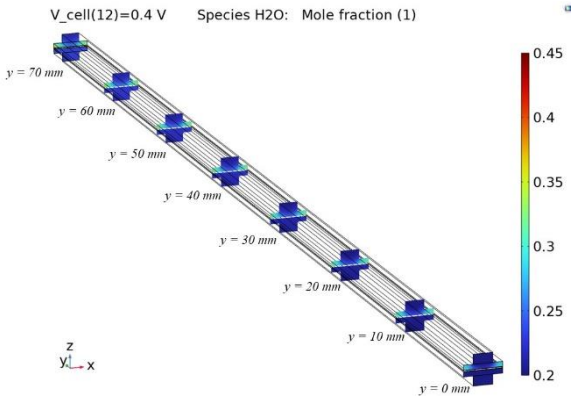

(e)

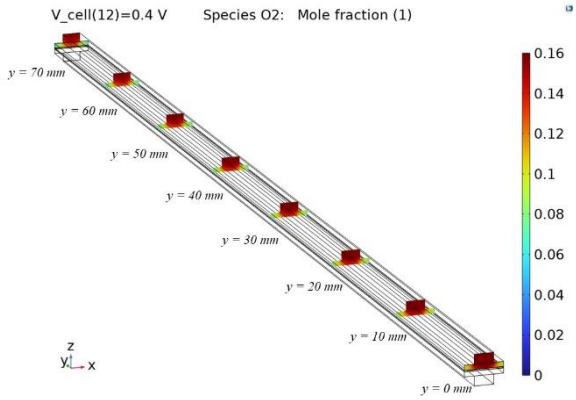

(f)

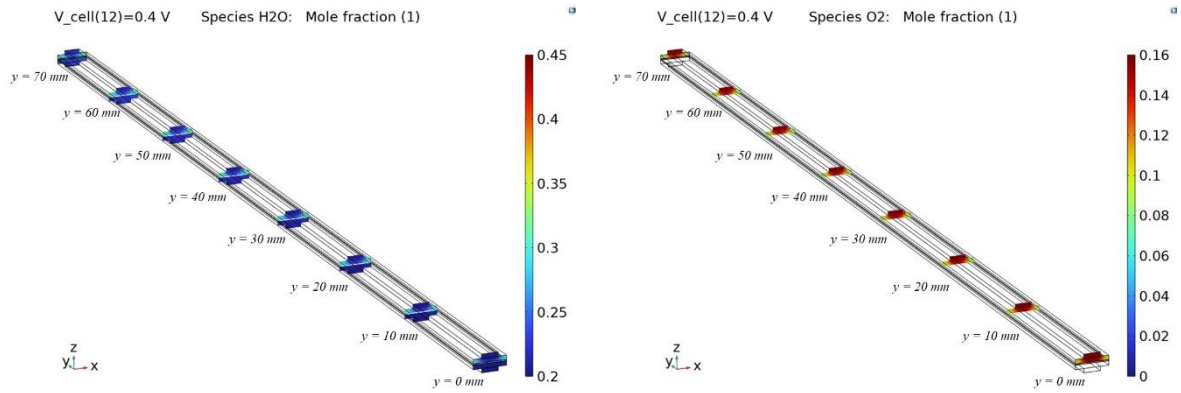

(g) (h)

Figure A.6.1 – Water and oxygen mole fraction distribution within the modelled fuel cell equipped with carbon fibre-based GDLs for four different channel heights: 1 mm (a and b), 0.75 mm (c and d), 0.5 mm (e and f), and 0.25 mm (g and h).

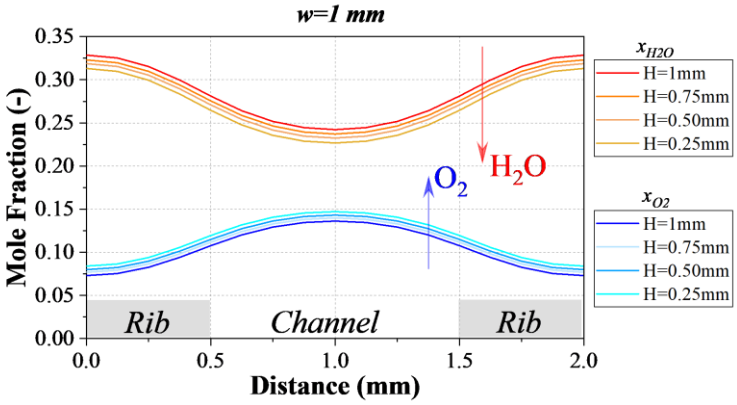

(a)

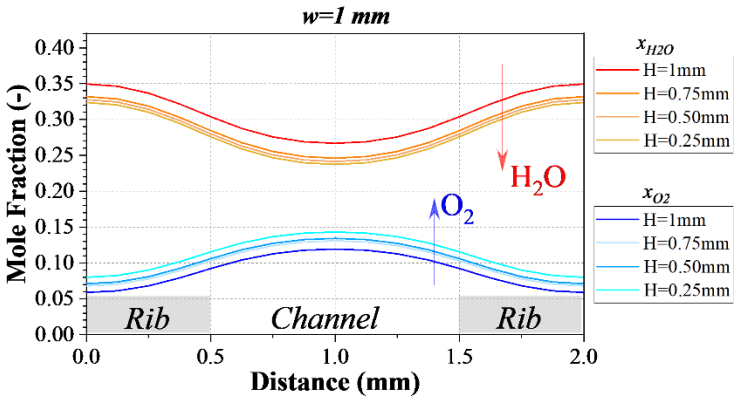

(b)

Figure A.6.2 – Water and oxygen mole fractions at 0.4 V at the interface between the cathode carbon fibre-based GDL and the cathode catalyst layer near: (a) the inlet (y = 10 mm) and (b) the outlet across different channel heights with 1 mm channel width.

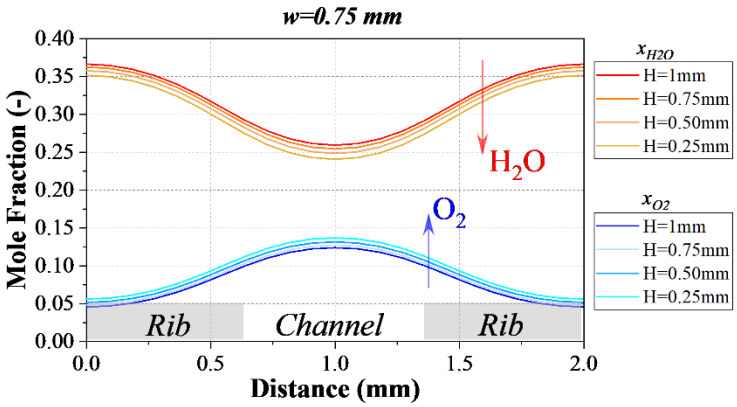

(a)

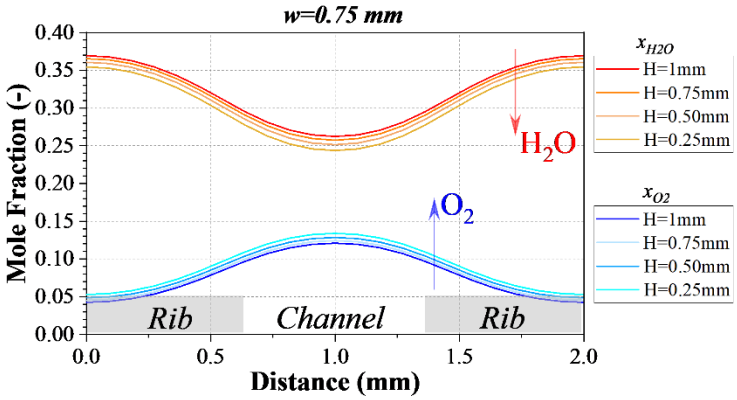

(b)

Figure A.6.3 – Water and oxygen mole fractions at 0.4 V at the interface between the cathode carbon fibre-based GDL and the cathode catalyst layer near: (a) the inlet (y = 10 mm) and (b) the outlet across different channel heights with 0.75 mm channel width.

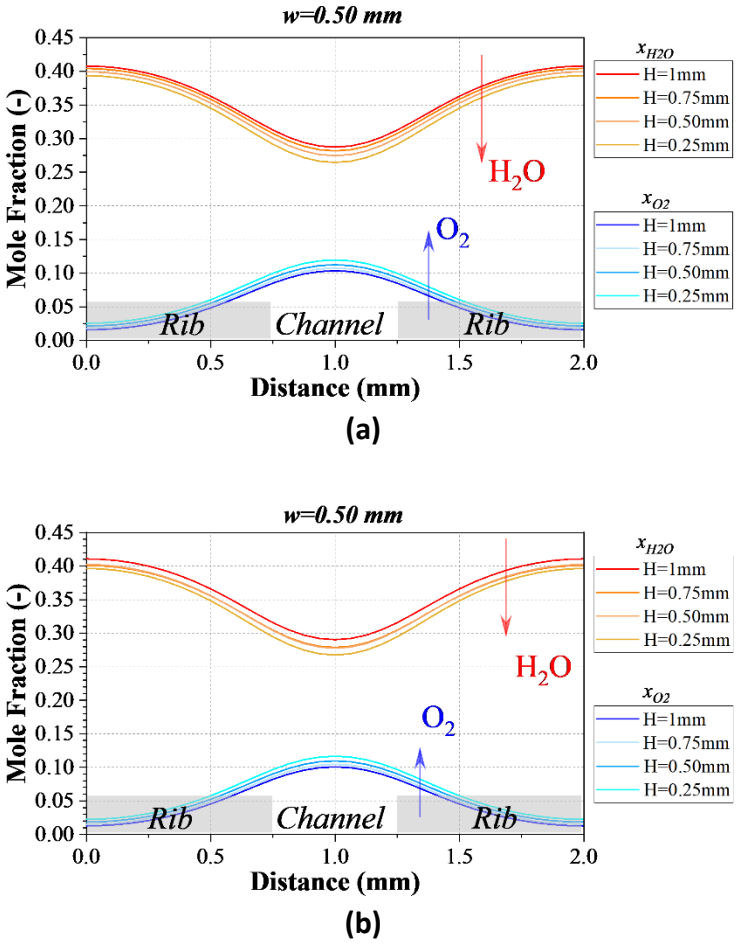

Figure A.6.4 – Water and oxygen mole fractions at 0.4 V at the interface between the cathode carbon fibre-based GDL and the cathode catalyst layer near: (a) the inlet (y = 10 mm) and (b) the outlet across different channel heights with 0.5 mm channel width.

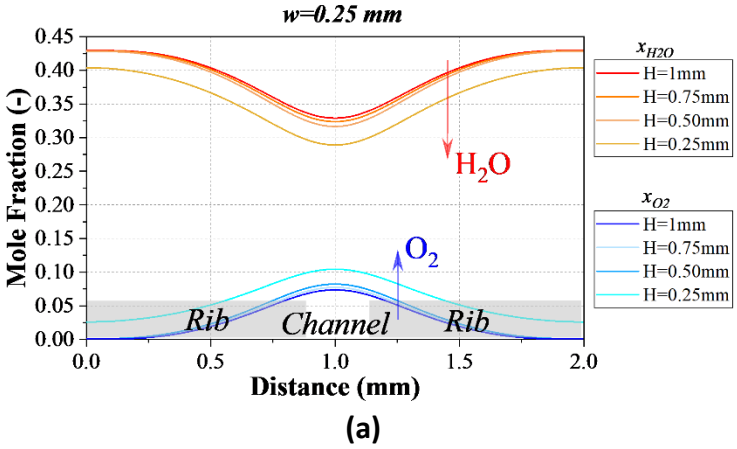

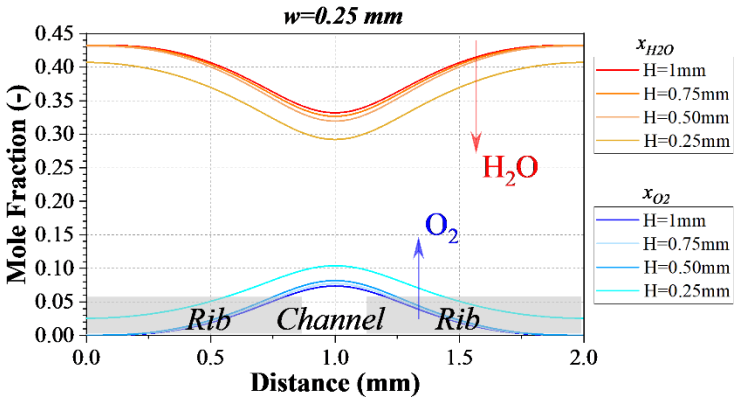

(b)

Figure A.6.5 – Water and oxygen mole fractions at 0.4 V at the interface between the cathode carbon fibre-based GDL and the cathode catalyst layer near: (a) the inlet (y = 10 mm) and (b) the outlet across different channel heights with 0.25 mm channel width.

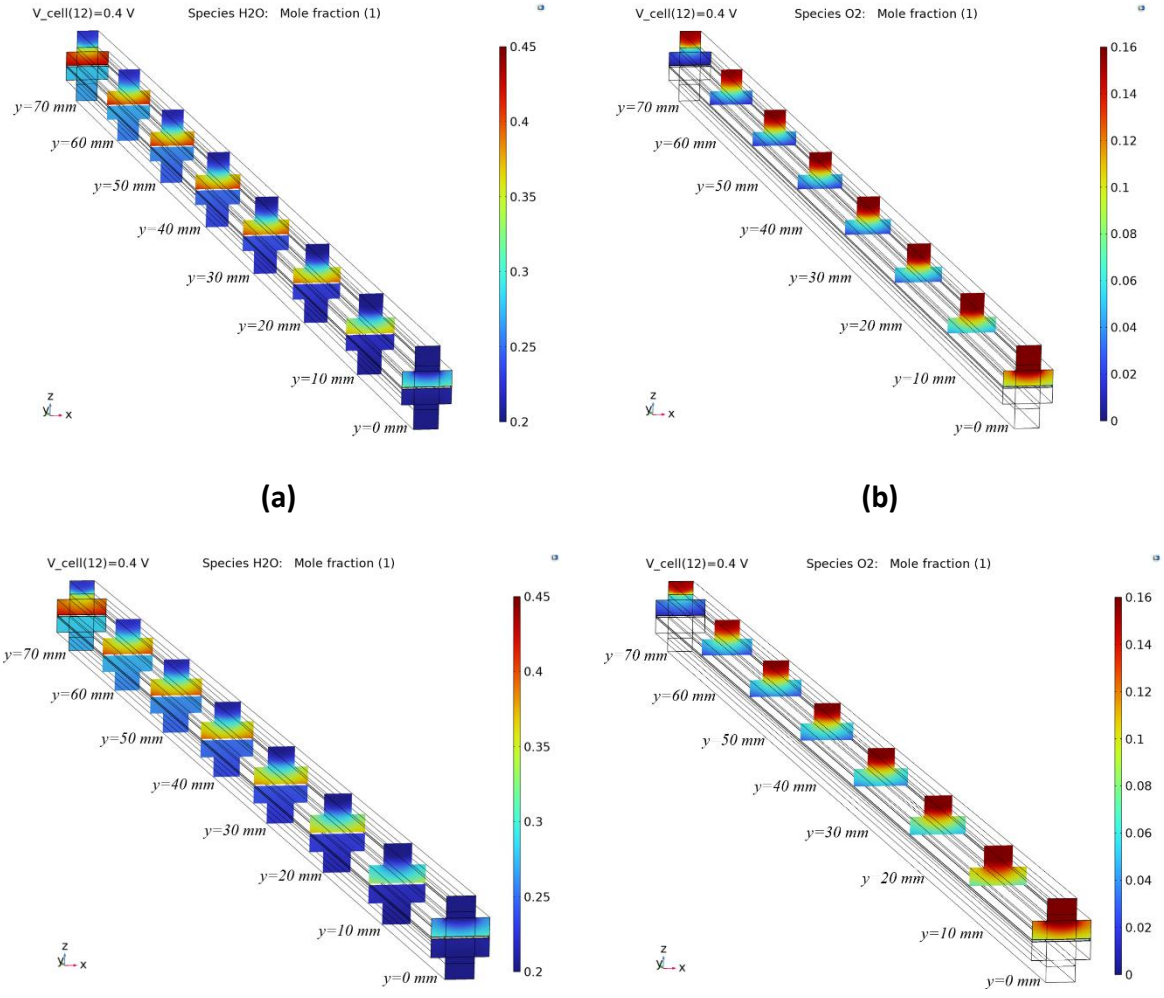

(a) (b)

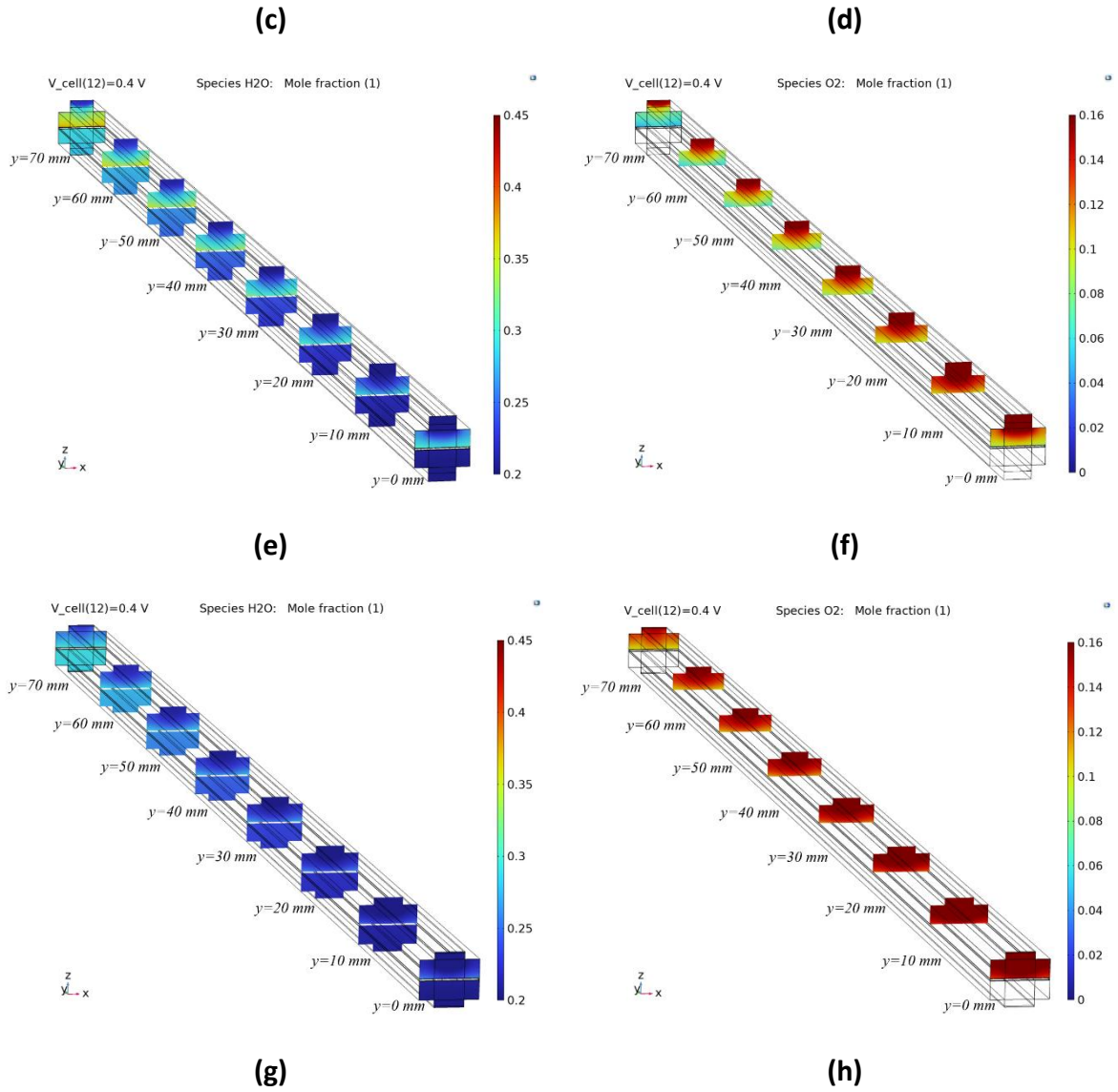

Figure A.6.6 – Water and oxygen mole fraction distribution within the modelled fuel cell equipped with nickel foam-based GDLs for four different channel heights: 1 mm (a and b), 0.75 mm (c and d), 0.5 mm (e and f), and 0.25 mm (g and h).

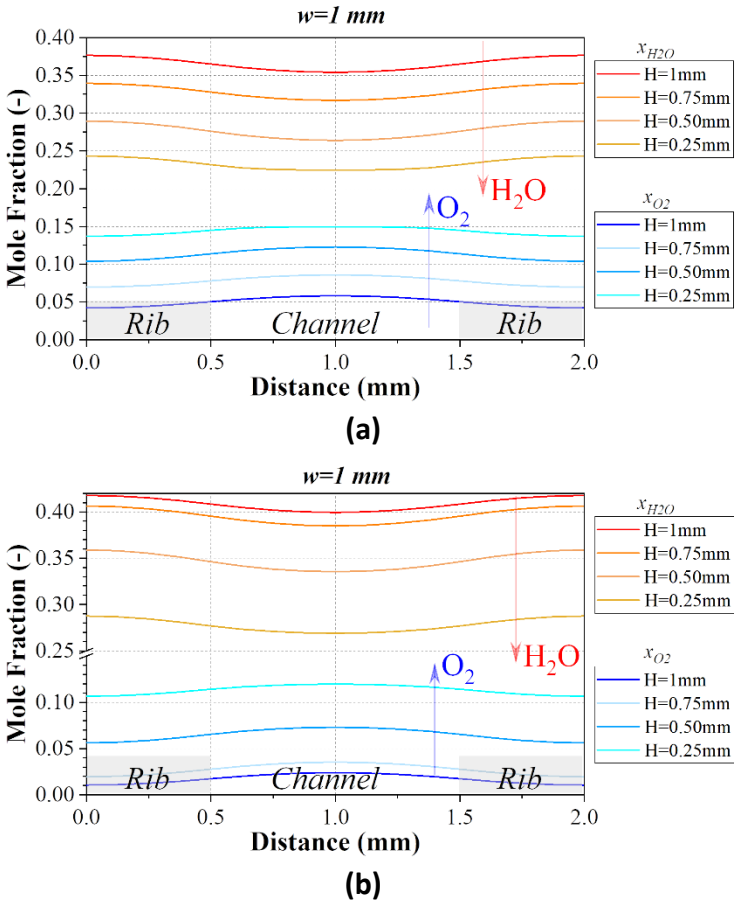

Figure A.6.7 – Water and oxygen mole fractions at 0.4 V at the interface between the cathode nickel foam-based GDL and the cathode catalyst layer near: (a) the inlet (y = 10 mm) and (b) the outlet across different channel heights with 1 mm channel width.

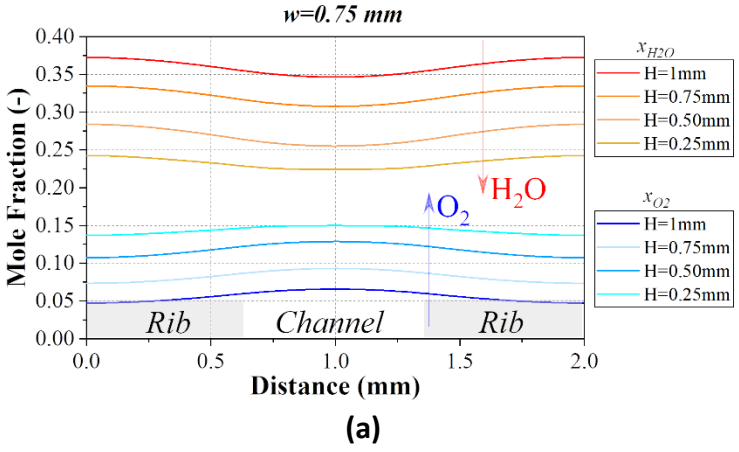

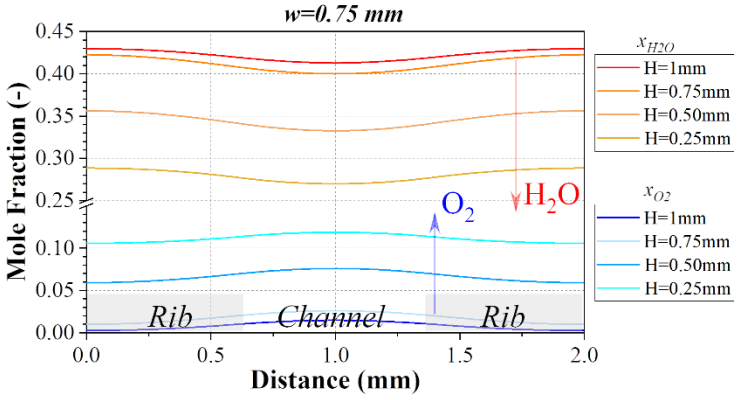

(b)

Figure A.6.8 – Water and oxygen mole fractions at 0.4 V at the interface between the cathode nickel foam-based GDL and the cathode catalyst layer near: (a) the inlet (y = 10 mm) and (b) the outlet across different channel heights with 0.75 mm channel width.

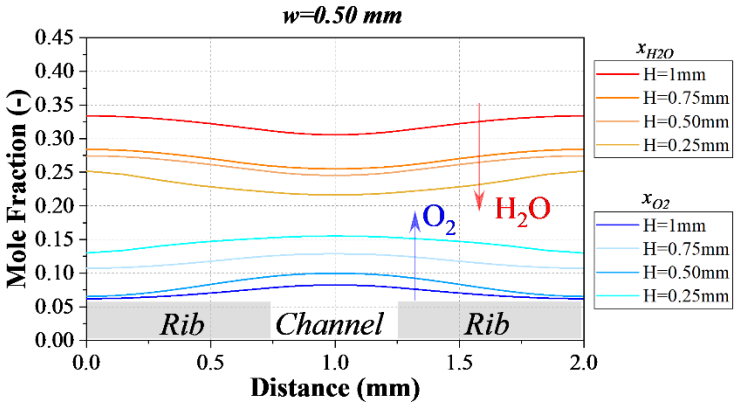

(a)

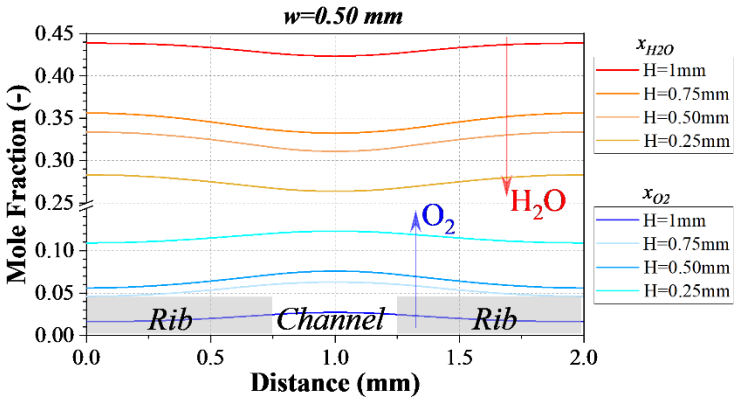

(b)

Figure A.6.9 – Water and oxygen mole fractions at 0.4 V at the interface between the cathode nickel foam-based GDL and the cathode catalyst layer near: (a) the inlet (y = 10 mm) and (b) the outlet across different channel heights with 0.50 mm channel width.

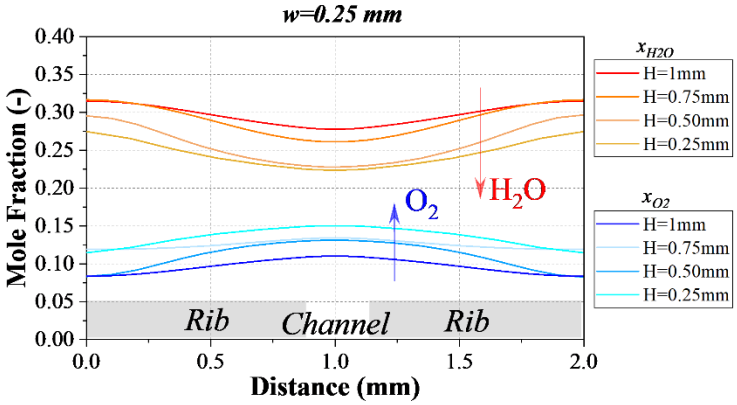

(a)

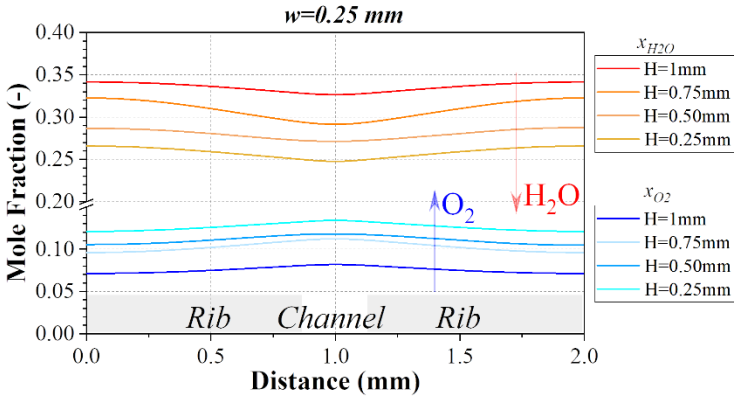

(b)

Figure A.6.10 – Water and oxygen mole fractions at 0.4 V at the interface between the cathode nickel foam-based GDL and the cathode catalyst layer near: (a) the inlet (y = 10 mm) and (b) the outlet across different channel heights with 0.25 mm channel width.